Modelling the vibrations generated by turbulent flows in ducts

Florian Hugues

Par **Florian HUGUES**

Modelling the vibrations generated by turbulent flows in ducts

Thèse présentée
pour l'obtention du grade
de Docteur de l'UTC

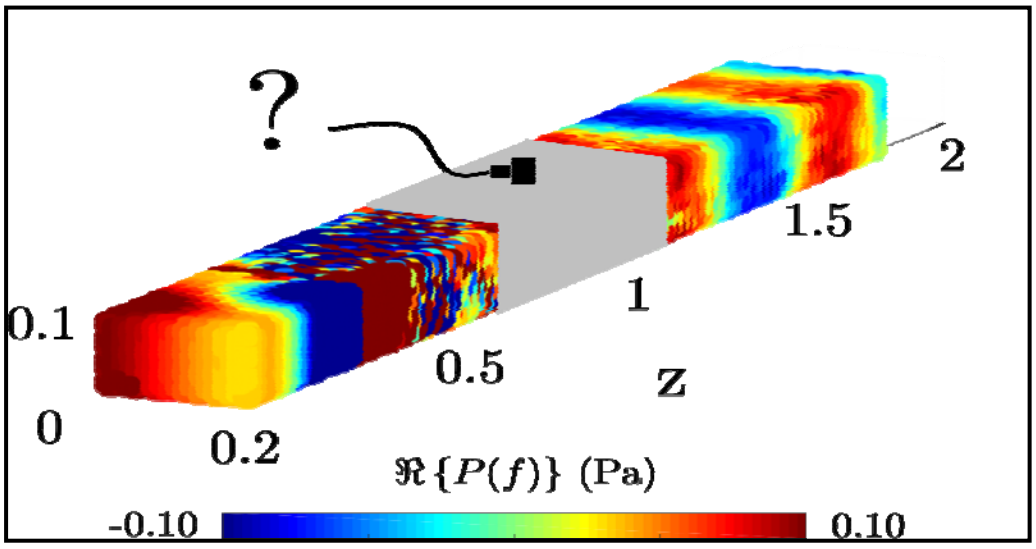

Soutenue le 20 décembre 2018
Spécialité : Acoustique et Vibrations : Unité de recherche en Mécanique - Laboratoire Roberval (UMR-7337)
D2470

Thèse de doctorat

de

l'Université de Technologie de Compiègne

Spécialité : Acoustique et Vibrations

Présentée par

Florian HUGUES

Modelling the vibrations generated by turbulent flows in ducts

Soutenue le 20 décembre 2018 devant le jury composé de :

Pierre-Olivier MATTEI	Chargé de Recherche, CNRS HDR, LMA, Marseille, France	(Rapporteur)
Laurent MAXIT	Maître de Conférences, HDR, LVA, Lyon, France	(Rapporteur)
Stephen A. HAMBRIC	Professeur, ARL/Penn State, State College, USA	(Examinateur)
Marie-Laure GOBERT	Maître de conférences, INSA Centre Val de Loire, Blois, France	(Examinateur)
Jean-Michel VILLE	Professeur des Universités, UTC, Compiègne, France	(Examinateur)
Emmanuel PERREY-DEBAIN	Professeur des Universités, UTC, Compiègne, France	(Directeur de thèse)
Nicolas DAUCHEZ	Professeur des Universités, UTC, Compiègne, France	(Co-Directeur de thèse)

utc
SORBONNE UNIVERSITES

Laboratoire **Roberval**
Unité de recherche en mécanique

Remerciements

Ce manuscrit et les résultats qui y sont présentés sont le fruit d'un travail de trois ans que je n'aurai pas pu réaliser seul. C'est pourquoi je tiens à remercier ici toutes les personnes qui m'ont aidé de manière professionnelle ou personnelle.

Je tiens, en premier lieu, à remercier très chaleureusement mon directeur de thèse Emmanuel Perrey-Debain, pour son aide précieuse, sa disponibilité, ses conseils et la liberté qu'il m'a accordé durant ces trois années. Je remercie également mon co-directeur de thèse Nicolas Dauchez. C'était un plaisir d'échanger et de travailler ensemble pour porter la filière AVI au sein des étudiants UTC, à travers notamment l'enseignement ou de discussions plus informelles.

Je remercie Pierre-Olivier Mattei et Laurent Maxit, pour avoir accepté de rapporter ma thèse.

Je remercie Marie-Laure Gobert et Jean-Michel Ville, pour avoir accepté d'examiner ma thèse. Je tiens à remercier sincèrement Stephen A. Hambric. Ses publications ont eu un grand impact dans ma formation en aéro-vibro-acoustique, ainsi que l'invitation à la conférence FLINOVIA.

Un grand merci à toute l'équipe AVI du laboratoire Roberval qui m'a soutenu et aidé grâce à leurs conseils avisés. Je tiens à remercier notamment Félix Foucart et Jean-Marc Gherbezza pour leur sympathie, leur disponibilité et l'aide qu'ils m'ont accordées pour la réalisation des expérimentations. Les anciens qui sont partis : Antoine, B. Saâd et P. Nicolas qui m'ont formé sur le banc d'essai et le logiciel CFD. Une pensée aux étudiants que j'ai pu encadrer, notamment Dorine, L. Saad et R. Nicolas, qui m'ont aidé dans mes travaux de thèse. Je salue également tous les autres doctorants et leur souhaite de réussir dans leurs travaux. Je souhaite également remercier, plus particulièrement, Thibaut, Lei Lei, Amine et Johan pour tout ce que nous avons pu partager durant cette thèse.

Pour terminer, je souhaite remercier affectueusement ma famille pour votre soutien indéfectible tout au long de mon cursus à l'UTC.

Enfin, je remercie ma compagne, Nadja, pour son soutien et son amour.

Résumé

La prédiction des vibrations induites par un écoulement est essentielle dans la conception des conduits de nombreuses installations industrielles, en particulier dans l'industrie du gaz. Notre étude concerne la prévision du bruit et la vibration des conduits soumis à un écoulement turbulent à faible nombre de Mach. Notre objectif est de présenter une étude numérique et expérimentale permettant aux ingénieurs de mieux comprendre le couplage entre l'excitation aléatoire et le conduit pour deux géométries (circulaire ou rectangulaire). Une approche expérimentale est développée et utilisée pour valider les prévisions numériques. Deux cas sont étudiés : (i) un conduit droit sans singularité, où les modes acoustiques du conduit sont excités par une couche limite turbulente (TBL) et (ii) un conduit droit avec un diaphragme inséré en amont qui génère une source acoustique localisée. La contribution acoustique est déterminée soit par des méthodes de mesure d'interspectres, soit à l'aide des outils de mécanique des fluides numérique (CFD) et d'analogies aéroacoustiques. La réponse de la structure est estimée par une approche dite de 'couplage faible' qui utilise des fonctions de transfert modale d'un conduit fini simplement appuyé. Les mesures conduiront à évaluer et suggérer des améliorations de modèles empiriques existants de densité interspectrale de puissance (CPSD) dans un contexte d'écoulements internes turbulents. Une analyse modale expérimentale d'un conduit rectangulaire finie est confrontée à des méthodes de calcul pour évaluer l'effet des conditions aux limites, du rayonnement acoustique et de l'amortissement aérodynamique. Le couplage fluide-structure est analysé par la fonction de 'joint acceptance' à la fois dans le domaine spatial et dans le domaine des nombres d'onde. L'excitation comprend à la fois les contributions acoustiques et hydrodynamiques à l'aide des CPSD exprimées sur la base des fonctions de cohérence de type Corcos, champ diffus et modes acoustiques d'ordre élevé. Enfin, les études numériques et expérimentales de cette thèse ont été utilisées pour développer un cadre d'étude et de modélisation du bruit et des vibrations dans les conduites, qui relie la dynamique des fluides, les modèles analytiques et empiriques à des techniques efficaces d'analyse aléatoire.

Abstract

Pipeline and duct vibrations can cause a range of issues from unplanned shutdowns to decreased equipment life time. Thus, the prediction of flow-induced vibrations is essential in piping design in many industrial plants, especially, for Gas industry. This study deals with the prediction of pipe flow noise and vibration at low Mach number. We aim to present a numerical and experimental study which can offer engineers a better understanding of the coupling between random excitation and duct section for two geometries (circular or rectangular). An experimental facility and measurement approach is developed and used to validate numerical predictions. Two cases are investigated: (i) a straight duct with no singularity, duct acoustic modes are excited by the Turbulent Boundary Layer (TBL) and (ii) a straight duct with a diaphragm inserted upstream generating a localized acoustic source. The acoustic contribution is either measured *via* cross-spectra based methods or calculated using Computational Fluid Dynamics (CFD) and aeroacoustic analogies. The response of the structure is estimated *via* a 'blocked' approach using analytical modal Frequency Response Functions (FRFs) of a simply supported finite duct. Measurements will lead to evaluate and suggest improvements to existing Cross Power Spectral Density (CPSD) empirical models in a context of internal turbulent flows. Experimental modal analysis of a finite rectangular duct are confronted to computational methods to assess the effect of the Boundary Conditions (BCs), the resistive damping from coupling with the internal acoustic medium and aerodynamic damping. The fluid-structure coupling is analyzed through the joint acceptance function both in the spatial and wavenumber domain. The excitation includes both the acoustic and hydrodynamic contributions using CPSD written on the basis of Corcos, Diffuse Acoustic Field (DAF) and acoustic duct mode coherence functions. Finally, the numerical and experimental studies in this thesis were used to develop a framework for studying and modelling pipe flow noise and vibration which links CFD, analytical and empirical models to efficient random analysis techniques.

Keywords: Flow induced Noise and Vibration, Aero-Vibro-Acoustics, Turbulent Flow, Joint Acceptance Function, Acoustic duct modes.

Contents

Introduction

0.1 Context

This PhD originated from 3 previous PhD programs. David [1] started his PhD in 2013 to study the vibration of gas transport network in partnership with FIVES company, a world's leader for equipment used in aluminum production. The vibration response of finite duct with rectangular cross-section has been investigated using empirical models to calculate the wall pressure field. In parallel, Bennouna [2] and Papaxanthos [3] started their PhD the same year in partnership with the CEVAS (Conception d'Equipements de Ventilation d'Air Silencieux) project, funded by the Picardie region and FEDER (Fonds Européen de Développement Régional). The aeroacoustic of Heating, Ventilation and Air-Conditioning (HVAC) components has been studied both numerically and experimentally. The present PhD was initiated to combine the main results of these previous studies in order to tackle more broadly pipe vibrations generated by internal flow disturbances (see Fig. 1). The following PhD is founded by the French government.

0.2 Present Research Objectives

Flow induced noise vibrations are often encountered in piping systems in a variety of applications: (air conditioning systems (HVAC) or gas transmission pipelines in the industry, for instance). Pipe vibrations can cause noise disturbances and premature aging structures sometimes requiring interventions after installation, difficult to implement and very expensive.

The main objective of this thesis is to develop numerical models for a better understanding of the physical phenomena of noise generation and the vibration generated by (i) a turbulent flow in a straight duct and (ii) a vortex shedding after a discontinuity in the pipe (elbow, constriction or the presence of a diaphragm).

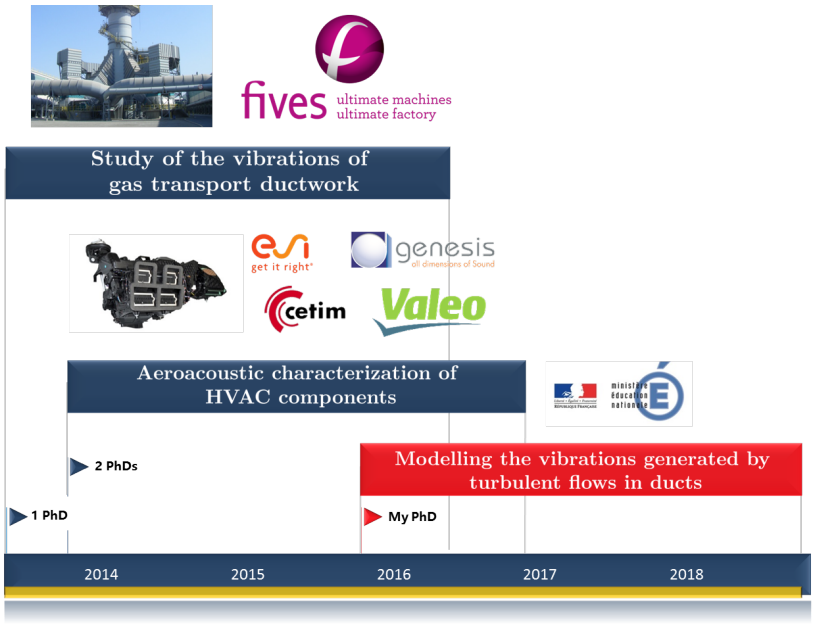

Figure 1: Origins of the present PhD thesis.

Simulations (numerical models) will be confronted with experimental data, hereby by two strategies:

- Analysis of the generation mechanisms for the unsteady wall pressure by using numerical simulation with CFD commercial code (Computational Fluid Dynamics): STAR-CCM+.
- Development and use of appropriate numerical methods to develop a framework for studying and modelling pipe flow noise and vibration which links CFD, analytical and empirical models to efficient random analysis techniques.

This work has been partly addressed in 2 papers published during the first and second year of the PhD:

- A paper in the Journal of Sound and Vibration [4] as second author. Hence, the first version paper (see Chapter 3 in [1]) could not be published in its current form.
- A paper in the book research Flinovia II [5] as main author appended to this thesis in Chapter 5.

The chapter 4 is written in the form of a paper, yet to be submitted to an academic journal.

Chapter 1

Background and Literature review

This chapter presents the state-of-the-art research in flow induced noise and vibration for piping systems submitted to internal turbulent flow at low Mach number. The relation between internal wall pressure fluctuations and the structure response of the pipe wall is highlighted using modern and standard representations. A choice of methodology will be proposed to tackle flow induced noise and vibration issues in a context of finite pipe excited by low Mach number flows.

Excitation of structures by flows and the resulting vibration and radiated noise is a problem of practical interest in various fields; as example of applications one can cite the prediction and reduction of cabin noise in aircrafts, sound in sonar domes in underwater acoustics, and vibration and noise generated in pipes. Analyses of the vibroacoustic response of a structure to the stochastic loading by TBL pressure fluctuations have been investigated extensively over the past forty years. The list is not exhaustive and we just cite research which may offer a relevant framework for this PhD. A starting point is Blake's book [6, 7], which remains to this day, a reference in the field of Flow induced Noise and Vibration. Due to the interdisciplinary nature of the subject, this book unifies all disciplines: fluid mechanics, structural dynamics, vibration, acoustics, and statistics.

For a more specific application in the field of pipe flow noise and vibration, the reader is referred to Norton's book [8] (see Chap.7) for discussion on a case study of steel pipelines with internal gas flows. Hambric *et al.* published an overview about noise sources and transmission in piping systems [9], and a review of analysis methods for structural and acoustic noise sources due to turbulent flow through an elbow [10]. Durant *et al.* performed both numerical simulation and experimental investigation of the vibroacoustic response of a thin cylindrical shell excited by a turbulent internal air flow [11, 12]. Bonness *et al.* also performed a complete analysis with internal water flow [13, 14].

1.1 Fundamentals of low Mach number wall pressure fluctuations

The basic fluid dynamics equations for an incompressible fluid in terms of velocity and pressure fluctuations writes

$$\frac{\partial(\rho u_i)}{\partial x_i} = 0, \tag{1.1}$$

$$\frac{\partial(\rho u_i)}{\partial t} + \frac{\partial(\rho u_j u_i)}{\partial x_j} = -\frac{\partial p}{\partial x_i} + \frac{\partial \tau_{ij}}{\partial x_j}, \tag{1.2}$$

where ρ, u_i and p are the density, the i-component of the velocity and the pressure. The viscous stress tensor τ_{ij} writes

$$\tau_{ij} = \mu \left(\frac{\partial u_i}{\partial x_j} + \frac{\partial u_j}{\partial x_i} \right), \tag{1.3}$$

where μ is the dynamical viscosity of the fluid. The equation governing the pressure field is obtained by taking the divergence of the momentum equation. It writes for an incompressible flow

$$\nabla^2 p = -\rho \frac{\partial u_i}{\partial x_j} \frac{\partial u_j}{\partial x_i}. \tag{1.4}$$

In practice, the pressure field governed by Eq.(1.4) is not analyzed in the time or frequency domain due to its random nature. Hence, the overall framework for the analysis is based on random analyze techniques. Thus, mean quadratic quantities, spectra, space-time correlation, cross-spectra are required to analysis the flow field. All statistical ingredients necessary to calculate these quantities are recalled in Appendix A. In general, the key quantity to evaluate the influence of the flow is the cross spectral density (CSD) of wall pressure fluctuations. Three approaches can be distinguished in order to evaluate this quantity:

1. The time resolved flow field is available (unsteady approach) and averaged quantities are computed *a posteriori*.

2. The time resolved flow is not available and a statistical expression is required (through the Poisson equation (1.4)). This statistical approach uses time averaged turbulence statistics from Reynolds-averaged Navier-Stokes Simulation (RANS).

3. Semi-empirical models based on experimental data are used.

The first approach consists of performing unsteady simulation such as Direct Numerical Simulations (DNS) or Large Eddy Simulations (LES). A direct estimation of the time-evolution of the pressure fluctuations allows to obtain statistical properties by signal post-processing [15]. To take into account compressibility effects (the acoustic part of the pressure fluctuations), the Poisson equation (1.4) has to be replaced by a 'wave equation'. However, and despite the continuous development of computational tools and resources, it is still challenging to solve aeroacoustic problems following a direct manner, such as, *via* a single calculation. In general, the simulation method

is a two-step approach assuming the decoupling of noise generation and propagation [16–18]. This leads to different strategies to compute the aeroacoustic field as shown in Fig. 1.1. In Chapter 5, a two-step approach is proposed to calculate the acoustic part of the pressure fluctuations in a context of pipeline singularity using LES and aeroacoustic analogies (green line in Fig. 1.1). It will allow to quantify the relative weight of each contribution (acoustic and hydrodynamic) on the structure response.

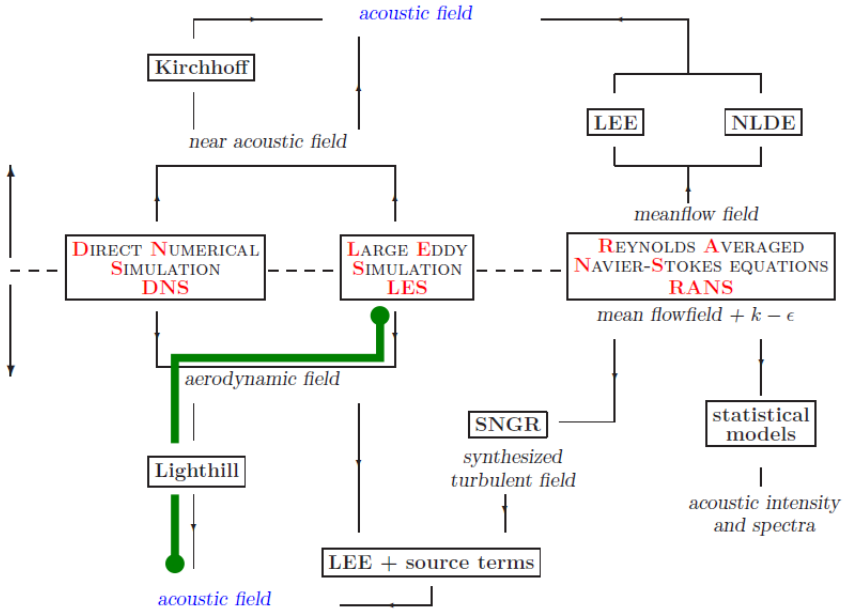

Figure 1.1: Different numerical strategies to compute aerodynamic noise from [19]. **LEE**: Linearized Euler's Equations; **NLDE**: Non Linear Disturbance Equations, **SNGR**: Stochastic Noise Generation and Radiation. In green, the strategy adopted in Chapter 5.

The second approach consists in forming a statistical expression (through the Poisson equation (1.4)) expressed as the space-time correlation function, or its wavevector frequency spectrum. In general, it started with analytical expressions [20] of the fluctuating pressure which is calculated from the convolution of the free-space Green function of the Poisson equation (1.4) with the right-hand side source term. A statistical expression is written in term of correlation function (also called surface-pressure covariance). The cross-spectral density function defined as the Fourier transform of the space-time correlation function is also frequently used. Statistical modelling has been first developed for jet noise evaluation. The input data needed by the stochastic model only stem from preliminary steady RANS computations. The k-ϵ model is

usually chosen to provide turbulence statistics. The main idea is that turbulent field is generated by a sum of Fourier modes [21]. Bailly *et al.* [22] used this idea to predict the noise of free turbulent flows using a volume source model based on the Stochastic Noise Generation and Radiation (SNGR) approach [23–25]. Further improvement of these methods have been conducted at ONERA (see for instance [26–28]). Tam and Auriault also developed a stochastic method to evaluate jet mixing noise from fine scale turbulence [29]. Hu [30] predicted the turbulent boundary layer wall pressure fluctuations by solving Poisson equation using synthetic turbulence generated by the Fast Random Particle-Mesh Method (FRPM) of Ewert [31, 32]. Here, the velocity fluctuations are deduced from the convolution of the correlation functions with a filter based on the spatial filtering of white noise. Peltier and Hambric [33] also published a stochastic method to estimate the turbulent-boundary-layer wall-pressure contribution.

The third approach consists of using semi-empirical models based on experimental data. A detailed overview of the last 50 years of development of semi-empirical models to predict the turbulent boundary layer wall pressure frequency spectrum (auto-spectrum, cross-spectrum, wavenumber-spectrum) has been summarized by Hwang [34], whose work is based on observations from Bull [35], Farabee [36] and Blake [37]. Many fundamental experiments have been carried out to measure the characteristics of the wall pressure fluctuations. It started with the measurements of the statistical properties of the wall-pressure field beneath turbulent boundary layers made by Willmarth and Wooldridge [38], Bull [39] and Corcos [40]. Measurements are presented in term of cross-spectral densities and they are found to agree closely with the model proposed by Corcos, which is expressed in a separable form

$$S_{pp}(\mathbf{s}_1 - \mathbf{s}_2, \omega) = \Phi_{pp}(\omega) A(\omega \xi_s / U_c) B(\omega \xi_z / U_c) \exp(-\mathrm{i}\omega \xi_z / U_c), \tag{1.5}$$

where $\mathbf{s}_1 - \mathbf{s}_2 = (\xi_s, \xi_z)$ is the separation vector. Here $\mathbf{s} = (s, z)$ are the coordinates of a point on the duct wall, s corresponds to the spanwise and z the streamwise direction. In this work, we shall follow the work of Durant *et al* [11, 12] for circular pipes and consider the Corcos model for the TBL excitation. Note that the model is no longer truly valid for ducts with rectangular sections due to the corner edges. The TBL is supposed to be fully developed, stationary and homogeneous so that the point auto-spectrum Φ_{pp} is spatially independent and the cross spectrum is only function of the separation vector. The sign in the last exponent depends on the definition of

the Fourier transform. Thus, the CSD of wall pressure fluctuations can be written in its general form as the product of the power spectral density $\Phi_{pp}(\omega)$ and a spatial correlation function $\Gamma(\mathbf{s}_1 - \mathbf{s}_2, \omega)$ as follows:

$$S_{pp}(\mathbf{s}_1 - \mathbf{s}_2, \omega) = \Phi_{pp}(\omega)\Gamma(\mathbf{s}_1 - \mathbf{s}_2, \omega). \tag{1.6}$$

Eq.(1.5) shows that pressure fluctuations are convected with the flow at mean convection velocity U_c. The unknown functions A and B are determined from experimental data and suggested an approximation by decreasing exponential function as

$$A(\omega\xi_s/U_c) = \exp(-|\xi_s|/L_s(\omega)), \quad B(\omega\xi_z/U_c) = \exp(-|\xi_z|/L_z(\omega)), \tag{1.7}$$

where $L_s(\omega)$ and $L_z(\omega)$ are respectively the longitudinal and circumferential correlation lengths of pressure fluctuations. In the standard form of the Corcos model, A and B are expressed in terms of two parameters γ_s and γ_z related to the coherence lengths by $\gamma_s = U_c/(\omega L_s)$ and by $\gamma_z = U_c/(\omega L_z)$.

A quantity of pratical interest in the framework of flow induced noise and vibration is the 2D wavenumber spectrum of pressure fluctuations $\tilde{\Phi}_{pp}(\mathbf{k}, \omega)$. The knowledge of the wavenumber spectrum is essential to study the coupling between the structure and a random pressure load. The 2D wavenumber spectrum can be obtained by taking the spatial Fourier transform of Eq.(1.6) defined as :

$$\tilde{\Phi}_{pp}(\mathbf{k}, \omega) = \Phi_{pp}(\omega) \iint \Gamma(\mathbf{s}_1 - \mathbf{s}_2, \omega)\exp[-\mathrm{i}(k_s\xi_s + k_z\xi_z)]\mathrm{d}\xi_s\mathrm{d}\xi_z, \tag{1.8}$$

with $\mathbf{k} = (k_s, k_z)$, the wavenumbers of a plane structure.

Note that equation (1.8) assume an homogeneous pressure field depending only on the separation vector $\mathbf{s}_1 - \mathbf{s}_2 = (\xi_s, \xi_z)$. In practice, it is also possible to define an estimation of the 2D wavenumber spectrum even in presence of non homogeneous flow. According to the knowledge of temporal (or frequency) pressure field data at each point of a given spatial grid, it writes

$$\tilde{\Phi}_{pp}(\mathbf{k}, \omega) = \lim_{T\to\infty} \lim_{D\to\infty} \frac{2\pi}{T} \frac{(2\pi)^2}{D} \mathbb{E}\left[p(\mathbf{k}, \omega)p^*(\mathbf{k}, \omega)\right], \tag{1.9}$$

where $p(\mathbf{k}, \omega)$ is obtained after successively applying a temporal fourier transform over a time domain T and a spatial fourier transform over a spatial domain D. These steps are recalled in Appendix A and more details can be found in Van Herpe's paper [41]

for the case study of the wind noise from a vehicle's side windows.

The measurement of wavenumber-frequency spectrum has attracted considerable attention for now more than 50 years. The main difficulty is to cover high spatial frequencies (hydrodynamic contribution) and low spatial frequencies (acoustic contribution). First measurements were performed by Wills [42], Blake and Chase [43]. The limitations were primarily due to acoustic contamination and spatial aliasing. More recently, better measurements have been obtained using either linear array of microphones [44], irregular sensor arrangement [45], microphones mounted on a rotating disk [46] or on a spiral-shaped rotative array [47]. These 50 years of measurement has driven the community to adopt the following view of the wavenumber spectrum illustrated in Fig. 1.3. The 1D wavenumber spectrum is here a function of the streamwise wavenumber, k_z, for a fixed frequency ω. The majority of the energy is concentrated in what is termed the convective domain. This part of the spectrum is often referred to as the convective ridge. It is centered on the convective wavenumber, $k_c = \omega/U_c$, where U_c, is the convection velocity. The convection velocity is the speed at which the large scale eddies within the turbulent boundary layer travel. The sonic or acoustic domain ($k_z \simeq \omega/c_0$) is expected to have a local finite peak in the vicinity of k_0. The Corcos wall pressure wavevector frequency spectrum can be obtained by taking the spatial Fourier transform of Eq.(1.5)

$$\tilde{\Phi}_{pp}(\mathbf{k},\omega) = \Phi_{pp}(\omega)\left(\frac{U_c}{\omega}\right)^2 \frac{4\gamma_z\gamma_s}{\left[\gamma_z^2 + \left(1-\frac{k_x}{k_c}\right)^2\right]\left[\gamma_s^2 + \left(\frac{k_y}{k_c}\right)^2\right]}. \tag{1.10}$$

Fig. 1.2 shows the Corcos's coherence function in both the spatial and wavenumber domain. Corcos's spectrum is considered to be 'wavenumber white', since there are only slight variations of the spectral levels in the low-wavenumber region. In comparison to Fig. 1.3, the Corcos model suffers from deficiencies. In particular, it can be shown that for strictly incompressible flows, the pressure spectrum must display a variation in k_z^2 at low wavenumbers (known as the Kraichnan condition [48, 49]). This feature is absent in the Corcos model (Fig. 1.2(d)). Although most of the theorists accept the so-called Kraichnan-Philips theorem, there is no experimental evidence to support it. Bull [35] reported that there is no indication that the incompressible k_z^2 low wavenumber limit of Kraichnan is approached in any way. This observation is based on the contribution of Leehey [50] whose measurements have shown that the low-wavenumber region domain become independent of wavenumber ("wavenumber

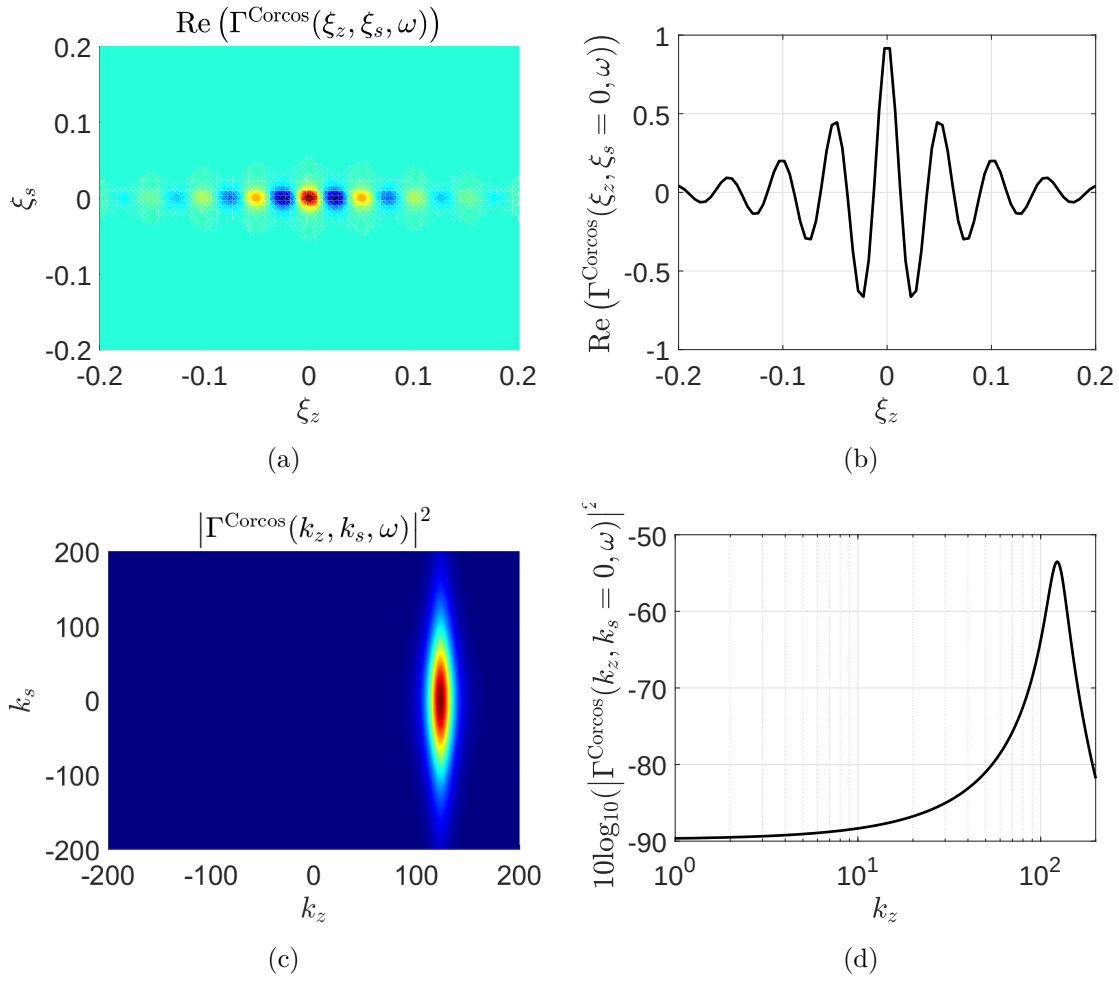

Figure 1.2: Different representations of the Corcos's coherence function at 500 Hz with correlation values $(\gamma_z, \gamma_s) = (0.125, 1)$: (a) and (b) in the spatial domain; (c) and (d) in the wavenumber domain.

white"). Another deficiency of the model is that it does not take into account the compressibility of the fluid. Even for low Mach number flows, compressibility effects are important for very low values of the wavenumber associated with supersonic phase velocities. The spectrum in this region is dominated by acoustic wave propagation due to the noise generated by the turbulent structures in the boundary layer. Chase [51–54]) reexamined the character of the wavevector-frequency spectrum and modified the spectrum to be consistent with experimental data in the subconvective domain. Chase model's is believed to better describe the low-wavenumber domain compared to the Corcos's one which overpredicts experimental data. Other empirical models have also been developed in the 1980's and 1990's. For examples: Efimtsov [55], Ffowcs Williams [56], Witting [57], Smol'yakov and Tkachenko [58] and the Modified Corcos models used by Ko and Schloemer [59]. The reader is referred to [34] where various models of wavenumber spectrum are reviewed and analyzed.

The last quantity of interest is the point autospectrum Φ_{pp} which can be obtained using semi-empirical models. A comparison of semi-empirical models for TBL wall pressure spectra can be found in [60–62]. Its value is usually determined according to experimental curves plotted according to certain scaling laws where the dimensionless spectral density is represented as a function of dimensionless frequency. The point spectrum can be scaled with inner, outer or mixed variable to provide the collapse of experimental data. In general, for the case of a boundary layer along a flat plate, the outer scales: U_∞, $\frac{1}{2}\rho U_\infty^2$, δ, δ^* and the inner scales: u_τ, τ_w, ν are commonly used. They are respectively the free stream velocity, the dynamic pressure, the boundary layer and displacement thickness for the outer variables and the friction velocity, the wall shear stress and the kinematic viscosity of fluid for the inner variables. Unfortunately, there is no single scaling that leads to a satisfactory collapse of experimental data at all pertinent frequencies. This is due to the repartition of energetic structures all over the TBL. From very close to the wall up to the boundary layer thickness, wall-bounded flows are more complex than free flows (jets for example) due to the coexistence of various length and velocity scales. It can be divided into two distinct families, associated to motion near the wall (known as the inner layer) and the other with motion in the region away from the wall (known as the outer layer). In the near vicinity of the wall, viscous effects are dominant over turbulent effects and outer scales (or global scales) are no more characteristic of the local flow structure. In this case, new scales have to be defined based on the viscosity of the fluid and on the wall shear stress. The separation of this two regions occurs at the frequency where the

point spectrum exhibits its maximum value. The universal region can be interpreted as an overlap of the two region as shown Fig. 1.4. A number of point spectral models have been developed for the last 30 years [37, 61]. The more comprehensive multiple scale models were published recently by Smol'yakov [63] and Goody [64]. In practice, models of point spectra are expressed with only global flow quantities called inner or outer variables. These quantities can be easily obtained trough standard RANS. This approach gives satisfying results but only for a Zero Pressure Gradient (ZPG). Schloemer [65] experimentally observed the strong effect of the mean-pressure gradient on the wall-pressure fluctuations. Rozenberg *et al.* [66] more recently found that the effect of an Adverse Pressure Gradient (APG), which is the part of the wind tunnel where the flow is decelerated, cannot be neglected because it leads to an underestimation of the point autospectrum. It is also proposed a modification of the initial Goody's formula to predict APG wall pressure spectrum. Note that the model is limited to APG flows and cannot be applied to Favorable Pressure Gradient (FPG) which is the part of the wind tunnel where the flow is accelerated.

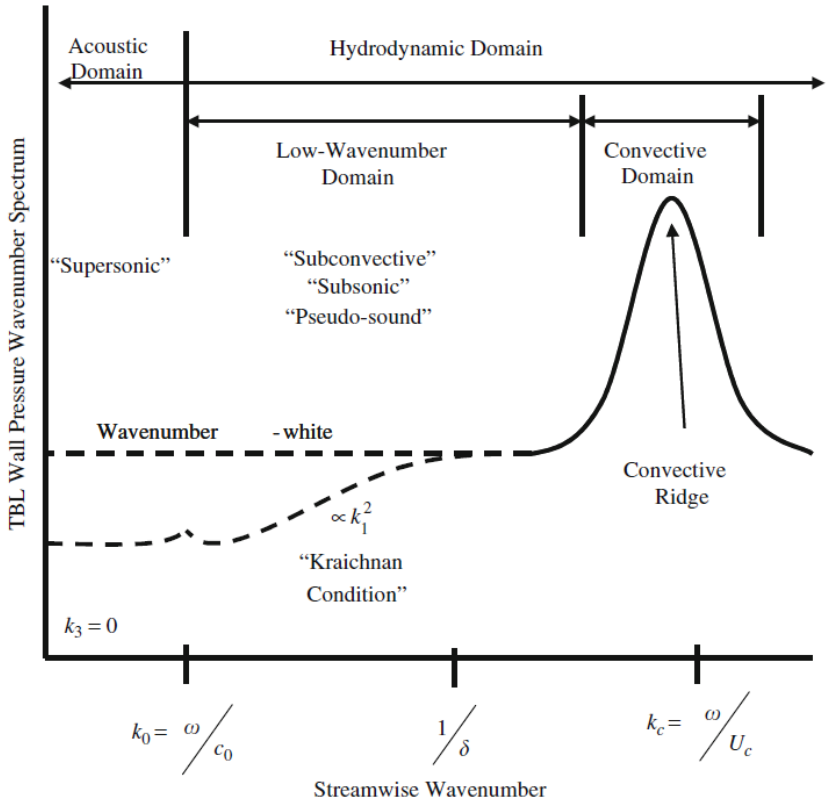

Figure 1.3: A scheme representing the wavenumber-frequency spectrum as a function of the streamwise wavenumber, at constant frequency [14].

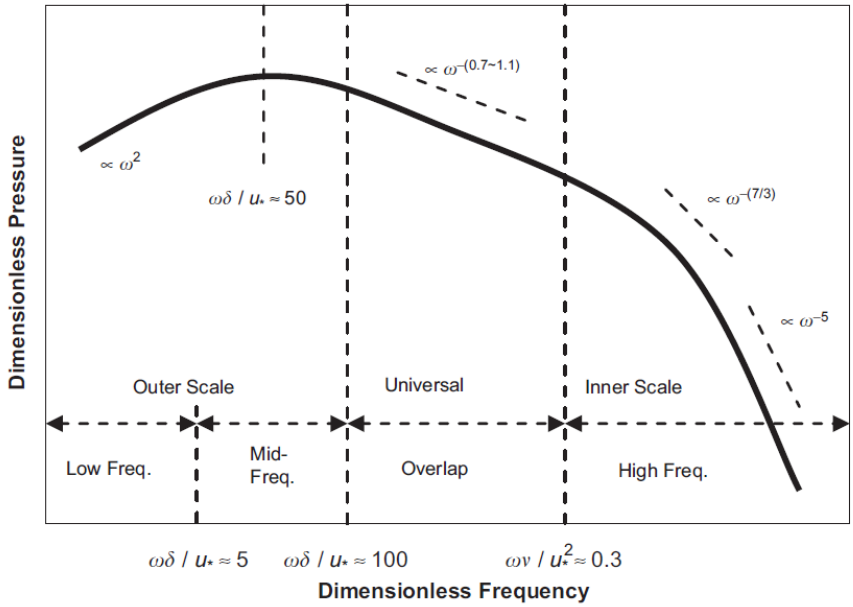

Figure 1.4: General spectral characteristics of a TBL wall pressure spectrum at various frequency regions [61]. Here, u_* stands for the friction velocity.

1.2 Response of structures to random pressure fields

The response of structure to a random pressure field requires random analysis techniques. Many articles, publications are available about the mathematics of random variables. Paez [67] published an interesting paper about the history of random vibration through 1958. The starting point of the modern field of probabilistic structural dynamics is credited to Crandall and its famous proceeding [68] of 1958. Standard texts on this topic have been published since this date. Bendat et Piersol [69], Newland [70] or Elishakoff [71] are particularly referred to introduce random vibration analysis techniques to take account a stochastic load distribution. Thus, the cross power spectral density of the resulting vibration between points $\mathbf{r}_1$ and $\mathbf{r}_2$ located on the duct due to a random pressure field is defined as

$$S_{ww}(\mathbf{r}_1, \mathbf{r}_2, \omega) = \int_S \int_S H^*(\mathbf{r}_1, \mathbf{s}_1, \omega) S_{pp}(\mathbf{s}_1, \mathbf{s}_2, \omega) H(\mathbf{r}_2, \mathbf{s}_2, \omega)\, \mathrm{d}\mathbf{s}_1\, \mathrm{d}\mathbf{s}_2, \tag{1.11}$$

where H corresponds to the frequency response function (FRF), which represents the FRFs between input forces on the surface S and vibration at desired response location. The CPSD of the wall pressure fluctuations, also called, the forcing function, is assumed to be stationary and ergodic. This essentially means that the system is in a steady state response and that the forcing function time history repeats itself for

all time. Different strategies exist to calculate the frequency response functions. For instance, FRFs may be computed using finite element (FE) or analytical models. The dynamic response of the structure can be described by a modal expansion method or a wave method. The modal method is particularly suitable for excitation at lower frequencies. Peak responses are generally dominated by the response of a few individual modes. The total frequency response function is therefore easily represented as a superposition of modal responses. A wave method may be preferable since resonance response predicted by the modal expansion method can be interpreted as the coincidence superposition of traveling waves with opposite wave-number vectors described as incident and reflected waves [72]. Reaching a boundary or discontinuity in the surface, these waves are partly reflected, partly transmitted across the boundary, and also possibly partly transformed into different types of waves. Certain specific problems are more easily solved using wave concepts rather than the mode viewpoint. At higher frequencies, however, several modes contribute strongly to the response at each frequency (high modal overlap), and the frequency response function is more easily calculated using statistical methods, like Statistical Energy Analysis (SEA). For the current work, the highest vibration responses are assumed to be at frequencies low enough to justify a modal approach over statistical analysis. Simply supported boundary conditions (BCs) are considered, since the modes obtained are easy to incorporate into analyses of flow turbulence acting on structures. Analytical modal FRFs for simply supported geometry can be obtained and make Eq.(1.11) easy to obtain.

In practice, flexible rubber sections, flanges or other expansion joints are used to separate sections of pipe. These discontinuities at the interface of two pipe sections induces additional stiffness and mass. For finite pipe encountered in industrial plants, BCs are likely to be a mix between pinned BCs and clamped BCs which differ from the standard simply supported BCs. Non ideal BCs can be incorporated in analytical models to predict more accurately the effect of flanges or other expansion joints. Sub-structuring approaches allow to couple semi-analytical models with finite element method (FEM). Maxit *et al.* [73] developed the Circumferential Admittance Approach (CAA) to estimate the vibro-acoustic behaviour of infinite axisymmetric submerged shell periodically or non-periodically stiffened by internal frames. This infinite approach estimates the power energy dissipated at the interfaces and wavenumber diagrams can be plotted to see the wave contributions during propagation. The wave finite element (WFE) method can also be considered to address this task [74]. It constitutes an efficient means to describe the dynamic behavior of waveguides whose

cross-section can be multi-physics. It involves an elastic part (pipe) coupled with other expansion joints. This approach has been used to compute the dynamic response of an infinite railway track [75].

In our case, the frequency response function H is written using a modal expansion or sometimes called eigenmode series representation. This approach requires subtle attention for solving fluid loading problems with finite geometries as reported in [76, 77]. In general, the standard expression writes

$$H(\mathbf{r}, \mathbf{s}, \omega) = \sum_{mn} W_{mn}(\omega)\phi_{mn}(\mathbf{r})\phi_{mn}(\mathbf{s}), \tag{1.12}$$

where ϕ_{mn} is the structural mode *in vacuo* for a given mode (m, n). However, as pointed in Durant paper's [12], two different expansions of the response of a duct can be built: the outer expansion which is valid far from the resonant frequencies of the structure and the inner expansion which is valid at and near these frequencies. In any case, to find a solution, it is necessary to begin with a rather good approximation. When the fluid is air, the *in vacuo* resonant frequencies provide a satisfying prediction. The receptance function W_{mn} may be defined as

$$W_{mn}(\omega) = \frac{1}{M_{mn}[\omega_{mn}^2(1 + \mathrm{i}\eta) - \omega^2]}, \tag{1.13}$$

and has a sharp maximum at the resonance frequency for any given structural mode. $M_{mn} = \int_S \rho h \phi_{mn}^2 \, \mathrm{d}\mathbf{s}$ is the generalized mass where S is the surface of structure, ρ its density, h the thickness, ω_{mn} the natural frequency of mode (m, n) and η the loss factor. From a physical point of view, the case $\eta = 0$ means that there is no energy loss through the ends of the structure, by material damping or acoustic radiation. Here, the structural problem is not coupled to a fluid medium. The loss factor is accounted for as a complex factor in the stiffness matrix. In the following thesis, the properties of a system with general structural damping is considered following the same procedure as for proportionally damped system [78]. In any case, the use of any theoretical analysis for the determination of the response of a structure to one or more excitation forces will strongly depend on the accurate estimation of the structural or acoustic damping quantity. Damping values are usually determined from measurements, and values derived from past experience are used. Therefore, the reader should keep in mind that the results from a response analysis will be approximated only.

The frequency response function H defining the steady state harmonic response of the duct at point $\mathbf{r}$ excited by a point force located at $\mathbf{s}$ is the solution of the fundamental system

$$\mathfrak{L}[H] - \rho h \omega^2 H = \delta(\mathbf{r} - \mathbf{s}), \tag{1.14}$$

where $\mathfrak{L}$ is the structure operator obtained from a beam, plate or shell theory. Once again, this approach assumes no fluid loading effects since the structural problem is not coupled to a fluid medium.

1.2.1 Vibro-acoustic coupling

In practice, a pipe is coupled to an internal and external fluid. A vibrating structure in contact with a compressible fluid such as air or water will generate pressure fluctuations in the fluid which, in turn, will react back on the structure and modify its vibration behaviour. This loading by the pressure waves in the fluid is known as radiation loading. The importance of this interaction depends on the fluid nature and on the structure of interest. For this reason the area of Fluid Structure Interaction (FSI) and Flow-Induced Vibration (FIV) are distinguished. FSI generally involves two-way coupling that means a feedback loop between structure and fluid needs to be fully captured (fluid and solid solution variables are solved simultaneously). FSI problems are generally associated with large amplitude structure vibrations. Sometime, the above-made definitions of FSI and FIV overlap. The reader is refereed to Ohayon and Soize book's [79] for a rigorous formulation of structures surrounding by light or heavy fluids. In general, it is important to distinguish between structures radiating into air or relatively dense fluids such as water or oil. For light fluids, it is commonly admitted that the structural vibration and acoustic pressure can be evaluated independently. It means that structural motion has negligible impact on flow field and surface pressure fluctuations (called sometime 'blocked' approach because a blocked wall pressures is applied to the structure without creating a feedback). The acoustic radiation calculated using the structural displacements *in vacuo* is considered as a good approximation. For dense fluids, the forces acting on the structure are significantly modified by the radiation loading, and since the acoustic pressure is dependent upon the structural response, a feedback coupling between the fluid and structure exists. Thus, the structural vibration and acoustic pressure responses must be evaluated simultaneously. In general, the fluid is assumed inviscid, that means, the acoustic fluid has no viscosity and therefore cannot support shear forces. The only

component of structural displacement that contributes to the radiated sound field is the one normal to the surface of the structure. Similarly the acoustic medium can only apply normal loads to a structure. Therefore, the coupling with a fluid can be represented by adding a reacting pressure term p in the right-hand side of the structure equation governing the radial component. Vibro-acoustic analysis are generally classified into three main categories: interior problems, exterior problems and mix interior/exterior problems. The last one corresponds to our analysis since pipe structures contain an internal fluid surrounded by an external fluid. This vibro-acoustic problem can be solved analytically and two main approximations are distinguished in the literature.

In a context where the pipe is assumed infinite, shell theories are adopted and modes of vibration are only in the circumferential direction. The fluid coincides with the structure and both domains are infinite. Therefore, circumferential modes and axial wavenumber are the same for the structure and the acoustic medium. The pressure satisfies the Sommerfeld radiation condition and Euler's relation at the interface with the shell. As described by Junger and Feit [80], the solution to the problem of infinite submerged shells can be solved in the wavenumber domain separately for each circumferential mode n and axial wavenumber k_z. Skelton and James' book [81] is particularly referred to as it provides all numerical ingredients to deal with the case of an infinite shell with layered media and periodic rib stiffening including internal and external acoustic radiation. Applying a 2D spatial Fourier transform of Eq.(1.14), the radiation loading is taken into account by adding a fluid-loading term f_L in the shell operator defined as

$$f_L = \rho_0^{\mathrm{e}}\omega^2 \frac{H_{|n|}(\gamma^{\mathrm{e}}R)}{\gamma^{\mathrm{e}}H'_{|n|}(\gamma^{\mathrm{e}}R)} - \rho_0^{\mathrm{i}}\omega^2 \frac{J_{|n|}(\gamma^{\mathrm{i}}R)}{\gamma^{\mathrm{i}}J'_{|n|}(\gamma^{\mathrm{i}}R)}, \tag{1.15}$$

where $H_{|n|}$ and $J_{|n|}$ are the nth order Hankel and Bessel functions respectively, ρ_0^{e} is the exterior/interior density, $\gamma^{\mathrm{e,i}} = \sqrt{(k_0^{\mathrm{e,i}})^2 - k_z^2}$, $k_0^{\mathrm{e,i}} = \omega/c_0^{\mathrm{e,i}}$ and $c_0^{\mathrm{e,i}}$ is the exterior/interior fluid sound speed. This fluid-loading terms can be decomposed into its real and imaginary parts, respectively called resistance and reactance. The resistance represents energy dissipation through acoustic radiation, while the reactance describes the added mass or stiffness effect.

In a context where the pipe is assumed finite, a finite length isotropic shell is connected to infinite rigid baffles. The structure response can be expressed as an expansion over the *in vacuo* structural modes. According to Guyader and Laulagnet [82],

it is always possible to expand the structural vibratory field of fluid-loaded structures using the *in vacuo* structural basis (let us recall that an analytical approach is considered here). A linear system is obtained with new modal amplitudes a^{α}_{pqk} as unknowns. These amplitudes modify the orthogonal properties of the eigenvector components due to the fluid loading so that the resulting linear system is no longer diagonal. The non-diagonal terms correspond to the cross-terms of the internal/external radiation impedances. The linear system takes the following form

$$\underbrace{\begin{bmatrix} \ddots & & \\ & m_{pqk}(\omega^2_{pqk}(1+\mathrm{i}\eta)-\omega^2) & \\ & & \ddots \end{bmatrix}}_{\text{diagonal matrix}} \begin{Bmatrix} \vdots \\ a^{\alpha}_{pqk} \\ \vdots \end{Bmatrix} = \begin{Bmatrix} \vdots \\ F^{\alpha}_{pqk} \\ \vdots \end{Bmatrix} - \mathrm{i}\omega \underbrace{\begin{bmatrix} & \vdots & \\ \cdots & Z^{\mathrm{e,i}}_{pqk}(\omega) & \end{bmatrix}}_{\text{full matrix}} \begin{Bmatrix} \vdots \\ a^{\alpha}_{pqk} \\ \vdots \end{Bmatrix} \tag{1.16}$$

where F^{α}_{pqk} is the generalized force due to a point excitation applied to the shell, ω^2_{pqk} is the *in vacuo* resonance frequencies, m_{pqk} is the generalized mass and $Z^{\mathrm{e,i}}_{pqk}(\omega)$ is the internal or external radiation impedance. The notation is taken from [83] and the reader will note that the most difficult part of the calculation is to keep tracking of the subscripts. Once again, the fluid acts not only as an added mass (real part of $Z^{\mathrm{e,i}}_{pqk}(\omega)$), but also as radiated loss (imaginary part of $Z^{\mathrm{e,i}}_{pqk}(\omega)$). For many acoustic problems in air, the cross-modal coupling terms are weak and can be neglected. In this case, the acoustic radiation can be seen only as an added structural damping.

Numerical solutions exist to tackle complex geometries surrounded by a fluid for all kinds of boundary conditions. FEM consists in solving the partial differential equations by using the variational formulation of the local equations associated to the structure and fluid problems. The latter are discretized into elements and lead to a vibro-acoustic formulation. The boundary element method (BEM) can also be considered for the acoustic problem starting from the Helmholtz integral equation. Details of the BEM and FEM modeling procedures, as well as examples and some practical suggestions, are provided in [84, 85].

1.3 Analysis of the coupling of structural modes and flow-induced excitation

Powell [86] introduced the concept of joint acceptance function to understand how the forcing function couples with the modes of the structure. This concept was further developed by Wilby [87] to study the response of simple panels to TBL excitation. At that time, the response of flat plates due to TBL had been the subject of considerable research. The contributions of Dyer [88], Maidanik [89], Ribner [90], Maestrello [91, 92], White [93] and Davies [94] can be cited. Hence, it has been shown that FRFs can be determined by using a modal expansion, adding up the responses of the individual modes so that Eq.(1.11) becomes

$$S_{ww}(\mathbf{r},\omega) = \sum_{mn}\sum_{m'n'} W_{mn}(\omega)W^*_{m'n'}(\omega)\phi_{mn}(\mathbf{r})\phi^*_{m'n'}(\mathbf{r}) \times I_{mnm'n'}(\omega), \tag{1.17}$$

where $*$ indicates the complex conjugate. In this thesis mode shapes are deliberately assumed real. The integrals $I_{mnm'n'}$ is commonly called the joint acceptance function for $(m,n) = (m',n')$ and the cross-joint acceptance function for $(m,n) \neq (m',n')$. It writes

$$I_{mnm'n'}(\omega) = \int_S \int_S \phi_{mn}(\mathbf{s}_1) S_{pp}(\mathbf{s}_1,\mathbf{s}_2,\omega)\phi^*_{m'n'}(\mathbf{s}_2)\,\mathrm{d}\mathbf{s}_1\,\mathrm{d}\mathbf{s}_2. \tag{1.18}$$

Note that a joint acceptance of unity means complete correlation of the forcing function and perfect matching between the pressure field and the mode shape. In some instances, FRFs are expressed on the basis of infinite plate assumption. Strawderman [95] reviewed turbulent-flow-induced plate-vibration models using finite or infinite thin plates theory. The infinite-plate model is useful due to its simplicity in the mathematical developments for the estimation of the injected power by the TBL. Especially, at high frequency, the type of boundary condition does not influence the vibratory behaviour so that there is an 'equivalence' between finite and infinite structure. This principle is often used in SEA.

For finite or infinite structure, it is useful to represent the vibration behavior in the wavenumber domain. This approach have been first dedicated to predict the sound radiation of standard geometry such as flat, baffled surfaces, spherical and cylindrical shells. General books such as those written by Junger and Feit [80], Fahy [72], Skelton and James [81], and William [96] have introduced this representation. The spatial or wavenumber Fourier transform of a structural mode (only for plane structures) writes

$$S_{mn}(\mathbf{k}) = \int_S \phi_{mn}(\mathbf{s}) \mathrm{e}^{\mathbf{iks}} d^2\mathbf{s}. \tag{1.19}$$

The squared magnitude of this function is usually called the wavenumber sensitivity function. The reader is referred to Shepherd [97] and Robin [98] papers to have an update of its representation for the case of a rectangular, simply supported plate. Note that the term 'panel acceptance' is consistent with the term 'sensitivity function' according to Blake's textbook [99]. The inverse transform of Eq.(1.8) is

$$S_{pp}(\mathbf{s}_1 - \mathbf{s}_2, \omega) = \frac{1}{(2\pi)^2} \int_{-\infty}^{+\infty} \tilde{\Phi}_{pp}(\mathbf{k}, \omega) \mathrm{e}^{-\mathbf{ik}(\mathbf{s}_2 - \mathbf{s}_1)} d^2\mathbf{k}. \tag{1.20}$$

The results Eq.(1.19) and Eq.(1.20) inserted in Eq.(1.18) give the joint acceptance function expressed in the wavenumber domain and writes

$$I_{mn}(\omega) = \frac{1}{(2\pi)^2} \int_{-\infty}^{+\infty} \tilde{\Phi}_{pp}(\mathbf{k}, \omega) |S_{mn}(\mathbf{k})|^2 d^2\mathbf{k}. \tag{1.21}$$

This formulation is of a particular concern as TBL wall pressure fluctuations are often analyzed in wavenumber space. In addition, the double integral over the spatial domain in Eq.(1.18) is transformed into a single integral over the wavenumber domain which leads to reduced computing time. Graham [100–102] proposed this approach to calculate boundary layer induced cabin noise. Maury *et al.* [103, 104] also applied the wavenumber approach to obtain the vibro-acoustic response of a panel excited by random excitations. This results led to the standard representation in the wavenumber domain (see Fig 3.6 to 3.10 in Blake's textbook [99]) because the evaluation of the coupling is obtained by integration over the wavenumber of the product of the sensitivity function and the TBL wavevector spectrum. Hwang and Maidanik [105] showed that the matching depends on the shape of the sensitivity function $S_{mn}(\mathbf{k})$ and its associated boundary conditions. Following this work, Hambric *et al.* [106] examined the importance of surface and edge interaction between the plate structural modes and the TBL wall pressure wavenumber content. Hence, mode shapes with non ideal boundaries follow similar trends than those with simply supported BCs. The differences are observed near the edges. The modes of a finite pipe may be subdivided into two region: the center pipe region, and pipe edge ends. Similarly, in the wavenumber domain, the flexural vibration response of structures excited by a TBL is splitted into two regions [106]: the low-wavenumber region; where so-called 'surface interaction' dominates the structural acceptance and the convective wavenumber region so-called

'edge interactions' dominate the response.

1.4 Wavenumber spectrum, coincidence and panel acceptance

There are different kinds of wavenumbers involved in the flow forcing function and the structure. A typical plot is the wavenumber-frequency (k-ω) diagram for surface pressure spectrum $\tilde{\Phi}_{pp}(\mathbf{k}, \omega)$ as indicated in Fig. 1.5. This permits to examine wave types on frequency-wavenumber plots. For instance, flexural waves travel along the structure–fluid interface and match with more or less success to the acoustic or hydrodynamic waves in the fluid. Flexural waves in plates are characterized by the flexural wavenumber defined as

$$k_f(\omega) = \left(\frac{\rho h}{D}\right)^{\frac{1}{4}} \sqrt{\omega}, \tag{1.22}$$

where D is the flexural rigidity, ρ the mass density and h the plate thickness. Flexural waves are dispersive, meaning that their wave speeds increase with increasing frequency. Flexural waves matching with the surrounding fluids depends on whether these waves are subsonic (slower than the waves speed in the fluid) or supersonic (faster than the waves speed in the fluid). For problems associated with low speed flows ($M \approx 0.1$), convected wavenumbers k_c are up to two orders of magnitude greater than corresponding acoustical k_0 and structural k_f wavenumbers as shown in Fig. 1.5.

If the dispersion relation of any two types of wave motions intersect, they then have the same frequency, wavenumber, wavelength and wave speed. This condition (termed 'coincidence') leads to an efficient interactions between the two wave-types. The hydrodynamic coincidence is obtained at the angular frequency ω_c for $k_c = k_f$ and the acoustic coincidence at ω_0 for $k_0 = k_f$. At this stage, it is important to distinguish infinite from finite structure to study the coincidences (hydrodynamic and acoustic). For infinite panels free bending waves occur at any frequency. The reader is referred to Pezerat *et al.* publication [108, 109] to have a clear overview of the coincidence mechanism.

For finite panels, the discontinuities at the boundaries leads to a superposition of traveling waves with opposite free bending waves vectors described as standing waves which appear at natural or discrete frequencies ω_{mn} (respectively discrete wavenumber k_{mn}) such as $k_f(\omega = \omega_{mn}) = k_{mn} = k_{\text{resonance}}$ as shown Fig. 1.5. In principle, the panel

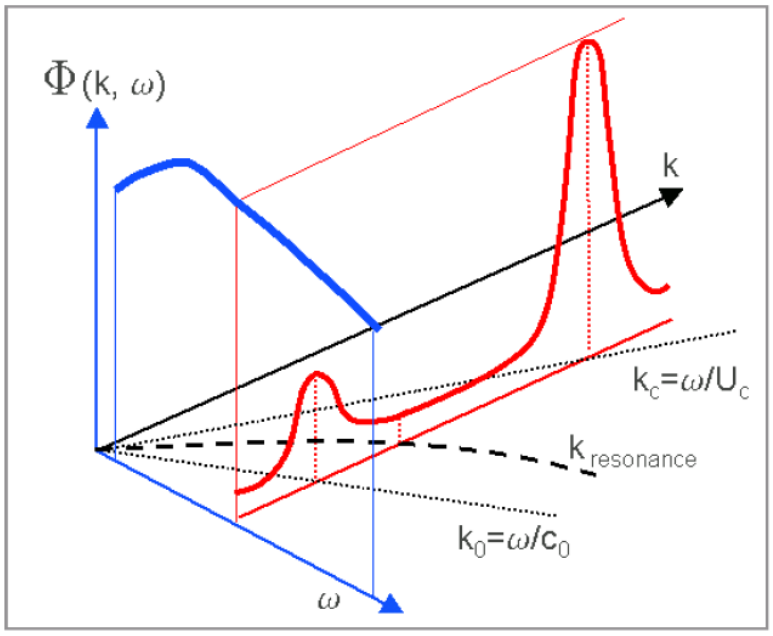

Figure 1.5: Wavenumber-frequency (k-ω) diagram for surface pressure spectrum $\tilde{\Phi}_{pp}(\mathbf{k},\omega)$ of a sub-sonic flow from [107]. Typical resonance wavenumber $k_{\text{resonance}}$ obtained by interference between waves propagating at the free wavenumber k_f.

is finite in the streamwise and spanwise direction. Therefore, standing waves form in wavenumber space a two-dimensional regular lattice described by the sensitivity function defined in Eq.(1.19). At a given frequency ω, the resonant modes are located on a circle of radius k_f. If a mode of vibration has its wavenumbers close to k_c or k_0, $S_{mn}(\mathbf{k})$ is peaked about its wavenumbers and will preferentially accept power from the flow for this mode of vibration. This is the concept of panel acceptance. This condition might be termed 'wavenumber coincidence'. 'Complete coincidence' can be defined further as the condition in which there is not only wavenumber coincidence, but also matching of frequencies. To illustrate the concept of spatial and frequency filter, the averaged kinetic energy of the structure can be introduced and writes

$$E_c(\omega) = \frac{\rho h}{2}\frac{\omega^2}{S}\int_S S_{ww}(\mathbf{r},\omega)\,\mathrm{d}\mathbf{r}. \tag{1.23}$$

Introducing Eq.(1.17) into Eq.(1.23) yields:

$$E_c(\omega) = \frac{\rho h}{2}\frac{\omega^2}{S}\int_S \sum_{mn}\sum_{m'n'} W_{mn}(\omega)W^*_{m'n'}(\omega)\phi_{mn}(\mathbf{r})\phi^*_{m'n'}(\mathbf{r}) \times I_{mnm'n'}(\omega)\,\mathrm{d}\mathbf{r}. \tag{1.24}$$

In the ideal case where the fluid loading effects are neglected and accounting to only

the real part of modes shapes, the average operation in Eq.(1.24) permits to use the orthogonality of the mode shapes and finally one gets an approximation of the averaged kinetic energy

$$E_c(\omega) \simeq \frac{1}{2}\frac{\omega^2}{S}\sum_{mn} M_{mn}|W_{mn}(\omega)|^2 \times I_{mn}(\omega). \tag{1.25}$$

This result shows that the vibrational response is proportional to the product of the receptance function and the joint acceptance function. Thus, the coupling of the structure with a turbulent flow act not only as a spatial filter traduced by the panel acceptance mechanism in the joint acceptance function, but also as a frequency filter traduced by the receptance function. This shows that at a given frequency ω modes for finite panels can be

1. resonant (amplification of $W_{mn}(\omega)$ at $\omega = \omega_{mn}$). The resonant modes are located on a circle of radius $k_f = \omega/c_f(\omega)$, where c_f is the phase speed of flexural waves.

2. in hydrodynamic or acoustic coincidence (maximum of $I_{mn}(\omega)$ at $\omega \neq \omega_{mn}$). The convection wavenumber k_c is equal or close to the axial structural wavenumber k_m (at $\omega = \omega_{mc}$) and the longitudinal and transverse projections of the acoustic wavenumber k_0 are equals or close to k_m (at $\omega = \omega_{m0}$) and k_n (at $\omega = \omega_{n0}$).

3. both resonant and in hydrodynamic or acoustic coincidence (at $\omega = \omega_{mn} = \omega_{mc}$ for the hydrodynamic excitation for instance).

Therefore, the term 'complete coincidence' corresponds to the third condition. It cannot in general be satisfied for a finite structure (see Norton's book [8] Fig. 7.8 and [110]). One can recall that the more frequencies of resonant and in coincidence modes become close, the more coincidence effects are significant (the product $|W_{mn}(\omega)|^2 \times I_{mn}(\omega)$ is important).

Finally, the acoustic and hydrodynamic contributions do not control the structural response in the same manner. This can be observed in the dispersion relationship which exhibits 3 main zones:

1. Below the hydrodynamic coincidence ($\omega < \omega_c$), the structural wavenumbers are higher than those of the hydrodynamic and acoustic contributions ($c_f < U_c$ and $c_f < c_0$), some of the resonant modes are in hydrodynamic or acoustic coincidence and the sum of the product $|W_{mn}(\omega)|^2 \times I_{mn}(\omega)$ is important. The effect of hydrodynamic coincidence is maximum when $c_f \sim U_c$ as the number of resonant modes in hydrodynamic coincidence is maximum.

2. Between the hydrodynamic and acoustic coincidences ($\omega_c < \omega < \omega_0$), the structural wavenumbers are higher than those of the acoustic contribution and lower than those of the hydrodynamic contribution ($c_f > U_c$ and $c_f < c_0$). Some of the resonant modes are in acoustic coincidence and the sum of product $|W_{mn}(\omega)|^2 \times I_{mn}(\omega)$ is maintained due to the acoustic component. The hydrodynamic contribution contributes only on the panel edge vibration rather beyond the hydrodynamic coincidence. The effect of acoustic coincidence is maximum when $c_f \sim c_0$ as the number of resonant modes in acoustic coincidence is maximum.

3. Above the acoustic coincidence ($\omega > \omega_0$), effects are only observed on the panel edges.

These qualitative aspects are valid for a flat plate. Heckl [111] showed that the main effect of curvature on the vibration modes of a cylinder is to increase their structural wavespeeds. Therefore, the analysis of coincidences for pipes is studied according to the shell 'ring frequency' defined as

$$f_r = \frac{1}{2\pi}\frac{c_l}{R}, \tag{1.26}$$

where $c_l = (E/(\rho(1-\nu^2)))^{1/2}$ is the velocity of compressional waves and R the radius. The ring frequency is of practical interest because above this frequency, flexural wavelengths become short with respect to the radius of curvature and the shell effectively becomes a flat plate. From that, the analysis of pipe coincidences become similar of those of plates.

1.5 Introduction of the acoustic contribution into the CSD expression of the wall pressure distribution

1.5.1 Diffuse Acoustic Field

The low wavenumber region or the acoustic contribution is usually modeled as a diffuse field in a context of external flow. It is assumed that a diffuse field is a reasonable approximation for low Mach number flows, on the basis that the turbulent eddies are random acoustic sources in space and time. This acoustic contribution is assumed to be generated by the turbulent boundary layer itself. The description of the acoustic pressure field produced by the turbulent boundary layer over a flat plane is far from being resolved. It requires subtle assumptions as well as sophisticated theoretical developments and we can refer to well known standard textbooks (see Ch.16 by Dowling [20] and Ch.2 in [37]) for further details. The coherence function of a Diffuse Acoustic Field (DAF) excitation writes [112–115]

$$\Gamma(\mathbf{s}_1, \mathbf{s}_2) = \frac{\sin k_0|\mathbf{s}_1 - \mathbf{s}_2|}{k_0|\mathbf{s}_1 - \mathbf{s}_2|}. \tag{1.27}$$

This is in general directly added to the Corcos formulation by using a coefficient which traduces the energy ratio between the acoustic and aerodynamic terms as shown Fig. 1.6. Arguillat *et al.* [116] measured the acoustic contribution by integrating the measured $\tilde{\Phi}_{pp}(\mathbf{k}, \omega)$ over the acoustic disk of radius k_0. The energy ratio between the acoustic and aerodynamic parts was found to decrease with frequency from approximately 10 to 0.1% . In addition, the same author proposed a second method to extract the acoustic component using a least mean square procedure. Starting from the measurement of the CPSD in the spatial domain, it was assumed a model of CPSD on the basis of the sum of an aerodynamic contribution provided by the Corcos model and an acoustic part given by a DAF coherence function written as:

$$S_{pp}(\mathbf{s}_1 - \mathbf{s}_2, \omega) = \Phi_{pp}(\omega)\left(\Gamma^{\text{Corcos}} + A(\omega)\Gamma^{\text{DAF}}\right), \tag{1.28}$$

with $A(\omega)$ the ratio between the aerodynamic and the acoustic energies. For automotive application [117], a constant ratio of 10 percent is applied, $A(\omega) = 0.1$. Lecoq [109] used this approach to model both aerodynamic and aeroacoustic contributions

and applied a ratio of 5 percent following Arguillat work's [116].

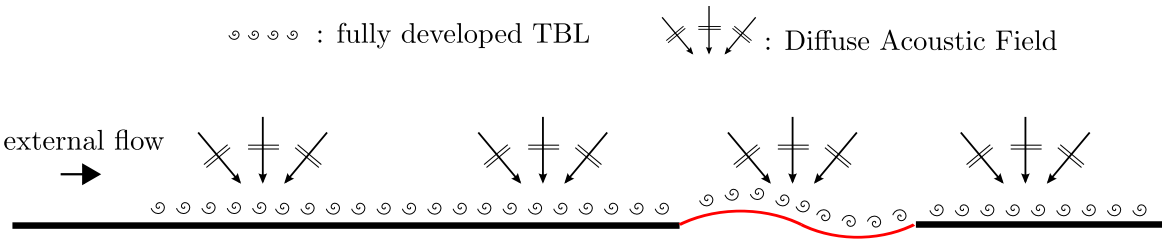

Figure 1.6: External turbulent flow: the acoustic contribution is generally modeled as a DAF excitation and added to the Corcos coherence function.

1.5.2 Acoustic duct modes

In the context of an internal flow in straight pipes, the situation is quite different as shown Fig. 1.7 (case 1). Boundary layer pressure fluctuations are distributed over the entire surface of the duct and acoustic waves within the TBL flow excite acoustic duct modes, which in turn excite the duct walls. Therefore, the duct pressure field of an infinite rigid duct is written as a sum of propagating modes at a point $\mathbf{s} = (s, z)$ of the wall and writes

$$p(\mathbf{s}_1, \omega) = \sum_{pq} C^{+}_{pq} \psi_{pq}(s) e^{\mathrm{i}k^{+}_{pq} z} + \sum_{pq} C^{-}_{pq} \psi_{pq}(s) e^{\mathrm{i}k^{-}_{pq} z}, \tag{1.29}$$

where $C^{\pm}_{pq}$ stands for amplitude of the downstream (+) and upstream (-) propagating mode and ψ_{pq} the acoustic mode (p, q). The convention $\mathbf{s} = (s, z)$ is adopted so that s stands for the curvilinear abscissa and z the coordinate along the duct. Therefore, the modes ψ_{pq} are defined as the projection of the acoustic mode along the curvilinear abscissa s. The flow is assumed uniform and thermo-viscous attenuation is neglected so that the axial wavenumbers $k^{\pm}_{pq}$ writes

$$k^{\pm}_{pq} = \frac{kM \pm \sqrt{k^2 - (1 - M^2)\, k^2_{\perp}}}{1 - M^2}, \tag{1.30}$$

where M is the Mach number and $k_{\perp}$ is the transverse wavenumber. The condition for an acoustic mode to propagate is that the wavenumber $k^{\pm}_{pq}$ must be real. Otherwise the wave is evanescent and decays exponentially. The frequency at which a mode (p, q) begins to propagate is known as the cut-off frequency of the mode. For the sake of clarity, the modal sums will be written with the symbol $\pm$ to include both

positively and negatively propagating modes. In addition, the suffix pp of the function S_{pp} should not be confused with pq used to designate the acoustic duct modes.

To our knowledge, Norton's thesis [118] was one of the first contribution to introduce plane waves and higher order modes expressed in term of CPSD forcing function in a context of internal flow induced vibration of pipes. The CPSD between the pressure at 2 points $\mathbf{s}_1 = (s_1, z_1)$ and $\mathbf{s}_2 = (s_2, z_2)$ writes

$$\begin{aligned} S_{pp}(\mathbf{s}_1, \mathbf{s}_2, \omega) &= \sum_{pq} \mathbb{E}\left[\left|C_{pq}^{\pm}(\omega)\right|^2\right] \underbrace{\psi_{pq}(s_1)\psi_{pq}(s_2)\mathrm{e}^{\mathrm{i}k_{pq}^{\pm}(z_1-z_2)}}_{\Gamma_{pq}^{\pm}(\mathbf{s}_1,\mathbf{s}_2)} \\ &+ \sum_{\substack{pq \\ pq\neq rs}} \mathbb{E}\left[C_{pq}^{\pm}(\omega)C_{rs}^{\pm}(\omega)^*\right] \psi_{pq}(s_1)\psi_{rs}(s_2)\mathrm{e}^{\mathrm{i}(k_{pq}^{\pm}z_1 - k_{rs}^{\pm}z_2)}, \end{aligned} \tag{1.31}$$

where $\mathbb{E}[]$ is the ensemble average. The suffix rs is used to introduced the cross modal amplitudes which are assumed all uncorrelated random variables so that $\mathbb{E}\left[C_{pq}^{\pm}(\omega)C_{rs}^{\pm}(\omega)^*\right] = 0$. It is further assumed that the same mode propagating in opposite directions are also uncorrelated.

The situation with an internal flow disturbance in the duct due to a singularity such as a bend, a junction or a flow constriction is shown Fig. 1.7 (case 2). The flow/obstacle interaction generates internal sound waves which propagate through the piping system. The additional propagating sound waves are then superimposed on the hydrodynamic TBL fluctuations. In the vicinity of an obstacle placed in the duct, the 'near-field' is associated with strongly turbulent flow and non-propagating acoustic waves which are attenuated rapidly with distance from the disturbance. In what may be termed the 'far-field' of a flow disturbance in the duct, the pressure fluctuations are associated with duct acoustic modes propagating downstream and the distance is sufficient for the re-establishment of an undisturbed mean flow profile with fully developed TBL. Rennison [119] examined in detail the coupling of the resulting vibrational response of the pipe with the random wall pressure field associated with (i) fully developed turbulent pipe flow and (ii) acoustic plane waves propagating inside the pipe by focusing his study in the analysis of the joint acceptance functions of both contributions. Finally, this PhD attends to bring Rennison and Norton thesis up to date with comprehensive theoretical and experimental background to study vibrational and acoustic effects of various internal flow disturbances in pipes with an internal fully-developed turbulent flow. Sound generated by these disturbances in duct and pipe systems is a strong contributor to the vibrational response and

external acoustic radiation of the pipe from, for example, ventilation systems, air-conditioners or intake and exhaust systems [2, 120, 121]. In addition, flow instabilities caused by geometric features may generate acoustic signals. For instance, corrugated flow pipes may produce powerful pure tones leading to major issues in Oil & Gas industry [122, 123]. Such systems are often complex as they consist of many in-duct components of individual intricacy like rotating machines (fans, compressors), heat-exchangers, side branches, orifices, valves, silencing devices, and so on, which scatter and generate acoustic fields when interacting with the fluid flow through the system. The so-called two-port model [124] is a well-recognized model that uses the plane wave to describe aeroacoustic disturbances in terms of their acoustic source strength and their reflection/transmission or impedance/mobility properties. However, when investigating systems with larger radius and higher frequency content higher-order acoustic duct modes can propagate within the frequency range that contributes to the vibration or noise annoyance. The two-port model can be extended to a multi-port model, as demonstrated by Lavrentjev *et al.* [125]. On this basis, multi-modal acoustic measurements can be performed to access to the auto-power spectrum $\mathbb{E}\left[\left|C_{pq}^{\pm}(\omega)\right|^2\right]$ of a mode (p, q).

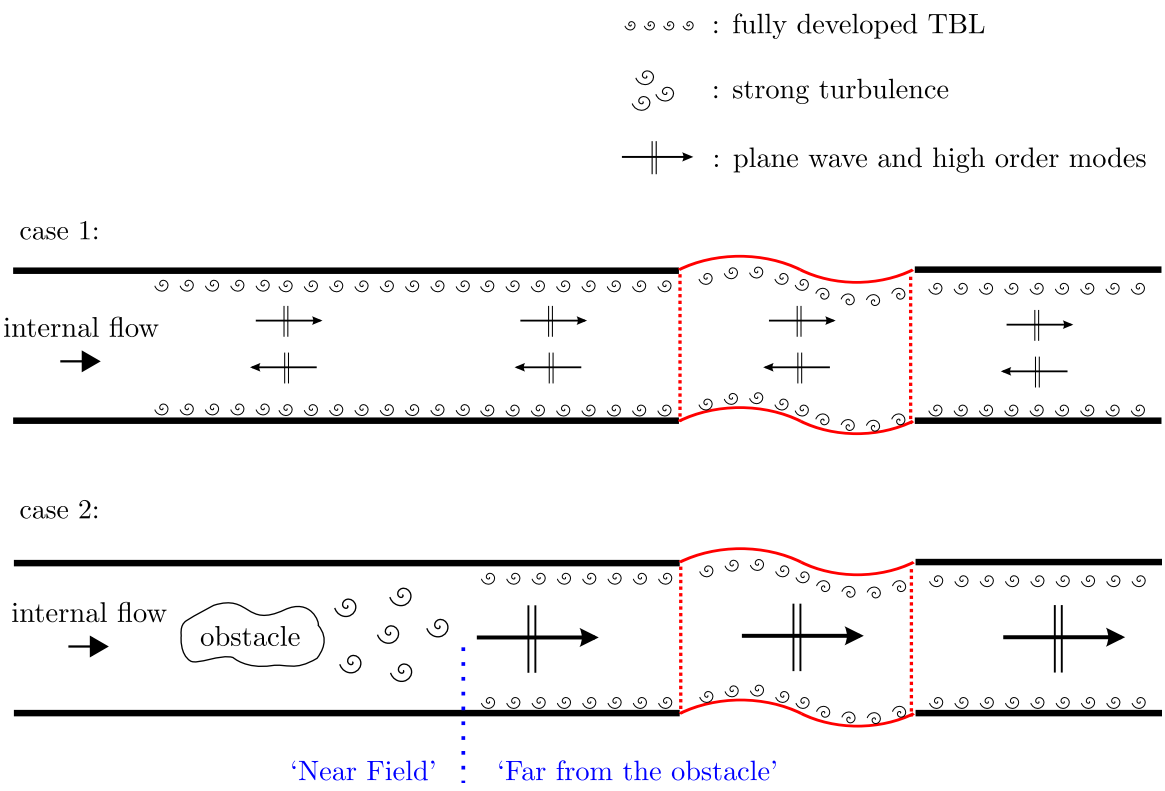

Figure 1.7: Internal turbulent Flow with or without obstacle: 2 scenarios are investigated.

1.6 Contribution to research

Many researches can be found about the vibrations of cylindrical pipes excited by fluid flow, to the authors' knowledge, no publications concerning rectangularly-shaped ducts can be found in the scientific literature. Although most of the fluid conveying ducts are cylindrical, specific applications require the use of rectangular ducts. This is the case of ventilation and air conditioning systems in buildings for space saving, or in industrial applications requiring large duct sections for gas transportation. Gas treatment centers used in the aluminum industry require such rectangular ducts due to manufacturing purpose as shown in Fig.1.8.

Figure 1.8: Gas transport ductwork made of circular and rectangular cross sections from [1].

Here we aim to present a numerical study which can offer engineers greater understanding of the coupling between the duct section (circular or rectangular) and the excitation including both the acoustic, hydrodynamic contributions. This work extends earlier work utilizing analysis of the forcing function and the fluid-structure coupling through the joint acceptance, allowing for better prediction of structural response. The experimental setup at the Roberval research laboratory used to validate the methods will be described, and comparisons will be made between the simulations and measurements. The generation of flow induced noise and vibration will be distinguished through 2 scenarios: (i) a straight duct with no singularity, acoustic waves are generated by the TBL itself and (ii) a straight duct with a flow constriction inserted upstream generating a localized acoustic source.

This thesis is structured as follows:

Chapter 2 presents the experimental facility and the measurement procedure, which is developed for measuring the acoustic and hydrodynamic contribution of a straight rectangular duct with and without singularities.

In chapter 3, the dynamic response of the structure due to an impulsed force is analyzed. Two specific cross-sections are investigated and in both cases, material properties and dimensions, i.e. width and cross-sectional aeras, are identical. Experimental modal analysis of a finite rectangular duct are confronted to computational methods to assess the 'blocked' approach using analytical modal FRFs of a simply supported finite duct. Attention will be payed to quantify the effect of the Boundary Conditions (BCs), acoustic radiation and aerodynamic damping.

In chapter 4, the fluid-structure coupling of both geometry (rectangular and cylindrical sections) is analyzed through the joint acceptance function. The excitation includes both acoustic and hydrodynamic contributions written on the basis of Corcos model and using acoustic duct mode coherence functions. Attention will be devoted to study the spatial coupling in the wavenumber domain and the evolution of the vibration response due to each contribution.

In chapter 5, the structural response of a rectangular duct due to wall pressures induced by turbulent flow is computed and confronted to measurements. Two scenarios, *i.e* with and without singularity, are investigated. The CPSD is calculated using Computational Fluid Dynamics and aeroacoustic analogies to tackle complex and no homogeneous flow in the vicinity of a singularity. This hybrid approach allows to separate the acoustic and hydrodynamic contributions and study their influence separately on the structural response. This chapter corresponds to the paper version accepted in the research book 'flow induced noise and vibration issues and aspects' (FLINOVIA) [5]. The proceedings of the Second International Workshop on Flow Induced Noise and Vibration which was held in Penn State, USA, in April 2016.

1.7 Outline

The remainder of this thesis is organized as follows:

- Chapter 2 Measurement of the cross power spectral density $S_{pp}(\mathbf{s}_1, \mathbf{s}_2, \omega)$ for both contributions: acoustic and hydrodynamic.
- Chapter 3 Study of the frequency response function $H(\mathbf{r}, \mathbf{s}, \omega)$ of a finite duct with two specific cross-sections: rectangular and circular.
- Chapter 4 Prediction of the coupling through the joint acceptance function $I_{mn}(\omega)$ for both contributions and cross-sections.
- Chapter 5 Prediction and confrontation with measurements of the kinetic energy of the structure $E_c(\omega)$ for the two scenarios.

Following the main body of this thesis are several appendices with additional information and a bibliography.

Chapter 2

Measurement of wall pressure fluctuations in duct

This chapter presents an experimental approach to characterize wall pressure fluctuations in a straight rectangular duct flow with or without flow constriction. An experimental facility originally designed to measure the acoustic power produced by HVAC components is used. It is desired to quantify the relative weight of the hydrodynamic and acoustic contributions on the structure response. Therefore, attention will be devoted to separate the contributions of the turbulent flow to the acoustic mode amplitudes. These measurements will lead to evaluate and suggest improvements to existing CPSD empirical models in a context of internal flow with disturbances or not at low Mach number.

2.1 Experimental set up

Experiments were performed on a test rig at the Roberval research laboratory. The rig dimensions correspond to common dimensions of automotive heating, ventilation, and air-conditioning (HVAC) systems. The primary air located in a first room (as shown in Fig. 2.1(a)) is propelled at a slow speed by a centrifugal compressor with frequency variator for controlling the flow speed, this can reach 20 m/s (with no obstacle). Two mufflers connected with an elbow located upstream of the blower are designed to reduce fan and flow noise. The air passes through a flow tranquillizing box which minimizes the turbulence and a flow nozzle equipped with a differential pressure gauge to measure the volumetric flow rate. Finally, the air arrives in the last assembly (see Fig. 2.1(b)), which is made from interchangeable sections of steel rectangular duct with hydraulic diameter of around 133 mm, a wall thickness of 3 mm and an overall length of about 8 m with anechoic termination at both ends. The hydraulic diameter D_h is defined as

$$D_h = \frac{4A_c}{P} = \frac{2L_xL_y}{L_x + L_y}, \tag{2.1}$$

where $A_c = L_x \times L_y = 0.2 \times 0.1$ m^2 is the cross-sectional area of the pipe and P is its wetted perimeter. The pipe rig is guided over its entire length by a series of supports effectively isolated from the building by anti-vibration rubber shock absorbers. The interchangeable sections are connected to each other at their downstream and upstream ends by small butterfly twist latch with keeper plate. To prevent air leakage, sealing between two sections is ensured by single sided gasket tapes. Every section is centered in connection with the adjacent one so that the internal flow does not experience any surface discontinuities. The pipe rig contained probes and source sections upstream and downstream of an exchangeable test-section. The order of the different sections from upstream to downstream side is as follows: *anechoic termination* → *probe section* → *source section* → *probe section* → ***test section*** → *probe section* → *source section* → *probe section* → *anechoic termination*. A sketch of the pipe rig can be found in Fig. 2.2.

(a) Flow generation facility

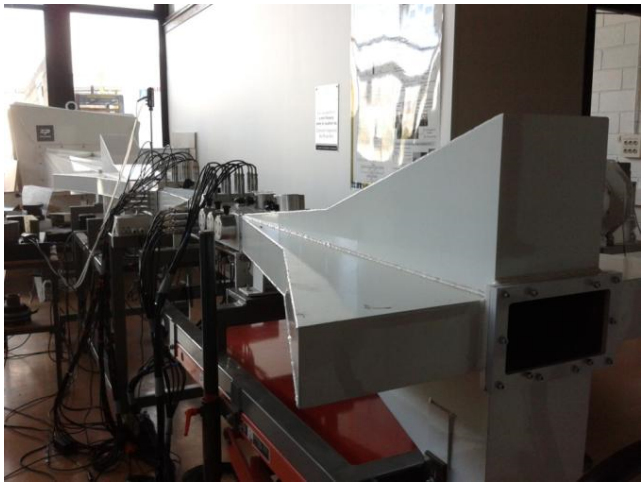

(b) Aero-acoustic measurements facility

Figure 2.1: Experimental flow noise test rig.

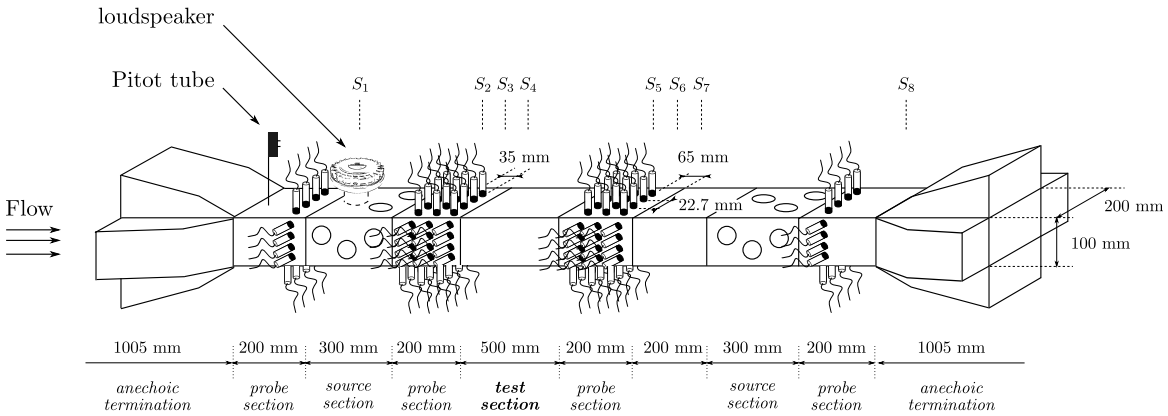

Figure 2.2: Sketch of the pipe rig.

2.1.1 Measurement devices

A testo 435 Pitot tube is inserted in the first probe section and placed in the duct centerline. The pipe centerline velocity is computed from

$$U_\infty = s\sqrt{\frac{2\Delta P}{\rho}}, \tag{2.2}$$

where s is the Pitot tube factor (here a straight Pitot tube so that $s = 0.67$), ρ the air density and ΔP the differential pressure equals to the difference between total pressure (at the stagnation pressure hole) and static pressure (at the plane of the hole drilled parallel to the flow direction). In addition, 12 Brüel and Kjær 1/2-inch 4947 microphones are wall-mounted. The two source sections consists of loudspeaker entrances mounted in a short side-branch connected to the main duct at 2×10 different positions. Two probe sections with 3 arrays of 12 microphones are connected on both sides of the test section. The last probe section which is the furthest downstream from the test section is equipped with 12 microphones wall-mounted. Pressure signals are recorded by a 96 channels LMS Scadas acquisition with a bandwidth of 6400 Hz and 4096 spectral lines. The measurement procedure was performed using an averaging process over 600 realizations to achieve statistical convergence.

2.1.2 Calibration procedure

The microphones are calibrated relative to each other for amplitude and phase by exposing them to the same sound field. The microphones are inserted into opposing holes at the ends of a GRAS Phase Calibrator type 51AB. The transfer function between the reference B&K 4231 type microphone (with sensibility of 11.71 mV/Pa) and the ith microphone to be calibrated has to be measured (H_1 estimator):

$$H_{\mathrm{ref}/i} = G_{\mathrm{ref},i}/G_{\mathrm{ref,ref}} \quad \text{in V/Pa}, \tag{2.3}$$

where $G_{\mathrm{ref,ref}}$ is the autospectrum of the reference microphone and $G_{\mathrm{ref},i}$ the cross-spectrum between reference and the ith microphone. Only the reference microphone is calibrated, so the transfer function is obtained in V/Pa. This transfer function is used as a correction function for the transfer functions, cross-spectra and auto-spectra measured subsequently in the pipe rig.

2.2 Hydrodynamic contribution

In our study, the vibration response will be calculated on the basis of empirical models of wall pressure fluctuations. The prefix 'hydro' is used here to remind that this corresponds to the incompressible part of the flow. Although the pipe was originally designed for acoustic measurements, it is desired to quantify the relative weight of the hydrodynamic and acoustic contributions on the structure response. Therefore, the spectral and cross-spectral features of the hydrodynamic contribution have to be analyzed to assess the use of appropriate empirical TBL models. These empirical forcing functions are postulated assuming certain functional forms like exponential decays over space or oscillation in the convection direction according to Eq.(1.5). Also, TBL parameters need to be known such as the boundary layer thickness or the friction velocity. The hydrodynamic contribution is assumed to be fully developed and homogeneous.

2.2.1 Static pressure

The test section is located 13 D_h (around 1.7 m) downstream of the pipe entrance which seems a little too low to assure a fully developed turbulent pipe flow. For space reason, the pipe length can not be increased. In many pipe flows of practical engineering interest, the entrance effects become insignificant beyond a pipe length of about 25 to 40 diameters according to Schlichting [126]. The velocity profile is known to remain unchanged in the hydrodynamically fully developed region and the wall shear stress also remains constant in that region. This last quantity can be estimated *via* static pressure drop measurements because the pressure loss for all types of fully developed internal flows is expressed as

$$\Delta P = f \frac{L}{D_h} \frac{\rho U_\infty^2}{2}, \tag{2.4}$$

where $\rho U_\infty^2/2$ is the dynamic pressure and f is the Darcy friction factor related to the wall shear stress through

$$f = \frac{8\tau_w}{\rho U_\infty^2}. \tag{2.5}$$

It should not be confused with the friction coefficient C_f defined as $C_f = f/4$. Static pressure measurements have been performed at different distances along the pipe and different flow speeds as shown in Fig. 2.3(a). Static pressure is given by the difference

between the pressure in the pipe and the atmospheric pressure. It follows a linear law along the wall of the straight duct. The slope of each linear curve allow to calculate the wall shear stress according to Eq.(2.5) and Eq.(2.6). The wall friction velocity is defined as:

$$u_\tau = \sqrt{\frac{\tau_w}{\rho}}. \tag{2.6}$$

Results are shown in Fig. 2.3(b) and measured friction velocities show good agreement with the Darcy friction factor for rectangular section according to [127]:

$$f = \frac{0.178}{\mathrm{Re}_{D_h}^{1/5}}, \tag{2.7}$$

where Re_{D_h} is the Reynolds number ranging from 4.4×10^4 to 1.8×10^5 in this study. It is also consistent with calculations based on the Moody diagram or equivalently from the Colebrook equation for turbulent pipe flow:

$$\frac{1}{\sqrt{f}} = -2\log_{10}\left(\frac{\varepsilon/D_h}{3.7} + \frac{2.51}{\mathrm{Re}_{D_h}\sqrt{f}}\right), \tag{2.8}$$

with ε the roughness of a commercial steel taken from the literature ($\varepsilon = 0.045$ mm). Note that Eq.(2.8) cannot be solved analytically for f when ε/D_h and Re_{D_h} are given and has to be computed using a numerical root-finding procedure. These previous agreements can not be considered sufficient in this study to confirm that the turbulent flow in the pipe test section is fully developed since the experimental set up is limited. The wall shear stress and friction velocity values at different flow speeds are summarized in Table 2.1. Values obtained from the Colebrook equation are used in the next step to calculate TBL wall pressure empirical models.

U_∞ (m/s)	5	10	15	20
τ_ω (Pa)	0.10	0.40	0.73	1.17
u_τ (m/s)	0.28	0.58	0.78	1.00

Table 2.1: Wall shear stress and friction velocity

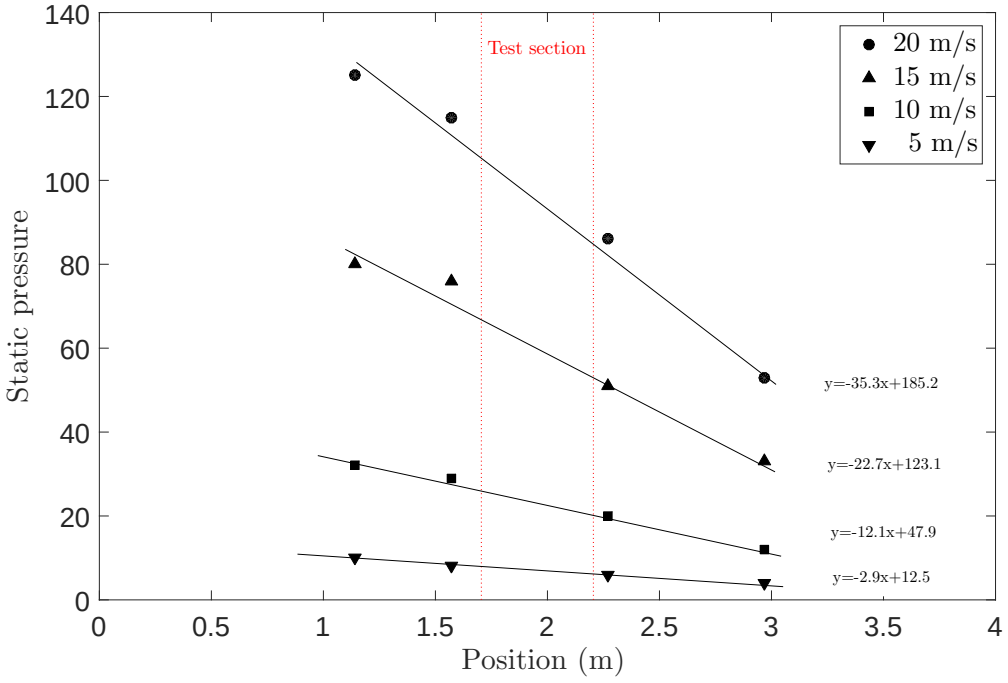

(a)

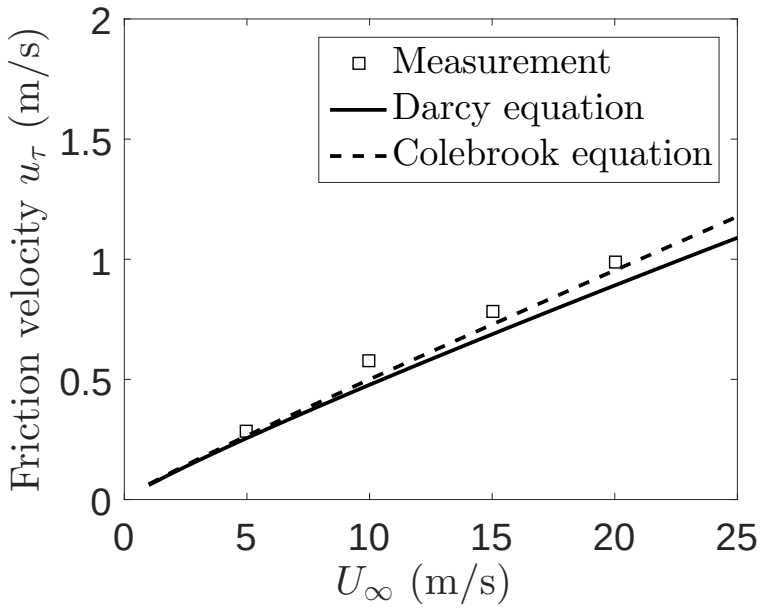

(b)

Figure 2.3: (a) Static pressure evolution along the duct. (b) Friction velocity: comparison between measurement and Darcy law.

2.2.2 Calculation of TBL parameters

Numerical ingredients are recalled to estimate TBL parameters. These quantities are provided by empirical approximation of the boundary layer equations. Most empirical estimates of TBL wall pressure fluctuations are based on ideal flat plate, straight channel and straight pipe flow measurements.

The boundary layer thickness δ is defined as the distance to the wall where the longitudinal velocity is equal to 99 percent of the external velocity:

$$u(x, y = \delta) = 0.99\ U_\infty. \tag{2.9}$$

The boundary layer thickness is a function of the distance x along the plate. This classical length scale is considered as "outer" variable in the same way as U_∞. In practice it is difficult to measure δ with precision as the velocity profile tends asymptotically to U_∞. Two other outer scales are generally preferred, defined by integrals of the velocity profiles: the displacement thickness δ^* and the momentum thickness θ. These scales are defined by:

$$\delta^* = \int_0^\infty \left(1 - \frac{u}{U_\infty}\right) \mathrm{d}y \tag{2.10}$$

$$\theta = \int_0^\infty \frac{u}{U_\infty} \left(1 - \frac{u}{U_\infty}\right) \mathrm{d}y \tag{2.11}$$

One common empirical approximation for the time-averaged velocity profile of a turbulent flat plate boundary layer is the one-seventh-power law such as

$$\frac{u}{U_\infty} \cong \left(\frac{y}{\delta}\right)^{1/7}. \tag{2.12}$$

Note that the first derivative of u with respect to y at the wall is directly proportional to the wall shear stress $[\tau_w = \mu \left(\partial u/\partial y\right)_{y=0}]$. Another common approximation is the log law, a semi-empirical expression that turns out to be valid not only for flat plate boundary layers but also for fully developed turbulent pipe flow velocity profiles. The log law is commonly expressed in dimensionless variables by a characteristic velocity which is actually the friction velocity u_τ defined in Eq.(2.6) such as:

$$\frac{u}{u_\tau} = \frac{1}{\kappa} \ln \frac{y u_\tau}{\nu} + B, \tag{2.13}$$

where ν is the kinematic viscosity, κ is a universal constant equal to 0.41 (von Kármán's constant) and B is slightly depending upon the Reynolds number and is approximately equal to 5. Hence, the wall shear stress τ_w and the friction velocity u_τ are characteristic of the flow in the near vicinity of the wall where viscous effects are dominant over turbulent effects. These two variables are considered as "inner" or viscous scales.

In many practical engineering applications, we do not need to know all the details inside the boundary layer. The momentum integral technique utilizes a control volume approach to obtain such quantitative approximations of boundary layer properties along surfaces with zero or nonzero pressure gradients. A result of this technique is the Kármán integral equation which is useful to estimate boundary layer properties such as boundary layer thickness and skin friction. It writes

$$\frac{C_{f,x}}{2} = \frac{\mathrm{d}\theta}{\mathrm{d}x} + (2+H)\,\frac{\theta}{U}\frac{\mathrm{d}U}{\mathrm{d}x}, \tag{2.14}$$

where we define the shape factor H as

$$H = \frac{\delta^*}{\theta} \tag{2.15}$$

and the local skin friction coefficient $C_{f,x}$ as

$$C_{f,x} = \frac{\tau_w}{\frac{1}{2}\rho U^2}. \tag{2.16}$$

Note that both H and $C_{f,x}$ are functions of x for the general case of a boundary layer with a nonzero pressure gradient developing along a surface (Eq.(2.17) is equivalent to Eq.(2.5) but x dependent). For the special case of the boundary layer on a flat plate, $U(x) = U = U_\infty$ and Eq.(2.15) reduces to the Kármán integral equation for flat plat boundary layer:

$$C_{f,x} = 2\frac{\mathrm{d}\theta}{\mathrm{d}x}. \tag{2.17}$$

Hence, if two quantities are known about the turbulent boundary layer over a flat plate such as the local skin friction coefficient and the one-seventh-power law approximation for the boudary layer profile shape, then the quantities δ, δ^* and θ can be calculated using the definitions of displacement thickness, momentum thickness and employing the Kármán integral for flat plat boundary layer. Fig. 2.4 shows a summary of expressions for laminar and turbulent boundary layers on a smooth flate

plate. Note the value of the local skin friction coefficient obtained from empirical data for turbulent flow through smooth pipe (column (b)) in comparison with Eq.(2.7) (divided by 4). In fact, the expression used for the rectangular duct is reduced slightly from the common expression used for a circular duct. The expressions in Fig. 2.4 for the turbulent flat plate boundary layer are valid only for a very smooth surface. Even a small amount of surface roughness greatly affects properties of the turbulent boundary layer, such as momentum thickness and local skin friction coefficient. The effect of surface roughness on a turbulent flat plate boundary layer has been subject of considerable research and the reader is refereed to [7, 128, 129] for instance.

Summary of expressions for laminar and turbulent boundary layers on a smooth flat plate aligned parallel to a uniform stream*

		(a)	(b)
Property	Laminar	Turbulent(†)	Turbulent(‡)
Boundary layer thickness	$\frac{\delta}{x} = \frac{4.91}{\sqrt{\mathrm{Re}_x}}$	$\frac{\delta}{x} \cong \frac{0.16}{(\mathrm{Re}_x)^{1/7}}$	$\frac{\delta}{x} \cong \frac{0.38}{(\mathrm{Re}_x)^{1/5}}$
Displacement thickness	$\frac{\delta^*}{x} = \frac{1.72}{\sqrt{\mathrm{Re}_x}}$	$\frac{\delta^*}{x} \cong \frac{0.020}{(\mathrm{Re}_x)^{1/7}}$	$\frac{\delta^*}{x} \cong \frac{0.048}{(\mathrm{Re}_x)^{1/5}}$
Momentum thickness	$\frac{\theta}{x} = \frac{0.664}{\sqrt{\mathrm{Re}_x}}$	$\frac{\theta}{x} \cong \frac{0.016}{(\mathrm{Re}_x)^{1/7}}$	$\frac{\theta}{x} \cong \frac{0.037}{(\mathrm{Re}_x)^{1/5}}$
Local skin friction coefficient	$C_{f,x} = \frac{0.664}{\sqrt{\mathrm{Re}_x}}$	$C_{f,x} \cong \frac{0.027}{(\mathrm{Re}_x)^{1/7}}$	$C_{f,x} \cong \frac{0.059}{(\mathrm{Re}_x)^{1/5}}$

* Laminar values are exact and are listed to three significant digits, but turbulent values are listed to only two significant digits due to the large uncertainty affiliated with all turbulent flow fields.
† Obtained from one-seventh-power law.
‡ Obtained from one-seventh-power law combined with empirical data for turbulent flow through smooth pipes.

Figure 2.4: Summary of classical expressions to calculate TBL variables [130].

2.2.3 Measurement of the Power Spectral Density

The pressure spectra at the different section locations are recorded. Fig. 2.5 shows the spectra from the 12 microphones of sections S_4 and S_5. A variation of 5 dB can be observed between microphones over the entire frequency range and a variation of 10 dB between 200-600 Hz. It is chosen to average autospectra measured by microphones located at the same section. The average power spectral densities $\Phi_{pp}(\omega)$ from different sections are displayed in Fig. 2.6. The frequency range for which measurements were conducted varies from 1 up to 6 kHz. The levels appear to be rather similar except for the frequency bands 200-600 Hz with a variation of 5 dB. From these results, it can be noted that the TBL is not fully developed and homogeneous. In addition, the corner

edges may be responsible of these discrepancies. However, in the following step, the point frequency spectrum will be considered as homogeneous despite some obvious differences between 200 and 600 Hz. The averaged power spectral density (in blue) from S_4 and S_5 (in red) shall be retained in our analysis. The averaged PSD is shown in Fig. 2.7 for four retained centerline velocities. The overall shape remains nearly identical except at 5 m/s. In this latter case, the spectrum decreases more rapidly with increasing frequency from 600 Hz and the presence of sharp peaks above 2000 Hz is thought to be due to background fan noise. It will be shown that this behavior is due to the effect of area averaging over the sensor. Hence, pressure fluctuations smaller than the transducer sensing area are spatially integrated, and thereby attenuated. This causes the measured power spectrum of surface pressure fluctuations to be attenuated at high frequencies. At low frequencies, standing waves can occur due to imperfect anechoic terminations. The acoustic pressure field is amplified at discrete frequencies approximatively given by $f_m = mc_0/2L_p$, where L_p is the total pipe length ($\simeq 8.5$ m). Note the emergence of the second transverse acoustic propagating duct mode f_{10}^{rec} in blue at 1700 Hz. The first duct frequency cut on $f_c = f_{01}^{\text{rec}}$ appears at 850 Hz.

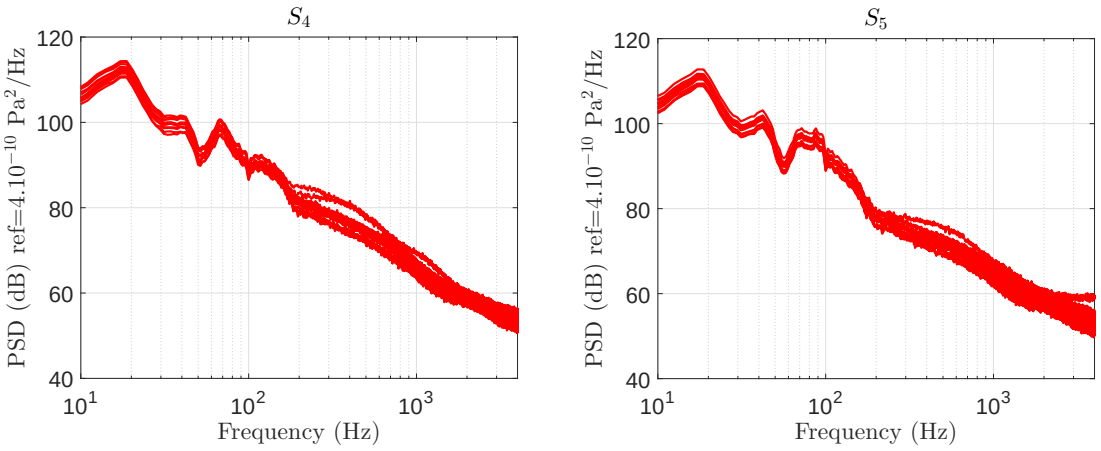

Figure 2.5: PSD of the 12 microphones at (a) the inlet test section S_4 and (b) the outlet test section S_5.

2.2.4 Background noise decontamination and effect of area averaging over the sensor

As mentioned above, the wall pressure is likely to be subject to acoustic or unwanted signal contamination especially at low frequencies. These components can be removed

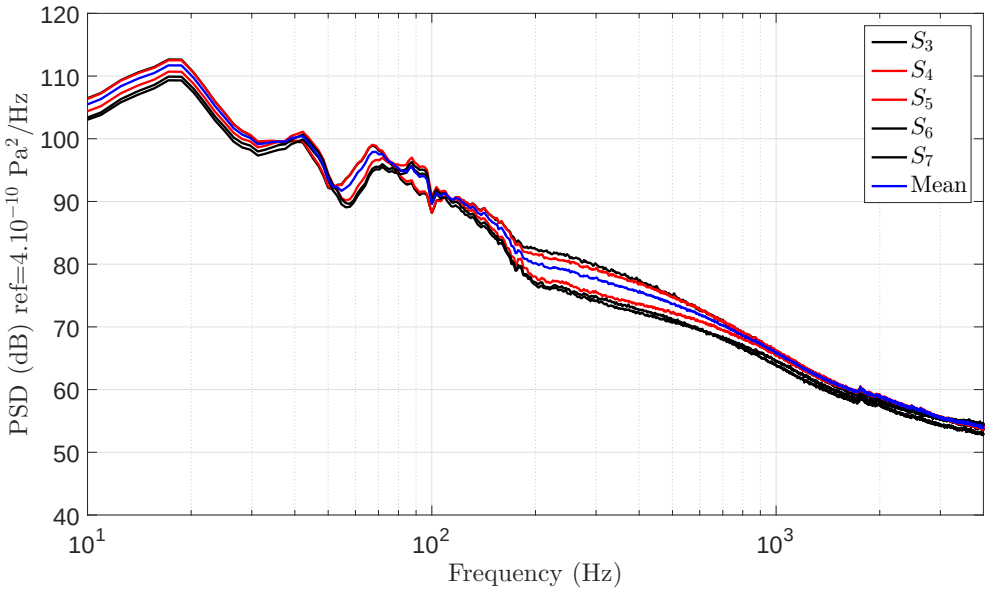

Figure 2.6: Evolution of PSD at different sections at 20 m/s (in red microphones sections between the test section).

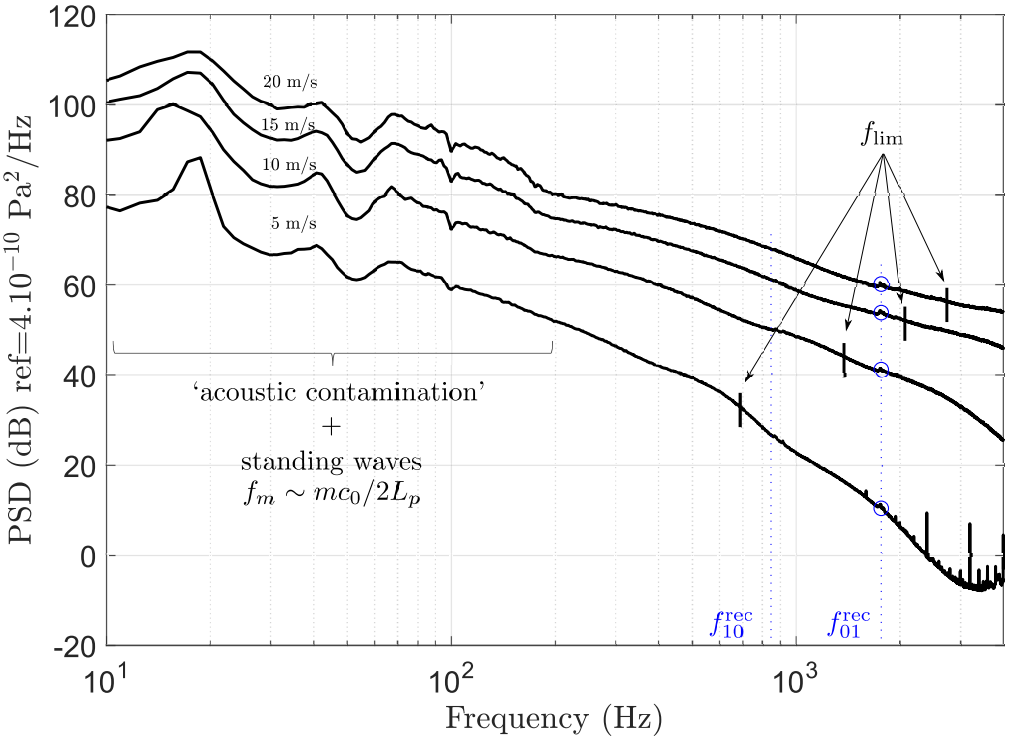

Figure 2.7: Evolution of PSD with velocity at 5 m/s, 10 m/s, 15 m/s and 20 m/s.

using coherence with microphones mounted at section S_8. Unwanted acoustic pressure waves are expected to produce coherent signals over long distance. This is not the case for TBL. The unwanted signals can be canceled using either a Coherent Output Power (COP) technique or a temporal subtraction method. Durant [11] analyzed the difference between these two methods. He concluded that the COP technique proves to be the most robust and the simplest solution to implement since the subtraction technique requires acquisition of the time signals plus a post-processing. This technique described by Bendat and Persol [69] allows to decontaminate the PSD $\Phi^i_{pp}(\omega)$ 'measured' at the ith microphone, using the coherence $\gamma_{i,j}$ between microphone i and j (the latter is mounted at section S_8 far enough from the others). It writes

$$\Phi^{i,\mathrm{cor1}}_{pp}(\omega) = \Phi^i_{pp}(\omega)\,(1-\gamma_{i,j})\,, \tag{2.18}$$

where $\Phi^{i,\mathrm{cor1}}_{pp}(\omega)$ is the corrected auto spectrum at the ith microphone using the COP technique. At higher frequencies, the decrease in PSD is accentuated by the effect of area averaging over the sensors. In this work, 1/2-inch microphones are used which corresponds to a sensing radius for a circular transducer $r = 6.35$ mm. Autospectra are corrected following Corcos' work (see Table I in [40]) who provides an attenuation table in the form

$$\frac{\Phi_{pp}(\omega)}{\Phi^{\mathrm{cor2}}_{pp}(\omega)} \tag{2.19}$$

as a function of $\omega r/U_c$, where $\Phi^{\mathrm{cor2}}_{pp}(\omega)$ is the autospectrum corrected following Corcos' table. As pointed by Durant [11], the effective sensing radius r_{eff} of the active face of the microphone (where the sensibility is constant) is given approximatively by $r_{\mathrm{eff}} \simeq 0.62r$. In the following, $r = r_{\mathrm{eff}}$ is adopted and $U_c = 0.85U_\infty$. Goody in [64] reported that the true high-frequency spectral values are correctly recovered for $\omega r/U_c < 4$. This condition gives the limit frequencies f_{lim} for the different speed flows as depicted in Fig. 2.7.

Corrected values $\Phi^{\mathrm{cor1}}_{pp}(\omega)$ and $\Phi^{\mathrm{cor2}}_{pp}(\omega)$ are reported in Fig. 2.8 and compared to the wall pressure spectrum $\Phi_{pp}(\omega)$ without correction. Results are given at 20 m/s and show that the effects of unwanted signal contamination and the size of the microphones are non-negligible. The first shaded area indicates the frequency band where the background noise and standing waves resonances dominate. The second corresponds to the frequency limit beyond which the spectral level is assumed to be attenuated more than 10 dB at 20 m/s. At low frequencies $\Phi^{\mathrm{cor1}}_{pp}(\omega)$ is about 20-15 dB lower up to

200 Hz than the original spectrum. The corrected $\Phi_{pp}^{\mathrm{cor2}}(\omega)$ spectrum is 10 dB higher above 1400 Hz. The small vertical line indicates the limit frequency f_{lim} of the Corcos correction. This limit corresponds to a step change, as it can be observed at 2700 Hz. It should be recalled that this pipe rig was designed to measure the acoustic power produced by inserted HVAC component and further improvement would give more accurate measurement of the hydrodynamic contribution. Nevertheless, it allows to validate measurements with semi-empirical models from the literature and quantify the relative weight of the hydrodynamic contribution in comparison with the acoustic one.

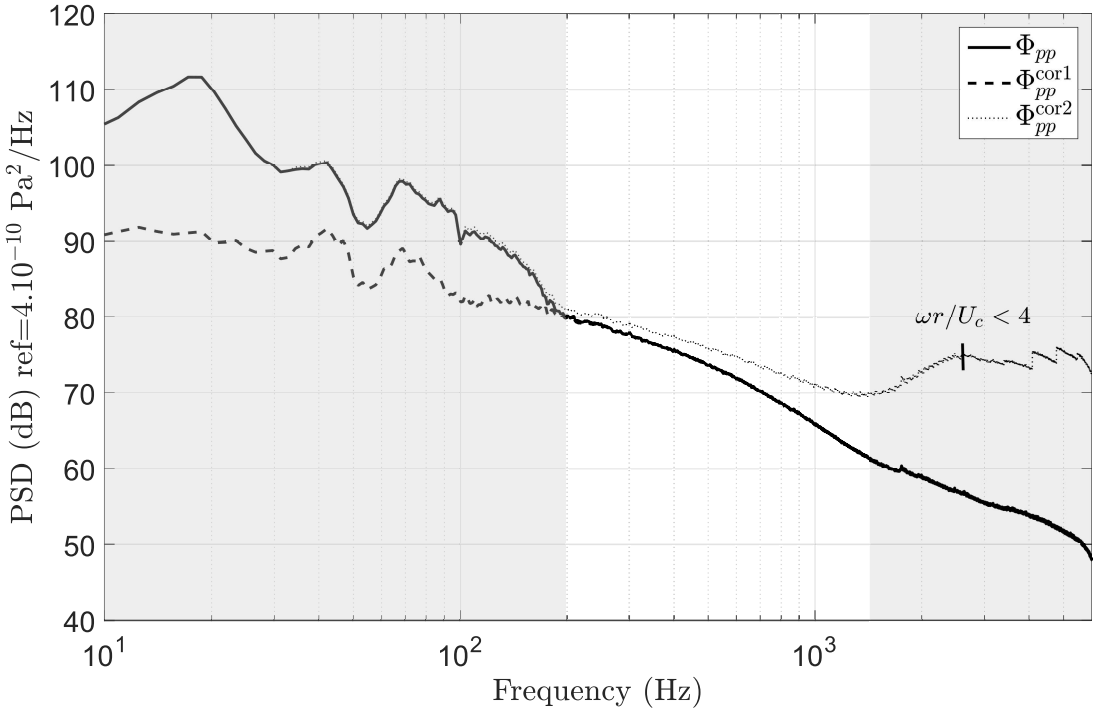

Figure 2.8: Corrected values $\Phi_{pp}^{\mathrm{cor1}}$ (after noise reduction) and $\Phi_{pp}^{\mathrm{cor2}}$ (after taking into account sensor area averaging) at 20 m/s. The grey area indicates the uncertainties about the true low and high frequency spectral components of the point spectrum.

2.2.5 Dimensionless point spectrum

The analysis of the dimensionless point spectrum allows to reveal important properties of the phenomenon under consideration which is its self-similarity, which means that a phenomenon reproduces itself on different length scales. But the application of self-similarity principles to turbulent boundary layers is complicated because the character of the boundary layer varies with the distance to the wall. The different boundary layer scales (inner, outer or a 'mixed' of both) are related to organized motions or coherent structures that exist in the boundary layer which vary in the regions normal to the wall. It is divided into two families: one associated to motion near the wall ("inner" variables) and the other to motion in the region away from the wall ("outer" variables). Since the structure of the wall pressure field is complex, it is very difficult to find a single universal scaling for the boundary layer. It is generally agreed the outer region determines the pressure levels at low frequencies and the inner region is most responsible for the high frequency content of the point spectrum as shown in Fig. 1.4. The separation between this two regions occurs where the point auto-spectrum exhibits its maximum value.

For the case of a boundary layer along a flat plate, the outer scales: U_∞, $\frac{1}{2}\rho U_\infty^2$, δ, δ^* and the inner scales: u_τ, τ_w, ν are commonly used. However, for an internal flow, the outer scales δ and δ^* are not defined explicitly. It is common [12, 14] to assimilate δ to the radius R_h and δ^* to $R_h/8$. In this section, three point spectra found in the literature expressed in outer or mixed variable scaling are chosen and confronted with measurements. In the comparisons presented here, all ambiguities with regard to single or double-sided spectra, or from factors of 2π have been taken into account. The one-sided spectrum can be calculated from $\Phi_{pp}(\omega)$ using

$$G_{pp}(f) = 2\pi\Phi_{pp}(2\pi f). \tag{2.20}$$

Note that G_{pp} is defined so that $\overline{p^2} = \int_0^\infty G_{pp}(f)df$ and the wall-pressure spectra Φ_{pp} follows the single-sided convention $\overline{p^2} = \int_0^\infty \Phi_{pp}(\omega)d\omega$.

The first one comes from Durant's measurement [11, 12]. It is expressed in outer variable scaling:

$$\begin{aligned}\log_{10}\left[\frac{G_{pp}(f)U_\infty}{q^2R}\right] &= -5.1 - 0.9\log_{10}(fR/U_\infty) \\ &- 0.34\left[\log_{10}(fR/U_\infty)\right]^2 \\ &- 0.04\left[\log_{10}(fR/U_\infty)\right]^3,\end{aligned} \tag{2.21}$$

where $q = \frac{1}{2}\rho U_\infty^2$ is the dynamic pressure. The second one is the Goody's model [64] which has become a widely used point spectrum model. It is expressed in mixed variable scaling and writes:

$$\frac{\Phi_{pp}(\omega)U_\infty}{\tau_w^2\delta} = \frac{C_2(\omega\delta/U_\infty)^2}{[(\omega\delta/U_\infty)^{0.75} + C_1]^{3.7} + [C_3(\omega\delta/U_\infty)]^7}, \tag{2.22}$$

where $R_T \equiv (u_\tau\delta/\nu)\sqrt{C_f/2}$ can be interpreted as a Reynolds number. In this formula, coefficients C_1, C_2 and C_3 are three empirical constants obtained by fitting a large number of experimental data, and are set to $C_1 = 0.5$, $C_2 = 3$ and $C_3 = 0.11R_T^{-0.57}$. The third one is the Lysak fit of the Chase-Howe model [131]:

$$G_{pp}(f) = \frac{3\rho^2u_\tau^4}{f^*}\left(\frac{f}{f^*}\right)^2\frac{\mathrm{e}^{-14f\nu/u_\tau^2}}{\left[(f/f^*)^2 + \hat{\alpha}^2\right]^{3/2}}, \tag{2.23}$$

where $f^* = U_\infty/(2\pi\delta^*)$. This model has been developed for modeling the wall pressure spectrum in turbulent pipe flows. In Lysak's paper, the final form of the model is expressed as an integral of the turbulent sources over the boundary layer thickness. Its expression can be found in [132, 133].

Fig. 2.9(a),(b) and Fig. 2.9(c),(d) show the measured wall spectra with or without correction for different flow speeds expressed in either outer or mixed variable scaling to allow a comparison with Durant measured data and Goody model. In all cases, data collapses relatively well using both scaling over the majority of the measured frequency range. The correction procedure described earlier allows to obtain the general trend of the wall pressure fluctuations. According to the literature (see Fig. 1.4), the shape of the point wall pressure spectrum exhibits a slope of ω^2 as the frequency goes to zero, a slope of around ω^{-1} in the overlap region, and a slope of between $\omega^{-7/3}$ and ω^{-5} in the high frequency range. The measured spectra level with corrections are about 15 dB higher than Durant measured data and 5 dB lower than the Goody model.

It is recalled that the Colebrook equation is chosen to obtain the friction velocity because it gives the most satisfactory results compared to experimental data from static pressure measurements. However, the constant pressure fluctuation region corresponding to developed turbulent flow is not observed especially between 100 and 1000 Hz (Fig. 2.5, 2.6). It was also observed (Fig. 2.3(a)) that the static pressure has not a linear decrease near the test section region. In addition, the boundary layer thickness is assimilated to the radius R_h. As pointed out by some authors [134, 135], flows in 'complex' ducts (here of rectangular cross-section) are understood to a much lesser extent compared to canonical flows in plane channels and circular pipes, particularly with respect to turbulence modeling close to the wall and corner regions. Hence, secondary flows appear near the corners of the duct cross-section, leading to a deformation of the mean velocity contours [136, 137]. Based on all these considerations, it can be concluded that uncertainties remain about the true friction velocity and boundary layer thickness values.

The measured data is compared to the Chase-Howe-Lysak model using different boundary layer heights as well as flow speeds as shown Fig. 2.10(a). Red curves correspond to a boundary layer thickness of $D_h/2$. In blue, it corresponds to boundary layer thicknesses taken at a downstream distance x of about 2 meters using the standard formula taken from Fig. 2.4:

$$\frac{\delta}{x} \cong \frac{0.38}{(\mathrm{Re}_x)^{1/5}}. \tag{2.24}$$

Fig. 2.10(b) shows the boundary layer displacement thickness as a function of the downstream distance. It appears that the Chase-Howe-Lysak model gives the best results (difference lower than 4 dB in our frequency range). The calculated point spectra are only modified at low frequencies when the boundary layer thickness formula Eq.(2.24) is used. The approximation $\delta = D_h/2$, therefore, is acceptable. Results are mainly sensitive to friction velocity values in our frequency range. This is due to the test section position in the pipe rig. Recently, Selvam *et al* [138] have shown that the entrance region effect can be neglected for x/D_h above 30 ($x/D_h \approx 13$ in our case).

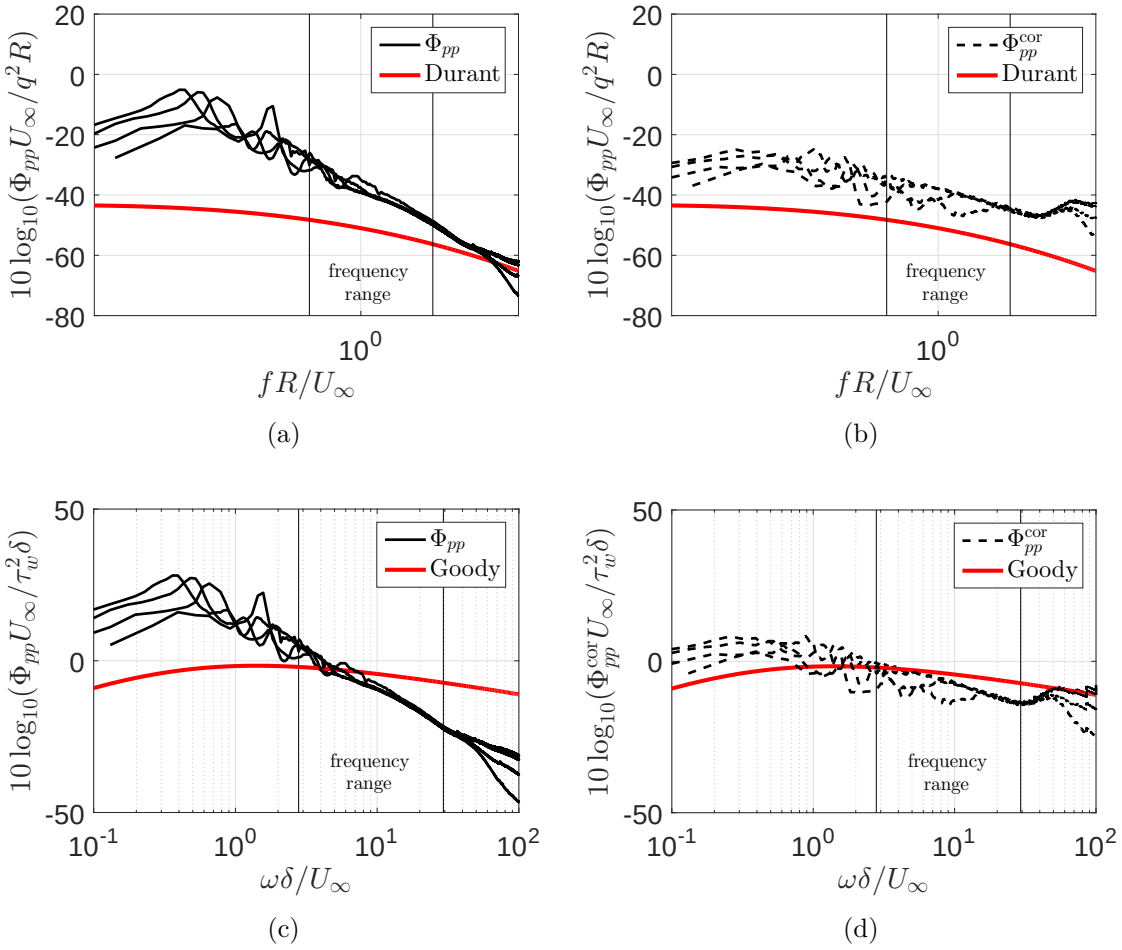

Figure 2.9: Dimensionless point spectrum: (a) and (b) comparison with Robert model's and (c) and (d) with Goody model's. The point spectrum without correction Φ_{pp} is used (left) and with correction Φ_{pp}^{cor} (right).

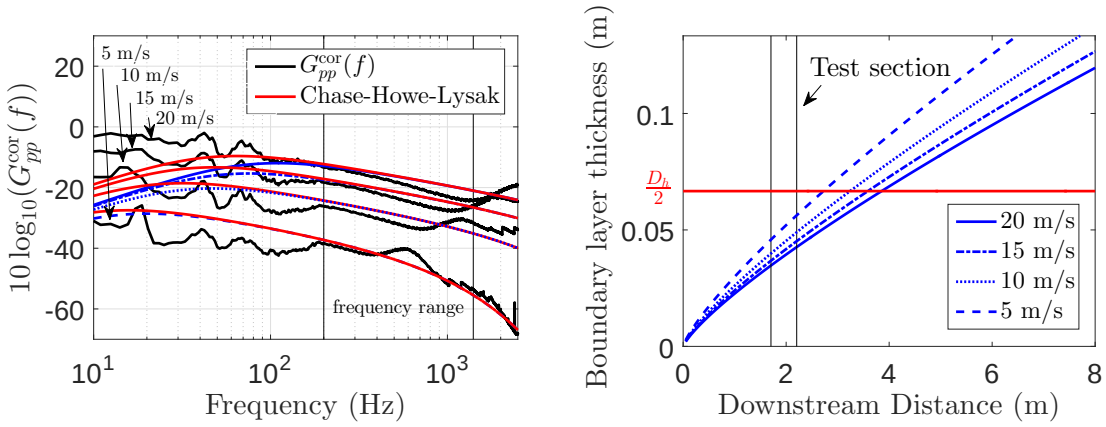

(a) (b)

Figure 2.10: (a) Comparison with the Chase-Howe-Lysak model using different boundary layer heights as well as flow speeds. (b) Boundary layer displacement thickness as a function of downstream distance for TBL flow at 5, 10, 15 and 20 m/s.

2.2.6 Measurement of the Cross Power Spectral Density

The following is an attempt to predict some key parameters of the cross spectral empirical models defined in Eq.(1.5) according to Corcos' work, namely the exponential decays rate of coherence functions and convection velocity of oscillations in the flow direction. These features stem from the fact that the turbulent wall spectrum is partially correlated over space and convected at a certain velocity. The cross-spectrum is a complex function, ie $S_{pp} = |S_{pp}|\,\mathrm{e}^{\mathrm{i}\theta}$ and the results in this section are presented in terms of coherence, or normalized cross-spectral magnitude, between two microphones located in $\mathbf{s}_1$ and $\mathbf{s}_2$, defined by

$$\gamma(\mathbf{s}_1, \mathbf{s}_2) = \frac{|S_{pp}(\mathbf{s}_1, \mathbf{s}_2, \omega)|}{\sqrt{\Phi_{pp}(\mathbf{s}_1, \omega)\Phi_{pp}(\mathbf{s}_2, \omega)}}. \tag{2.25}$$

All acquisitions data use an averaging process over 600 realizations. According to Eq.(1.5), convection velocity can be computed from the phase between pairs of dynamic pressure sensors in the streamwise direction

$$U_c \approx \frac{-\omega\xi_z}{\theta(\omega, \xi_z)}. \tag{2.26}$$

Fig. 2.11(a) shows the unwrapped phase $\theta(\omega, \xi_z)$ as a function of frequency with the shortest streamwise separation distance $\xi_z = 3.5$ cm. The phase decreased linearly with frequency up to 500 Hz. Note that background noise is not removed from the

phase as indicated in the small 'bump' in the spectrum at very low frequencies. Corresponding values for normalized convection velocity, U_c/U_∞, are plotted in Fig. 2.11(b). It is compared with an estimate for convection velocity suggested by Ko [139] based on Bull's work [39] where

$$U_c \cong 0.6 + 0.4\mathrm{e}^{-0.8\omega\delta^*/U_\infty}. \tag{2.27}$$

The phase noise contamination appears to have a major influence on the convection velocity prediction at low frequencies. The size of the sensor and the streamwise separation distance seem to be unadapted for the estimation of the convection velocity. Despite this, the linear dashed blue curve from Fig. 2.11(b) is used to estimated the ratio between the convection velocity and the centerline velocity. A ratio of 0.85 is found between the convection velocity and the centerline velocity.

The TBL wall pressure coherences are estimated in the spanwise and streamwise direction for different flow speeds and separation distances. Results are given in Fig. 2.12. An exponential shape is expected for the coherences according to Corcos model, see Eq.(1.5). The spanwise coherence is defined as:

$$A(\xi_s, \omega) = \frac{|S_{pp}(\xi_s, \omega)|}{\sqrt{\Phi_{pp}(s_1, \omega)\Phi_{pp}(s_2, \omega)}}, \tag{2.28}$$

and the streamwise coherence as:

$$B(\xi_z, \omega) = \frac{|S_{pp}(\xi_z, \omega)|}{\sqrt{\Phi_{pp}(z_1, \omega)\Phi_{pp}(z_2, \omega)}}. \tag{2.29}$$

Note that the coherence $\gamma_{i,j}$ used in Eq.(2.18) to decontaminate the measured PSD is consistent with Eq.(2.29). The coherences for the shortest spanwise and streamwise separation distances at various flow speeds are shown respectively in Fig. 2.12(a) and Fig. 2.12(b). As expected, coherences become stronger as the flow speed increases except at low frequencies. Coherences for a fixed flow speed at various spanwise and streamwise separation distances are shown respectively in Fig. 2.12(c) and Fig. 2.12(d). The correlations decrease as the spanwise and streamwise separation distances between the pressure probes increase. The spanwise coherence is weak and concentrated in a small frequency band whereas the streamwise coherence decrease gently over a largest frequency range. Note that there is any significant changes in the spanwise coherence with separations distances. The streamwise coherence is

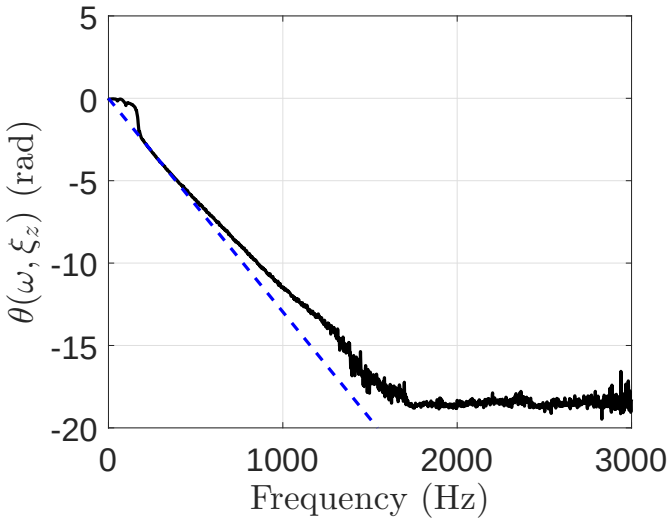

(a)

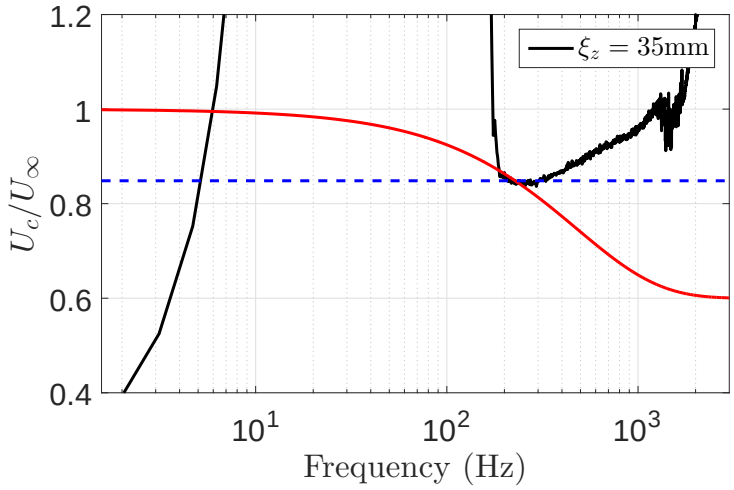

(b)

Figure 2.11: (a) Phase function of the cross-spectrum. (b) Comparison of measured convection velocity with Ko model's (in red) according to Eq.(2.27). The dashed blue curve comes from the corresponding linear asymptote in Fig. 2.11(a).

the strongest for the smallest streamwise separation and decreases as the streamwise separation increases. These measurements are limited since the greatest spanwise separation for which there is any significant coherence is the shortest spanwise separation distance given by the pipe rig set up. In addition to that, the evolution of the streamwise coherence is limited to two streamwise separation distances since the next accessible streamwise separation is irrelevant and corresponds to a separation distance of 70 cm. In all cases, the residual coherence at low frequencies corresponds to the background noise. Despite the limitations imposed by the pipe rig, it suggests a simple formulation for the coherences by fitting data with Corcos' exponential functions. The coefficients found are $\gamma_s = 1$ and $\gamma_z = 0.18$ as shown in Fig. 2.12(e) and Fig. 2.12(f).

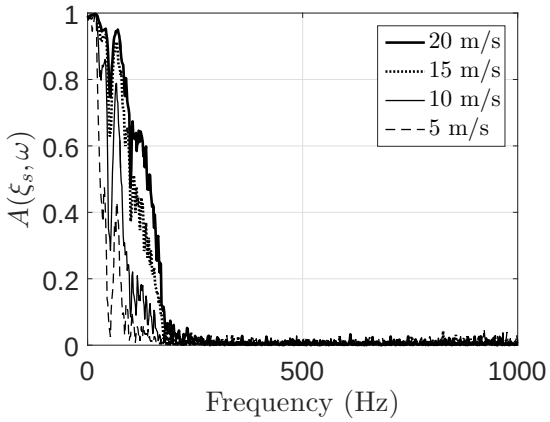

(a) Spanwise coherence with $\xi_s = 2.27$ cm

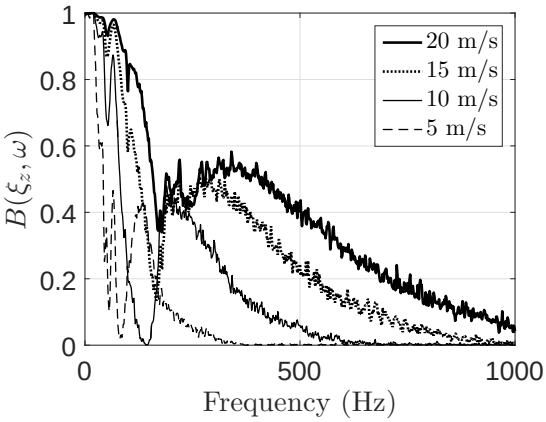

(b) Streamwise coherence with $\xi_z = 3.50$ cm

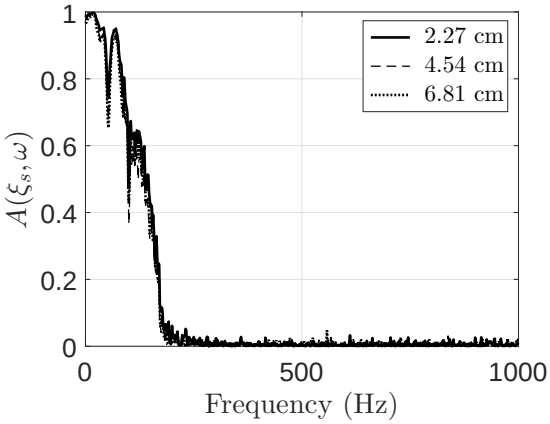

(c) Spanwise coherence with at 20 m/s

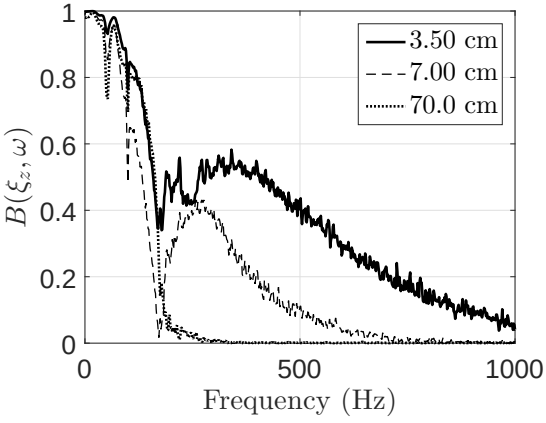

(d) Streamwise coherence at 20 m/s

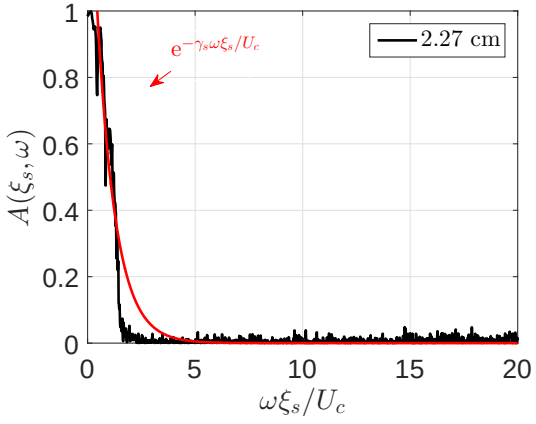

(e)

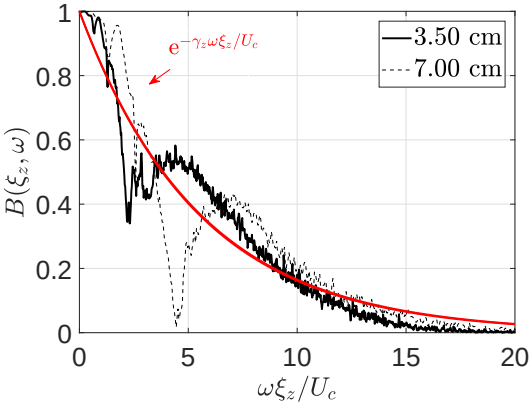

(f)

Figure 2.12: Spanwise and Streamwise coherences: (a) and (b) for different flow speeds; (c) and (d) for different separation vectors; and, (e) and (f) with Corcos correlation envelope for $(\gamma_z, \gamma_s) = (0.18, 1)$.

2.3 Acoustic contribution

The acoustic modal amplitudes $\left|C_{pq}^{\pm}(\omega)\right|$ are measured using two methods. For the first scenario, the estimation of the acoustic contribution is performed using a method based on the measurement of several cross-spectra between microphones at the four sections S_1, S_4, S_7 and S_8. For the second scenario, the duct is obstructed by a diaphragm and the 2N-port method is used.

2.3.1 Cross-spectra based method: no obstruction in the duct

The duct is straight with no singularity, so that propagating acoustic modes are generated by the TBL itself all along the duct. The input data is a set of cross-spectra between microphones at the four sections S_1, S_4, S_7 and S_8 as illustrated in Fig. 2.13. The pressure fields that we will consider can be decomposed into three parts, such that,

$$p(\mathbf{s}_1, \omega) = p_h(\mathbf{s}_1, \omega) + p_{ac}(\mathbf{s}_1, \omega) + n, \tag{2.30}$$

where p_h gathers the turbulent fluctuations, p_{ac} represents the acoustic pressure field and n is some measurement noise inherent to the acquisition process (including vibration of supporting structures, electrical perturbations occurring in electronic circuits). It is assumed that distances between microphones are much larger than the correlation

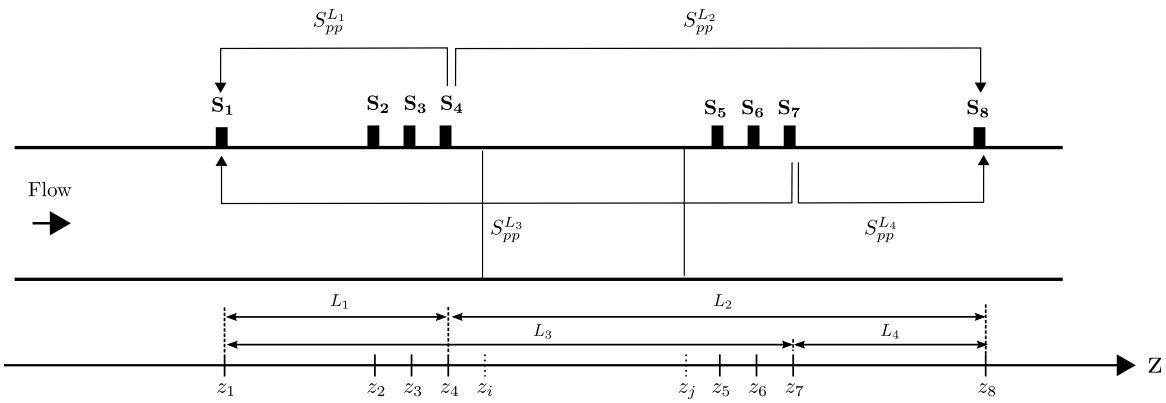

Figure 2.13: Illustration of the set of cross-spectra between microphones at the four sections S_1, S_4, S_7 and S_8.

lengths of the hydrodynamic wall pressure fluctuations so that turbulent fluctuations and the acoustic component are assumed uncorrelated random variables. According to the cross spectrum definition between 2 microphones placed fairly far away and assuming that all uncorrelated random variables tends to zero with the averaging

process, the measured cross spectrum is approximated by the following relationship

$$S_{pp}^{\Delta z \gg 1}(\mathbf{s}_1, \mathbf{s}_2, \omega) \approx \lim_{T\to\infty} \frac{2\pi}{T} \mathbb{E}\left[p_{ac}(\mathbf{s}_1, \omega) p_{ac}^*(\mathbf{s}_2, \omega)\right], \tag{2.31}$$

with Δz a fairly large distance between two microphones. It is assumed that the pressure field is written as a sum of propagating modes, for instance at point $\mathbf{s}_1 = (s_1, z_1)$ can be

$$p_{ac}(\mathbf{s}_1, \omega) = \sum_{pq} C_{pq}^{+} \psi_{pq}(s_1) e^{\mathrm{i}k_{pq}^{+} z_1} + \sum_{pq} C_{pq}^{-} \psi_{pq}(s_1) e^{\mathrm{i}k_{pq}^{-} z_1}, \tag{2.32}$$

where $C_{pq}^{\pm}$ stands for amplitude of the downstream (+) and upstream (-) propagating mode and ψ_{pq} the acoustic mode (p, q). Transverse acoustic modes ψ_{pq} are conveniently defined as the projection of the acoustic mode along the curvilinear abscissa s giving

$$\psi_{pq}(s) = \begin{cases} \cos\left(\dfrac{p\pi s}{L_x}\right) & ; \quad s \in [0; L_x] \\ \cos(p\pi)\cos\left(\dfrac{q\pi\left[s - L_x\right]}{L_y}\right) & ; \quad s \in [L_x; L_x + L_y] \\ \cos\left(\dfrac{p\pi\left[2L_x + L_y - s\right]}{L_x}\right)\cos(q\pi) & ; \quad s \in [L_x + L_y; 2L_x + L_y] \\ \cos\left(\dfrac{q\pi\left[2L_x + 2L_y - s\right]}{L_y}\right) & ; \quad s \in [2L_x + L_y; 2L_x + 2L_y] \end{cases} \tag{2.33}$$

The pressure field given by Eq.(2.32) is introduced in Eq.(2.31), thus the cross spectrum between two microphones separated with a sufficient distance $\Delta z = z_2 - z_1$ writes

$$\begin{aligned} S_{pp}^{\Delta z \gg 1}(\mathbf{s}_1, \mathbf{s}_2, \omega) &= \sum_{pq} \mathbb{E}\left[\left|C_{pq}^{\pm}(\omega)\right|^2\right] \psi_{pq}(s_1)\psi_{pq}(s_2) \mathrm{e}^{\mathrm{i}k_{pq}^{\pm}\Delta z} \\ &+ \sum_{\substack{pq \\ pq\neq rs}} \mathbb{E}\left[C_{pq}^{\pm}(\omega) C_{rs}^{\pm}(\omega)^*\right] \psi_{pq}(s_1)\psi_{rs}(s_2) \mathrm{e}^{\mathrm{i}(k_{pq}^{\pm} z_1 - k_{rs}^{\pm} z_2)}, \end{aligned} \tag{2.34}$$

where $\mathbb{E}[]$ is the ensemble average. The mode amplitudes are assumed all uncorrelated so that $\mathbb{E}\left[C_{pq}^{+}(\omega) C_{rs}^{+}(\omega)^*\right] = 0$. It is further assumed that the same mode propagating in opposite directions are also uncorrelated $\mathbb{E}\left[C_{pq}^{+}(\omega) C_{pq}^{-}(\omega)^*\right] = 0$. Here, acoustic modes are deliberately not normalized (for instance the plane mode is simply $\psi_{00} = 1$) so the quantity $\mathbb{E}\left[|C_{pq}(\omega)|^2\right]$ can be regarded as the auto-power spectrum. To simplify the analysis, the flow is assumed uniform and we neglect thermo-viscous attenuation. The axial wavenumbers $k_{pq}^{\pm}$ including convection have the following expression (here

$k = \omega/c$):

$$k_{pq}^{\pm} = \frac{kM \pm \sqrt{k^2 - (1-M^2)\left(\left(\frac{p\pi}{L_x}\right)^2 + \left(\frac{q\pi}{L_y}\right)^2\right)}}{1-M^2}, \tag{2.35}$$

where M is the Mach number. The condition for an acoustic mode to propagate is that the wavenumber $k_{pq}^{\pm}$ must be real. Otherwise the wave will decay exponentially and is known as an evanescent wave. The frequency at which a mode (p, q) begins to propagate is the cut-off frequency of the mode. Note that evanescent waves are neglected here. The study is limited to the plane wave and the first transverse duct mode so that Eq.(2.34) contains only four terms:

$$\begin{aligned} S_{pp}^{\Delta z \gg 1}(s_i, s_j, \omega) &= \left|C_{00}^{+}\right|^2 \psi_{00}(s_i)\psi_{00}(s_j) \exp\left[\mathrm{i}k_{00}^{+}\Delta z\right] \\ &+ \left|C_{00}^{-}\right|^2 \psi_{00}(s_i)\psi_{00}(s_j) \exp\left[\mathrm{i}k_{00}^{-}\Delta z\right] \\ &+ \left|C_{10}^{+}\right|^2 \psi_{10}(s_i)\psi_{10}(s_j) \exp\left[\mathrm{i}k_{10}^{+}\Delta z\right] \\ &+ \left|C_{10}^{-}\right|^2 \psi_{10}(s_i)\psi_{10}(s_j) \exp\left[\mathrm{i}k_{10}^{-}\Delta z\right]. \end{aligned} \tag{2.36}$$

Here, s_i and s_j are the locations of the microphone at each section (remind that each section is equipped with 12 microphones regularly distributed on the duct wall for mode separation). The $\mathbb{E}\,[]$ notations are omitted for the sake of clarity. Considering all sensor points, we can rewrite Eq.(2.36) in matrix notation

$$\mathbf{s}_{pp}^{\Delta z}(\omega) = \mathbf{\Phi}_{\pm}(\omega)\mathbf{g}_{s\pm}^{\Delta z}(\omega) \tag{2.37}$$

where $\mathbf{s}_{pp}^{\Delta z}(\omega) \in \mathbb{C}^{[n\times 1]}$ is the vector containing the cross spectra sampled at $n = 12 \times 12$ spatial positions, $\mathbf{g}_{s\pm}^{\Delta z}(\omega) \in \mathbb{C}^{[4\times 1]}$ is the vector containing the mode amplitudes $\langle \left|C_{00}^{-}\right|^2 \left|C_{00}^{+}\right|^2 \left|C_{00}^{-}\right|^2 \left|C_{10}^{+}\right|^2 \rangle$ and $\mathbf{\Phi}_{\pm}(\omega) \in \mathbb{C}^{[n\times 4]}$ contains the values of acoustic modes at each sensor. The duct mode amplitudes are obtained by minimizing the overdetermined system in Eq.(2.37). The solution is given by inverting $\mathbf{\Phi}_{\pm}$ using the Moore-Penrose pseudo inverse. The solutions for the four different distances $\Delta z = L_1, L_2, L_3, L_4$ between sections are simply averaged.

Results for the plane wave using 600 averages are shown in Fig. 2.14(a) for each flow velocity. Fig. 2.14(b) shows the modal coefficients and the auto-spectrum wall pressure at 20 m/s. The energy ratio between the acoustic and hydrodynamic parts decreases with frequency from approximately 10 %(-10 dB) to 0.1 %(-30 dB) showing a slight increase of acoustic energy with the emergence of the transverse mode.

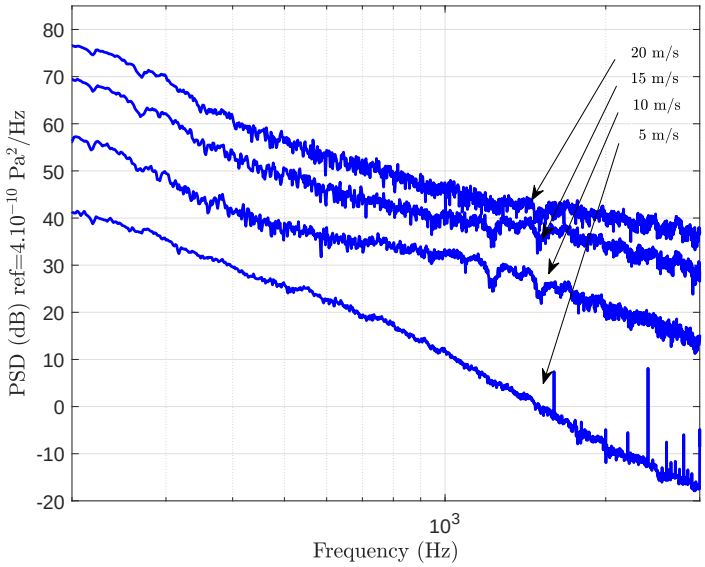

(a) Evolution of plane wave amplitudes $|C_{00}|^2$ with velocity at 5 m/s, 10 m/s, 15 m/s and 20 m/s.

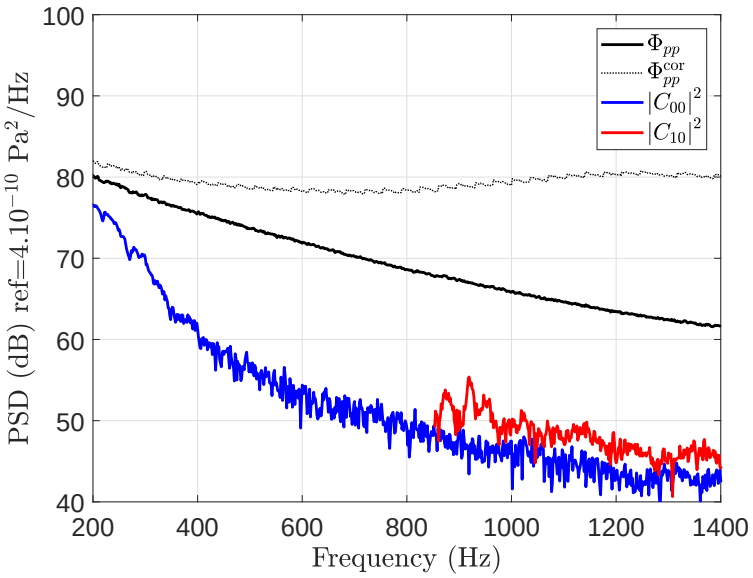

(b) Estimation of the acoustic plane wave and transverse propagating duct mode in the case of a straight duct with no singularity, the flow speed is 20 m/s.

Figure 2.14

2.3.2 $2N$ port method

Acoustic measurements can be performed on the basis of the so-called $2N$ port method [120, 125] to tackle the problem of a pipeline singularity. In this study, a rigid obstacle is inserted in the test section. It is appropriate to recall some of the main outline of the $2N$ port method and all necessary details are given in Appendix B. The multiport formulation in a duct, as in Fig. 2.15, can be written in a compact form

$$\mathbf{a}^{\text{out}}(\omega) = \mathbf{S}(\omega)\mathbf{a}^{\text{in}}(\omega) + \mathbf{a}^{s}(\omega), \tag{2.38}$$

with

$$\mathbf{a}^{\text{out}} = \begin{bmatrix} \mathbf{c}_{\text{I}}^{-} \\ \mathbf{c}_{\text{II}}^{+} \end{bmatrix}, \quad \mathbf{a}^{\text{in}} = \begin{bmatrix} \mathbf{c}_{\text{I}}^{+} \\ \mathbf{c}_{\text{II}}^{-} \end{bmatrix} \text{ and } \mathbf{a}^{\text{s}} = \begin{bmatrix} \mathbf{c}_{s}^{+} \\ \mathbf{c}_{s}^{-} \end{bmatrix}. \tag{2.39}$$

The scattering matrix $\mathbf{S} \in \mathbb{C}^{[2N\times 2N]}$ contains the transmission and reflection of all N modes at the inlet and the outlet. The complex vectors $\mathbf{a}^{\text{in,out}} \in \mathbb{C}^{[2N\times 1]}$ are respectively the incident and outgoing modal pressure amplitudes. The source vector $\mathbf{a}^{s} \in \mathbb{C}^{[2N\times 1]}$ contains the sound waves which are generated by the element itself under reflection-free conditions. We refer to the scattering matrix as passive part and to

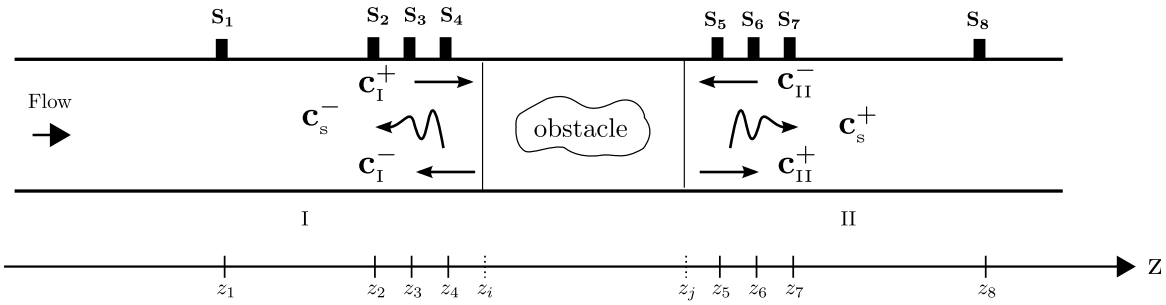

Figure 2.15: An illustration of an acoustic multi-port. The vectors $\mathbf{a}^{\text{in}}$ and $\mathbf{a}^{\text{out}}$ contain respectively the incident and outgoing modal pressure amplitudes, $\mathbf{S}$ is the scattering matrix and $\mathbf{a}^{s}$ the source vector. The indices I and II denote the upstream and downstream side of the multi-port.

the source vector as active part of the multi-port, where the aim of a full multi-port analysis is to determine such characteristic properties.

The acoustic scattering matrix is first identified by measuring the acoustic response to given external excitations. A transfer function method is implemented so that the measured pressure signals at $l = 12$ sensor points in a section are expressed formally by:

$$p(s_l, z, \omega) = H_{\text{e}/l}^{z}(\omega)e(\omega), \tag{2.40}$$

where e is the electrical signal (set to 1V) driving the external loudspeaker and $H^z_{e/l}$ the transfer function between the lth microphone at section located in z and the electrical signal. Here, the transfer function is defined using the 'H$_1$ estimator' convention (see Eq.(2.4)) so that the pressure signals and the reference signal e are correlated which allows to suppress the vector source term contribution in Eq.(2.38) ($\mathbf{a}^s = 0$). Here, the external sound fields were excited with a pseudo white noise. The scattering matrix has the dimension $2N \times 2N$ and therefore, we need $2m$ configurations linearly independent with $m \geqslant N$. In addition, the complex mode amplitudes contained in vectors $\mathbf{a}^{\text{in,out}}$ need to be calculated in both propagating directions at the multi-port inlet and outlet by applying a modal decomposition technique which is reminded in Appendix B. The scattering matrix can be extracted solving Eq.(2.38) such as

$$\mathbf{S} = \mathbf{a}^{\text{out}}(\omega) \left(\mathbf{a}^{\text{in}}(\omega)\right)^{-1}, \tag{2.41}$$

where $(\cdots)^{-1}$ denotes the pseudo-inverse, matrix $\mathbf{a}^{\text{in}}$ and $\mathbf{a}^{\text{out}}$ contain the decomposed acoustic fields for each test case $1, 2, ..., 2N$ (denoted by the superscript), as columns and writes

$$\mathbf{a}^{\text{in}} = \begin{bmatrix} \begin{bmatrix} \mathbf{c}^+_{\text{I}} \\ \mathbf{c}^-_{\text{II}} \end{bmatrix}_1 & \begin{bmatrix} \mathbf{c}^+_{\text{I}} \\ \mathbf{c}^-_{\text{II}} \end{bmatrix}_2 & \cdots & \begin{bmatrix} \mathbf{c}^+_{\text{I}} \\ \mathbf{c}^-_{\text{II}} \end{bmatrix}_{2N} \end{bmatrix} \tag{2.42}$$

and

$$\mathbf{a}^{\text{out}} = \begin{bmatrix} \begin{bmatrix} \mathbf{c}^-_{\text{I}} \\ \mathbf{c}^+_{\text{II}} \end{bmatrix}_1 & \begin{bmatrix} \mathbf{c}^-_{\text{I}} \\ \mathbf{c}^+_{\text{II}} \end{bmatrix}_2 & \cdots & \begin{bmatrix} \mathbf{c}^-_{\text{I}} \\ \mathbf{c}^+_{\text{II}} \end{bmatrix}_{2N} \end{bmatrix}. \tag{2.43}$$

In a second step, the source vector can theoretically be solved directly from Eq.(2.38) turning off the loudspeakers. However, because of the turbulence, the acoustic field is not directly accessible and a flow-noise suppression technique has to be applied. The formulation extracts the source strength using cross-spectrum densities between the four different sections S_1, S_4, S_7, S_8 as previously illustrated in Fig. 2.13. The reflections induced by the test-rig terminations are accounted for, incident from outgoing modes are separated and no assumption is made about the modal cross coupling. The matrix of the test rig terminations is introduced as follows

$$\mathbf{R} = \mathbf{a}^{\text{in}} \left(\mathbf{a}^{\text{out}}\right)^{-1} = \begin{bmatrix} \mathbf{R}_{z_i} & 0 \\ 0 & \mathbf{R}_{z_j} \end{bmatrix}, \tag{2.44}$$

and calculated using the same data to solve the scattering problem Eq.(2.41). The excitations at the downstream side is used to determine the reflection of the termination at the upstream side and vice versa. The matrix of the test rig termination couples the incident and the outgoing modal pressure so that Eq.(2.38) can be rearranged to solve for the modal source vector as following

$$\mathbf{a}^s = [\mathbf{I}_{2N} - \mathbf{SR}]\,\mathbf{a}^{\text{out}}. \tag{2.45}$$

The algorithm is built to post-process cross-spectra between section S_1, S_4, S_7, S_8. Hence, sections S_4 and S_7 are defined as inlet and outlet so that in all previous equations, $z_i = z_4$ and $z_j = z_7$. In addition, Eq.(2.45) can be transported to the furthest upstream and downstream sections S_1 and S_8. These steps require some algebra and are detailed in Appendix B. The source vector $\mathbf{a}^s$ at sections S_4 and S_7 is expressed in term of a source cross-spectrum matrix $\mathbf{G}^s \in \mathbb{C}^{[2N\times 2N]}$ to get a formulation valid for random signals. One finally get

$$\mathbf{G}^s = \mathbb{E}\left[\mathbf{a}^s\,(\mathbf{a}^s)^c\right], \tag{2.46}$$

where the superscript c denotes transpose and complex conjugate. The diagonal terms represent the modal auto-spectra respectively at the section S_4 and S_7:

$$\mathbf{G}^s = \left[\begin{array}{ccc|ccc} \ddots & & \mathbb{E}\left[C^-_{pq}(\omega)C^-_{rs}(\omega)^*\right] & & \text{Modal cross terms: } \mathbb{E}\left[\mathbf{c}_s^{-,z_4}(\mathbf{c}_s^{+,z_7})^*\right] & \\ & \mathbb{E}\left[\left|C^-_{pq}(\omega)\right|^2\right] & & & & \\ & & \ddots & & & \\ \hline & \text{Modal cross terms: } \mathbb{E}\left[\mathbf{c}_s^{+,z_7}(\mathbf{c}_s^{-,z_4})^*\right] & & \ddots & & \mathbb{E}\left[C^+_{pq}(\omega)C^+_{rs}(\omega)^*\right] \\ & & & & \mathbb{E}\left[\left|C^+_{pq}(\omega)\right|^2\right] & \\ & & & & & \ddots \end{array}\right]. \tag{2.47}$$

2.4 Application of $2N$-port method: noise due to an air flow through a constriction

One of the originality of this PhD is to write the forcing function on the basis of a sum of an hydrodynamic contribution provided by the Corcos's model and an acoustic part given by the coherence function of high order modes in the spirit of Norton's work. The forcing function adopted for the study of vibrations due to an internal wall pressure fluctuation writes

$$S_{pp}(\mathbf{s}_1, \mathbf{s}_2, \omega) = \Phi_{pp}(\omega)\Gamma^{\text{Corcos}} + \sum_{pq} \left|C_{pq}^{\pm}(\omega)\right|^2 \Gamma_{pq}^{\pm}, \tag{2.47}$$

with

$$\Gamma_{pq}^{\pm}(\mathbf{s}_1, \mathbf{s}_2, \omega) = \psi_{pq}(s_1)\psi_{pq}(s_2)\mathrm{e}^{\mathrm{i}k_{pq}^{\pm}\Delta z}. \tag{2.48}$$

This formalism is adopted for the scenario without singularity and the scenario with a flow constriction (in the region far from the obstacle). The auto-spectral quantity $\Phi_{pp}(\omega)$ is computed on the basis of Goody model using Eq.(2.8) and Eq.(2.5) to compute the wall shear stress τ_w. An attempt to measure the acoustic energy $\left|C_{pq}^{\pm}(\omega)\right|^2$ has been proposed for the case with no constriction.

In the case of an obstacle inserted in the duct, the acoustic energy can be extracted using the $2N$ port method as described previously. In the following, a reliable trend based on the scaling law introduced by Nelson & Morphey [140] is proposed in order to directly calculate the acoustic energy $\left|C_{pq}^{\pm}(\omega)\right|^2$ (at least for the plane wave) from only the knowledge of geometrical characteristics of the obstacle. The flow constriction is a diaphragm which is a 10 $\times$ 5 cm constriction centered in the duct as shown in Fig. 2.16. Its thickness is 8 mm. The $2N$ port method is applied and results for amplitudes of the downstream plane wave are shown in Fig. 2.17(a) at different flow speeds. The drop loss caused by the diaphragm limits the study to a speed flow of 10 m/s. The cross-spectra are averaged over 600 realizations. As expected, the acoustic pressure level increases with speed flow. Fig. 2.17(b) shows plane wave along with the first transverse mode at 6.5 m/s.

The scaling law approach introduced by Nelson & Morphey relies on the pressure drop and a scaled spectrum specific to the studied obstacle. To obtain this scaled spectrum, experiments or RANS computation can be performed [141, 142]. Below the first cut-off frequency, only the plane wave mode is allowed to propagate and, for

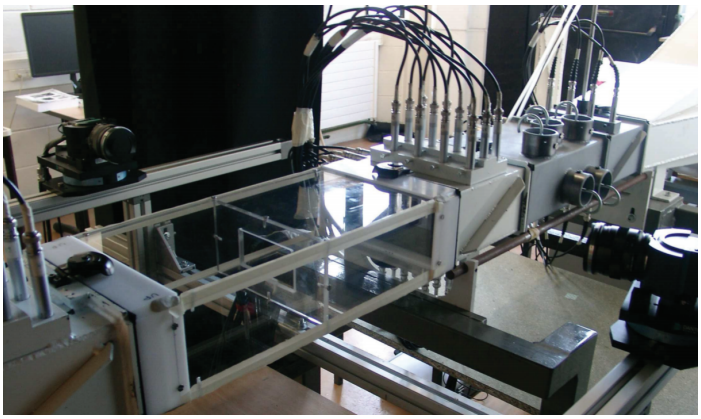

Figure 2.16: Application of the $2N$-port method for a diaphragm inserted in the duct.

compact obstacles, acoustic strength is approximated such as

$$p^{\mathrm{ac}} \approx \frac{\mathrm{e}^{\mathrm{i}kz}}{2A_c} F_z, \tag{2.49}$$

where

$$F_z = \int_{S_{obs.}} p\, n_z \mathrm{d}S \tag{2.50}$$

represents the fluctuating drag force acting on the obstacle. The hypothesis used in Nelson & Morphey paper is that the root mean square fluctuating drag force on the obstacle is proportional to the steady drag force at a certain frequency band. The fluctuating force is a broad-band random type of signal and best described by its spectral density such as

$$\sqrt{\mathbb{E}\left[|F_z(\omega)|^2\right]} = K(St)\overline{F_z}. \tag{2.51}$$

where the Strouhal number writes

$$St = \frac{f L_c}{u_c}, \tag{2.52}$$

with f the frequency band, L_c and u_c are typical length and velocity scale. Here, the plane wave coefficient is simply given by

$$C_{00}^{+} = \frac{F_z}{2A_c}. \tag{2.53}$$

The mean drag force $\overline{F_z}$ acting on the diaphragm is balanced by an equal and opposite mean force acting on the fluid. The force on the fluid (which acts in the upstream direction) is given by the product of the static drop pressure across the diaphragm

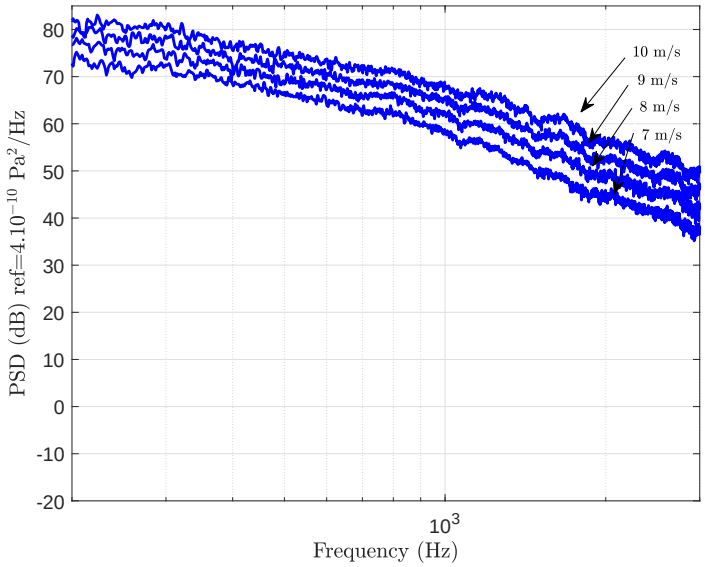

(a) Evolution of plane wave amplitudes $|C_{00}|^2$ with velocity at 7 m/s, 8 m/s, 9 m/s and 10 m/s.

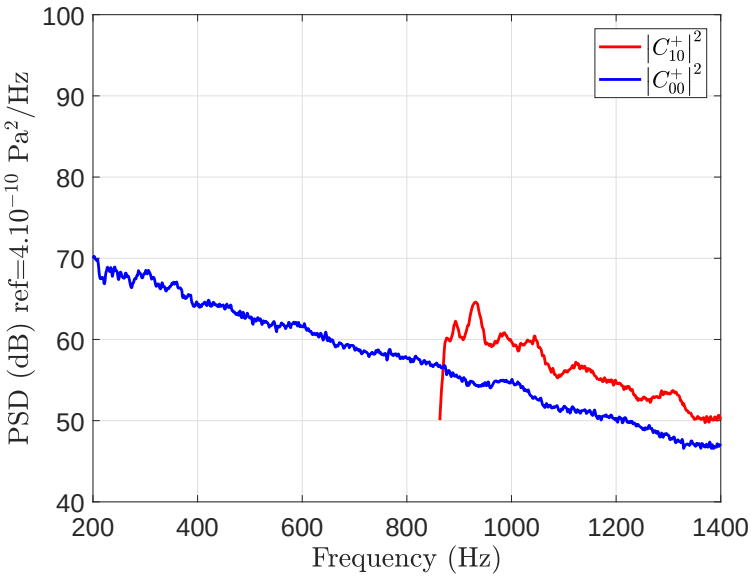

(b) Estimation of the acoustic plane wave and transverse propagating duct mode in the case of a straight duct with a diapgram inserted, the flow speed is 6.5 m/s.

Figure 2.17

and the area of the duct. Hence, the mean drag force $\overline{F_z}$ can thus be written as

$$\overline{F_z} = A_c \delta p, \tag{2.54}$$

where δp is the pressure drop over the constriction defined as

$$\delta p = \frac{1}{2} \rho U_\infty^2 C_L, \tag{2.55}$$

with C_L the pressure loss coefficient. To get a formulation valid for random signals the plane wave amplitude from Eq.(2.53) and Eq.(2.51) writes

$$\mathbb{E}\left[\left|C_{00}^{+}\right|^2\right] = \frac{\mathbb{E}\left[\left|F_z(\omega)\right|^2\right]}{4A_c^2} = \frac{K^2(St)\overline{F_z}^2}{4A_c^2} = \frac{K^2(St)(\delta p)^2}{4}. \tag{2.56}$$

The acoustic plane wave energy obeys the following scaling law $|C_{00}^{+}|^2 \sim (\delta p)^2\, K^2(St)$ and can be computed directly from at least one measurement or calculation of the static pressure loss and an appropriate definition of the Strouhal number. Several definitions have been proposed, for instance, the component flow constriction u_c is defined as

$$u_c = \frac{U_\infty}{\sigma}, \tag{2.57}$$

with σ the '*vena contracta*' ratio. Kårekull *et al.* [142, 143] defined the characteristic length with an alternative definition of the the hydraulic diameter:

$$L_c = \sqrt{\frac{4A_c\sigma}{\pi}}. \tag{2.58}$$

In our case, the hydraulic diameter D_h as defined Eq.(2.1) is retained. This yields a definition of the strouhal number as

$$St = \frac{f D_h \sigma}{U_\infty}. \tag{2.59}$$

In the case of a diaphragm, it can be useful to use the recent development of Kårekull *et al* [143]. They revisited the Nelson-Morfey semi-empirical scaling law by suggesting that the dynamic force is assumed to scale with the momentum flux, given by

$$\overline{F_z} \propto \rho A_c U_\infty U_{vc} = \frac{\rho A_c U_\infty^2}{\sigma}, \tag{2.60}$$

where $\rho A_c U_\infty^2$ corresponds to the mass flow and U_{vc} to the mean velocity at the *vena contracta* area $A_{\nu c}$. Hence, the flow is constricted across the diaphragm orifice and a jet is produced. This jet is smaller than the physical dimensions of the orifice due to the '*vena contracta*' effect. The *vena contracta* ratio σ, i.e. the constriction openness, is given by

$$\sigma = \frac{A_{\nu c}}{A_c}. \tag{2.61}$$

The *vena contracta* ratio is evaluated from the formula presented by Durrieu *et al.* [144] and given by

$$\sigma = \frac{\frac{A_{\text{orifice}}}{A_c}}{1 + \sqrt{0.5\left(1 - \frac{A_{\text{orifice}}}{A_c}\right)}}. \tag{2.62}$$

This approach proposed by Kårekull allow us to directly access to the acoustic energy from only the geometrical characteristics of the diagram according to Eq.(2.61) and Eq.(2.62). Hence, no calculations or measurements of the static pressure loss due are required. Therefore, injecting Eq.(2.60) to Eq.(2.56) yields to a new acoustic plane wave amplitude expression and writes

$$\left|C_{00}^{+}\right|^2 = \frac{\rho^2 K^2(St) U_\infty^4}{4\sigma^2} = \frac{q^2 K^2(St)}{\sigma^2}, \tag{2.63}$$

with q is the dynamic pressure.

In Kårekull papers [142, 143], several publications are used to review orifice noise in order to obtain a universal scaling spectrum $K^2(St)$. The general trend is

$$10\log_{10}\left(K^2/10^{-12}\right) = \begin{cases} 60 & St < 1, \\ 60 - (20 \sim 28)\log(St) & St > 1. \end{cases} \tag{2.64}$$

The symbol $\sim$ stands for the incertitude about the true slope value. The general inclination of $-28\log(St)$ can be seen as a mix between the source mechanisms of a pure dipole, $-20\log(St)$, and a pure quadrupole $-40\log(St)$. Therefore, we propose the following model to compute the acoustic energy of the plane wave generated by a diaphragm:

$$\frac{\left|C_{00}^{+}(\omega)\right|^2 \sigma^2}{q^2} = \begin{cases} 10^{-6} & St < 1, \\ 10^{-6} \times 10^{-2\log(St)} & St > 1. \end{cases} \tag{2.65}$$

Here, the slope of a pure dipole, $-20\log(St)$, is considered. One may prefer a more refined model of the scaled spectrum K^2 as suggested by the results of Nelson &

Morphey in [140]. Here, the model represents the best fit calculation of a large range of orifice results.

Results from Fig. 2.17(a) are scaled following the model proposed and are given Fig. 2.18 for a diaphragm whose area orifice is $A_{\text{orifice}} = 0.1 \times 0.05$ m^2 and a vena contracta ratio $\sigma = 0.16$ (evaluated using Eq.(2.62)). A good collapse is found for all velocities over the majority of the measured frequency range. The proposed model takes the general trend of the 'universal' spectrum $K^2(St)$ from several experimental investigations reviewed in [142]. Although, the general behavior of the 'universal spectrum' is somewhat more consistent with a inclination of $-28\log(St)$. But uncertainties remain on the slope of the 'universal spectrum' for $St > 1$ and the choice of an appropriate characteristic length in the stroual number definition.

Finally, this chapter is concluded by plotting the mean square value of the pressure field as a function of the flow velocity for each scenario as shown in Fig. 2.19. The acoustic energy of the plane wave mode obeys a velocity dependence of U_∞^4 for the case of a diaphragm inserted upstream (scenario 2), and U_∞^6 for the case without singularity (scenario 1). The general trend of scenario 1 is consistent with analytical prediction given by Davies and Williams [145]. The latter found that the sound power varies as the sixth power of velocity below a Mach number of 0.2. In the same spirit, Van Herpe and Crighton [146] found a U_∞^7 for their lowest Mach numbers value, and a U_∞^6 variation for their highest velocity. The scenario 2 obeys as expected to prediction obtained by Nelson-Morphey dimensional analysis.

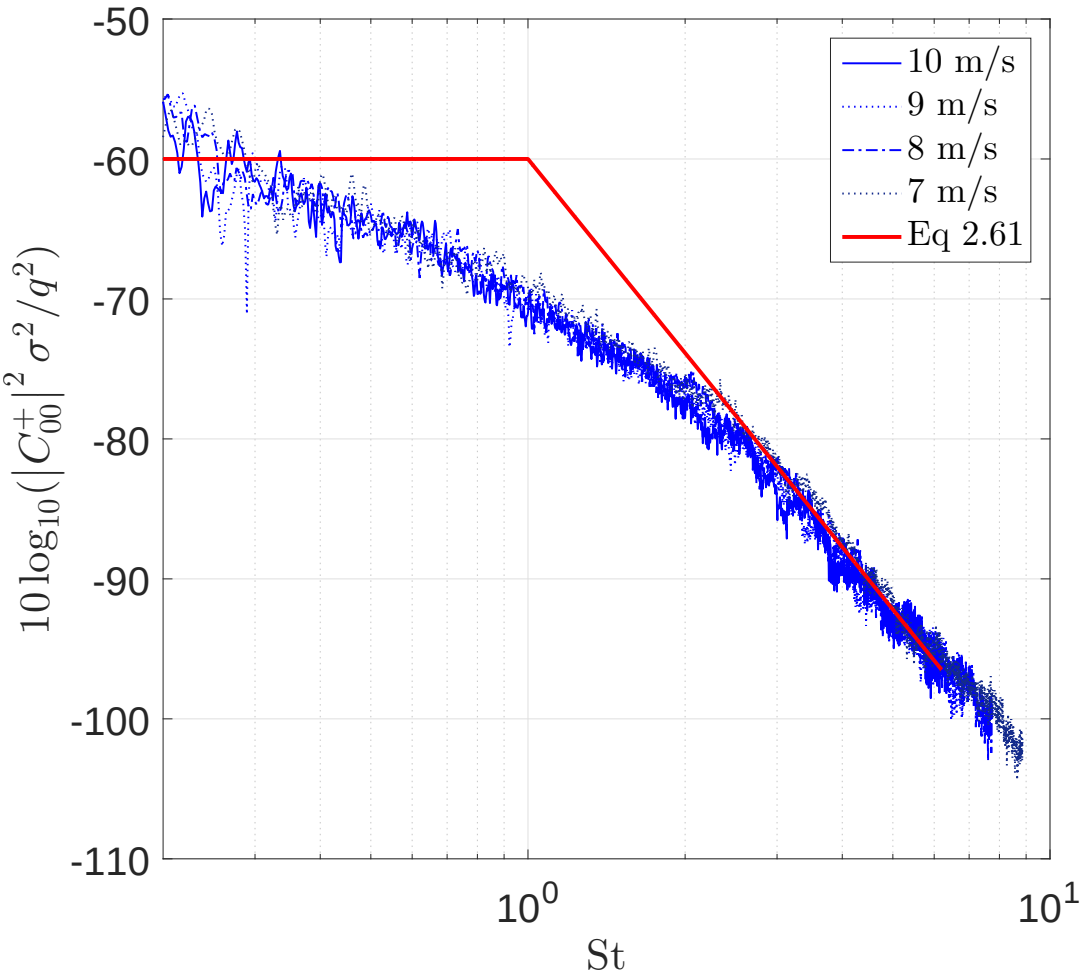

Figure 2.18: Best Fit model according to a collection of experimental data reported in [142, 143].

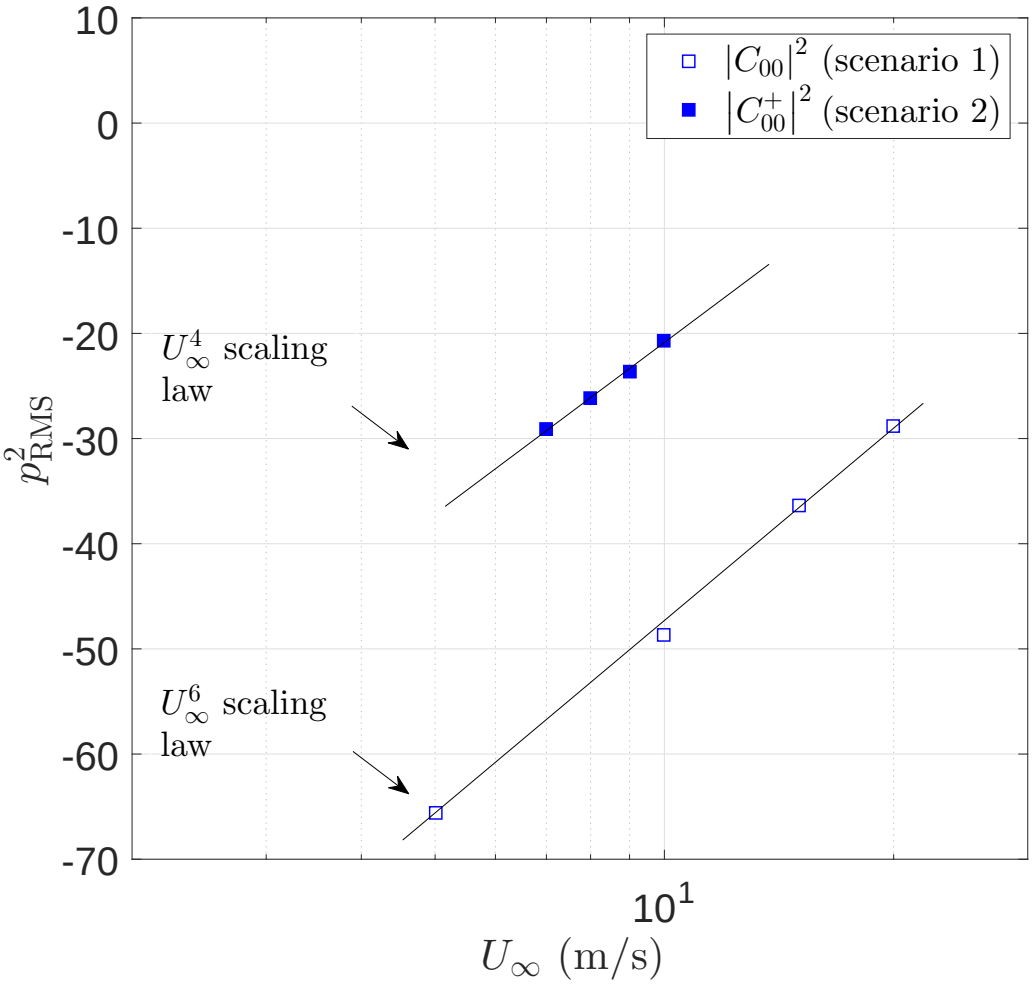

Figure 2.19: Scaling law for the variation of the acoustic energy with flow velocity.

2.5 Conclusion

Aero-acoustic test campaign has been performed in the experimental set up at the Roberval research laboratory. Although the pipe rig was originally designed for acoustic measurements, attempts were made to characterize the wall pressure fluctuations beneath a turbulent boundary layer. It has shown the importance of using reliable measurement techniques and instrumentation. This has allowed us to collect general trends about the turbulent energy level and cross-spectral features in order to assess the use of empirical models in the calculation of the structure response. The acoustic energy has been extracted from the turbulent flow using cross-spectra based techniques or *via* the $2N$-port method. Multi-modal decomposition has been performed to calculate modal amplitudes of propagating acoustic duct modes. It has been distinguished through the 2 scenarios: (i) without singularity and (ii) with a diaphragm inserted upstream. Cross-spectral measurements have allowed us to quantify the relative weight of the hydrodynamic and acoustic contributions, which will be used in a second step for the vibrational response analysis. The case with a singularity will serve as a reference to evaluate and suggest improvements to existing CPSD empirical models in a context of internal flow with disturbances. In addition, the collected data will be confronted to CFD calculation in Chapter 5.

Chapter 3

Response of a finite duct to a point force

This chapter presents the study of the dynamic response of a duct. Two specific cross-sections are compared: circular and rectangular. In both cases, material properties and dimensions, i.e. width and cross-sectional aeras, are identical. Simply supported structures are considered, since the modes obtained are easy to incorporate into analyses of flow turbulence acting on the structures. Moreover, simply supported geometry can be used as a guideline for more complex geometries since it follows similar trends in terms of energy levels and modal pattern behavior. Analytical modal Frequency Response Functions are derived and will be used in a second step to study the coupling with the wall pressure fluctuations. Experimental modal analysis of a finite rectangular duct are confronted to computational methods. Attention will be payed to quantify the effect of the Boundary Conditions (BCs), the resistive damping from coupling with the internal acoustic medium and aerodynamic damping.

3.1 Analytical formulation for a simply supported circular duct

Since cylindrical shells are typical components in pipeline designs, it is particularly important that their governing dynamics and structural response be understood. There have been extensive studies related to shell theory. The reader is referred to the work of Leissa [147] for a comprehensive review. Shell theory does not take into account stress through the thickness (i.e., perpendicular to the midsurface). That is the reason why it is refereed as a 2D theory. Three kinds of analytical models can be distinguished in the literature:

- The Classical thin Shell Theory (CST). It is based on Kirchhoff-Love assumptions where transverse shearing effects are neglected and the line originally normal to the midsurface remain perpendicular to the midsurface during deformations. The shell motion is governed by three coupled equations and described by three components u, v and w which are respectively the longitudinal, tangential and radial displacement.

- The First-order Shear Deformation Theory (FSDT). It is based on Reissner-Mindlin assumptions where shear deformations are included, and therefore the line originally normal to the midsurface in general does not remain perpendicular to the midsurface during the deformations. This theory takes into account shear resistance (linearly with respect to thickness) and rotary mass inertia. This introduces two additional degrees of freedom relative to the classical theory: ψ_θ and ψ_z, corresponding to two rotations of the normal to the midsurface during deformations about the θ and z axes respectively. This theory is thus an alternative to tackle larger thickness (thick shell) and valid for higher frequencies.

- Higher order Shear Deformation Theories (HSDT). It allows to take into account shear deformation more accurately. Daneshjou *et al.* [148] made a comparison between results obtained with CST, FSDT and a developed Third-order Shear Deformation Theory (TSDT) for different geometric ratios h/R where h is the thickness and R is the radius of the cylinder. They showed that the three methods give similar results on the Transmission Loss in the low frequency domain, but differences appear at higher frequencies.

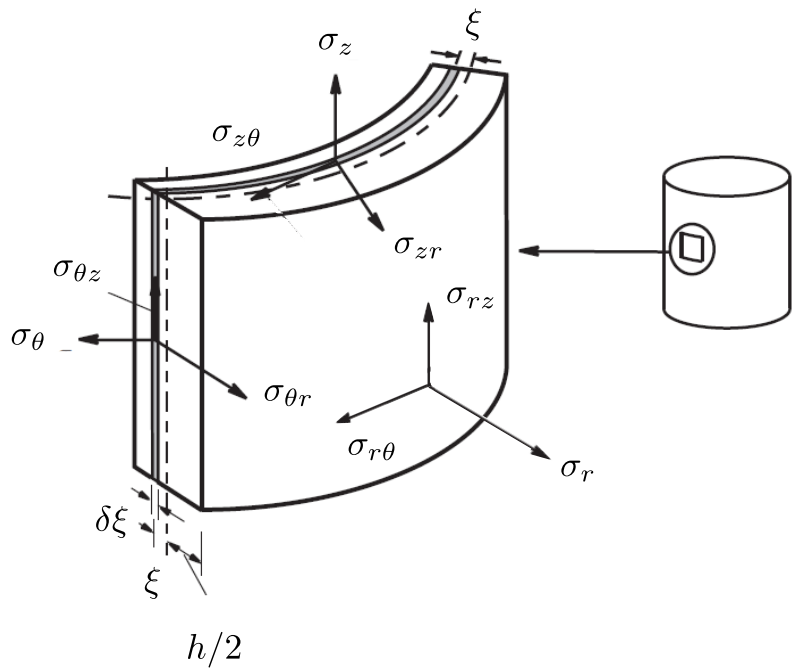

Figure 3.1: Cylinder element showing normal and shear stresses.

In this study, the simplest possible constitutive law corresponding to an isotropic, linear elastic material are considered and all materials will exhibit elastic behavior under small deformations. The cylinder wall thickness is uniform and small compared with the cylinder radius and length. For the element shown in Fig. 3.1, R is its radius of curvature, $\sigma_{\theta r}$, σ_{zr} and $\sigma_{z\theta}$ are shear stresses, σ_z, σ_θ and σ_r are normal stresses in the axial, tangential and radial directions respectively. The transverse normal stress, σ_r, is small and may be neglected in comparison with the other normal stress components. This implies that $\sigma_r = 0$. Normals to the undeformed middle surface of the wall of the cylinder remain straight and normal to the deformed middle surface. This last assumption is known as Kirchoff's hypothesis and implies that:

$$\sigma_{\theta r} = \sigma_{zr} = \gamma_{\theta r} = \gamma_{zr} = 0, \tag{3.1}$$

where $\gamma_{\theta r}$ and γ_{zr} represents the shear strain at element δ_z. To satisfy Kirchhoff hypothesis, the displacement field is restricted to the following linear relationships:

$$u(z, \theta, \xi) = u_0(z, \theta) + \xi\phi_z(z, \theta), \tag{3.2a}$$

$$v(z, \theta, \xi) = v_0(z, \theta) + \xi\phi_\theta(z, \theta), \tag{3.2b}$$

$$w(z,\theta,\xi) = w_0(z,\theta), \tag{3.2c}$$

where u_0, v_0 and w_0 are the displacements at $\xi = 0$ in the axial, circumferential and radial directions, ϕ_z and ϕ_θ are the rotations of the normal to the median surface respect to z- and θ-axes. ξ is the distance of the infinitesimal segment, $\delta\xi$, from the central axis of the shell element. Note that ξ rather than r is used as the radial coordinate, as it has its origin at the center of the shell element rather than the center of curvature of the element. The strain displacement equations for a circular cylinder may be derived from different shell theories, for instance, for the segment, $\delta\xi$, it is written for three shell theories widely used as [78]:

$$\varepsilon_z = \epsilon_z + \xi\kappa_z \tag{3.3}$$

$$\varepsilon_\theta = \begin{cases} \epsilon_\theta + \xi\kappa_\theta & \text{case 'D',} \\ \frac{1}{1+\xi/R}\left(\epsilon_\theta + \xi\kappa_\theta\right) & \text{case 'F'.} \end{cases} \tag{3.4}$$

$$\gamma_{z\theta} = \begin{cases} \epsilon_{z\theta} + \xi\tau & \text{case 'D',} \\ \frac{1}{1+\xi/R}\left(\epsilon_{z\theta} + \xi\left(1+\frac{\xi}{2R}\right)\tau\right) & \text{case 'F'.} \end{cases} \tag{3.5}$$

where ε_z, ε_θ and $\gamma_{z\theta}$ are the normal and shear strains of the arbitrary segment, $\delta\xi$, and ϵ_z, ϵ_θ and $\epsilon_{z\theta}$ are the normal and shear strains of the surface in the middle of the wall thickness (mid-surface, $\xi = 0$). τ is the angular twist of this mid-surface and κ_z and κ_θ are the changes in curvature of the same surface. These six latter quantities corresponding to the Donnell–Mushtari (case 'D') and Flügge (case 'F') shell theories writes

$$\epsilon_z = \frac{\partial u_0}{\partial z}, \tag{3.6}$$

$$\epsilon_\theta = \frac{1}{R}\frac{\partial v_0}{\partial \theta} + \frac{w_0}{R}, \tag{3.7}$$

$$\epsilon_{z\theta} = \frac{1}{R}\frac{\partial u_0}{\partial \theta} + \frac{\partial v_0}{\partial z}, \tag{3.8}$$

$$\kappa_z = -\frac{\partial^2 w_0}{\partial z^2}, \tag{3.9}$$

$$\kappa_\theta = \frac{1}{R^2}\left[\frac{\partial v_0}{\partial \theta} - \frac{\partial^2 w_0}{\partial \theta^2}\right], \tag{3.10}$$

$$\tau = -\frac{2}{R}\frac{\partial^2 w_0}{\partial z \partial \theta} + \frac{2}{R}\frac{\partial v_0}{\partial z}. \tag{3.11}$$

For Donnell–Mushtari theory, the same previous six equations apply except that the term involving v_0 in Equations Eq.(3.10) and Eq.(3.11) is omitted. The strain-stress relationship is obtained from the well known three-dimensional form of Hooke's law. In cases of plane stress, this yields

$$\begin{Bmatrix} \sigma_z \\ \sigma_\theta \\ \sigma_{z\theta} \end{Bmatrix} = \frac{E}{1-\nu^2}\begin{bmatrix} 1 & \nu & 0 \\ \nu & 1 & 0 \\ 0 & 0 & \frac{1-\nu}{2} \end{bmatrix}\begin{Bmatrix} \varepsilon_z \\ \varepsilon_\theta \\ \gamma_{z\theta} \end{Bmatrix}, \tag{3.12}$$

where ν is Poisson's ratio and E the Young Modulus. The equations of motion for the cylinder may be derived by invoking Hamilton's variational principle. That is:

$$\delta \int_{t_1}^{t_2} (E_k - E_p)\, dt = 0 \tag{3.13}$$

where E_k is the kinetic energy of the cylinder defined as

$$E_k = \frac{1}{2}\rho h \int_0^{2\pi}\int_0^L \left[\left(\frac{\partial u}{\partial t}\right)^2 + \left(\frac{\partial v}{\partial t}\right)^2 + \left(\frac{\partial w}{\partial t}\right)^2\right] R \mathrm{d}z \mathrm{d}\theta, \tag{3.14}$$

and E_p the strain energy derived from the theory of elasticity for a circular cylinder, the following is obtained:

$$E_p = \iiint_V (\sigma_z \varepsilon_z + \sigma_\theta \varepsilon_\theta + \sigma_{z\theta}\gamma_{z\theta})\, \mathrm{d}V \tag{3.15}$$

where dV is an elemental volume, which, when expressed in cylindrical shell coordinates, is:

$$\mathrm{d}V = (1 + \xi/R)\, R \mathrm{d}\xi \mathrm{d}\theta \mathrm{d}z. \tag{3.16}$$

Substituting the strain-stress relationship into Eq.(3.15) gives:

$$E_p = \frac{E}{2(1-\nu^2)} \iiint_V \left[\varepsilon_z^2 + \varepsilon_\theta^2 + 2\nu\varepsilon_z\varepsilon_\theta + \frac{1-\nu}{2}\gamma_{z\theta}^2\right] \mathrm{d}V. \tag{3.17}$$

After substitution of the strain–displacement relations, the derivation of Lagrange's equations of motion using Hamilton's principle allows to obtain the shell equations of motion. The details are not discussed here and only the results are given. The shell equations of motion for harmonic free vibration take the following form

$$\frac{E}{1-\nu^2}\left[\mathfrak{L}\right]\begin{Bmatrix} u_0 \\ v_0 \\ w_0 \end{Bmatrix} + \rho h\omega^2 \begin{Bmatrix} u_0 \\ v_0 \\ w_0 \end{Bmatrix} = \begin{Bmatrix} 0 \\ 0 \\ 0 \end{Bmatrix}, \tag{3.18}$$

where $[\mathfrak{L}]$ is the shell matrix differential operator. This operator can be treated as the sum of two operators

$$[\mathfrak{L}] = [\mathfrak{L}_{\mathrm{D-M}}] + \frac{h^2}{12}[\mathfrak{L}_{\mathrm{MOD}}] \tag{3.19}$$

where $[\mathfrak{L}_{\mathrm{D-M}}]$ is the differential operator according to the Donnell–Mushtari theory, $[\mathfrak{L}_{\mathrm{MOD}}]$ is a 'modifying' operator which alters the Donnell–Mushtari operator to yield another shell theory. The boundary conditions are specified in terms of cylinder displacements at each end and the forces and moments acting on the cylinder at each end. Four boundary conditions must be specified for each end, one from each of the pairs listed below [78]:

$$u = 0 \ \text{ or } \ N_z = 0, \tag{3.20}$$

$$v = 0 \ \text{ or } \ N_{z\theta} + \frac{M_{z\theta}}{R} = 0, \tag{3.21}$$

$$w = 0 \ \text{ or } \ Q_r + \frac{1}{R}\frac{\partial M_{z\theta}}{\partial \theta} = 0, \tag{3.22}$$

$$\frac{\partial w}{\partial z} = 0 \ \text{ or } \ M_z = 0. \tag{3.23}$$

The quantities, N_z, $N_{z\theta}$, Q_r, $M_{z\theta}$ and M_z, have not yet been defined. The first two are in-plane forces, the third is a force normal to the cylinder surface, the fourth is a twisting moment and the fifth term is a bending moment. The boundary condition which is closest to the equivalent of a simply supported plate boundary condition is referred to as the shear diaphragm (or SD) condition where:

$$v = w = M_z = N_z = 0. \tag{3.24}$$

This is equivalent to a cylinder closed at the end with a thin flat circular cover plate. The plate has considerable stiffness in its own plane, thus, restraining the v and w components of cylinder displacement. As the end plate is not very stiff in its transverse plane, it would generate very little bending moment, M_z, and very little longitudinal membrane force, N_z. For a simply-supported shell of length L_z the structural mode shapes are expressed as following

$$\begin{Bmatrix} u^{\alpha}_{mnj}(\theta,z) \\ v^{\alpha}_{mnj}(\theta,z) \\ w^{\alpha}_{mnj}(\theta,z) \end{Bmatrix} = \begin{Bmatrix} D_{nmj}\sin(n\theta+\alpha\pi/2)\cos(m\pi z/L_z) \\ E_{nmj}\cos(n\theta+\alpha\pi/2)\sin(m\pi z/L_z) \\ 1 \qquad \sin(n\theta+\alpha\pi/2)\sin(m\pi z/L_z) \end{Bmatrix}. \tag{3.25}$$

Each mode can be distinguished by being either anti-symmetric or symmetric with the index $\alpha = 0$ (resp. 1), n is the circumferential order, m is the longitudinal order, and j denotes the types of mode (extension-compression, torsion, bending). The $n = 0$ modes of a cylindrical shell are clustered around the ring frequency, which is the frequency at which a membrane wave is continuous around the circumference:

$$f_r = \frac{1}{2\pi}\frac{c_l}{R}, \tag{3.26}$$

where $c_l = (E/(\rho(1-\nu^2)))^{1/2}$ is the velocity of compressional waves. The ring frequency is sometimes expressed in dimensionless form, normalized to the radius and longitudinal wave speed: $\Omega_r = 2\pi f_r R/c_l$. $n = 0$ modes are called 'breathing' modes. $n = 1$ modes correspond to a rigid body motion about the cylinder cross section. These modes generally occur in long cylinders, and can be represented more simply using beam theory. For long cylinders, beam theory can be used to model vibrations up to the frequency where the higher order harmonics cut on. When harmonics above $n = 1$ appear in a cylinder's vibration, they are called 'lobar' modes. The first lobar mode is $n = 2$, where the cross section deforms as an oval. Fig. 3.2 shows some of these mode shapes. Substituting Eq.(3.25) into Eq.(3.18) yiels an eigenproblem of the form

$$\begin{bmatrix} \rho h\omega^2 - k_{11} & k_{12} & k_{13} \\ k_{21} & \rho h\omega^2 - k_{22} & k_{23} \\ k_{31} & k_{32} & \rho h\omega^2 - k_{33} \end{bmatrix} \begin{Bmatrix} A \\ B \\ C \end{Bmatrix} = 0, \tag{3.27}$$

where coefficients k_{ij} are detailed in Appendix C for the Donnell–Mushtari, Goldenveizer–Novozhilov, Reissner-Naghdi-Berry and Flügge shell theories. In order to solve for the natural frequencies, the determinant has to be zero. Expanding the

determinant gives

$$\omega^6 + a_1\omega^4 + a_2\omega^2 + a_3 = 0, \tag{3.28}$$

which leads to a bi-cubic equation whose solutions have for every (m, n) combination three frequencies (detailed in Appendix C). The lowest is associated with the mode where the bending component dominates. According to Soedel's book [149] the eigenvector components (D_{nmj},E_{nmj},1) and natural frequencies ω_{mnj} can be calculated analytically (see Appendix for details). The analytical FRF of a simply supported circular duct due to an harmonic point force located at $\mathbf{s}$ in the radial direction has the following expression:

$$H_w(\mathbf{r}, \mathbf{s}, \omega) = \sum_{\alpha=0}^{1} \sum_{j=1}^{3} \sum_{m,n} \frac{w^\alpha_{mnj}(\mathbf{r}) w^\alpha_{mnj}(\mathbf{s})}{M^\alpha_{mnj}[\omega^2_{mnj}(1 + \mathrm{j}\eta) - \omega^2]}. \tag{3.29}$$

where $M^\alpha_{mn} = \int_S \rho h ||\mathbf{q}||^2 \mathrm{d}\mathbf{s}$ is the generalized mass (detailed in Appendix C) and η the loss factor. The averaged Root Mean Square (RMS) acceleration is defined as

$$A_c^{\mathrm{RMS}}(\mathbf{s}, \omega) = \sqrt{\frac{\int_S |H_a(\mathbf{r}, \mathbf{s}, \omega)|^2 d^2\mathbf{r}}{S}}, \tag{3.30}$$

with $H_a = -\omega^2 H_w$. As underlined by Hambric in [150], point mobility equations of

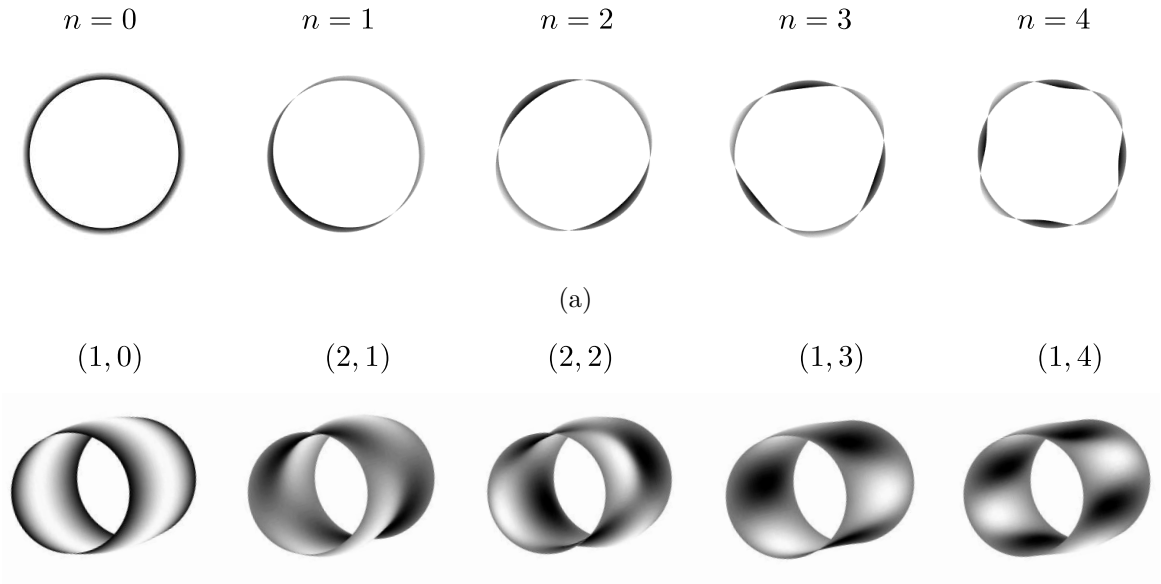

Figure 3.2: (a) Section mode shapes ; (b) 3D illustration of some global modes of the duct.

infinite structures can be useful, since they represent the mean vibration response of finite structures to force and moment drives. The mobility $Y_\infty = (V/F)_\infty$ of an infinite pipe where V and F represent respectively the complex amplitude of the velocity and that of the force, may be computed as [111, 151]

$$\Re(Y_\infty) = \begin{cases} 1/\left(4\pi R\rho h\sqrt{\frac{\Omega c_l^2}{\sqrt{2}}}\right) & \Omega < 0.77\frac{h}{R}, \\ \frac{0.66}{2.3c_l\rho h}\sqrt{\Omega} & 0.77\frac{h}{R} < \Omega < 0.6, \\ \frac{1}{8\sqrt{D\rho h}} & \Omega > 0.6. \end{cases} \tag{3.31}$$

Note that the 3rd case corresponds to the infinite plate mobility. Thus, when the frequency is close to the ring frequency, the cylindrical shell mobility approaches that of a flat plate. The flexural wavelengths become short with respect to the radius of curvature of the shell and the flexural motion is uncoupled from the membrane motion. This can be observed by plotting the wavenumber diagram of a simply supported circular duct. Following [72], it is useful for the analysis to define the effective wavenumber for the circular duct

$$k_{mn}^{\mathbf{cyl}} = (k_s^2 + k_m^2)^{1/2}, \tag{3.32}$$

where $k_s = n/R$ is the circumferential wavenumber and $k_m = m\pi/L_z$ is the axial wavenumber. Fig. 3.3 shows the dispersion curves of the effective wavenumbers along with the free flexural wavenumber defined as:

$$k_f = \sqrt{\omega}\sqrt[4]{\frac{\rho h}{D}}. \tag{3.33}$$

Shell resonance frequencies $f_{mn}^{\mathbf{cyl}}$ do not increase with the number of nodal lines. The first lobar mode $n = 2$ is often the first mode to cut on in cylinders of medium length. This well known phenomenon is characteristic of shells where a competition occurs between axial and tangential membrane strains of the median surface of the shell, and the strain energy associated with wall flexure. Above the ring frequency f_r, the effective wavenumber for the circular duct follows that of a flat plate.

Fig. 3.4 shows the averaged RMS acceleration due to a point force with coordinates $\mathbf{s}$=(θ=0°, z=30 cm) for different shell operators. The precision with the Donnell's operator ('D') decreases as the frequency increases in comparison to other theories. The Goldenveiser ('G') and Reissner-Naghdi ('R') models provides similar results

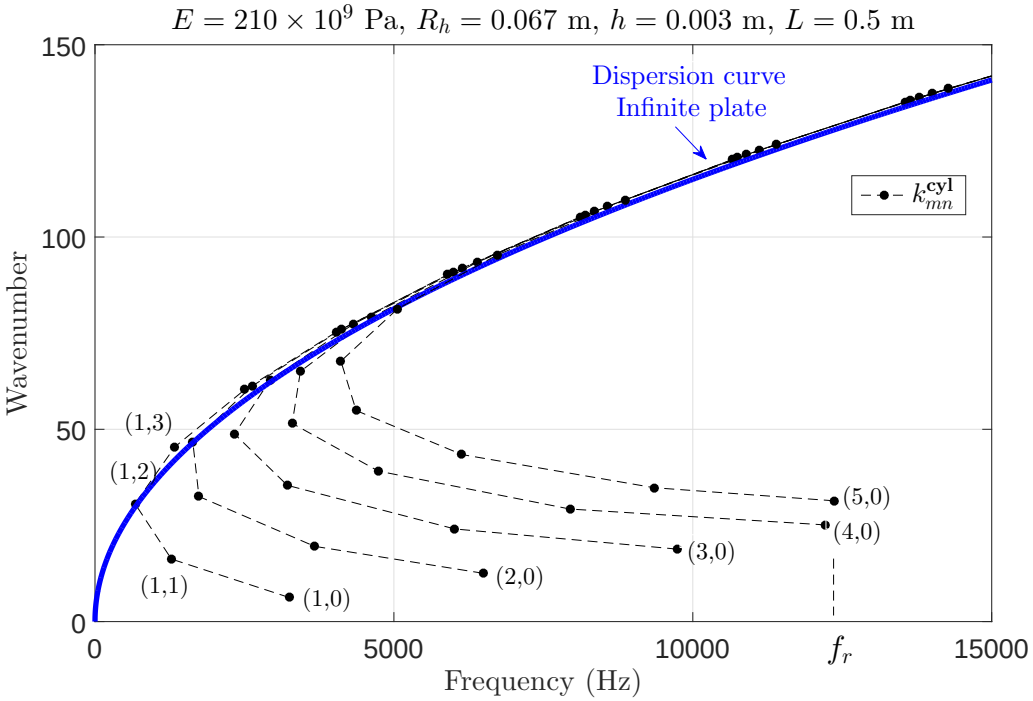

Figure 3.3: Dispersion curves for a circular duct and an infinite plate.

to the Flügge's operator ('F') which is the most accurate thin shell operator. The shell parameters are defined in Table 3.1. The shell diameter is computed according to Eq.(2.1) with diameter corresponding to the rectangular duct, so $D_h \approx 13$ cm. Despite the small ratio $h/R = 4.5\%$, there is a significant difference between the Donnell's operator and the other shell theories. The spectrum associated to the Donnell's operator is slightly offset toward the high frequencies. This trend seems to be confirmed in Leissa's textbook [147]. In that book, the percent by which the shell frequency parameters differ from those found by an exact three-dimensional elesticity solution is reported. In our case, the first resonant frequency corresponds to the circumferential wave numbers $n = 2$, a length/radius ratio $L/mR = 7.5$, for $(R/h \approx 22)$ and for $\nu = 0.22$. In Leissa's textbook (see Table 2.6 p 52), the agreement among the theories is less than $\pm 0.15\%$, except for the Donnell theory showing significant deviation (around 4.85%).

The analytical model is validated using the commercial FE solver COMSOL Multiphysics ® software. The FEM model is assumed to be valid for higher frequencies than the classical shell theory used to calculate the analytical FRFs. It is considered as a reference since it takes into account more mechanical and geometrical effects in the thickness such as the transverse shearing effect. MITC4 QUAD shell elements

in COMSOL have a mixed interpolation formulation (also called MITC - Mixed Interpolated Tensorial Components) derived from the theory presented in [152]. Shell elements in COMSOL refer to Naghdi shell theory and Mindlin-Reissner formulation, so that transverse shear deformation is accounted for. Such a formulation includes large deformation capabilities and can be used for thin and thick shells. The numerical model has simply supported BCs at both ends and the geometry and material parameters are those listed previously. To maintain at least 6 elements for each flexural wavelength up to 5000 Hz, a mesh size of 1 cm is used. The mobility in the radial direction due to a concentrated load (set to unity) on node **s** located at (θ=0°, z=30 cm) is considered. Results are shown in Fig. 3.5. The levels are the same between the two spectra. The damped resonant frequencies of the FEM solution agree with the analytical solution with a maximum difference of approximately 2%. Finally, the results from this study validate our analytical solution for this type of geometry and allow us to neglect the transverse shearing effect.

Young's modulus E	210×10^9 GPa	Poisson's ratio ν	0.22
Density ρ	7800 kg/m^3	Section $L_x \times L_y$	0.2×0.1 m^2
Thickness h	3 mm	Length L_z	0.5 m
Loss factor η	5.10^{-3}	Diameter D_h	$2L_xL_y/(L_x+L_y)$

Table 3.1: Parameters of the tested duct.

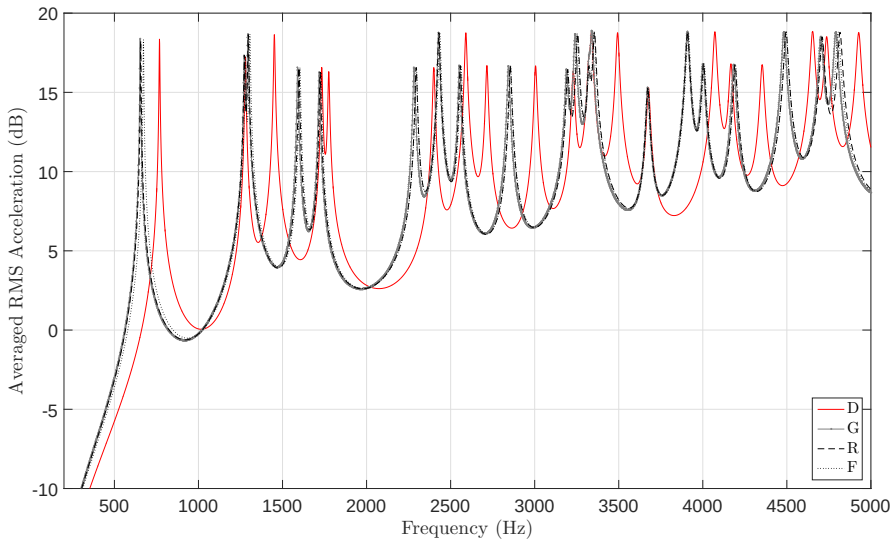

Figure 3.4: Comparison between the Donnell–Mushtari, Goldenveizer–Novozhilov, Reissner-Naghdi-Berry and Flügge shell theories.

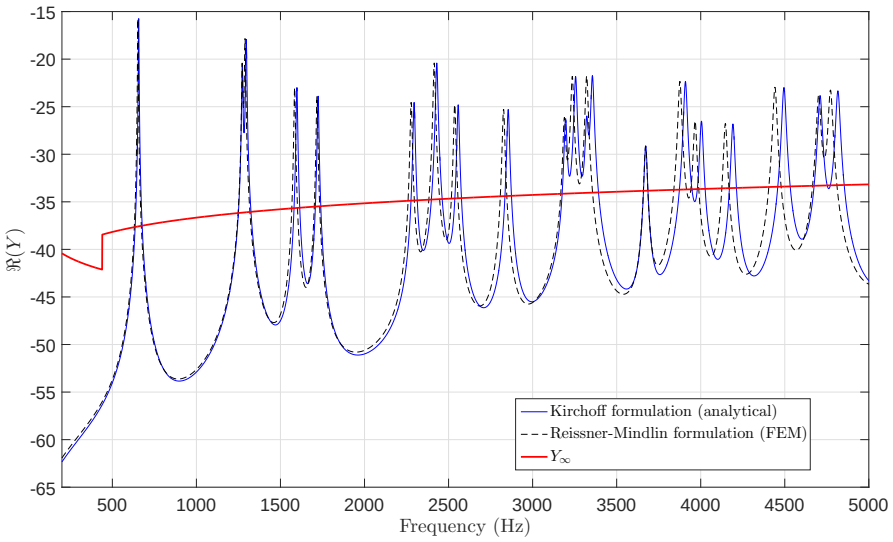

Figure 3.5: Comparison between Kirchoff and Reissner-Mindlin formulation. The Reissner-Naghdi ('R') shell operator has been chosen for the analytical solution.

3.1.1 Comments on BCs

In practice, flexible rubber sections, flanges or other expansion joints are used to separate sections of pipe. These discontinuities at the interface of two pipe sections induces additional stiffness and mass. For finite pipe encountered in industrial plants, BCs are likely a mix between pinned BCs and clamped BCs which differ from the standard simply supported BCs. Although computationally difficult, it is possible to analytically obtain the eigenvector components (D_{nmj},E_{nmj},1) and natural frequencies ω_{mnj} for the different boundary conditions possible at each end of the cylinder. In this study, the previous FE model is used to illustrate the BCs effects. Fig. 3.6 shows the results for the free (FF), simply supported (SS) and the clamped (CC) cases at both ends. As expected, the structure becomes stiffer by increasing constraints at the edge ends and resonant frequencies are shifted toward higher frequencies.

3.1.2 Fluid loading effects

Numerical solutions exist to tackle complex geometries surrounded by a fluid for all kinds of boundary conditions. For instance, the finite element method consists in solving the partial differential equations by using the variational formulation of the local equations associated to the structure and fluid problems. The latter are discretized into elements and lead to the most basic form of vibro-acoustic formulation

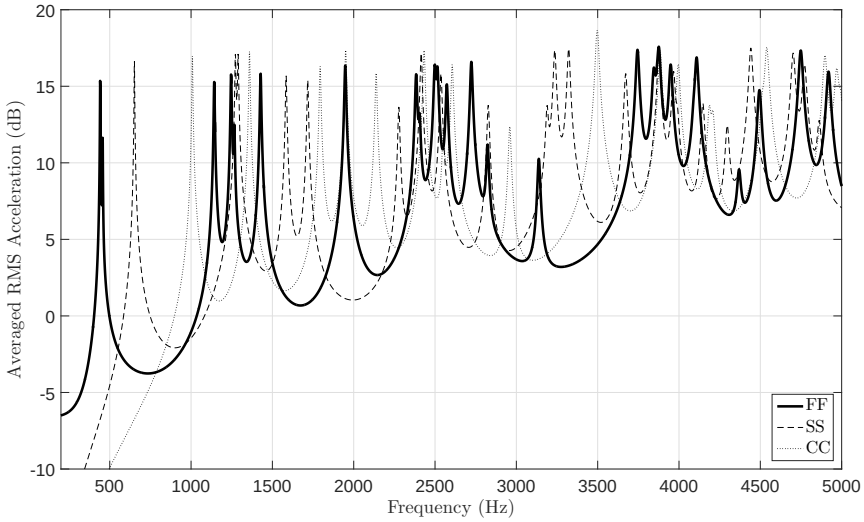

Figure 3.6: Averaged structure response for different BCs.

described by an unsymmetrical system of equations [84]

$$\begin{bmatrix} \mathbf{K} - \omega^2 \mathbf{M} & -\mathbf{C} \\ -\omega^2 \mathbf{C}^T & \mathbf{H} - \omega^2 \mathbf{Q} \end{bmatrix} \begin{Bmatrix} \mathbf{u} \\ \mathbf{p} \end{Bmatrix} = \begin{Bmatrix} \mathbf{f} \\ \mathbf{0} \end{Bmatrix}, \tag{3.34}$$

where $\mathbf{u}$, and $\mathbf{p}$ denote the nodal vector of unknowns for the structure and the fluid, respectively. Matrices $\mathbf{M}$ and $\mathbf{K}$ denote the mass and stiffness matrices of the structure, respectively. $\mathbf{f}$ is the external loading nodal vector acting on the structure. Matrices $\mathbf{H}$ and $\mathbf{Q}$ are related to the kinetic energy and compressional energy matrices of the fluid. Note that this formulation stands for interior problem and is altered for a interior/exterior problem. Hency, matrices $\mathbf{H}$ and $\mathbf{Q}$ are corrected to include a Perfectly Match Layer (PML). Matrix $\mathbf{C}$ is a surface coupling matrix between the structure and the fluid. In our case, a numerical study is performed with the commercial software COMSOL Multiphysics® to illustrate the fluid-loading effect. An enclosed spherical volume bounded by a Perfectly Match Layer (PML) is modeled and meshed to describe the acoustic medium. The mesh size and PML properties are chosen to maintain enough elements for each acoustic wavenumber and checked by convergence. A direct frequency domain analysis is performed to solve Eq.(3.34). The model is simple and does not allocate too much memory. Thus, solving Eq.(3.34) in a direct manner requires reasonable computation time with a modern machine. Fig. 3.7(a) shows the averaged acceleration due to a point force for a simply supported shell surrounded by a fluid or without. Air or water are considered and compared to the case 'in vacuo'.

There are no major changes when the structure is coupled to air. However, the impact is far more important with water. The acoustic power radiated by the shell surface vibrations at 643 Hz is shown in Fig. 3.7(b). The fluid domain including a common PML can be seen.

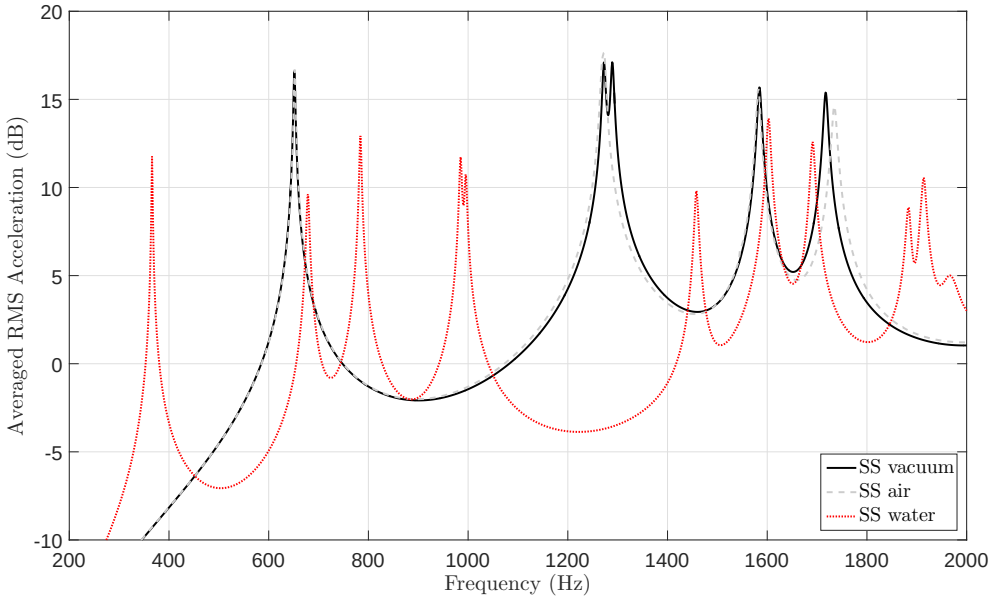

(a)

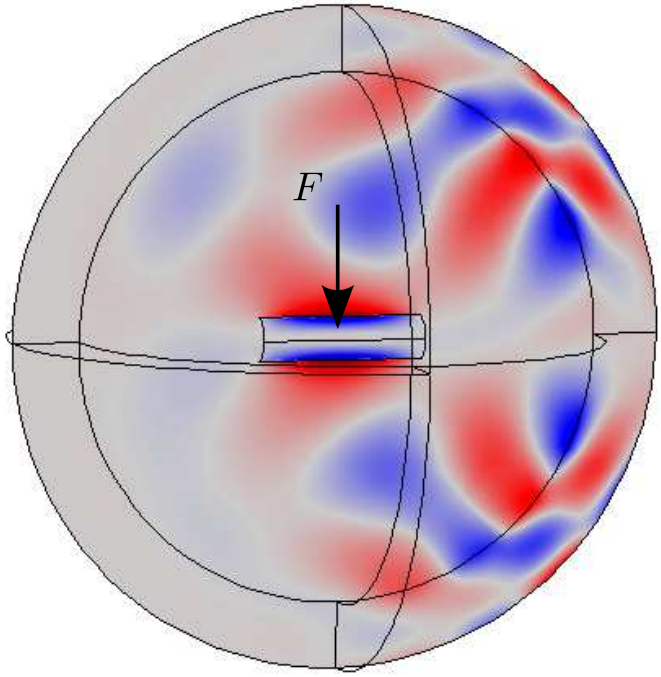

(b)

Figure 3.7: Fluid loading effect: (a) averaged acceleration and (b) acoustic radiation in air of a circular duct due to a point force F using PML at 643 Hz.

3.2 Analytical formulation for a simply supported rectangular duct

Although most of the fluid conveying ducts are cylindrical, specific applications require the use of rectangular ducts. This is the case of ventilation and air conditioning systems in buildings for space saving, or in industrial applications requiring large duct sections for gas transportation. At first sight, the geometry suggests the use of thin plate theory which solves only flexural wave. However, a pure bending wave impinging at a corner junction will induce in-plane longitudinal and in-plane shear waves, as well as other flexural waves in the connected plates. This phenomenon is a well-know problem for SEA specialists as in-plane waves becomes significant in high frequency region. The inclusion of in-plane modes using SEA models of plate structures has been investigated by several researchers [153–155]. They emphasize the importance of the in-plane response at high frequencies and in large coupled plate-like structures. Fig. 3.8 shows the displacements and coordinate system for the rectangular duct. The adjacent plates are coupled to the other edges along the z axis. To facilitate the geometrical coordinate system, the duct is modeled as a plate in its unrolled form, thus the coordinate system (s,z) is adopted. The differential equations of motion for the flexural, in-plane longitudinal, and in-plane shear free wave motions are respectively given by

$$D\nabla^4 w - \rho h\omega^2 w = 0, \tag{3.35}$$

$$\frac{\partial^2 u}{\partial s^2} + \frac{1-\nu}{2}\frac{\partial^2 u}{\partial z^2} + \frac{1+\nu}{2}\frac{\partial^2 v}{\partial s \partial z} + \frac{1-\nu^2}{E}\rho\omega^2 u = 0, \tag{3.36}$$

$$\frac{\partial^2 v}{\partial s^2} + \frac{1-\nu}{2}\frac{\partial^2 v}{\partial z^2} + \frac{1+\nu}{2}\frac{\partial^2 u}{\partial s \partial z} + \frac{1-\nu^2}{E}\rho\omega^2 v = 0, \tag{3.37}$$

where w, u and v represent the flexural, in-plane longitudinal and in-plane shear plate displacements, respectively. $D = Eh^3/12(1-\nu^2)$ is the bending stiffness. Recall that $c_l = \sqrt{E/(1-\nu^2)\rho}$ is the velocity of longitudinal waves (L-waves) for a thin homogeneous plate, $G = E/2(1+\nu)$ is the shear modulus and $c_t = \sqrt{G/\rho}$ is the velocity of transverse/shear waves (T-waves). Note that the coupled wave equations for longitudinal and transverse waves are of second order contrary to the bending wave equation which is of four order in space. Also, the wave speed does not appear explicitly in the flexural wave equation since bending wave speeds are dispersive. The

flexural wave speed in plates is defined as $c_f = \sqrt[4]{D\omega^2/\rho h}$. Fig. 3.8 also shows the forces and moments acting on the edges of two plate elements i,j. N_s^i is the in-plane longitudinal force, N_{sz}^i is the in-plane shear force and M_s^i is the bending moment. V_s^i is the net vertical shear force. The force and moment equations are given by

$$N_s^i = \frac{Eh}{1-\nu^2}\left(\frac{\partial u}{\partial s} + \nu\frac{\partial v}{\partial z}\right), \tag{3.38}$$

$$N_{sz}^i = \frac{Eh}{2(1+\nu)}\left(\frac{\partial u}{\partial s} + \frac{\partial v}{\partial z}\right), \tag{3.39}$$

$$M_s^i = -D\left(\frac{\partial^2 w}{\partial s^2} + \nu\frac{\partial^2 w}{\partial z^2}\right), \tag{3.40}$$

$$V_s^i = Q_s^i + \frac{\partial M_{sz}^i}{\partial z}, \tag{3.41}$$

with

$$Q_s^i = -D\left(\frac{\partial^3 w}{\partial s^3} + \nu\frac{\partial^3 w}{\partial s \partial z^2}\right), \tag{3.42}$$

$$M_{sz}^i = -D(1-\nu)\left(\frac{\partial^2 w}{\partial s \partial z}\right). \tag{3.43}$$

The plates are simply supported at both ends located at $z = 0$ and $z = L$, therefore the out-of-plane solution can be expressed as

$$w^i(s,z) = \sum_{mn} \underbrace{\left[A_n^i \sin(\alpha_1 s) + B_n^i \cos(\alpha_1 s) + C_n^i \sinh(\alpha_2 s) + D_n^i \cosh(\alpha_2 s)\right]}_{\varphi_n^i(s)} \sin\left(\frac{m\pi z}{L}\right), \tag{3.44}$$

where $m\pi/L$ is the modal wavenumber along the z direction and m corresponds to the number of half-periods along the z axis. The free flexural wavenumber $k_f = (\omega^4/c_f)^{1/4}$, $\alpha_1 = \sqrt{k_f^2 - (m\pi/L)^2}$ and $\alpha_2 = \sqrt{k_f^2 + (m\pi/L)^2}$ are respectively the wavenumbers along the s direction for the propagating and evanescent flexural waves. The in-plane deflections are respectively expressed as

$$u^i(s,z) = \sum_{mn} \underbrace{\left[E_n^i \lambda_1 \mathrm{e}^{\lambda_1 s} + F_n^i \lambda_2 \mathrm{e}^{\lambda_2 s} + G_n^i \frac{m\pi}{L}\mathrm{e}^{\gamma_1 s} + H_n^i \frac{m\pi}{L}\mathrm{e}^{\gamma_2 s}\right]}_{\xi_n^i(s)} \sin\left(\frac{m\pi z}{L}\right) \tag{3.45}$$

and

$$v^i(s,z) = \sum_{mn} \underbrace{\left[E_n^i \frac{m\pi}{L} \mathrm{e}^{\gamma_1 s} + F_n^i \frac{m\pi}{L} \mathrm{e}^{\gamma_2 s} + G_n^i \lambda_1 \mathrm{e}^{\lambda_1 s} + H_n^i \lambda_2 \mathrm{e}^{\lambda_2 s}\right]}_{\zeta_n^i(s)} \cos\left(\frac{m\pi z}{L}\right). \quad (3.46)$$

$k_l = \omega/c_l$ and $k_t = \omega/c_t$ are respectively the free wavenumbers of the L- and T-waves, $\lambda_{1,2} = \pm\sqrt{k_l^2 - (m\pi/L)^2}$ and $\gamma_{1,2} = \pm\sqrt{k_t^2 - (m\pi/L)^2}$ are respectively the associated wavenumbers along the s direction. $(\varphi_n^i, \xi_n^i, \zeta_n^i)$ represent the section mode shapes for the three components. For each plate $i = 1 \cdots 4$, 8 unknown coefficients must be solved. They are stored to the following vector $\mathbf{V}_i^T = \langle A_n^i, B_n^i, C_n^i, D_n^i, E_n^i, F_n^i, G_n^i, H_n^i \rangle$. Thus, 8×4 equations can be developed from the BCs at the junction of two adjacent plates i and j. These 8 BCs correspond to

- the continuity of displacements in the s and z directions for two consecutive plates i and j:

$$w^i = u^j, \;\; u^i = -w^j \;\text{ and }\; v^i = v^j. \quad (3.47)$$

- the continuity of the rotation for two consecutive plates i and j. The rotation is assumed to be constant even during bending. This leads to

$$\frac{\partial w^i}{\partial s} = \frac{\partial w^j}{\partial s}. \quad (3.48)$$

- the equilibrium of bending moments:

$$\frac{\partial^2 w^i}{\partial s^2} = \frac{\partial^2 w^j}{\partial s^2}. \quad (3.49)$$

- the equilibrium of forces:

$$N_s^i = -V_s^j, \;\; N_{sz}^i = N_{sz}^j \;\text{ and }\; V_s^i = V_s^j. \quad (3.50)$$

At first approximation, the thickness of the plates is assumed to remain small compared to the bending wavelength so that the shearing effect is not considered. The influence of in-plane wave generation is neglected. This last assumption implies that

$$u = v = N_s = N_{sz} = V_s = 0. \quad (3.51)$$

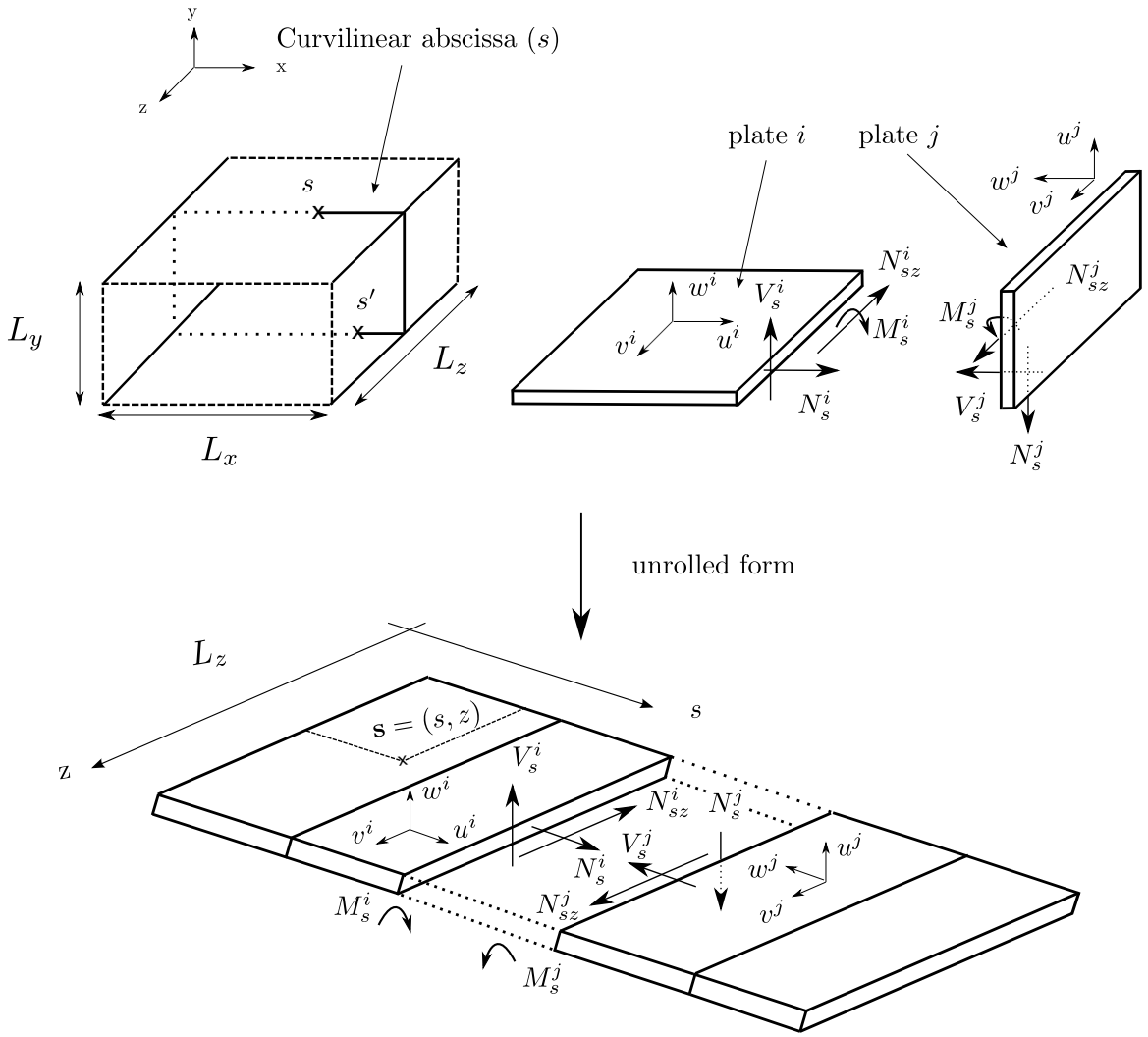

Figure 3.8: Coordinate system and resulting forces and moments between two plates i and j.

All that remains is 4 unknowns coefficients $\mathbf{V}_i^T = \langle A_n^i, B_n^i, C_n^i, D_n^i \rangle$ solved from the remaining 4 BCs for each plate $i = 1 \cdots 4$. These conditions between two adjacent plates i and j are written as

$$A_m^i \sin(\alpha_2 L_i) + B_m^i \cos(\alpha_2 L_i) + C_m^i \sinh(\alpha_1 L_i) + D_m^i \cosh(\alpha_1 L_i) = 0, \tag{3.52a}$$

$$A_m^j \sin(\alpha_2 L_j) + B_m^j \cos(\alpha_2 L_j) + C_m^j \sinh(\alpha_1 L_j) + D_m^j \cosh(\alpha_1 L_j) = 0, \tag{3.52b}$$

$$\begin{aligned} \alpha_2 \left[-A_m^i \cos(\alpha_2 L_i) + B_m^i \sin(\alpha_2 L_i) \right] + \alpha_1 \left[C_m^i \cosh(\alpha_1 L_i) + D_m^i \sinh(\alpha_1 L_i) \right] \\ = -\alpha_2 A_m^j + \alpha_1 C_m^j, \end{aligned} \tag{3.52c}$$

$$\begin{aligned} \alpha_2^2 \left[-A_m^i \sin(\alpha_2 L_i) - B_m^i \cos(\alpha_2 L_i) \right] + \alpha_1^2 \left[C_m^i \sinh(\alpha_1 L_i) + D_m^i \cosh(\alpha_1 L_i) \right] \\ = -\alpha_2^2 B_m^j + \alpha_1^2 D_m^j. \end{aligned} \tag{3.52d}$$

where L_i,$L_j = L_x$ or L_y according to the plate index. Then by writing these four equations at each coupled edges, we obtain a set of sixteen equations which can be expressed in a matrix form

$$\underbrace{\begin{bmatrix} \mathbf{Z}_{12} & \mathbf{Z}_{21} & \mathbf{0} & \mathbf{0} \\ \mathbf{0} & \mathbf{Z}_{23} & \mathbf{Z}_{32} & \mathbf{0} \\ \mathbf{0} & \mathbf{0} & \mathbf{Z}_{34} & \mathbf{Z}_{43} \\ \mathbf{Z}_{14} & \mathbf{0} & \mathbf{0} & \mathbf{Z}_{41} \end{bmatrix}}_{\mathbf{Z}(\omega,m)} \underbrace{\begin{Bmatrix} \mathbf{V}_1 \\ \mathbf{V}_2 \\ \mathbf{V}_3 \\ \mathbf{V}_4 \end{Bmatrix}}_{\mathbf{V}} = \begin{Bmatrix} \mathbf{0} \\ \mathbf{0} \\ \mathbf{0} \\ \mathbf{0} \end{Bmatrix}, \tag{3.53}$$

where $\mathbf{Z}$ is a 16×16 matrix which contains all the coupling terms and is composed of 4×4 sub-matrices $\mathbf{Z}_{ij}$ containing the coupling terms between plates i and j. Once the structural parameters of each plate are known, $\mathbf{Z}$ depends only on ω and m. According to Eq. (3.53), for a given m, the natural frequencies ω_{mn} of the duct are obtained by solving the non-linear equation

$$\det \mathbf{Z}(\omega, m) = 0 \ , \tag{3.54}$$

Finally, the shape associated with the mn^{th} mode is obtained by solving $\mathbf{Z}(\omega_{mn}, m)\mathbf{V} = \mathbf{0}$. The global shape of the unrolled duct ϕ_{mn} is given by

$$\phi_{mn}(\mathbf{s}) = \phi_{mn}(s, z) = \varphi_n(s) \sin\left(\frac{m\pi z}{L_z}\right). \tag{3.55}$$

The frequency reponse fonction H has the following expression:

$$H(\mathbf{r},\mathbf{s},\omega) = \sum_{i=1}^{4}\sum_{m,n} \frac{\phi^i_{mn}(\mathbf{r})\phi^i_{mn}(\mathbf{s})}{M_{mn}[\omega^2_{mnj}(1+\mathrm{j}\eta)-\omega^2]}, \tag{3.56}$$

where $M_{mn} = \int_S \rho h \phi^2_{mn}\,\mathrm{d}\mathbf{s}$ is the generalized mass.

The following model is compared with the commercial solver COMSOL Multiphysics ®. The rectangular duct is meshed with shell elements as for the cylindrical case. As previously explained, in the case of the cylindrical duct, the FEM model takes into account coupling between flexural and in plane waves as well as shearing effect within the duct thickness. The mesh is built for simulating the free flexural wavenumber of a plate up to 5000 Hz. A mesh size of 1 cm is used to maintain 6 elements for each flexural wavelength. Fig. 3.10 gives a comparison between the analytical and finite element solutions. The mobility in the transverse direction due to a point force located at (x=5 cm, y=0 cm, z=40 cm) is considered. The FEM mobility is compared to the analytical solution along with the point mobility of an infinite plate as shown in Fig. 3.10. The overall shape is respected and levels agree. However, some noticeable differences are observed for certain frequencies. The inclusion of the in-plane waves in the FEM solution may have the effect of modifying the structural behavior. Flexural waves are partly converted into in-plane waves upon transmission through a structural junction and then, converted back into flexural waves *via* other junctions. Above 900 Hz, the analytical solution seems to be slightly stiffer than the FEM solution. Finally, this preliminary study shows satisfactory agreement obtained by the analytical model when compared to a FEM solution. Discrepancies appear at higher frequencies with a maximum difference of 10% regarding the damped resonant frequencies.

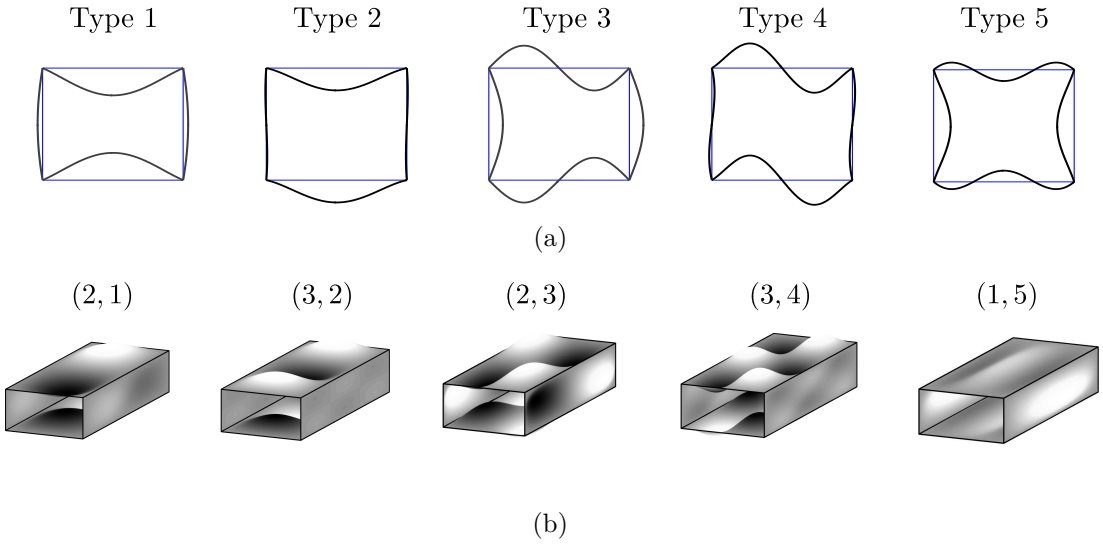

Figure 3.9: (a) Section mode shapes φ_n $(m = 1)$; (b) 3D illustration of some global modes of the duct ϕ_{mn}.

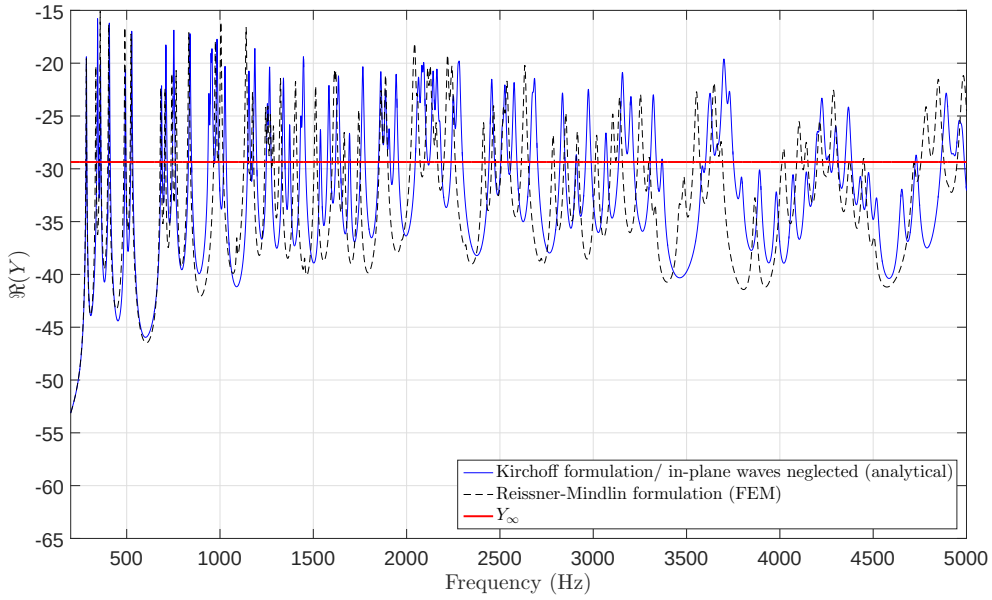

Figure 3.10: Comparison between the proposed analytical model and FEM calculation.

3.2.1 Identification of BC effects *via* measurement

The resonance frequencies calculated by the analytical model assume ideal boundary conditions. Thus, a modal analysis is performed to determine the experimental modal parameters for two configurations: (a) Free-Free (FF) and (b) operational (OP) BCs as shown in Fig. 3.11. These parameters, such as resonant frequencies, damping ratios and modal shapes are compared to the FEM solution and analytical model. Hence, the modal analysis provide an opportunity to verify the accuracy of FE modeling procedure and by extension, the limit of the analytical model.

Duct response was acquired using 3 axis accelerometer PCB 356A16 type (with sensibility of 103.5 mV/g) which allows to measure in-plane waves. A shock hammer is used (with sensibility of 2.56 mV/N) for the excitation. Signal processing and data acquisition was carried out using an 4-channel Siemens LMS Data acquisition system using the Siemens Impact Testing module to collect transient response of the duct. The reference point with coordinates (x=5 cm, y=10 cm, z=10 cm) is placed such that all modes are excited in the frequency range of interest (200 - 1400 Hz). A grid was drawn on the duct to locate the hammer impact positions with a regular interval of 2.5 cm along the cross-flow direction and 5 cm along the flow direction. The dynamic response was sampled at 4096 Hz with a spectral resolution of 0.5 Hz for a time period of 2 s. The time response data was processed using the Time MDOF module where damping and natural frequencies where extracted for the first $8th$ (then for the first $20th$ modes for the final analysis). The duct was hung vertically with 1/8 diameter bungee cords from a horizontal rod to provide 'free structure condition'. Here, rigid body modes are sufficiently low ($\approx$ 20 Hz) in relation to the first bending mode. The amplitude of the force spectrum is kept as much as possible constant over the frequency domain of interest. This set up can be seen in Fig. 3.11(a). In a second phase, the modal analysis is performed 'in situ', i.e., inserted in the aero-acoustic bench as shown in Fig. 3.11(b). The stabilization diagram obtained from a Least-Square Complex Exponential (LSCE) algorithm is represented Fig. 3.12. The evolution of the identified natural frequencies can be seen with the model order. To facilitate the extraction of the physical poles, the sum of the measure FRFs is superimposed. Physical modes can then be easily separated from spurious modes by looking for poles which appear at nearly identical frequencies for the different model orders considered. The natural frequency and the damping ratio of the stable poles are listed in Table 3.2. The extracted damping ratios are stable and not too high

when the model order increases. The extracted mode shapes exhibit very clear modal deformations and are shown in Fig. 3.13 for the 6 first. Note that only the modes 2 and 4 are torsional modes and the others are bending modes.

The commercial FE solver COMSOL Multiphysics® is used to calculate the mass-normalized displacement mode shapes and resonance frequencies of the duct as shown in Fig. 3.14. As shown in Table 3.2, the experimental resonance frequencies ($f_{\text{exp}}^{\text{FF}}$) are lower than the numerical frequencies ($f_{\text{FEM}-0}$) of the initial FE model presented in Fig. 3.14(a). The geometry is updated by including realistic frames. It is meshed with shell elements with different thicknesses and is shown in Fig. 3.14(b). The discrepancies between the experimental resonance frequencies and the numerical frequencies ($f_{\text{FEM}-F}$) after adding the frames are smaller, and more particularly the torsional modes (T) are correctly paired. Some adjustments or modification can be performed to accurately represent the dynamic behavior of the structure. For instance, including periodic frames to the structure would probably adjust sources of discrepancies. However, the mode shapes extracted provides an acceptable representation of the modal pattern behavior as shown in Fig. 3.15 from the MAC matrix representation. Thus, to compare the experimental and analytical mode shapes, $\boldsymbol{\phi}_i^{(1)}$ and $\boldsymbol{\phi}_j^{(2)}$ respectively, the modal assurance criteria (MAC) is computed and defined as

$$\text{MAC}(\boldsymbol{\phi}_i^{(1)}, \boldsymbol{\phi}_j^{(2)}) = \left(\frac{\boldsymbol{\phi}_i^{(1)^T} \boldsymbol{\phi}_j^{(2)}}{||\boldsymbol{\phi}_i^{(1)}||\,||\boldsymbol{\phi}_j^{(2)}||} \right)^2 . \tag{3.57}$$

The MAC matrix shows a good agreement between analytical and experimental mode shapes (MAC coefficients above 0.9). Finally, the analytical mode shapes are identified according to the highest MAC coefficients. The entire evaluation is summarized in Table 3.4 showing some of resonant frequencies and damping coefficients retained. The procedure described above is performed again for different flow speeds (varying from 10 m/s to 20 m/s) in order to quantify the impact of the flow on modal parameters. Table 3.5 shows the modal parameter extracted for two speed flows along with those obtained without flow. Small deviations of resonant frequencies and modal damping coefficients is found (less than 2% for all cases). The main sources of uncertainties is likely due to disassembling and reassembling the test apparatus between measurement periods which introduced slight structural differences rather than the effect of the flow. Depending on the flow speed, the natural frequencies and damping ratio of the analytical model are reassessed using values obtained in Table 3.5.

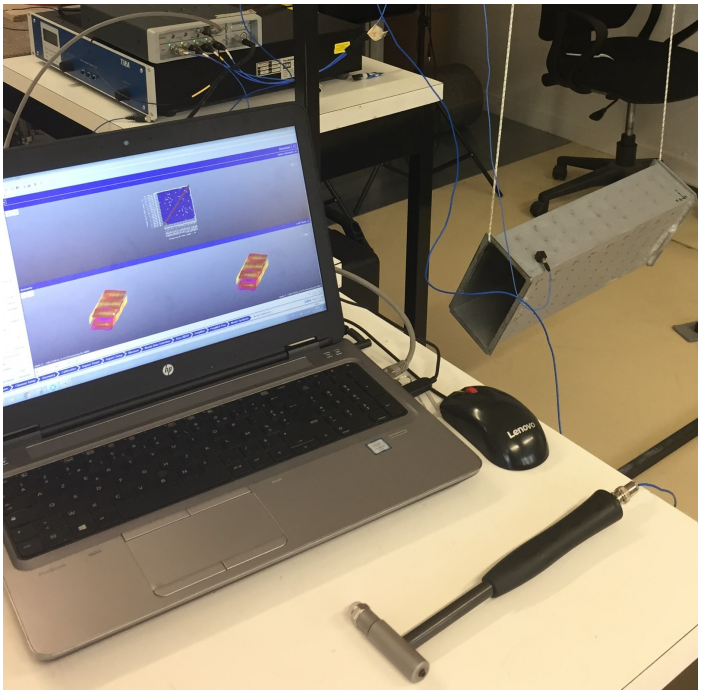

(a) Experimental setup using LMS impact Test capabilities. At the bottom, the impact hammer used for excitation can be seen.

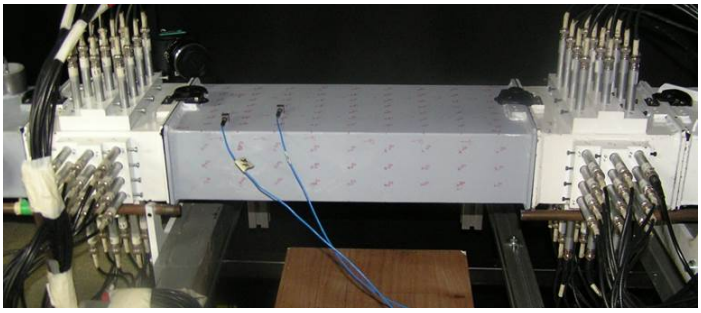

(b) Tested duct inserted in the aero-acoustic bench.

Figure 3.11: Experimental set up: (a) Free-Free (FF) and (b) Operational (OP) BCs.

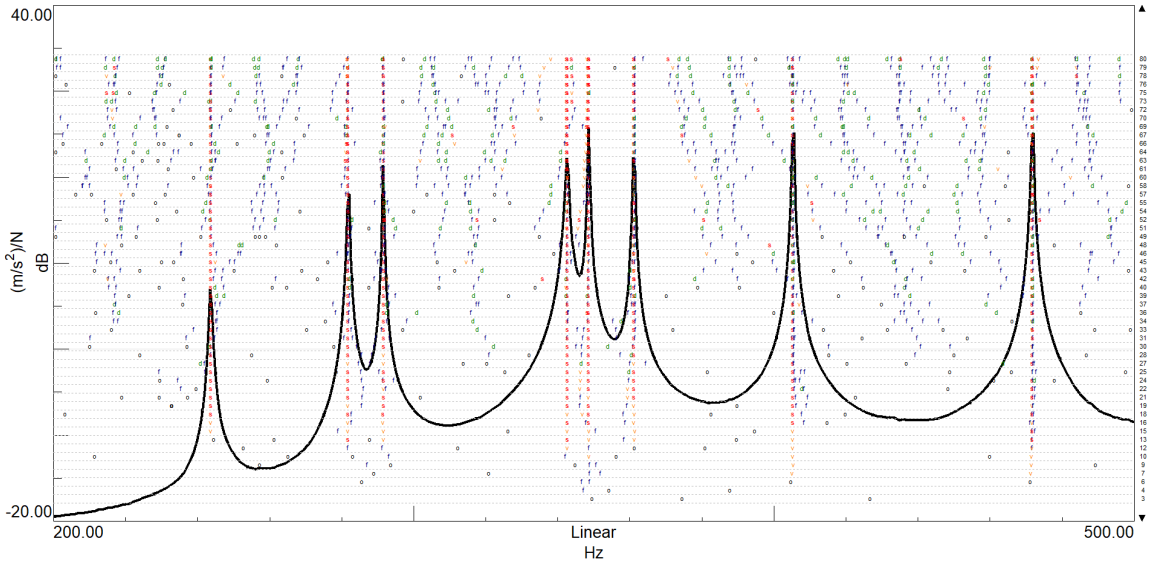

Figure 3.12: Stabilization diagram in the 200-500 Hz range.

Mode n°	$f_{\text{exp}}^{\text{FF}}$ (Hz)	$\xi(\%)$	mode description
1	244	0.17	1st bending
2	282	0.47	1st torsion
3	292	0.06	2nd bending
4	342	0.39	2nd torsion
5	349	0.05	higher bending mode
6	361	0.06	”
7	405	0.04	”
8	471	0.05	”

Table 3.2: Natural frequencies and damping ratios for Free-Free BCs.

Mode n°	$f_{\text{exp}}^{\text{FF}}$ (Hz)	$f_{\text{FEM}-0}$ (Hz)	$f_{\text{FEM}-\text{F}}$ (Hz)
1	244	188 (T)	244
2	282 (T)	206 (T)	270 (T)
3	292	259	313
4	342 (T)	279	327 (T)
5	349	344	360

Table 3.3: Experimental and numerical frequency comparison (Free-Free BCs). Influence of the frames: the initial geometry (FEM-0) is modified to take into account the frames (FEM-F) as shown in Fig. 3.14. The (T) letter stands for the torsional modes identified.

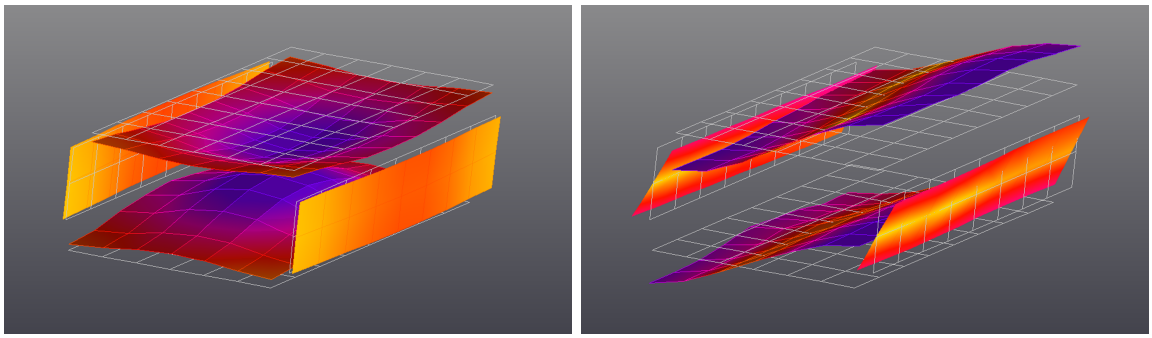

(a) Mode shape 1: first bending.

(b) Mode shape 2: first torsion

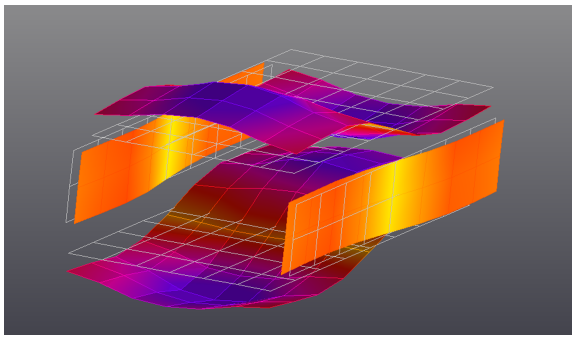

(c) Mode shape 3: second bending

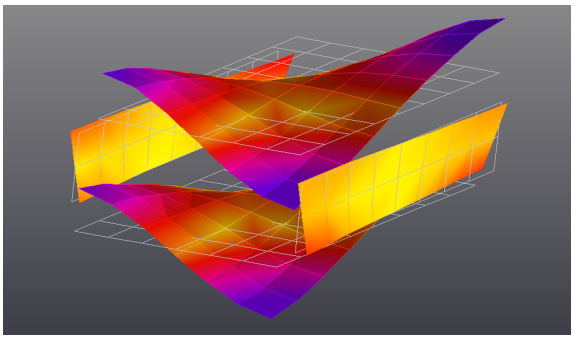

(d) Mode shape 4: second torsion

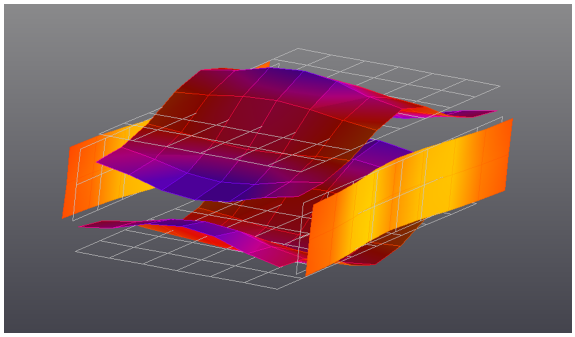

(e) Mode shape 5: third bending

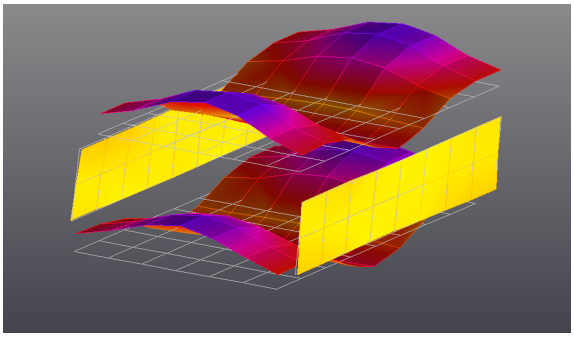

(f) Mode shape 6: forth bending

Figure 3.13: Representation of the extracted mode shapes for Free-Free BCs (LSCE method).

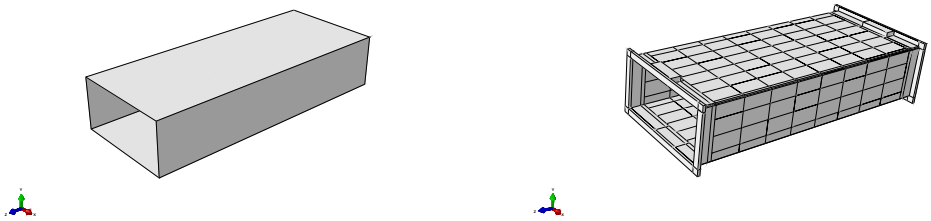

(a) (b)

Figure 3.14: Influence of the frames: (a) initial geometry (FEM-0) and (b) frames added (FEM-F).

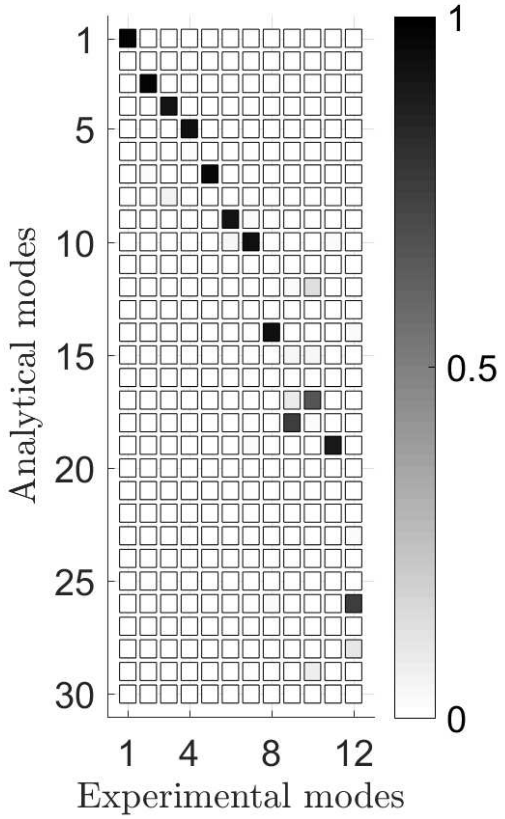

Figure 3.15: MAC matrix.

Mode n°	$f_{\text{exp}}^{\text{OP0}}$ (Hz)	ξ_0(%)	(m,n)	$f_{\text{AN}}^{\text{SS}}$ (Hz)	(m,n)	$\Delta f/f$	MAC
1	253	1.04	(1,1)	284	(1,1)	12%	0.97
				344	(1,2)	not	identified
2	293	0.73	(2,1)	360	(2,1)	23%	0.97
3	331	3.16	(2,2)	407	(2,2)	23%	0.91
4	410	0.78	(3,1)	493	(3,1)	20%	0.93
				527	(3,2)	not	identified
5	560	0.86	(4,1)	686	(4,1)	23%	0.96
				710	(4,2)	not	identified

Table 3.4: Natural frequencies and damping ratios for operational BCs without flow (OP0). The analytical mode shapes are well identified and selected according to the MAC matrix as shown in Fig. 3.15.

Mode n°	$f_{\text{exp}}^{\text{OP0}}$ (Hz)	ξ_0(%)	$f_{\text{exp}}^{\text{OP1}}$ (Hz)	ξ_1(%)	$f_{\text{exp}}^{\text{OP2}}$ (Hz)	ξ_2(%)
(1,1)	253	1.04	252	1.50	253	1.30
(2,1)	293	0.73	294	0.90	294	1.00
(2,2)	331	3.16	332	3.16	332	3.16
(3,1)	410	0.78	404	1.90	405	1.20
(4,1)	560	0.86	568	0.80	566	0.60

Table 3.5: Natural frequencies and damping ratios for operational BCs without flow (OP0), at 13 m/s (OP1) and at 20 m/s (OP2).

3.2.2 Fluid loading effect: experimental analysis in a vacuum chamber

A vacuo chamber has been used to asses the acoustic radiation effect of the rectangular duct. The whole test facility is mounted in a vacuum chamber. An ambient pressure of 3 hPa is applied inside the vacuum chamber. The duct is hanged with two strings in order to have free boundary conditions. A shaker is placed at x=20 cm, y=5 cm, z=5 cm to apply a harmonic point force to the duct. The measurements are made with a bandwidth of 1600 Hz and 3200 spectral lines to obtain frequency resolution $\Delta f = 0.5$ Hz. The study is focused at low frequency in order to have at least the first 8 modes with a good signal to noise ratio. A Polytec PSV400 scanning laser vibrometer was used and focused through a plexiglass door approximately 5 meters from the tested duct as shown in Fig. 3.16. At the end, the FRFs velocity/force are squared and averaged over the exposed face for the case with or without air as plotted in Fig. 3.17. The results presented in earlier sections showed that the first two resonances are 'bending' and 'torsion' type operating shapes. It is confirmed with Fig. 3.18 which shows the operating deflection shapes at 252 Hz and 283 Hz. Small discrepancies can be observed between the case in vacuum and with air. The first damped resonant frequency is shifted toward low frequencies due to a small added mass effect. The spectrum associated to the case with air is more damped due to the dissipation of vibration energy into acoustic radiation. The loss factor can be estimated based on values related to the sharpness of the resonance peaks. It can be approximated as

$$\eta \cong \frac{\omega_2 - \omega_1}{\omega_0} \tag{3.58}$$

where ω_2 and ω_1 are the two frequencies above and below the resonance frequency, ω_0, where the average power has dropped to one-half of its original resonace peak value (3 dB below). The structural loss factor η_s at the first 'in vacuo' resonant frequency is found to be 0.12%. The first 'wetted' resonant frequency gives a total damping η of 0.26%. The acoustic radiation damping η_a is then obtained by removing the structural loss from the total damping and equals to 0.14%.

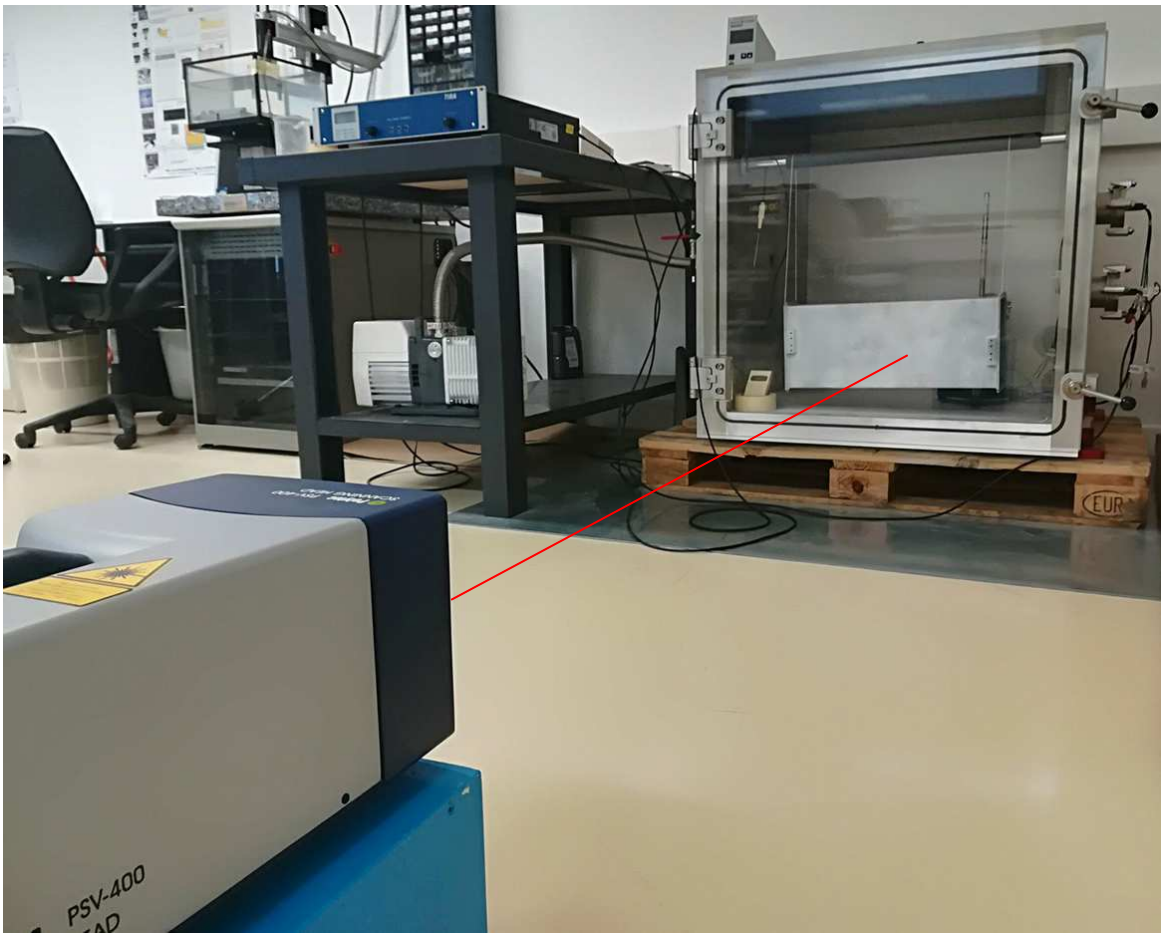

Figure 3.16: Experimental setup using a Polytec PSV400 scanning laser vibrometer. The tested duct is mounted in a vacuum chamber.

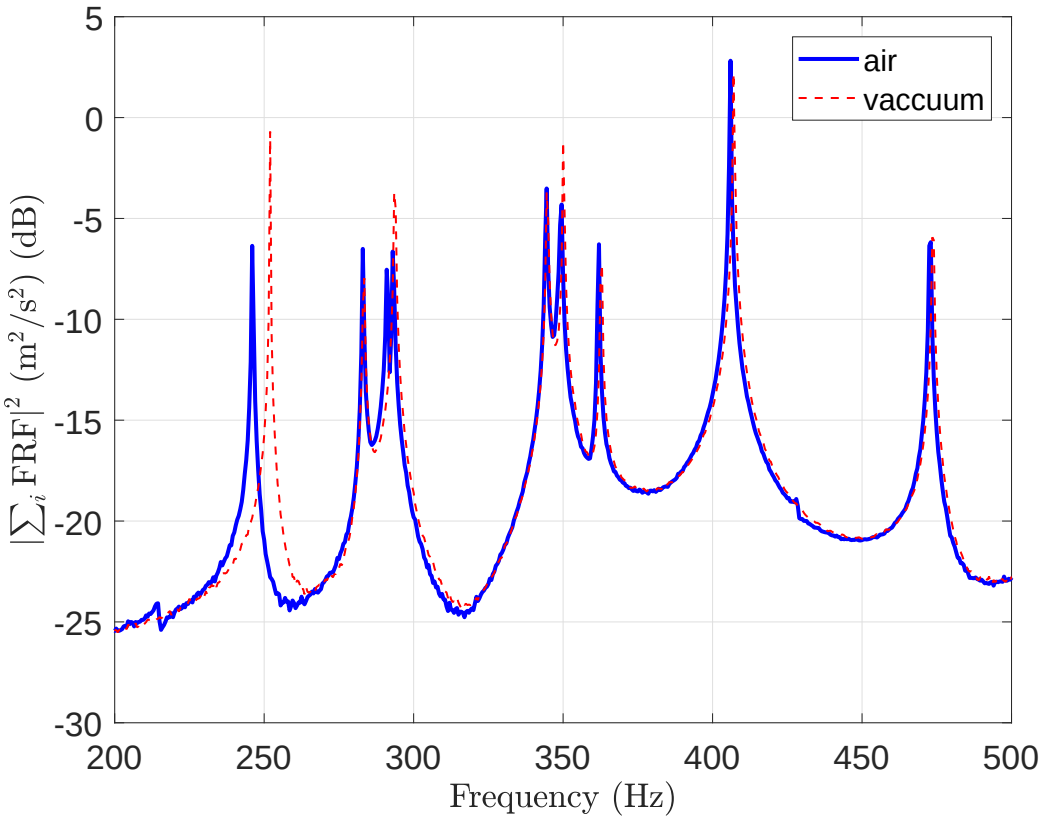

Figure 3.17: FRFs velocity/force averaged over the exposed face in presence of air or not.

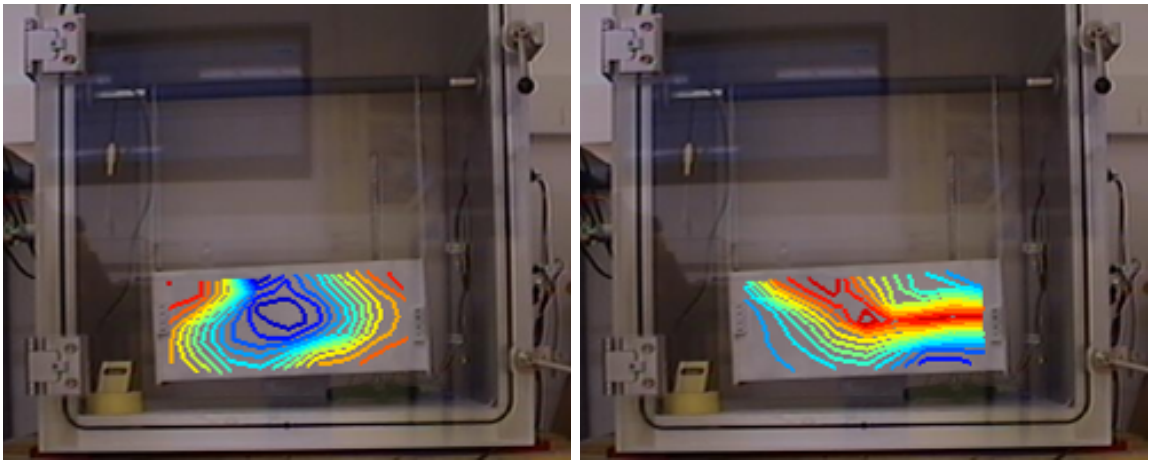

(a) Mode shape 1: first bending.

(b) Mode shape 2: first torsion

Figure 3.18: Operating deflection shapes at (a) 252 Hz and (b) 283 Hz.

3.3 Conclusion

The dynamic response of the duct has been investigated for two cross-sections: circular and rectangular. The classical thin shell theory is adopted for the circular geometry including the coupling between in-plane and out-of-plane waves. The rectangular duct model neglects in-plane longitudinal and in-plane shear waves induced at corner junctions. In both cases, simple analytical modal FRFs for simply supported geometry are adopted in order to facilitate numerical treatments for the calculation of the coupling between the turbulent flow and the structure. Small discrepancies are found between the proposed models and the FEM solution. In addition, a modal analysis has been performed on an operational rectangular pipe. The analytical mode shapes have shown good correlations after a confrontation with measurements. It suggests that simple analytical modal FRFs for simply supported geometry can be used as a guide for more complex geometry with complex BCs since it follows similar trends in terms of modal pattern and energy. For both cross-sections, the effects of the boundary conditions and acoustic radiation have been studied using either a commercial vibro-acoustic FEM solver or measurement performed in a *vacuo* chamber to ensure that the weak coupling assumption is reasonable for air fluid.

Chapter 4

Coupling between wall pressure fluctuations and the duct structure

This chapter presents numerical predictions of pipe flow noise and the associated vibration response of a straight duct of finite length due to a rigid obstacle inserted in the duct. Special attention will be paid on the coupling between acoustic propagating duct modes and the duct structure for two specific cross-sections: circular and rectangular. The wall pressure distribution is decomposed into hydrodynamic and acoustic contributions where the energy level is computed according to 'universal' trends found in the literature. In the following, a reliable spectrum based on the scaling law introduced by Nelson and Morphey is proposed in order to directly calculate the acoustic energy. The Turbulent Boundary layer (TBL) energy is calculated on the basis of the Goody's model. The excitation includes both acoustic and hydrodynamic contributions written on the basis of Corcos model and using acoustic duct mode coherence functions. Far from the obstacle, the relative weight of the hydrodynamic and acoustic contributions on the structural response is quantified for circular an rectangular ducts. The resulting chapter is written in order to be submitted to an academic journal, this explains why some theoretical ingredients already shown in previous chapter are reminded here briefly.

4.1 Introduction

Pipeline and duct vibrations can cause a range of issues from unplanned shutdowns to decreased equipment life. Thus, predicting flow-induced vibrations is essential in piping design in many industrial plants, especially for Oil & Gas industries.

In the ideal case of a fully developed turbulent flow in a straight cylindrical duct with no flow discontinuities or pipe fittings, vibrations are generally caused by the wall pressure fluctuations in the Turbulent Boundary Layer (TBL). This has been intensively investigated by Durant *et al.* [12] for internal air flow and Bonness *et al.* [14] for internal water flow. However, Norton's textbook (see Ch.7 in [8]) emphasizes the importance of considering plane wave and high order modes in the prediction of thin cylindrical pipe vibration. A study of the vibration response of a straight duct with rectangular cross-section [4] excited by a turbulent internal flow has shown that acoustic waves must be taken into account in the analysis to predict the vibration response. Hence, it appears that the prediction of pipe vibration due to internal turbulent flow gives different conclusions depending on the cross-section considered: circular or rectangular.

The origin of the sound is relatively well identified and localized in a context of internal flow disturbance due to a singularity in the duct (bend, junction, flow constriction or an obstacle). This generates internal broadband noise which propagate through the piping system. These additional sound waves are then superimposed on the hydrodynamic TBL fluctuations and are likely to dominate above a certain distance from the discontinuity. In the context of external flow, empirical models can be used to described the flow forcing function. The acoustic contribution written as a diffuse acoustic field (DAF) coherence function is directly added to the Corcos formulation [109, 116, 117] by using a coefficient which traduces the energy ratio between the acoustic and aerodynamic terms. For internal ducted flow, the acoustic energy produced by any given obstruction can be predicted according to the scaling law introduced by Nelson & Morphey [140]. This scaling law approach relies on the pressure drop and a scaled spectrum specific to the studied obstacle. To obtain this scaled spectrum, experiments or RANS computation can be performed [141, 142]. In the case of flow constriction, it can be useful to use the recent development of Kårekull *et al.* [143] where the only mere of the constriction geometrical characteristics, *ie*, the orifice and the duct cross-section area allows to predict the acoustic power. It is valid not only for the acoustic plane wave energy below the first cut-off frequency but also,

for high order acoustic modes.

Although most of the fluid conveying ducts are cylindrical, specific applications require the use of rectangular ducts. Here we aim to present a numerical study which can offer engineers a better understanding of the coupling between the duct section (circular or rectangular) and the excitation including both acoustic and hydrodynamic contributions. In this work, we are interested in the numerical prediction of flow-induced vibrations in the region where the entrance region effect is neglected as shown Fig. 4.1. In the vicinity of an obstacle placed in the duct, the 'near-field' is associated with strongly turbulent flow and non-propagating acoustic waves which are attenuated rapidly with distance away from the disturbance. The wall pressure fluctuations (including its acoustic part) can no more be analytically described and full computational aeroacoustic simulations are required [5]. 'Far from the obstacle', the pressure fluctuations are associated with duct acoustic modes propagating downstream and the distance is sufficient for the re-establishment of an undisturbed mean flow profile (the flow is considered uniform here) with fully developed TBL.

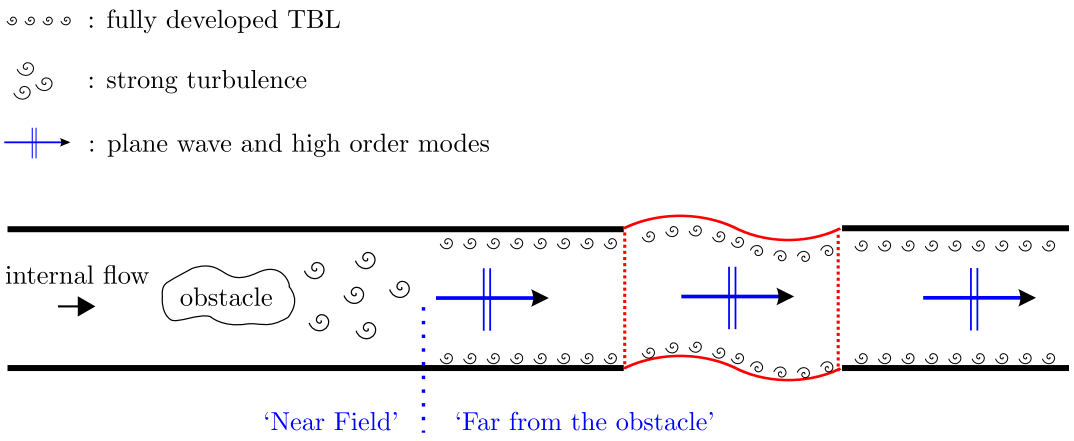

Figure 4.1: Flow-induced vibrations in the 'near-field' and 'far from the obstacle' due to an obstacle inserted in a duct (red lines denote the flexible part of the wall duct prone to vibrations).

The objective of this Chapter is to study the vibration response of a simply supported duct to a turbulent internal flow including both contributions (hydrodynamic and acoustic) for two specific cross-sections (circular and rectangular). In both cases, material properties and dimensions, i.e. width and cross-sectional aeras, are identical as shown in Fig. 4.2.

First, the flow forcing functions are described *via* Corcos model and acoustic duct mode coherence functions. The TBL and acoustic energies are based on the Goody

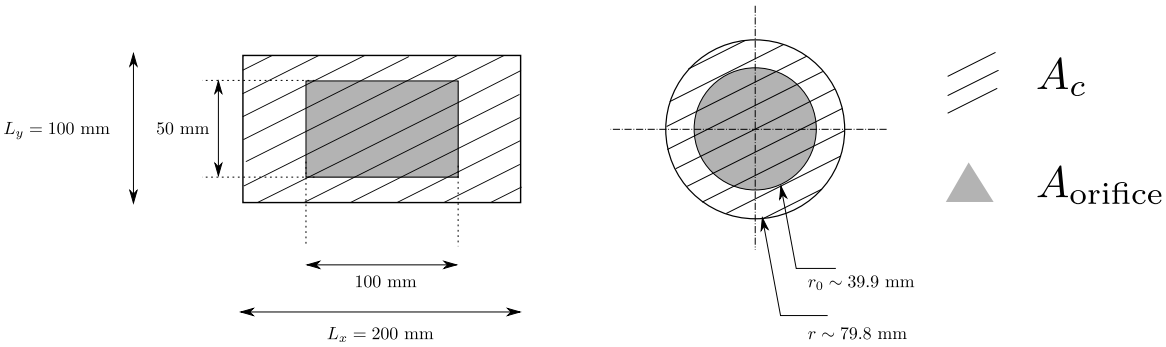

Figure 4.2: Two geometries are investigated with the same cross-sectional aeras $A_c = A_c^{\text{rec}} = A_c^{\text{cir}}$. The studied obstacle is a diaphragm with the same area orifice $A_{\text{orifice}} = A_{\text{orifice}}^{\text{rec}} = A_{\text{orifice}}^{\text{cir}}$ for each geometry.

model and a 'universal' trend based on the scaling law introduced by Nelson & Morphey respectively. Then, the numerical ingredients necessary for the prediction of flow induced vibration are described. It is based on a 'blocked' approach using analytical modal FRFs of a simply supported finite duct. Validations of our model are shown for the case of a simply supported plate excited by TBL, plane wave and diffuse acoustic field excitations. The coupling between the duct and the excitation is investigated in the wavenumber space. Finally, the duct vibration response due to a TBL and acoustic duct modes excitations are investigated for the two specific cross-sections. Attention is payed on the cylindrical duct which behavior depends on the modal density.

4.2 Acoustic and hydrodynamic contribution

4.2.1 Turbulent boundary layer

The Cross-Spectral Density (CSD) of the wall pressure fluctuation can be calculated using empirical models. Because the Corcos model is known to overestimate the levels in the subconvective domain, a modified Corcos model proposed in [34], which better estimates low-wavenumber excitation is considered in this work, so we take

$$S_{pp}^{\text{h}}(\mathbf{s}_1 - \mathbf{s}_2, \omega) = \Phi_{pp}(\omega)(1 + \gamma_z \omega |\xi_z|/U_c)\mathrm{e}^{-\gamma_s \omega |\xi_s|/U_c}\mathrm{e}^{-\gamma_z \omega |\xi_z|/U_c}\mathrm{e}^{-\mathrm{i}\omega \xi_z/U_c}, \tag{4.1}$$

where $\mathbf{s}_1 - \mathbf{s}_2 = (\xi_s, \xi_z)$ is the separation vector. The coefficient U_c defines the TBL velocity and is expressed as a fraction of the flow speed at the center of the duct U_∞ and this is set to $U_c/U_\infty = 0.85$. Corcos parameters γ_z and γ_s are related to the axial and lateral correlation lengths and set to $(0.125, 1)$ respectively. The point

spectrum is estimated on the basis of empirical models. In practice, empirical formula are considered such as the Goody model [64], Robert model formula [156] (see [157] for aeronautics application) or also a Chase model for the case of internal flow [14].

4.2.2 Acoustic field

The acoustic contribution is usually modeled as a diffuse field in a context of external flow. It is assumed that a diffuse field is a reasonable approximation for low Mach number flows, on the basis that the turbulent eddies are random acoustic sources in space and time. The coherence function of a Diffuse Acoustic Field (DAF) excitation writes [115]

$$\Gamma(\mathbf{s}_1 - \mathbf{s}_2) = \frac{\sin k_0|\mathbf{s}_1 - \mathbf{s}_2|}{k_0|\mathbf{s}_1 - \mathbf{s}_2|}. \tag{4.2}$$

This is in general directly added to the Corcos formulation by using a coefficient which traduces the energy ratio between the acoustic and aerodynamic terms. Arguillat *et al.* [116] measured the acoustic contribution by integrating the measured wavenumber cross spectrum over the acoustic disk of radius k_0. Starting from the measurement of the CPSD in the spatial domain, it was assumed a model of CPSD on the basis of the sum of an aerodynamic contribution provided by Corcos coherence function and an acoustic part given by a DAF written as:

$$S_{pp}(\mathbf{s}_1 - \mathbf{s}_2, \omega) = \Phi_{pp}(\omega)\left(\Gamma^{\text{Corcos}} + A(\omega)\Gamma^{\text{DAF}}\right), \tag{4.3}$$

with $A(\omega)$ the ratio between the aerodynamic and the acoustic energies frequently dependent. For instance, in automotive applications [117], a constant ratio of 10 percent is applied. Lecoq [109] used this approach to model both aerodynamic and aeroacoustic contributions and applied a ratio of 5 percent according to Arguillat work's [116] to an external flow exciting a flat plate.

The situation with an internal flow disturbance in the duct due to a singularity such as a bend, a junction or a flow constriction is different. 'Far from the obstacle', the flow/obstacle interaction generates internal sound waves which propagate through the piping system. The additional propagating sound waves are then superimposed on the hydrodynamic TBL fluctuations. The acoustic contribution is chosen to be described as a series of propagating acoustic duct mode. The duct pressure field of an infinite rigid duct is written for only modes propagating in the downstream direction,

for instance at point $\mathbf{s}_1 = (s_1, z_1)$ of the wall, it writes

$$p(\mathbf{s}_1, \omega) = \sum_{pq} C^+_{pq} \psi_{pq}(s_1) e^{\mathrm{i}k^+_{pq} z_1}, \tag{4.4}$$

where C^+_{pq} stands for amplitude of the downstream (+) propagating mode and ψ_{pq} the acoustic mode (p, q). The convention $\mathbf{s} = (s, z)$ is adopted so that s stands for the curvilinear abscissa and z the coordinate along the duct. Therefore, the modes ψ_{pq} are defined as the projection of the acoustic mode along the curvilinear abscissa s. The flow is assumed uniform and thermo-viscous attenuation is neglected so that the axial wavenumbers k^+_{pq} writes

$$k^+_{pq} = \frac{kM + \sqrt{k^2 - (1 - M^2)\, k^2_\perp}}{1 - M^2}, \tag{4.5}$$

where M is the Mach number and $k_\perp$ is the transverse wavenumber.

To our knowledge, Norton's thesis [118] was one of the first contribution to introduce plane waves and higher order modes expressed in term of CPSD forcing function in a context of internal flow induced vibration of pipes. The CPSD between the pressure at 2 points $\mathbf{s}_1 = (s_1, z_1)$ and $\mathbf{s}_2 = (s_2, z_2)$ writes

$$\begin{aligned} S_{pp}(\mathbf{s}_1, \mathbf{s}_2, \omega) &= \sum_{pq} \mathbb{E}\left[\left|C^+_{pq}(\omega)\right|^2\right] \underbrace{\psi_{pq}(s_1)\psi_{pq}(s_2)\mathrm{e}^{\mathrm{i}k^+_{pq}(z_1 - z_2)}}_{\Gamma^+_{pq}(\mathbf{s}_1, \mathbf{s}_2)} \\ &+ \sum_{\substack{pq \\ pq \neq rs}} \mathbb{E}\left[C^+_{pq}(\omega) C^+_{rs}(\omega)^*\right] \psi_{pq}(s_1)\psi_{rs}(s_2)\mathrm{e}^{\mathrm{i}(k^+_{pq} z_1 - k^+_{rs} z_2)}, \end{aligned} \tag{4.6}$$

where $\mathbb{E}\,[]$ is the ensemble average. The mode amplitudes are assumed all uncorrelated random variables so that $\mathbb{E}\left[C^+_{pq}(\omega) C^+_{rs}(\omega)^*\right] = 0$. The function $\Gamma^+_{pq}(\mathbf{s}_1, \mathbf{s}_2)$ is introduced in the spirit of the Corcos and the DAF coherence functions and writes

$$\Gamma^+_{pq}(\mathbf{s}_1, \mathbf{s}_2, \omega) = \psi_{pq}(s_1)\psi_{pq}(s_2)\mathrm{e}^{\mathrm{i}k^+_{pq}\Delta z}. \tag{4.7}$$

The coherence function range is from 0 to 1 to account for the effect of acoustic pressure 'node' and 'antinode'. Therefore, the acoustic energy $\left|C^+_{pq}(\omega)\right|^2$ represents the maximum value expected at an acoustic pressure 'antinode'. It is a measurable quantity expressed in Pa^2 where the acoustic pressure is maximum. Transverse acoustic

duct modes ψ_{pq}, for circular an rectangular ducts, are given by

$$\psi_{pq}^{\mathrm{cyl}}(s) = \mathrm{e}^{\mathrm{i}p\theta}, \tag{4.8}$$

where $p \in \mathbb{Z}$ because acoustic duct modes for circular ducts are 2π-periodic along the circumference, and

$$\psi_{pq}^{\mathrm{rec}}(s) = \begin{cases} \cos\left(\dfrac{p\pi s}{L_x}\right) & ; \quad s \in [0; L_x] \\ \cos(p\pi)\cos\left(\dfrac{q\pi\left[s - L_x\right]}{L_y}\right) & ; \quad s \in [L_x; L_x + L_y] \\ \cos\left(\dfrac{p\pi\left[2L_x + L_y - s\right]}{L_x}\right)\cos(q\pi) & ; \quad s \in [L_x + L_y; 2L_x + L_y] \\ \cos\left(\dfrac{q\pi\left[2L_x + 2L_y - s\right]}{L_y}\right) & ; \quad s \in [2L_x + L_y; 2L_x + 2L_y]. \end{cases} \tag{4.9}$$

4.2.3 Flow forcing function based on universal scaling law

In this study, the forcing function adopted for the study of vibrations due to an internal wall pressure fluctuation writes

$$S_{pp}(\mathbf{s}_1, \mathbf{s}_2, \omega) = \underbrace{\Phi_{pp}(\omega)\Gamma^{\mathrm{Corcos}}}_{\text{hydrodynamic (h)}} + \underbrace{\sum_{pq} \left|C_{pq}^{+}(\omega)\right|^2 \Gamma_{pq}^{+}}_{\text{acoustic (ac)}}, \tag{4.10}$$

where the point spectrum $\Phi_{pp}(\omega)$ is computed on the basis of the Goody model. It is expressed in mixed variable scaling and writes

$$\frac{\Phi_{pp}(\omega)U_\infty}{\tau_w^2\delta} = \frac{C_2(\omega\delta/U_\infty)^2}{\left[(\omega\delta/U_\infty)^{0.75} + C_1\right]^{3.7} + \left[C_3(\omega\delta/U_\infty)\right]^7}, \tag{4.11}$$

where $R_T \equiv (u_\tau\delta/\nu)\sqrt{C_f/2}$ can be interpreted as a Reynolds number. In this formula, coefficients C_1, C_2 and C_3 are set to $C_1 = 0.5$, $C_2 = 3$ and $C_3 = 0.11R_T^{-0.57}$. For an internal flow, the outer scale δ corresponds to the boundary layer thickness which is not defined explicitly. It is common [12, 14] to assimilate δ to the hydraulic diameter radius defined as $D_h = 4A_c/P$, where P is the duct wetted perimeter. The test section is assumed to be located far enough from the diaphragm (above 10 hydraulic diameters D_h) so the turbulent boundary layer is fully developed corresponding to an undisturbed mean flow profile. The inner scale τ_w corresponds to the shear stress at the wall. It is defined as $\tau_w = C_f\rho U_0^2/2$, where the friction coefficient C_f has been

estimated *via* empirical approximation of the boundary layer equations [127, 130]:

$$C_f^{\text{cir}} \cong \frac{0.059}{(\text{Re}_{D_h})^{1/5}} \quad \text{and} \quad C_f^{\text{rec}} \cong \frac{0.046}{(\text{Re}_{D_h})^{1/5}}, \tag{4.12}$$

where Re_{D_h} is the Reynold number of the pipe. The friction velocity is given through $u_\tau = (\tau_w/\rho)^{1/2}$ and ν is the kinematic viscosity.

The acoustic energy $\left|C_{pq}^{+}(\omega)\right|^2$ is calculated on the basis of scaling law introduced by Nelson & Morphey [140]. It is assumed that the acoustic power is equally distributed over N propaging duct modes as follows:

$$C_{pq}^{+}(\omega) = \sqrt{\frac{2\rho\omega W}{N k_{pq}^{+} N_{pq}}}, \tag{4.13}$$

where W stands for the acoustic power defined in dB as

$$L_w = 10\log_{10}\left(\frac{W}{W_0}\right), \tag{4.14}$$

where $W_0 = 10^{-12}$W. The normalization factor $N_{pq} = \int\limits_{A_c} \tilde{\psi}_{pq}^2 \, \mathbf{ds}$ becomes for the rectangular duct,

$$N_{pq}^{\text{rec}} = L_x L_y \Lambda_p \Lambda_q \quad \text{with} \quad \begin{cases} \Lambda_p = 1 & p = 0, \\ \Lambda_q = 1 & q = 0, \\ \Lambda_p = 1/2 & p > 0, \\ \Lambda_q = 1/2 & q > 0 \end{cases} \tag{4.15}$$

and for the circular duct

$$N_{pq}^{\text{cir}} = \pi r^2 (1 - \frac{p^2}{\chi_{pq}^2}), \tag{4.16}$$

where χ_{pq} are Bessel function zeros.

The scaling law approach introduced by Nelson & Morphey relies on the pressure drop and a scaled spectrum specific to the studied obstacle. To obtain this scaled spectrum, experiments or RANS computation can be performed [141, 142]. The hypothesis used in Nelson & Morphey paper is that the root mean square fluctuating drag force F_z on the obstacle is proportional to the steady drag force $\overline{F_z}$ at a certain frequency band. The fluctuating force is a broad-band random type and is described

by its spectral density such as

$$\sqrt{\mathbb{E}\left[|F_z(\omega)|^2\right]} = K(St)\overline{F_z}, \tag{4.17}$$

where the Strouhal number writes

$$St = \frac{fL_c}{u_c}, \tag{4.18}$$

with f the frequency band, L_c and u_c are typical length and velocity scale. Several definitions have been proposed for its definition, for instance, the component flow constriction u_c is defined as

$$u_c = \frac{U_\infty}{\sigma}, \tag{4.19}$$

with σ the '*vena contracta*' ratio. In our case, the hydraulic diameter D_h is retained for the length scale. This yields a definition of the strouhal number as

$$St = \frac{fD_h\sigma}{U_\infty}. \tag{4.20}$$

The sound power in a frequency band, generated in the downstream direction of the duct is given by

$$W = R\mathbb{E}\left[|F_z(\omega)|^2\right], \tag{4.21}$$

where R is the radiation resistance for an infinite duct [142]. According to Nelson & Morphey assumption law Eq.(4.17), the sound power writes

$$W = R\overline{F_z}^2 K^2(St). \tag{4.22}$$

The radiation resistance is depending on the duct dimensions and is divided into two regimes: a plane wave or high order acoustic modes propagation. Hence, for wavenumber above the first duct frequency cut on f_c, all propagating modes needs to be considered. The average radiation resistances in the downstream direction, for circular an rectangular ducts, are given by

$$R_{\text{pl.w.}} = \frac{1}{8A_c\rho c} \quad k < k_c, \tag{4.23}$$

$$R_{\text{cir}} = \frac{k^2\left(1 + (3\pi/4rk)\right)}{48\pi\rho c} \quad k > k_c, \tag{4.24}$$

$$R_{\text{rec}} = \frac{k^2\left(1+(3\pi/4k)\right)\left(L_x + L_y/A_c\right)}{48\pi\rho c} \qquad k > k_c. \tag{4.25}$$

In the case of a diaphragm, it can be useful to use the recent development of Kårekull *et al.* [143]. They revisited the Nelson-Morfey semi-empirical scaling law by suggesting that the dynamic force is assumed to scale with the momentum flux, given by

$$\overline{F_z} \propto \rho A_c U_\infty U_{vc} = \frac{\rho A_c U_\infty^2}{\sigma}, \tag{4.26}$$

where $\rho A_c U_\infty^2$ corresponds to the mass flow and U_{vc} to the mean velocity at the *vena contracta* area $A_{\nu c}$. The *vena contracta* ratio σ, i.e. the constriction openness, is given by

$$\sigma = \frac{A_{\nu c}}{A_c}. \tag{4.27}$$

The *vena contracta* ratio is evaluated from the formula presented by Durrieu *et al.* [144] and given by

$$\sigma = \frac{\frac{A_{\text{orifice}}}{A_c}}{1+\sqrt{0.5\left(1-\frac{A_{\text{orifice}}}{A_c}\right)}}. \tag{4.28}$$

In Kårekull papers [142, 143], several publications are used to review orifice noise in order to obtained a universal scaling spectrum $K^2(St)$. The general trend is

$$10\log_{10}\left(K^2/10^{-12}\right) = \begin{cases} 60 & St < 1, \\ 60-(20\sim 28)\log(St) & St > 1. \end{cases} \tag{4.29}$$

The symbol $\sim$ stands for the incertitude about the true slope value. The general inclination of $-28\log(St)$ can be seen as a mix between the source mechanisms of a pure dipole, $-20\log(St)$, and a pure quadrupole $-40\log(St)$. In this Chapter, the slope of a pure dipole, $-20\log(St)$, is considered.

Fig. 4.3 shows the acoustic power used in Eq.(4.13) to calculate the acoustic energy $\left|C^+_{pq}(\omega)\right|^2$ for circular an rectangular ducts at 10 m/s. Two regimes are dissociated: one corresponds to a plane wave propagation until the first duct frequency cut on f_c (continuous line) and the other is associated to high order acoustic modes propagating in the duct (dashed line). It can be shown that, Eq.(4.22) predicts $W \propto U_\infty^6 c^{-3}$ for multi-modal propagation ($f > f_c$) as for a free field dipole and $W \propto U_\infty^4 c^{-1}$ for plane wave propagation ($f < f_c$), which is usually associated with a free field monopole [140]. This explains why the acoustic power increases more rapidly above the first duct cut

on f_c. Here, the acoustic power W has been compared successfully with experimental data at low speed flow for the rectangular duct [121, 158]. It is extended for this study to higher speed flows and for the circular duct case.

Fig. 4.4 shows the acoustic modal amplitudes $\left|C^{+}_{pq}(\omega)\right|^2$ calculated trough Eq.(4.13) along with the TBL point spectrum calculated with the Goody model for two flow speeds for the rectangular case Fig. 4.4(a),(c) and the circular case Fig. 4.4(b),(d). As expected, the plane wave energy is the same for the two cross-sections. Above the first duct frequency cut on f_c, the acoustic energy is equally distributed over the N modes excited in the frequency range [200, 5000] Hz. Peaks appear at the natural frequencies of the acoustic propagating duct modes.'Far from the obstacle', the diaphragm generates acoustic waves which are more energetic (+20 dB) than the TBL. Some uncertainties remain about the TBL spectrum true value. Measurements in Chapter 2 for the rectangular duct have shown that the entrance region effect exists still for $x/D_h \approx 13$. This difference is underlined by an arrow.

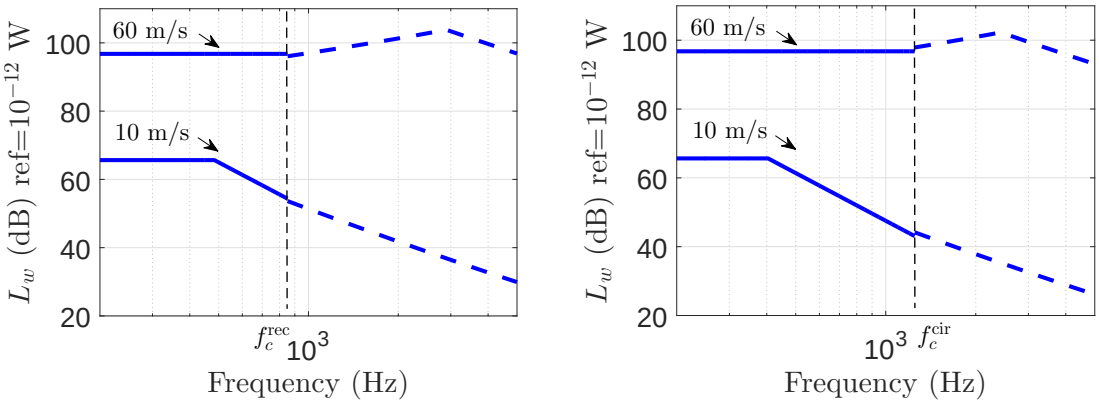

Figure 4.3: Acoustic power at 10 and 60 m/s: (a) rectangular and (b) circular cross-sections. Continuous and dashed lines stand respectively for the plane wave and multimodal propagation.

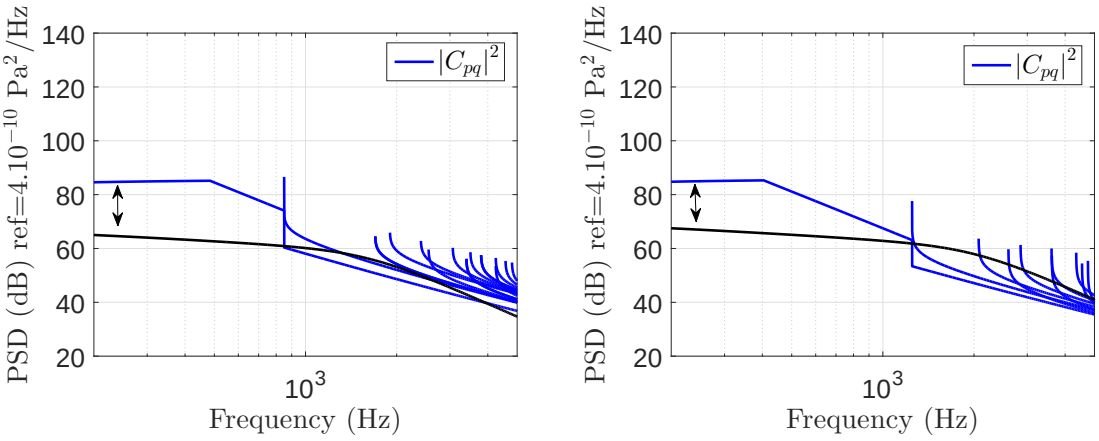

(a) rectangular case: 10 m/s.

(b) circular case: 10 m/s.

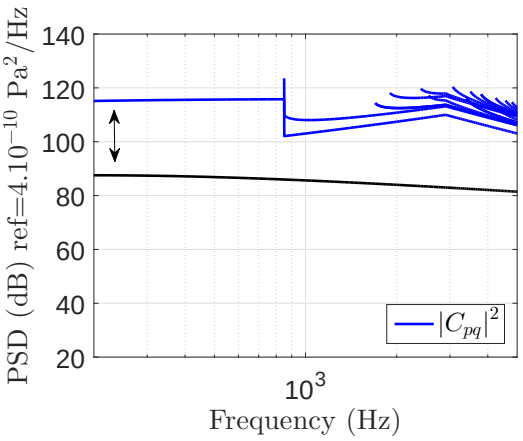

(c) rectangular case: 60 m/s.

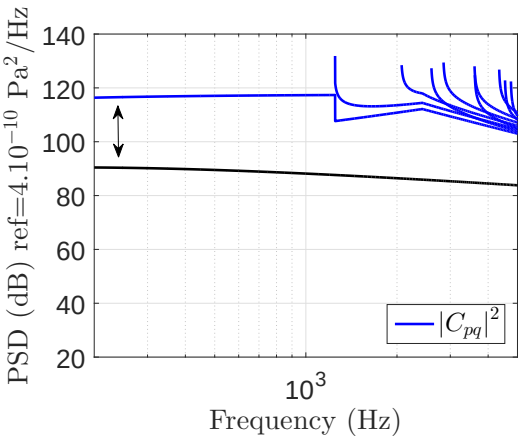

(d) circular case: 60 m/s.

Figure 4.4: TBL and acoustic energies in rectangular and circular ducts for two flow speeds. The arrow indicates uncertainties about the TBL spectrum true value.

4.3 Vibrating structures excited by random pressure

The overall framework for the analysis is based on random analysis techniques that takes into account the stochastic turbulent wall pressure distribution. Different techniques exist to take into account the TBL excitation in vibroacoustic models. A review of these methods can be found in [159]. The first one is the spatial method which consists in a direct computation of the PSD of the resulting vibration at a point $\mathbf{r}$ of the structure in the spatial domain:

$$S_{ww}(\mathbf{r},\omega) = \int_S \int_S H^*(\mathbf{r},\mathbf{s}_1,\omega) S_{pp}(\mathbf{s}_1,\mathbf{s}_2,\omega) H(\mathbf{r},\mathbf{s}_2,\omega)\,\mathrm{d}\mathbf{s}_1\,\mathrm{d}\mathbf{s}_2, \tag{4.30}$$

where H corresponds to the frequency response function (FRF) of the structure and S_{pp} the cross-spectral density (CSD) of the stochastic distributed excitation containing both the acoustic and turbulent component as defined in Eq.(4.10). A key parameter of this approach is the spatial resolution of the discretization to resolve both flexural waves and the excitation field under TBL. For finite element applications, this approach requires high memory capacity due to the difference in size of flexural and turbulent wavelengths and precautions had to be taken in terms of grid resolution. Contributions in search of innovative and fast solutions for combining empirical TBL forcing function models with complex FE structural models can be found in [160, 161]. The PSD of the resulting vibration at point $\mathbf{r}$ is computed using analytical modal FRFs associated with in-vacuum structural modes. The FRF defining the steady state harmonic response of the duct at point $\mathbf{r}_1$ excited by a point force located at $\mathbf{s}_1$ is written as a modal series:

$$H(\mathbf{r}_1,\mathbf{s}_1,\omega) = \sum_{m,n} W_{mn}(\omega)\phi_{mn}(\mathbf{r_1})\phi_{mn}(\mathbf{s_1}), \tag{4.31}$$

where ϕ_{mn} is the structural mode in vacuum for a given mode (m,n), $M_{mn} = \int_S \rho h \phi_{mn}^2\,\mathrm{d}\mathbf{s}$ is the generalized mass where S is the surface of structure, ω_{mn} the natural frequency of mode (m,n) and η the loss factor. The receptance function W_{mn} is defined as

$$W_{mn}(\omega) = \frac{1}{M_{mn}[\omega_{mn}^2(1+\mathrm{i}\eta) - \omega^2]}, \tag{4.32}$$

and has a sharp maximum at the resonance frequency for any given structural

mode. The response of the structure here is estimated *via* a 'blocked' approach. Thus, it is assumed that the structural motion has negligible impact on flow field and surface pressure fluctuation because a 'blocked' wall pressures is applied to the structure without created a feedback. This assumption is no longer valid for relatively dense fluids such as water or oil. Substituting the modal expansion relationship into Eq.(4.30) gives:

$$\begin{aligned} S_{ww}(\mathbf{r},\omega) &= \sum_{mn} \underbrace{\left(|W_{mn}(\omega)|\phi_{mn}(\mathbf{r})\right)^2}_{\text{modal receptance}} \times \underbrace{\int_S \int_S \phi_{mn}(\mathbf{s}_1) S_{pp}(\mathbf{s}_1,\mathbf{s}_2,\omega)\phi_{mn}(\mathbf{s}_2)\,\mathrm{d}\mathbf{s}_1\,\mathrm{d}\mathbf{s}_2}_{I_{mn}^{\mathrm{h,ac}}(\omega)\text{: joint acceptance function}} \\ &+ \sum_{mn} \sum_{\substack{pq \\ pq\neq mn}} \underbrace{\left(W_{mn}(\omega)W_{pq}^*(\omega)\phi_{mn}(\mathbf{r})\phi_{pq}(\mathbf{r})\right)}_{\text{modal cross-terms}} \times I_{mnpq}^{\mathrm{h,ac}}(\omega). \end{aligned} \tag{4.33}$$

The second term corresponds to the cross-joint acceptance which is generally very small compared with the joint acceptance. The averaged kinetic energy of the duct writes

$$E_c(\omega) = \frac{\rho h}{2}\frac{\omega^2}{S}\int_S S_{ww}(\mathbf{r},\omega)\,\mathrm{d}\mathbf{r}, \tag{4.34}$$

and allows us to quantify the global response of the structure. In the ideal case where the fluid loading effects are neglected, the average operation in Eq.(4.34) permits to use the orthogonality of the mode shapes and finally one gets an approximation of the averaged kinetic energy

$$E_c(\omega) \simeq \frac{1}{2}\frac{\omega^2}{S}\sum_{mn} M_{mn}|W_{mn}(\omega)|^2 \times I_{mn}^{\mathrm{h,ac}}(\omega). \tag{4.35}$$

This shows that the vibrational response is proportional to the product of two terms frequency dependent acting as frequency and spatial filters. The Corcos model and high order acoustic duct modes coherence functions are written as a separable form (in s and z) using exponential functions which allows analytical treatments. Therefore, in our case, it can be recast in the form of a product of two double integrals each relating the longitudinal coupling and the transverse coupling. The joint acceptance either for the hydrodynamic or the acoustic case according to Eq.(4.10) writes

$$I_{mn}^{\mathrm{h}}(\omega) = j_n^2(\omega)\, j_m^2(\omega) \quad \text{and} \quad I_{mnpq}^{\mathrm{ac}}(\omega) = j_{npq}^2\, j_{mpq}^{2+}(\omega). \tag{4.36}$$

These four double integrals are computed analytically by using a formal calculation software like Maple and appropriate change of variable.

4.3.1 Modal frequency response function of a simply supported finite duct

The simplest possible constitutive law corresponding to an isotropic, linear elastic material are considered and all materials exhibit elastic behavior under small deformations. The duct wall thickness is uniform and small compared with the cylinder radius and length. The duct response is based on Kirchhoff-Love assumptions where transverse shearing effects are neglected and the line originally normal to the midsurface remain perpendicular to the midsurface during deformations. It is assumed that the duct is simply supported at both ends located at $z = 0$ and $z = L_z$. The frequency response function for a rectangular duct section H^{rec} due to an harmonic point force located at $\mathbf{s}$ in the radial direction writes

$$H_w^{\text{rec}}(\mathbf{r}, \mathbf{s}, \omega) = \sum_{i=1}^{4} \sum_{m,n} \frac{\phi_{mn}^i(\mathbf{r_1})\phi_{mn}^i(\mathbf{s_1})}{M_{mn}[\omega_{mnj}^2(1 + \mathrm{j}\eta) - \omega^2]}, \tag{4.37}$$

where ϕ_{mn}^i stands for the mode associated to each plate $i = 1 \dots 4$ bonded together which form a rectangular shape. It is expressed [149] as :

$$\phi_{mn}^i(s, z) = \underbrace{\left[A_n^i \sin(\alpha_2 s) + B_n^i \cos(\alpha_2 s) + C_n^i \sinh(\alpha_1 s) + D_n^i \cosh(\alpha_1 s)\right]}_{\varphi_n^i(s)} \sin\left(\frac{m\pi z}{L_z}\right), \tag{4.38}$$

with $\alpha_1 = \sqrt{k_f^2 + (m\pi/L_z)^2}$, $\alpha_2 = \sqrt{k_f^2 - (m\pi/L_z)^2}$, k_f is the free flexural wavenumber $k_f = (\omega^4/c_f)^{1/4}$ and c_f the flexural wave speed in plates defined as $c_f = \sqrt[4]{D\omega^2/\rho h}$. Here, the bending stiffness D writes $D = Eh^3/12(1 - \nu^2)$, with h the duct thickness, ν is the Poisson's ratio and E the Young Modulus. The first index stands for the type of section mode and the second index corresponds to the number of half-periods along the z axis. For each mode m, the value of coefficients A_n, B_n, C_n and D_n is determined by writing the zero displacement conditions along the coupled edges, the continuity of the rotation and bending momentum. Note that the geometry suggests the use of thin plate theory which solves only flexural wave. However, a pure bending wave impinging at a corner junction will induce in-plane longitudinal and in-plane shear waves [155]. The present model neglects in-plane waves. However, it has been compared successfully with the commercial solver COMSOL Multiphysics® by meshing the geometry with shell elements. Discrepancies appear at higher frequencies with a maximum difference of 10% regarding the damped resonant frequencies. The

duct response due to a point force is quantified with the averaged Root Mean Square (RMS) acceleration, defined as

$$A_c^{\mathrm{RMS}}(\mathbf{s},\omega) = \sqrt{\frac{\int_S |H_a(\mathbf{r},\mathbf{s},\omega)|^2 d^2\mathbf{r}}{S}}. \tag{4.39}$$

For the circular duct, the Classical thin Shell Theory (CST) is used. The Donnell's operator $[\mathfrak{L}]$ is often referred as a reference and can be modified by adding higher order terms of $(h/r)^2$. Leissa discusses in Ref. [147] a number of additional models describing the vibration of cylinders. The Flügge's operator model which is one of the most accurate thin shell operator is chosen. The analytical FRF of a simply supported circular duct section H^{cir} due to an harmonic point force located at $\mathbf{s}$ in the radial direction has the following expression:

$$H_w^{\mathrm{cir}}(\mathbf{r},\mathbf{s},\omega) = \sum_{\alpha=0}^{1}\sum_{j=1}^{3}\sum_{m,n} \frac{w_{mnj}^{\alpha}(\mathbf{r_1}) w_{mnj}^{\alpha}(\mathbf{s_1})}{M_{mnj}^{\alpha}[\omega_{mnj}^2(1+\mathrm{j}\eta)-\omega^2]}, \tag{4.40}$$

where $M_{mn}^{\alpha} = \int_S \rho h ||\mathbf{q}||^2 \mathrm{d}\mathbf{s}$ is the generelized mass where $\mathbf{q}$ refers to three components u, v and w which are respectively the longitudinal, tangential and radial displacement. Each mode can be distinguished by being either anti-symmetric or symmetric with the index $\alpha = 0$ (resp. 1), n is the circumferential order, m is the longitudinal order, and j denotes the types of mode (extension-compression, torsion, bending). The shell 'ring frequency' is reminded here:

$$f_r = \frac{1}{2\pi}\frac{c_l}{r}, \tag{4.41}$$

where $c_l = (E/(\rho(1-\nu^2)))^{1/2}$ is the velocity of compressional waves.

Fig. 4.5 shows the averaged RMS acceleration due to a point force located at (s=5 cm, z=10 cm) and (θ=0°, z=30 cm) for the rectangular and circular duct respectively. The dimensions of duct cross-sections correspond to those depicted Fig. 4.2. Physical parameters are defined in Table 4.1. The mean level is the same between the two spectra. However, the modal content differs despite the same material properties and dimensions with 10 structural modes excited up to first acoustic duct frequency cut on f_c for the rectangular duct and only 2 for the circular duct. Attention is given to the first section mode shapes $n = 1$ and $n = 0$ for the rectangular and circular duct respectively. Four structural modes $n = 1$ are found in the frequency range [200 Hz, f_c] for the rectangular duct whereas the first mode family $n = 0$ of the circular duct

corresponding to breathing modes, appears at higher frequencies. The $n = 0$ modes of a cylindrical shell are clustered around the ring frequency as shown in Fig. 4.6. Therefore, breathing modes will contribute at very high frequencies (here $f_r = 10610$ Hz).

Young's modulus E	$210{\times}10^9$ Pa	Poisson's ratio ν	0.3
Density ρ	7800 kg/m^3	Thickness h	3 mm
Loss factor η	5.10^{-3}	Length L_z	0.5 m

Table 4.1: Physical parameters.

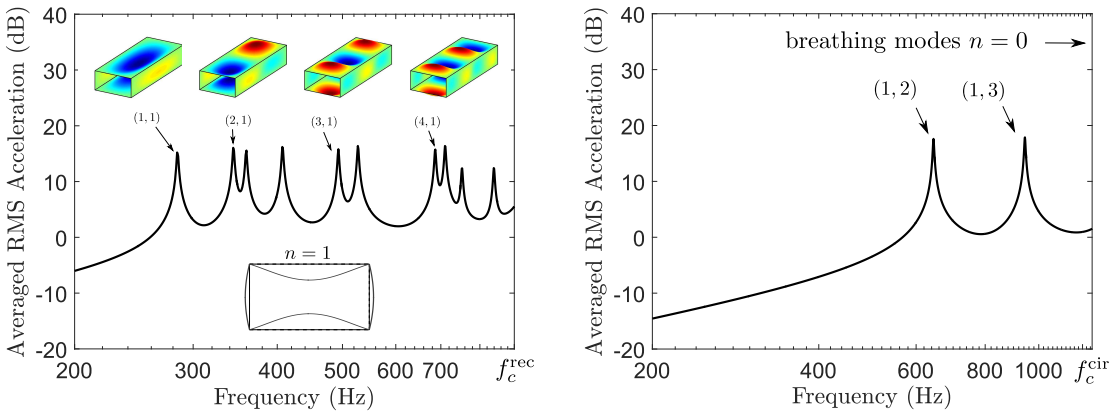

(a) Modes shapes $n = 1$.

(b) Modes shapes $n = 0$ appear at higher frequencies.

Figure 4.5: Analytical modal FRF: (a) rectangular and (b) circular cross-sections.

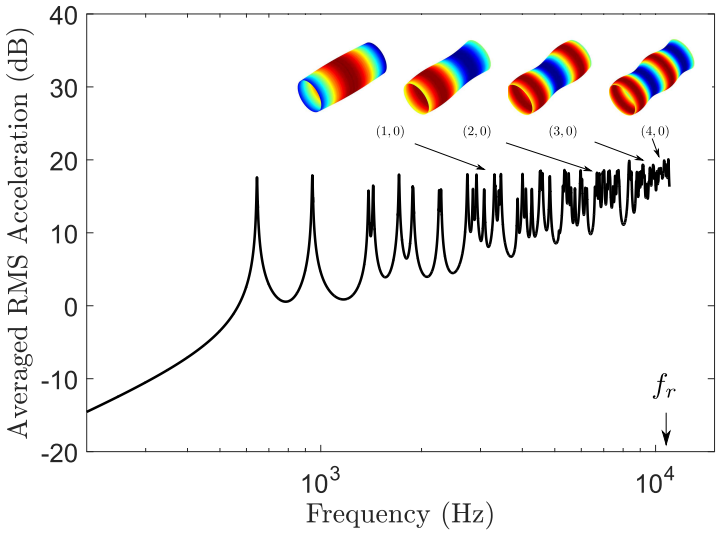

Figure 4.6: Visualization of breathing modes clustered around the ring frequency.

4.3.2 Coupling between the structure and TBL wall pressure fluctuations

Another approach consists in formulating Eq.(4.30) in the wavenumber domain [7]. If the forcing function depends on the separation vector $\mathbf{s}_1 - \mathbf{s}_2$ and defining the wavenumber-frequency spectrum of the wall pressure $\tilde{\Phi}_{pp}$ as the space Fourier transform of S_{pp} yields:

$$S_{pp}(\mathbf{s}_1 - \mathbf{s}_2, \omega) = \frac{1}{(2\pi)^2} \int_{-\infty}^{+\infty} \tilde{\Phi}_{pp}(\mathbf{k}, \omega) \mathrm{e}^{-\mathbf{i}\mathbf{k}(\mathbf{s}_2 - \mathbf{s}_1)} d^2\mathbf{k}. \tag{4.42}$$

Introducing the function $\tilde{H}(\mathbf{r}, \mathbf{k}, \omega)$ as

$$\tilde{H}(\mathbf{r}, \mathbf{k}, \omega) = \int_S H(\mathbf{r}, \mathbf{s}, \omega) \mathrm{e}^{\mathbf{i}\mathbf{k}\mathbf{s}} d^2\mathbf{s}, \tag{4.43}$$

the point spectrum of the structure displacement S_{ww} is transformed into a single integral over the wavenumber domain as follow

$$S_{ww}(\mathbf{r}, \omega) = \frac{1}{(2\pi)^2} \int_{-\infty}^{+\infty} \tilde{\Phi}_{pp}(\mathbf{k}, \omega) |\tilde{H}(\mathbf{r}, \mathbf{k}, \omega)|^2 d^2\mathbf{k}, \tag{4.44}$$

where $H(\mathbf{r}, \mathbf{k}, \omega)$ is generally called the sensitivity function. This technique is particularly use in aeronautics [162] and ship building industry [73] since the integration domain is transformed into a single integral which reduces computational time. There-

fore, the joint acceptance function can be evaluated in the wavenumber domain 'w' and writes

$$I^{\mathrm{h,ac}}_{mn,\mathrm{w}}(\omega) = \frac{1}{(2\pi)^2}\int_{-\infty}^{+\infty} \tilde{\Phi}_{pp}(\mathbf{k},\omega)|S_{mn}(\mathbf{k})|^2 d^2\mathbf{k}, \tag{4.45}$$

where

$$S_{mn}(\mathbf{k}) = \int_S \phi_{mn}(\mathbf{s})\mathrm{e}^{\mathrm{i}\mathbf{k}\mathbf{s}} d^2\mathbf{s}, \tag{4.46}$$

or in the spatial domain as seen previously in Eq.(4.33). This formulation is of a particular concern as the coupling of flexural waves with TBL wall pressure fluctuations is often analysed in wavenumber space. For instance, the wavenumber response of a plate bending mode superposed on a TBL wall pressure wavenumber frequency spectrum is illustrated in Ref. [99]. In our case, the duct refer to the simply supported boundary condition at both ends for which the related modal sensitivity function in the axial direction is the same as for the simply supported rectangular plate. The analytical expression can be found in Ref. [72, 97]. The Corcos coherence function and the modified one can be easily transformed into wavenumber space. The TBL streamwise wavenumber spectrum is plotted in Fig. 4.7 along with the modal sensitivity function at modal wavenumber $k_m = m\pi/L_z$ with $m = 3$, for two flow speeds. Most of the energy in the turbulent boundary layer is contained around $k_c = \omega/U_c$, where U_c is related to the average speed at which eddies are convected. The strong peak at the convective wavenumber is obtained as expected. If a mode of vibration has its wavenumbers close to k_c or k_0, $S_{mn}(\mathbf{k})$ is peaked about its wavenumbers and will preferentially accept power from the flow for this mode of vibration. At low Mach number, the convective wavenumber is too high to match wavenumbers of the bending waves as shown in Fig. 4.7(a),(b). For higher Mach number flow, convective wavenumbers in the flow tend to match wavenumbers of the bending waves as shown in Fig. 4.7(c). In all cases, the Corcos model is higher than the so-called Modified Corcos model from the low to intermediate wavenumber content in TBL wall pressures except for high flow speeds and relative low frequencies.

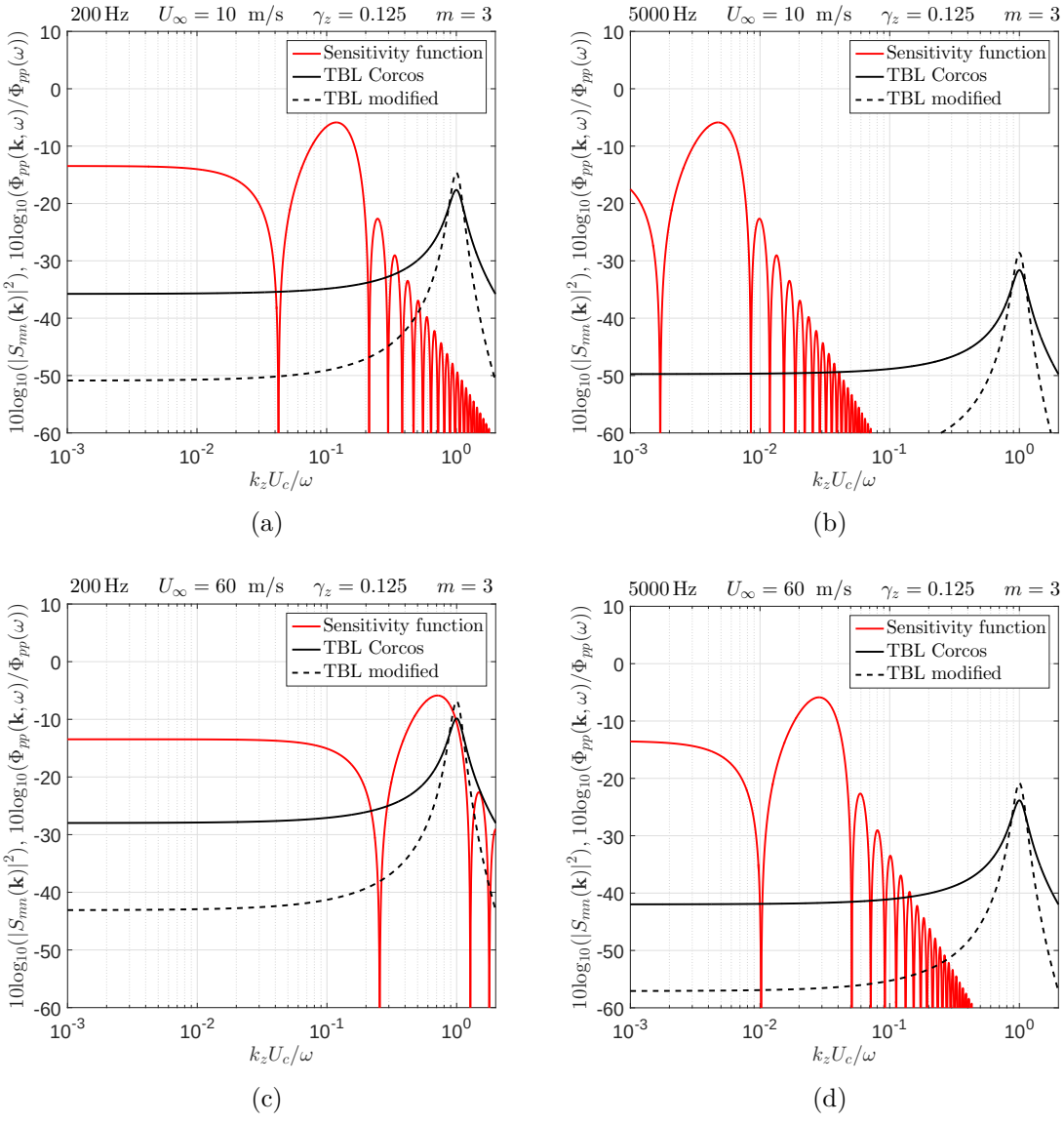

Figure 4.7: Coupling of flexural waves with TBL wall pressure fluctuations.

4.3.3 Coupling between the structure and a plane wave

As previously, the coupling between bending waves and a plane wave is analyzed in the wavenumber domain. The coherence function of an acoustic plane wave is defined as

$$\Gamma(\mathbf{s}_1, \mathbf{s}_2, \omega) = \mathrm{e}^{\mathrm{i}k_{00}^+ \xi_z}, \tag{4.47}$$

where k_{00}^+ is the acoustic wavenumber defined in Eq.(4.5). Thus, the associated 2D Fourier transform leads to the following analytical expression

$$\tilde{\Phi}_{pp}(\mathbf{k}, \omega) = \delta(k_s)\delta(k_z - k_{00}^+), \tag{4.48}$$

where δ is the Dirac function. According to Eq.(4.45), wavenumber transforms of the mode shapes are multiplied by the wavevector-frequency spectrum of a plane wave defined in Eq.(4.48), so that the joint acceptance function $I_{mn,\mathrm{w}}^{\mathrm{ac}}$ writes formally

$$I_{mn,\mathrm{w}}^{\mathrm{ac}}(\omega) = |S_{mn}(k_{00}^+, 0)|^2. \tag{4.49}$$

This expression shows that the coupling of the structure with a plane wave can be analyzed by looking at non zero values of the sensitivity function at wavenumbers $\mathbf{k} = (k_{00}^+, 0)$. A two-dimensional fast Fourier transform (FFT) needs to be performed for estimating the modal sensitivity function. The duct (rectangular or circular sections) is modelled in its unrolled form for the implementation of 2D FFT procedure. Note that precautions must be taken for cyclic function with period 2π to get a formulation valid between Fourier series and Fourier Transform. The modal sensitivity functions $S_{mn}(\mathbf{k}, \omega)$ with its associated mode shapes are shown in Fig. 4.8 for the rectangular case and Fig. 4.9 for the cylindrical case. It is shown that the sensitivity functions have non-zero values at $\mathbf{k} = (k_{00}^+, 0)$ with section modes type $n = 1$ or $n = 5$ for the rectangular duct case and only for the section mode $n = 0$ for the cylindrical case (i.e. only with breathing modes).

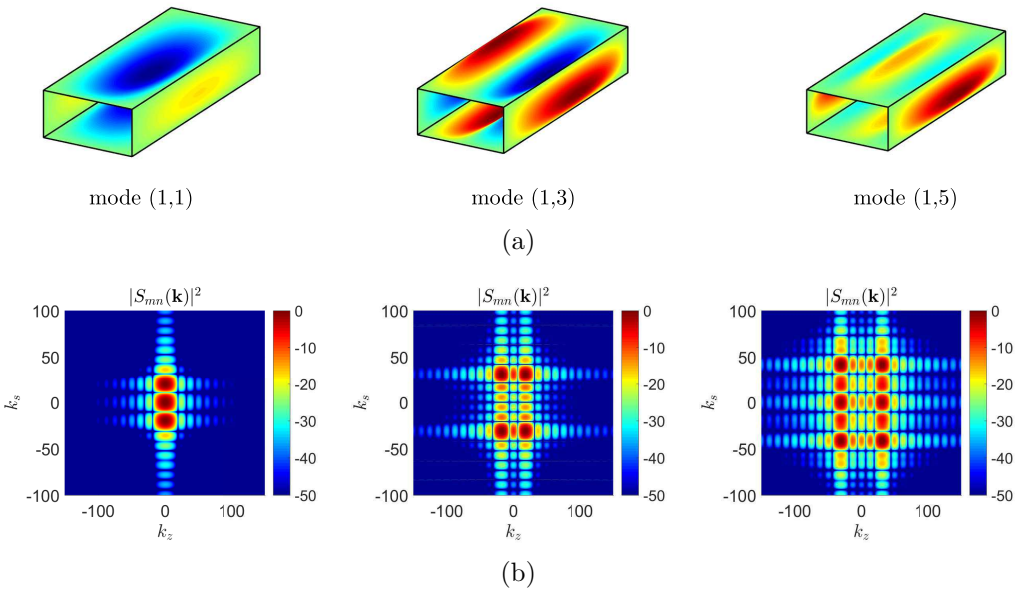

Figure 4.8: (a) Structural modes shapes and (b) the associated wavenumber transform

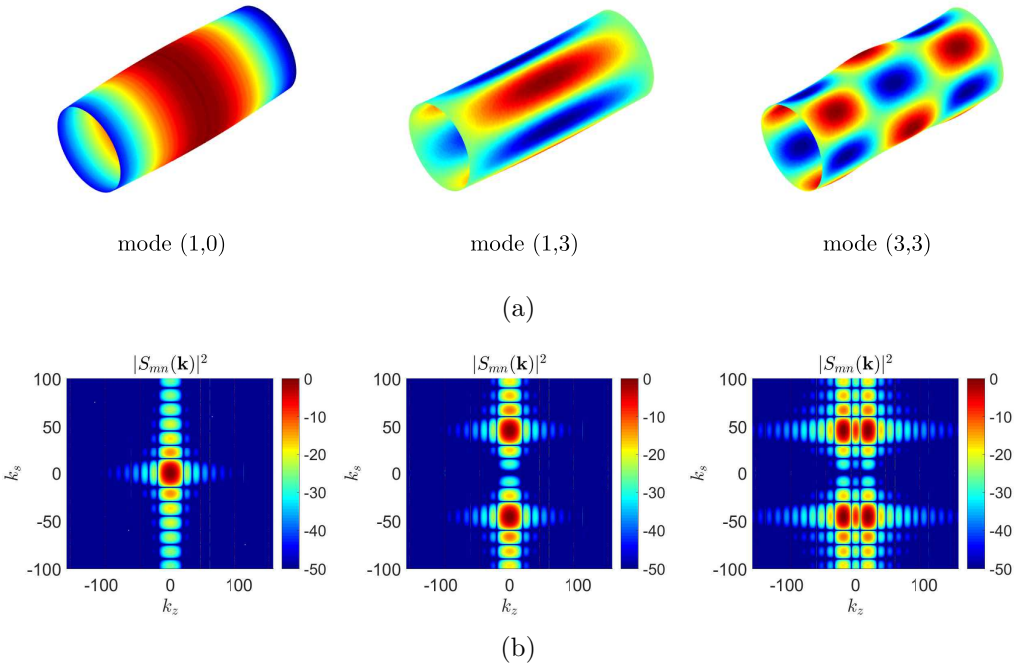

Figure 4.9: (a) Structural modes shapes and (b) the associated wavenumber transform

4.4 Validation for a simply supported rectangular plate

A validation has been made with a simply supported plate excited by TBL, plane wave and Diffuse Acoustic Field (DAF) excitations. The acoustic power is chosen in order to have the acoustic plane wave energy $|C_{00}^{+}(\omega)|^2$ equals to 1 Pa^2. It corresponds to an acoustic power of 52 dB ($W = 1.8 \times 10^{-7}$ W). This study case serves as a reference and validates the calculation of $I_{mn}^{\mathrm{h,ac}}(\omega)$ using both the analytical 's' and the wavenumber 'w' approach. Note that the coherence function of a DAF excitation is not a separable function in the axial and circumferential direction as it writes

$$\Gamma(\mathbf{s}_1, \mathbf{s}_2) = \frac{\sin k_0 |\mathbf{s}_1 - \mathbf{s}_2|}{k_0 |\mathbf{s}_1 - \mathbf{s}_2|}, \tag{4.50}$$

where $k_0 = \omega/c$ is the acoustic wavenumber. Thus, the joint acceptance is calculated *via* a simply regular spatial discretization of the panel surface and $I_{mn}^{\mathrm{h,ac}}(\omega)$ becomes:

$$I_{mn}^{\mathrm{DAF}}(\omega) \approx \sum_{i}^{N_p} \sum_{j}^{N_p} \phi_{mn}(\mathbf{s}_i) \Gamma^{\mathrm{DAF}}(\mathbf{s}_i, \mathbf{s}_j, \omega) \phi_{mn}(\mathbf{s}_j)\, \Delta^2, \tag{4.51}$$

where N_p is the number of cells and $\Delta = \mathrm{d}s\mathrm{d}z$ is the constant elementary surface. The discretized grid is chosen to resolve both flexural waves in the plate and the excitation field under the DAF. An exact solution of the joint acceptance function $I_{mn}^{\mathrm{h}}(\omega)$ using a Corcos coherence function can be found in chapter 15 of Nilsson textbook's [163] (see also Ref.[157] in the Appendix).

Fig. 4.10 shows the kinetic energy due to a TBL contribution (on the basis of Corcos's model), by using 144 modes for frequencies of resonance up to 7000 Hz. Good agreements are obtained and this validation will serve as a reference for the duct. Predicted kinetic energy due to different cross spectrm models with two different flow speeds are compared in Fig. 4.11. Prediction were made using acoustic (plane wave in flow direction and DAF) and TBL (Corcos and Modified Corcos) cross spectrum models. It shows that with equal energy the acoustic excitation clearly dominates. Similar results can be found in [164, 165]. In grey line are plotted the aerodynamic coincidence f_{aero} and the acoustic coincidence f_{ac}. Both DAF and Corcos models predict similar response below the aerodynamic coincidence (phenomenon much more pronounced with higher flow speed in Fig. 4.11(b)). Above the aerodynamic coincidence, the global energy level due to the TBL excitation decreases rapidly whereas levels due

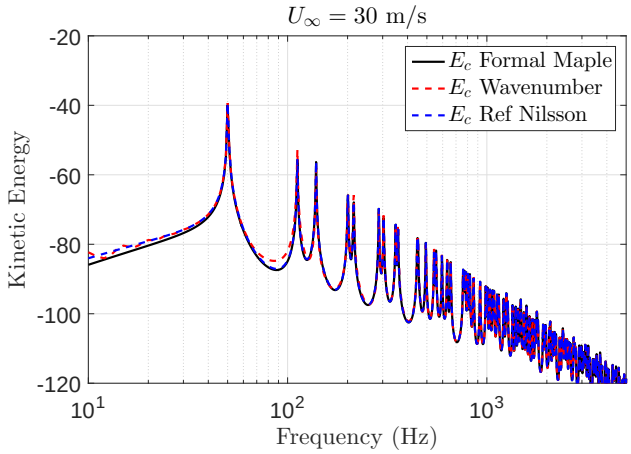

Figure 4.10: Validation method for the formal calculation: comparison with the wavenumber approach and Nilsson's reference.

to the acoustic excitations are maintained up to the acoustic coincidence frequency. This phenomena is well explained in the wavenumber domain (see Fig.3. in Ref.[109]) because the aerodynamic energy moves rapidly toward the high wavenumbers when increasing frequency whereas the acoustic and flexural wavenumbers have the same order of magnitude in a wide frequency range. At low mach number, the convection velocity is much lower than the speed of sound and convective wavenumbers are too high to match those of the vibrational modes. The original Corcos model is shown to differ from the Modified one, especially after the aerodynamic coincidence. Above this frequency, the response is clearly controlled by the low to mid wavenumber region of the TBL excitation which differs by 10 to 20 dB between the two models.

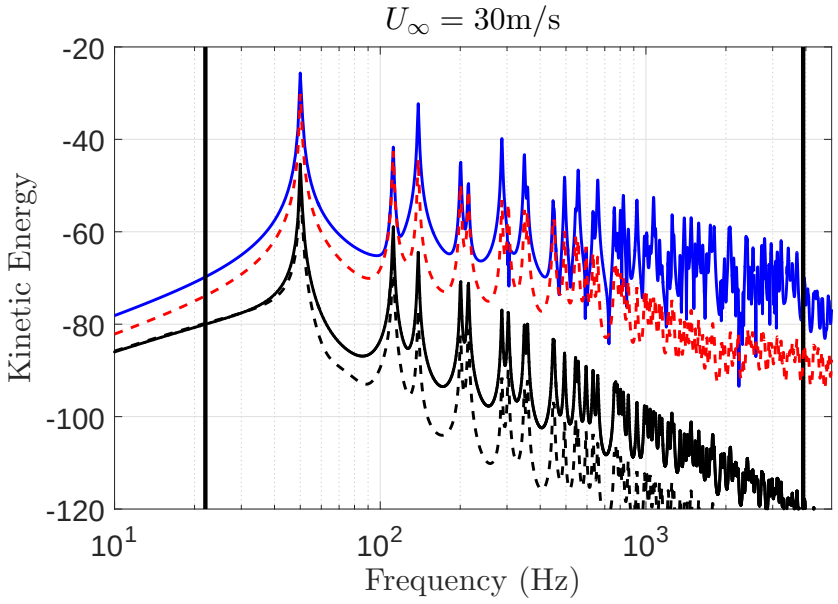

(a)

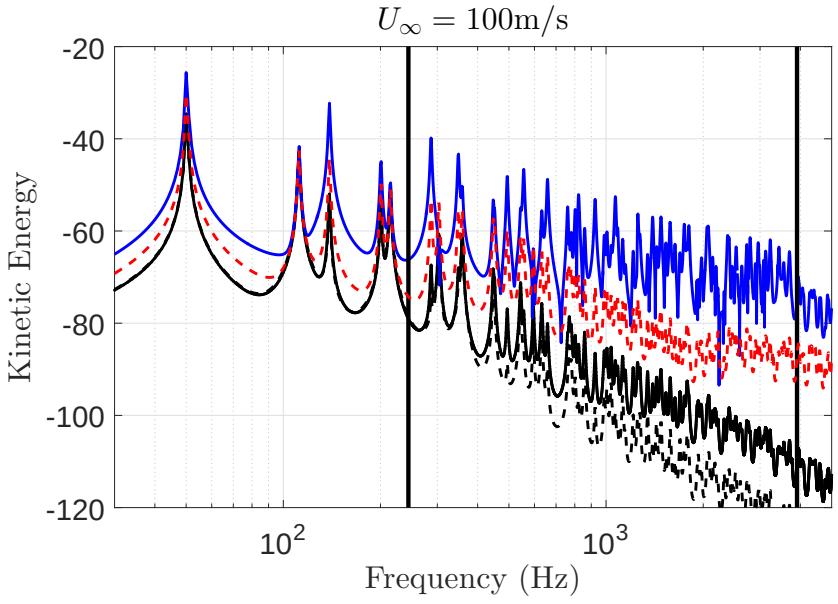

(b)

Figure 4.11: Effect of the acoustic and turbulent contributions on a simply supported plate: DAF (---), plane wave (—), Corcos (—) and Corcos Modified(---) at (a) 30 m/s and (b) 100 m/s

4.5 Results

In the following, a reliable spectrum based on the scaling law introduced by Nelson and Morphey is proposed in order to directly calculate the acoustic energy. The TBL energy is calculated *via* the Goody model. Results obtained in Fig. 4.4 are used for the calculation of the structural response according to Eq.(4.35) for the plane wave and multimodal regime.

4.5.1 Vibration response due to TBL and acoustic duct modes

The kinetic energy of the duct for rectangular and circular cross-sections due to a TBL and acoustic duct modes at various flow speeds are shown Fig. 4.12. The rectangular case is shown in Fig. 4.12(a),(c) and the circular case see Fig. 4.12(b),(d) at 10 and 60 m/s respectively. Below the first duct frequency cut on f_c, the plane wave contribution clearly dominates for the rectangular duct whereas it is not as pronounced for the cylindrical duct. As seen previously, acoustic plane waves couple only with section modes type $n = 1$ or $n = 5$ for the rectangular duct case and only with breathing modes clustered around the ring frequency for the cylindrical case (see Fig. 4.6). Only one breathing mode type belongs to the frequency range [200 Hz - 5000 Hz] which explains why the level due to the plane wave contribution is less pronounced for circular duct. The TBL remains lower than the plane wave contribution. For the two speed flows considered, the aerodynamic coincidences f_{aero} remain below 200 Hz. Therefore, the structure accepts energy only from the low to intermediate wavenumber content associated to the acoustic excitation. Therefore, the vibrational levels due to the two TBL models differs by 15 dB since the corresponding levels in the low to mid wavenumber region are different. Above, the first duct frequency cut on f_c, high order acoustic duct modes are coupled to the structure and the structure response is no longer controlled by the plane wave excitation. As expected, the vibration level is higher for high flow speed. The variation of the vibrational response with flow speeds agrees with a velocity depence of U_∞^4 for plane wave propagation and U_∞^6 for multi-modal propagation.

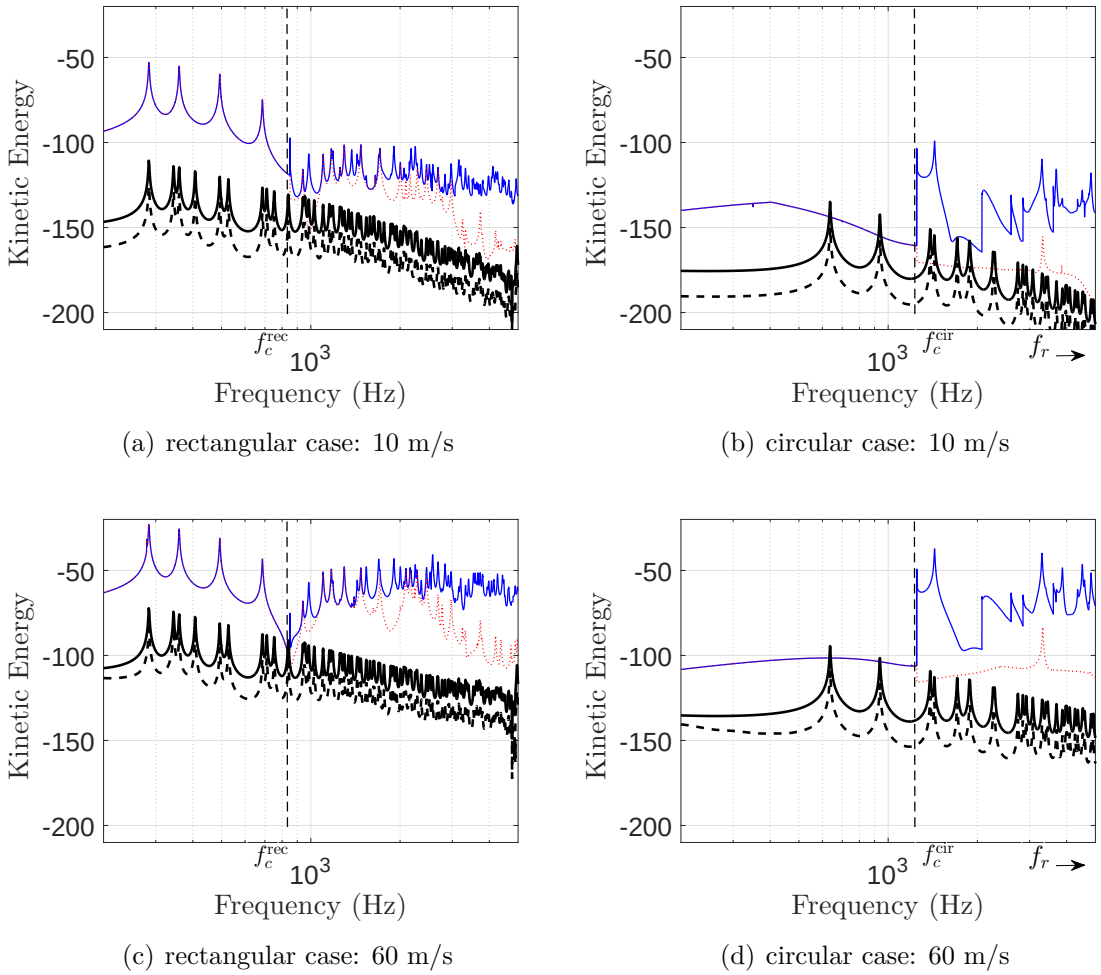

(a) rectangular case: 10 m/s

(b) circular case: 10 m/s

(c) rectangular case: 60 m/s

(d) circular case: 60 m/s

Figure 4.12: Kinetic energy for TBL and acoustic contributions: superposition of all acoustic duct modes (——), plane wave (·····), Corcos (——) and Corcos Modified(- - -).

4.5.2 Modification of the circular duct modal density: increasing r and decreasing h

The ring frequency is moved down by increasing r and the modal content is increased by decreasing the shell thickness h. Results are shown in Fig. 4.13. Trends are similar to those observed previously except when the thickness is divided by a factor 10. Below the first duct frequency cut on f_c, the vibration is controlled by the TBL alone, especially at high speed flows as shown in Fig. 4.13(d). This behavior seems to answer the question why TBL is often considered alone for pipe flow with no discontinuities as in Durant's paper [12]. Breathing modes are clustered around the ring frequency and the vibration level due to a plane wave becomes important when the ring frequency

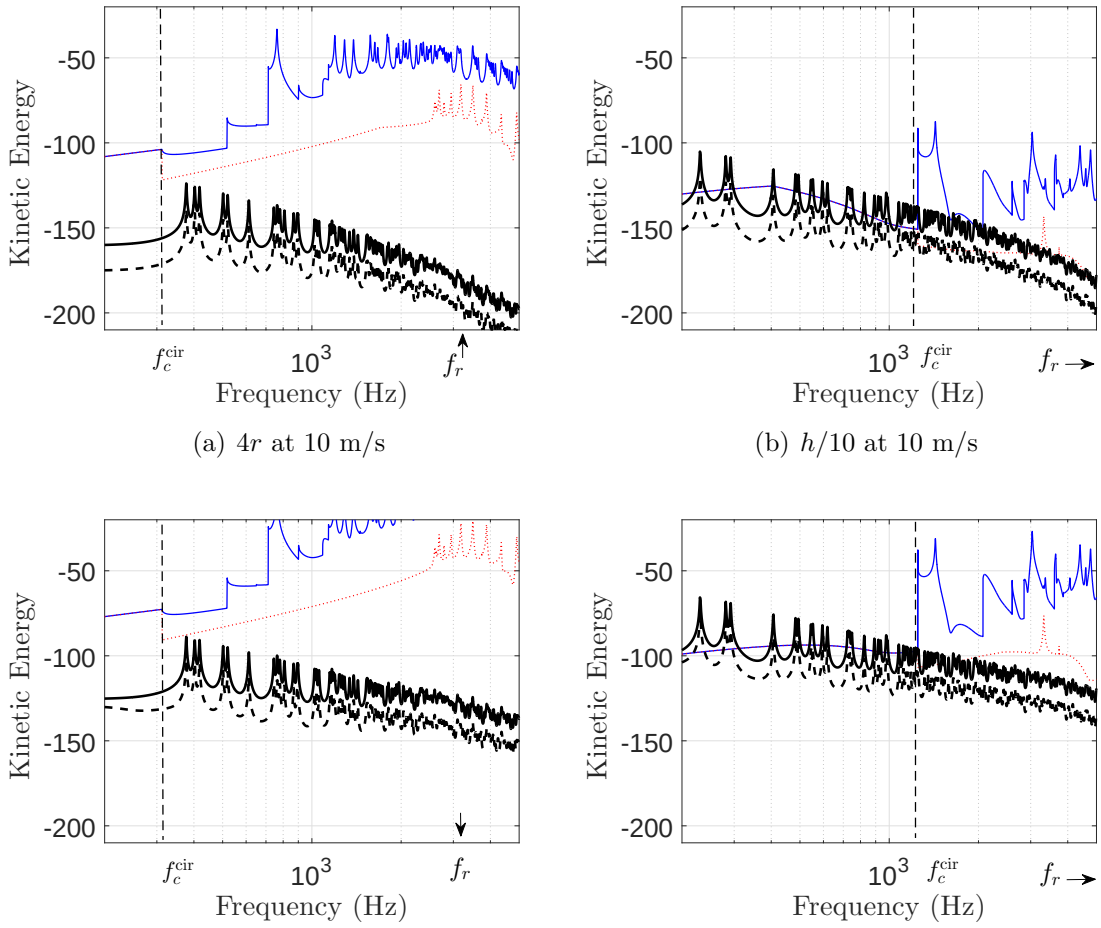

(a) $4r$ at 10 m/s

(b) $h/10$ at 10 m/s

(c) $4r$ at 60 m/s

(d) $h/10$ at 60 m/s

Figure 4.13: Kinetic energy for TBL and acoustic contributions for the circular duct: superposition of all acoustic duct modes (——), plane wave (·····), Corcos (——) and Corcos Modified(- - -). Increasing r by a factor 4 and decreasing h by a factor 10.

belongs to the frequency range of interest. This is confirmed in Fig. 4.13(a),(c) where several breathing modes are excited by the plane wave and clustered around the ring frequency.

4.6 Conclusion

The numerical prediction of pipe flow noise and vibration was investigated for two geometries: rectangular and cylindrical sections. The pressure loading on the structure is expressed in terms of CSD accounting for both hydrodynamic and acoustic contributions. These two contributions are expressed using (i) the Goody's model and the modified Corcos coherence function for the hydrodynamic excitation and (ii) the CSD of propagating acoustic duct modes. The acoustic energy is calculated according to scaling law introduced by Nelson and Morphey and the only knowledge of the constriction dimensions. The vibrational levels have been investigated for a straight duct with a flow constriction (i.e. a diaphragm) inserted upstream based on a 'blocked' approach using analytical modal FRFs. The analysis of the joint acceptance functions to study the transverse coupling between a section mode type n and the plane wave mode has shown that there is only a coupling with section modes type $n = 1$ or $n = 5$ for the rectangular duct case and only with section mode $n = 0$ for the cylindrical case (i.e. breathing modes). These observations can serve to explain why in a frequency range below the first duct frequency cut on f_c, the circular duct does not respond as strongly as for the rectangular case. Especially, when the modal behaviour is modified by moving the ring frequency in the low frequencies or decreasing stiffness. Above the first duct frequency cut on f_c, high order acoustic duct modes must be considered in the analysis.

Chapter 5

FLINOVIA paper

This chapter corresponds to the paper version accepted in the research book 'flow induced noise and vibration issues and aspects' (FLINOVIA). This is a follow-up to the second international workshop on flow induced noise and vibration organized in Penn State, USA, in April 2016. This chapter presents the structural response of a rectangular duct due to fluctuating wall pressure induced by turbulent flows. The two scenarios with or without singularity are investigated and confronted to measurements. In the vicinity of an obstacle placed in the duct, the 'near-field' is associated with strongly turbulent flow. Therefore, the wall pressure fluctuations (including its acoustic part) can no more be analytically described and full computational aeroacoustic simulations are required. The CPSD is calculated using CFD and aeroacoustic analogies to tackle complex and no homogeneous flow in the vicinity of a diaphragm. This hybrid approach allows to separate the acoustic and hydrodynamic contributions and study their influence separately on the structural response.

ERRATUM! the considered centerline line velocity without obstacle is $U_0 = 20$ m/s

Determination of the acoustic and hydrodynamic contributions to the vibrational response of an air-conveying rectangular duct

Florian Hugues, Emmanuel Perrey-Debain, Nicolas Dauchez, and Nicolas Papaxanthos

Sorbonne Université, Université de Technologie de Compiègne, Laboratoire Roberval UMR 7337
BP 20529, 60205 Compiègne Cedex, France
e-mail: florian.hugues@utc.fr, emmanuel.perrey-debain@utc.fr, nicolas.dauchez@utc.fr, nicolas.papaxanthos@utc.fr

Abstract. This paper focuses on the vibratory response of a rectangular duct of finite length excited by an internal turbulent flow. The wall pressure distribution is decomposed into an hydrodynamic and acoustic contribution. Two configurations are investigated: (i) a straight duct with no singularity, duct acoustic modes are excited by the TBL and (ii) a straight duct with a diaphragm inserted upstream generating a localized acoustic source. The acoustic contribution is either measured via cross-spectra based methods or calculated using Computational Fluid Dynamics and aeroacoustic analogies. Semi-analytical predictions are compared with experimental results. It is concluded that in both scenarios, the acoustic contribution is largely dominant.

Keywords: internal turbulent flow, vibroacoustic response, numerical methods

1 Introduction and problem statement

Gas transport ductwork in industrial plants or air conditioning networks can be subject to vibrations induced by the internal flow. Although most of the fluid conveying ducts are cylindrical, specific applications require the use of rectangular ducts. This is the case of ventilation and air conditioning systems in buildings for space saving, or in industrial applications requiring large duct sections for gas transportation. For instance, gas treatment centers used in the aluminum industry require such rectangular ducts due to manufacturing constraint. These ducts which convey gases at low speed flow condition, can be the subject to high levels of vibration induced by the flow acting on the internal faces of the duct. The prediction of such flow-induced vibrations is therefore essential in order to optimize the geometry and characteristics of the duct according to the vibration levels and mechanical fatigue objectives. While many studies have been published on the vibrations of cylindrical pipes excited by fluid flow, much less is known about rectangularly-shaped ducts.

The problem statement is showed Fig. 1. In a fully developed turbulent straight pipe flow with no discontinuity or pipe fittings, the vibration of the pipe wall are due to random fluctuating pressures along the inside wall of the pipe. In general, the hydrodynamic turbulent boundary layer (TBL) excitation is considered as responsible for the vibrations of the structure [1]. As a random stochastic source, the wall pressure fluctuation is generally defined via its cross-spectral density (CSD). Various semi-empirical models have been developed since the 60s and we can cite the well-known Corcos model [2] which is probably the most popular. However, the acoustical contribution produced by the turbulent flow is less understood and little data is available in the literature. Boundary layer pressure fluctuations are distributed over the entire surface of the duct and acoustic waves within the TBL flow excite acoustic duct modes, which in turn excite the duct walls [3]. In the present work, it is shown that the acoustic field is well described in terms of duct modes that corresponds to the primary excitation source of the structure.

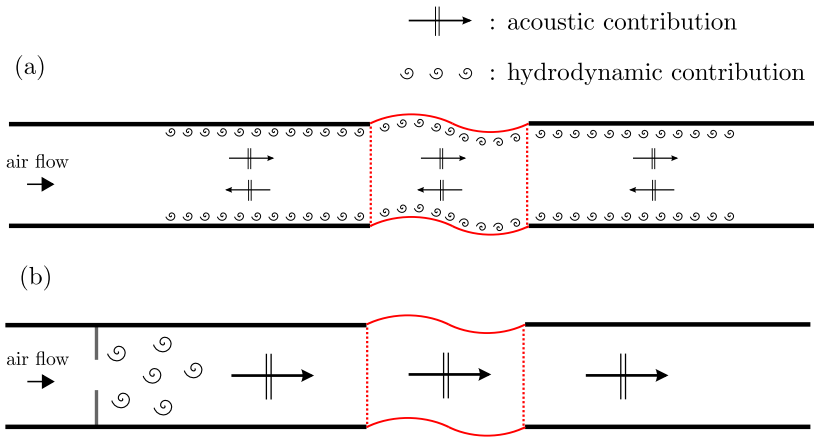

Fig. 1. Problem statement: two scenarios are investigated. (a) There is no singularity and the vibrating structure is subject to both TBL excitation and acoustic waves. (b) There is a flow constriction which generates flow disturbances in the vicinity of the singularity as well as acoustic waves radiating from the obstacle.

The situation is quite different with an internal flow disturbance in the duct due to a singularity such as a bend, a junction or a flow constriction as shown Fig. 1(b). The flow/obstacle interaction generates internal sound waves which propagate through the piping system. The origin of the sound is relatively well identified and localised. In many instances, the broadband nature of the source generation correponds to a dipole source due to the drag force fluctuations on the obstacle [4]. The additional propagating sound waves are then superimposed on the hydrodynamic TBL fluctuations. Furthermore, these sound sources are

likely to dominate above a certain distance from the discontinuity. Reference [5] offers an overview of the effects of flow disturbances on pipeline noise.

The purpose of this paper is to quantify the TBL and acoustic contributions to rectangular duct vibrations. The TBL excitation comprises an aerodynamic part based on the semi-empirical model of Corcos and an acoustical contribution described in terms of duct acoustic modes.The quantities of interest are the point auto-spectrum of the TBL and the amplitudes of acoustic waves. They are either measured or computed using aeroacoustics simulations.

The paper is organized as follows: the theoretical ingredients, including the vibration model for the structure as well as the hydrodynamic and acoustic excitations, are briefly presented in Section 2. The measurement and the numerical computation of both components of the pressure is presented in Sections 3 and 4. In Section 5, experimental results are compared with numerical predictions.

2 Modelling the vibrational response of a rectangular duct due to turbulent and acoustic excitation

The vibrational response is given for a $0.2\times0.1\times0.5$ m^3 duct made of 3 mm steel plates excited by 20 m/s or 30 m/s flows as shown Fig. 2. To facilitate the geometrical coordinate system, curvilinear abscissa s is used and the coordinate system becomes $\mathbf{s} = (s, z)$. The general bending solution w^i for each plate $i = 1 \dots 4$ can be expressed as a sum of shape functions ϕ^i_{mn} as

$$\phi^i_{mn}(s,z) = \underbrace{\left[A^i_m \sin(\alpha_2 s) + B^i_m \cos(\alpha_2 s) + C^i_m \sinh(\alpha_1 s) + D^i_m \cosh(\alpha_1 s)\right]}_{\varphi^i_m(s)} \sin\left(\frac{n\pi z}{L_z}\right), \tag{1}$$

with $\alpha_1 = \sqrt{\beta^2 + (n\pi/L_z)^2}$, $\alpha_2 = \sqrt{\beta^2 - (n\pi/L_z)^2}$ and $\beta^4 = \omega^2\rho h/D$. $D = Eh^3/12(1-\nu^2)$ is the bending stiffness of the plate, h the thickness and ω the angular frequency. The shape of the plate i along the s direction is defined as $\varphi^i_m(s)$. For each mode n, the value of coefficients A_m, B_m, C_m and D_m is determined by writing the zero displacement conditions along the coupled edges and the continuity of the rotation and bending momentum. The reader is referred to [6] for more details.

Fig. 3 shows global mode shapes computed analytically: the first index stands for the type of section mode and the second index corresponds to the number of half-periods along the z axis.

The frequency response function (FRF) H defining the steady state harmonic response of the duct at point $\mathbf{r}_1$ excited by a point force located at $\mathbf{s}_1$ writes

$$H(\mathbf{r}_1, \mathbf{s}_1, \omega) = \sum_{m,n} \frac{\phi_{mn}(\mathbf{r_1})\phi_{mn}(\mathbf{s_1})}{M_{mn} Z_{mn}}, \tag{2}$$

where $S = 2L_z(L_x + L_y)$ is the duct surface and for a given mode mn, $M_{mn} = \int_S \rho h \phi^2_{mn}\, \mathrm{d}\mathbf{s}$ is the generalized mass. The dynamic mechanical impedance is given

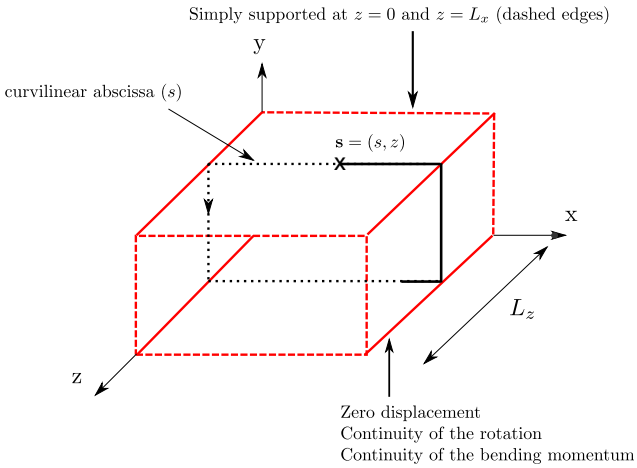

Fig. 2. The duct model

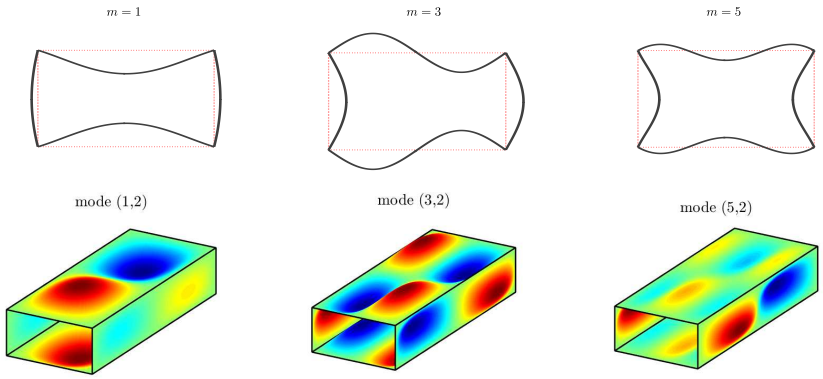

Fig. 3. Section mode shapes φ_m ($n = 1$) and 3D illustration of some global modes of the duct ϕ_{mn}.

by

$$Z_{mn}(\omega) = \omega_{mn}^2 - \omega^2 + 2\mathrm{i}\xi_{mn}\omega_{mn}\omega, \tag{3}$$

with ω_{mn} and ξ_{mn} the natural frequency and modal damping of mode (m, n). In this study, FRF are computed analytically (model in vacuum). The natural frequency and modal damping are reassessed from experimental data. The calculation of the vibrational response of the structure is based on random analysis techniques that takes into account the stochastic turbulent wall pressure distribution. The quantity of interest is the cross power spectral density of the

resulting vibration between points $\mathbf{r}_1$ and $\mathbf{r}_2$ located on the duct defined as

$$S_{ww}(\mathbf{r}_1, \mathbf{r}_2, \omega) = \int_S \int_S H^*(\mathbf{r}_1, \mathbf{s}_1, \omega) S_{pp}(\mathbf{s}_1, \mathbf{s}_2, \omega) H(\mathbf{r}_2, \mathbf{s}_2, \omega) \, \mathrm{d}\mathbf{s}_1 \, \mathrm{d}\mathbf{s}_2, \tag{4}$$

where H corresponds to the frequency response function (FRF) of the structure defined in Eq.(2) and S_{pp} the cross-spectral density (CSD) of the stochastic distributed excitation. This formula can be simplified by considering the modal decomposition response of the plate and by neglecting cross terms. The auto-spectrum is expressed when $\mathbf{r} = \mathbf{r}_1 = \mathbf{r}_2$ as

$$S_{ww}(\mathbf{r}, \omega) = \sum_{mn} \left(\frac{\phi_{mn}(\mathbf{r})}{M_{mn}|Z_{mn}|} \right)^2 \times \overbrace{\int_S \int_S \phi_{mn}(\mathbf{s}_1) S_{pp}(\mathbf{s}_1, \mathbf{s}_2, \omega) \phi_{mn}(\mathbf{s}_2) \, \mathrm{d}\mathbf{s}_1 \, \mathrm{d}\mathbf{s}_2}^{I_{mn}(\omega)}. \tag{5}$$

Finally, the quadratic acceleration of the duct:

$$\overline{S_{uu}}(\omega) = \frac{\omega^4}{S} \int_S S_{ww}(\mathbf{r}, \omega) \, \mathrm{d}\mathbf{r}, \tag{6}$$

allows us to quantify the global response of the structure.

The CSD of the wall pressure distribution can be decomposed into an hydrodynamic and acoustic contribution as follows

$$S_{pp}(\mathbf{s}_1, \mathbf{s}_2, \omega) = S^h_{pp}(\mathbf{s}_1, \mathbf{s}_2, \omega) + S^{ac}_{pp}(\mathbf{s}_1, \mathbf{s}_2, \omega). \tag{7}$$

The hydrodynamic contribution can be represented by the Corcos model. Because the Corcos model is known to overestimate the levels in the subconvective domain, a modified Corcos model proposed in [7] (see also [8]), which better estimates low-wavenumber excitation is also considered in this work so we take

$$S^h_{pp}(\mathbf{s}_1, \mathbf{s}_2, \omega) = \Phi_{pp}(\omega)(1 + \alpha\gamma_z\omega|\xi_z|/U_c) e^{-\gamma_s\omega|\xi_s|/U_c} e^{-\gamma_z\omega|\xi_z|/U_c} e^{-\mathrm{i}\omega\xi_z/U_c}. \tag{8}$$

If $\alpha = 0$, it corresponds to the original Corcos model and if $\alpha = 1$ to the modified Corcos. The coefficient U_c defines the TBL velocity and is expressed as a fraction of the flow speed at the center of the duct U_0 and this is set to $U_c/U_0 = 0.85$. Corcos parameters γ_z and γ_s are related to the axial and lateral correlation lengths. The Corcos model or the modified one may be easily transformed into wavenumber space and are compared to the wavenumber transform of a plate bending mode for the simply supported case (at modal wavenumber $k_n = n\pi/L_z$, where n is the number of half-periods along the z axis and L_z the plate dimension). This is shown Fig. 4 following a similar analysis presented in [9]. In the present study the frequency of interest ranges from 200 Hz to 1300 Hz and the flow speed is relatively low (30 m/s max) so the convective wavenumber remains always much higher than structural wavenumbers (note that this is not necessarily true for acoustic wavenumbers).

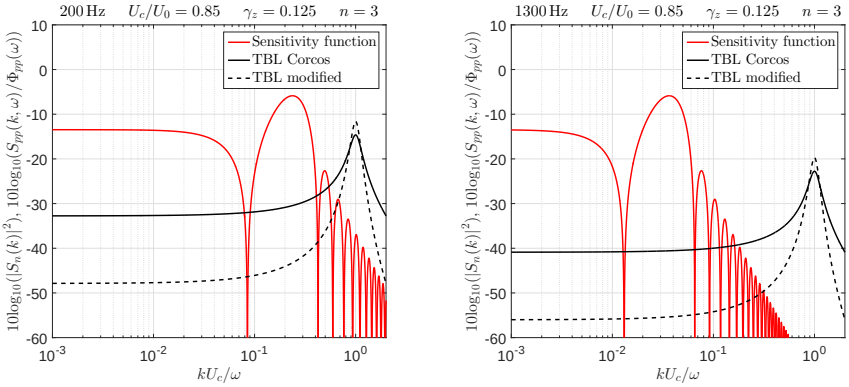

Fig. 4. Coupling of TBL wall pressure cross spectrum models and the wavenumber transform of a flexural plate mode (wavenumber sensitivity function) (a) at 200 Hz (b) 1300 Hz.

The acoustic contribution is described as a series of propagating duct acoustic mode. The contribution of the pq^{th} acoustic mode on the cross power spectral density is obtained in the manner of [10] as

$$S_{pp}^{ac}(\mathbf{s}_1, \mathbf{s}_2, \omega) = \sum_{pq} \underbrace{\left|C_{pq}^{\pm}\right|^2 \psi_{pq}(s_1)\psi_{pq}(s_2) \exp\left(\mathrm{i}k_{pq}^{\pm}(z_1 - z_2)\right)}_{S_{pq}^{ac\pm}(\mathbf{s_1},\mathbf{s_2},\omega)}, \tag{9}$$

where $C_{pq}^{\pm}$ stands for the amplitude of the downstream (+) and upstream (-) propagating mode. Here acoustic modes are deliberately not normalized so the quantity $|C_{pq}^{\pm}|^2$ can be regarded as the auto-power spectrum for the acoustic pressure on the duct wall. To simplify the analysis, the flow is assumed uniform and we neglect damping. The axial wavenumbers $k_{pq}^{\pm}$ have the well-known expression (here $k = \omega/c$):

$$k_{pq}^{\pm} = \frac{kM \pm \sqrt{k^2 - (1-M^2)\left(\left(\frac{p\pi}{L_x}\right)^2 + \left(\frac{q\pi}{L_y}\right)^2\right)}}{1-M^2}, \tag{10}$$

where M is the Mach number. The condition for an acoustic mode to propagate is that the wavenumber $k_{pq}^{\pm}$ must be real. Otherwise the wave will decay exponentially and is known as an evanescent wave. The frequency at which a mode (p, q) begins to propagate is known as the cut-off frequency of the mode. Note that the evanescent waves are neglected in our model. In all cases, the integration of Eq. (4) is carried out analytically.

3 Experimental determination of hydrodynamic and acoustic components

In this section, we present the experimental methods to determine the wall pressure distribution $\Phi_{pp}(\omega)$ and the acoustic modal amplitudes $C_{pq}^{\pm}$.

The experiments have been performed on a test bench, as shown in Fig. 5(a), designed for the multimodal characterization of the acoustic properties of obstacles in the presence of a low Mach number flow. The duct facility is a rigid rectangular duct of 0.2 m x 0.1 m section with an anechoic termination at both ends. It is equipped with a radial fan able to generate an air flow up to 30 m/s. The tested part of the duct is made of four 0.5 m long welded steel plates of 3 mm thickness and is inserted in the test section. The test bench is instrumented

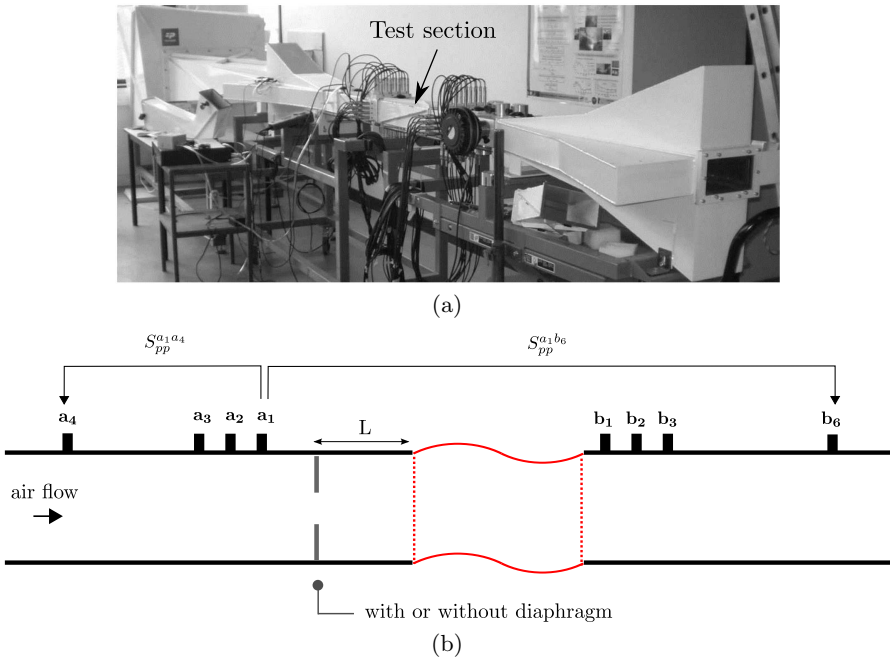

Fig. 5. Overview of the experimental set-up.

with 8 sets of 12 microphones mounted on the wall of the duct. Each set, named $\mathbf{a_4}, \mathbf{a_3}, \mathbf{a_2}, \mathbf{a_1}$ located upstream and $\mathbf{b_1}, \mathbf{b_2}, \mathbf{b_3}, \mathbf{b_6}$ located downstream the test section (as indicated in Fig. 5(b)) corresponds to a given position (in z) along the duct axis. The duct response is measured using two accelerometers, one of them being used as a reference, the other one being successively positioned on the measurement grid in order to get the average quadratic acceleration of the duct. The measurement grid is defined on the duct with a regular interval of 2.5 cm

along the cross-flow direction and 5 cm along the flow direction. The point pressure auto-spectrum $\Phi_{pp}(\omega)$ is determined experimentally using upstream as well as downstream microphones sections, $\mathbf{a_3}, \mathbf{a_2}, \mathbf{a_1}$ and $\mathbf{b_1}, \mathbf{b_2}, \mathbf{b_3}$ respectively.

Two methods are used for determining the acoustic modal amplitude $\left|C_{pq}^{\pm}\right|$ and are presented below.

3.1 Cross-spectra based method : case with no singularity

The duct is straight with no singularity, so that propagating acoustic modes are generated by the TBL itself all along the duct. The estimation of the acoustic component is performed by minimizing an overdetermined system (Eq. (11)). The input data is a set of cross-spectra between microphones at the four sections $\mathbf{a_1}, \mathbf{b_3}, \mathbf{a_4}, \mathbf{b_6}$ as illustrated in Fig. 5(b). Distances between microphones are much larger than the correlation lengths of the hydrodynamic wall pressure fluctuations so that only the acoustic part of the pressure is measured and estimated as follows

$$\begin{aligned} S_{pp}^{\Delta z}(s_i, s_j, \omega) = &\left|C_{00}^{+}\right|^2 \psi_{00}(s_i)\psi_{00}(s_j) \exp\left[\mathrm{i}k_{00}^{+}\Delta z\right] \\ &+ \left|C_{10}^{+}\right|^2 \psi_{10}(s_i)\psi_{10}(s_j) \exp\left[\mathrm{i}k_{10}^{+}\Delta z\right] + ... \end{aligned} \tag{11}$$

Results using 600 averages are shown in Fig. 6(a). The acoustic contribution is found to be 10 dB up to 20 dB lower than the turbulent wall pressure fluctuations. Note that upstream and downstream propagating modes are not distinguished as they have similar amplitudes.

3.2 2N-port method : case with a flow constriction

In the vicinity of a pipeline singularity such as a flow constriction, acoustic waves are generated due to the drag force fluctuations. In this context, acoustic measurements can be performed on the basis of the so-called Multiport method [11, 12]. The acoustic scattering matrix of the obstructed duct and the impedance of the surrounding environment are first identified by measuring the acoustic response to given external excitations. Then, the aeroacoustic noise produced by the interaction of the obstacle and the flow is extracted. The multiport formulation can be written in a compact form

$$\mathbf{p}^{out} = \mathbf{S}\mathbf{p}^{in} + \mathbf{p}^{s} \tag{12}$$

where $\mathbf{S}$ is the scattering matrix, vector $\mathbf{p}^{out}$ stands for the acoustic waves radiating away and $\mathbf{p}^{s}$ is the source vector containing the modal coefficients.

The quantity of interest is the source cross-spectrum matrix defined as

$$\mathbf{G^s} = E[\mathbf{p}^{s}(\mathbf{p}^{s})^{c}] \tag{13}$$

where the superscript c denotes transpose and complex conjugate. We obtain a $[2N \times 2N]$ matrix, where N is the number of acoustic duct modes considered,

and the diagonal terms $\langle |C_{00}^-|^2 ... |C_{NN}^-|^2, |C_{00}^+|^2 ... |C_{NN}^+|^2 \rangle$ represent the modal auto-spectra respectively at the section $\mathbf{a_1}(-)$ and $\mathbf{b_1}(+)$.

Results are shown in Fig. 6(b). We notice the emergence of the first tranverse acoustic mode above the cut-off frequency at 853 Hz (below that frequency, only the plane mode propagates).

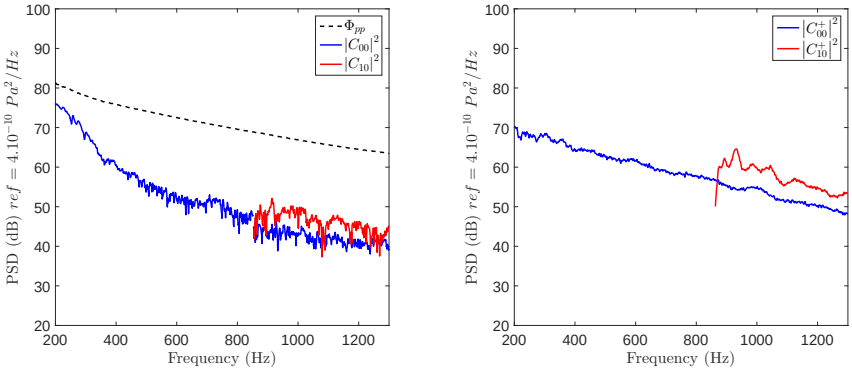

(a) (b)

Fig. 6. Estimation of the propagating duct acoustic modes. (a) In the case of a straight duct with no singularity, the flow speed is 30 m/s. (b) With a flow constriction, the flow speed is 6.5 m/s (measured upstream the constriction).

4 Numerical determination of the hydrodynamic and acoustic components

In this section, we present a method to determine the two components, on the basis of a Computational Fluid Dynamics approach coupled with an aeroacoustic analogy.

At low Mach number and for sufficiently high Reynolds numbers, the Large Eddy Simulation (LES) of an unsteady incompressible flow coupled with an acoustic analogy is classicaly used as it should deliver reasonably accurate predictions for both the hydrodynamic and acoustic pressure [13]. Let us recall that the hydrodynamic pressure p_h which is provided by the incompressible-flow simulation (Star-CCM+ is used here) must be solution to the Poisson's equation:

$$\Delta p_h = q \tag{14}$$

where q is the source term containing mean and fluctuating velocity terms (all physical quantities are interpreted in the frequency domain). Now, in order to

take into account compressibility effects, Lighthill's aeroacoustic analogy leads to a somewhat similar equation of the form

$$(\Delta + k^2)p = q \tag{15}$$

where k is the acoustic wavenumber and p can now be regarded as the true pressure. By combining Eq. (14) and Eq. (15) the acoustic pressure defined as the difference $p_a = p - p_h$ can be shown to be the solution to the following boundary integral equation [13]

$$p_a = \int_{\partial V} \left(p_h \frac{\partial \left(G - G_0\right)}{\partial n} + p_a \frac{\partial G}{\partial n} \right) \mathrm{d}S + \int_{S_\pm} \left(G_0 \frac{\partial p_h}{\partial n} - GT(p_h) \right) \mathrm{d}S \tag{16}$$

where the volume integral over the CFD domain, call it V, has been neglected [13]. G_0 is the static Green's function, G is the classical free-field Green's function and $T(p_h)$ is the operator associated with the anechoic condition at both ends of the duct (the sign $-$ and $+$ corresponds to left and right end respectively).

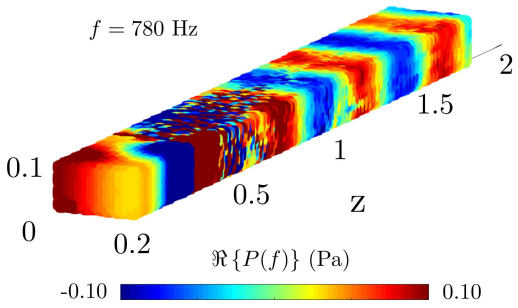

Fig. 7. Computed pressure distribution in the duct.

The resolution of Eq. (16) requires the storage of the incompressible-flow pressure p_h on the surface of the domain and its derivative $\partial_n p_h$ on the inlet and outlet. The mesh used for the CFD comprises 9 million cells. The mesh is built using 4 resolution levels ranging from 0.5 mm to 4 mm. The smallest cells are located in the vicinity of the diaphragm edges in order to capture correctly the physics of the shear layers. A RANS k-ϵ simulation is first performed to give an initial condition for the incompressible large eddy simulation. Inlet boundary conditions, velocity components and turbulent kinetic energy, are prescribed using realistic data provided by PIV measurement. The measured mass flow rate is 565 kg/h which corresponds to an average velocity over the duct section of 6.5 m/s. The LES is carried out with a simulated physical time of 0.32 s and a time step $\delta t = 10^{-5} s$. Due to the difference in size of acoustic and turbulent wavelengths, the requirement in terms of grid resolution is less severe for the

acoustic computation than for the CFD. The integral equation Eq. (16) is solved by collocation on a coarse mesh which is composed of around 8500 triangular surface cells of maximum dimension 2 cm, which corresponds to $\lambda/8$ at 2125 Hz. The temporal boundary data p_h and $\partial_n p_h$ are summed on the coarse mesh centroids using a conservative mapping from Star-CCM+. The Fourier analysis and the resolution of Eq. (16) is carried out on Matlab. The physical time of 0.32 s is divided into eight segments of 0.05 s each with 1/4 overlapping. A window function is applied on each segment. A typical results is shown in Fig. 7 where small scale wall hydrodynamic pressure fluctuations and long wavelength acoustic waves can be identified.

In order to compute the structural loads, two quantities of interest are considered: (i) the CSD of the wall pressure distribution, either of hydrodynamic or acoustic nature

$$S_{pp}^{h,\mathrm{CFD}}(\mathbf{s}_1,\mathbf{s}_2,\omega) = E\left[p_h p_h^*\right] \quad \text{and} \quad S_{pp}^{ac,\mathrm{CFD}}(\mathbf{s}_1,\mathbf{s}_2,\omega) = E\left[p_a p_a^*\right]. \tag{17}$$

and (ii) the duct acoustic modes radiating away from the obstacle, defined as

$$C_{pq}^{+} = \int_{S_+} p_a \psi_{pq} \mathrm{d}S. \tag{18}$$

Fig. 8 shows reasonably good agreement between measured data using the $2N$-port method and numerical predictions.

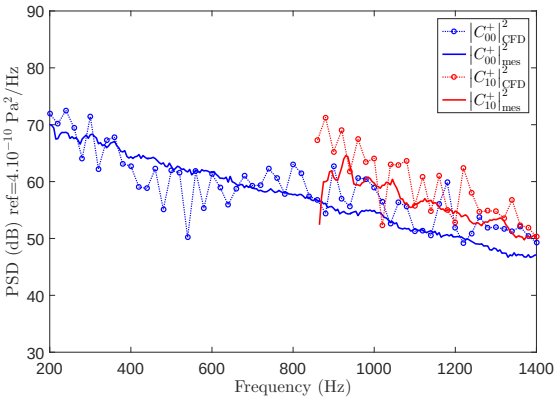

Fig. 8. Computed vs measured duct acoustic mode amplitudes radiating away from the obstacle.

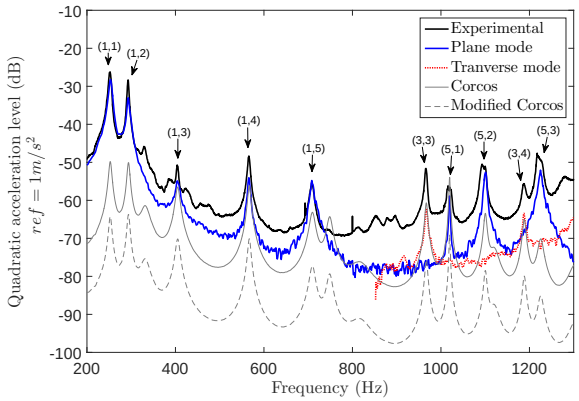

Fig. 9. Quadratic acceleration for each response contribution at 30 m/s.

5 Results and discussion

5.1 Straight duct with no obstacle

The global response of the duct, including both the aerodynamic and acoustic contributions, can now be estimated via

$$\overline{S_{uu}} = \overline{S^h_{uu}} + \overline{S^{ac}_{uu}} \tag{19}$$

where the hydrodynamic component is calculated via Corcos model. Here, Corcos coefficients are set to $\gamma_s = 1$ and $\gamma_z = 1/8$. Fig. 9 shows the quadratic acceleration due to each contribution, by using up to 20 structural modes. Note that as opposed to the modified Corcos model, the original Corcos model is known to overestimate low-wavenumber TBL loading showing 10-15 dB differences. Similar results can be found in [14]. In both cases, however, the hydrodynamic contribution remains marginal and the acoustic excitation clearly dominates.

Note that plane wave mode can only be coupled to the structural modes with section mode $m = 1$ or $m = 5$ whereas the first transverse acoustic mode can only be coupled to the section mode $m = 3$. Finally, reasonably good agreements with experimental results are found once all contributions are summed up.

5.2 Straight duct with a flow constriction

5.2.1 Direct approach The vibrating structure is situated at $L = 40$ cm downstream from the discontinuity. The vibrational response is estimated using a direct approach based on a regular discretization of the duct surface with triangular cells of average dimension of 2 cm. The computation of the quantity

$I_{mn}(\omega)$ defined in Eq. (5) is estimated as follows

$$I_{mn}(\omega) \approx \sum_{i}^{N_p} \sum_{j}^{N_p} \phi_{mn}(\mathbf{s}_i) S_{pp}^{h/ac,\mathrm{CFD}}(\mathbf{s}_i, \mathbf{s}_j, \omega) \phi_{mn}(\mathbf{s}_j)\, \Delta_i\, \Delta_j \tag{20}$$

where N_p is the number of cells and Δ_i is the elementary surface of the triangular cells. Predicted quadratic acceleration is compared to measured data in Fig. 10(a). The CSD matrix $S_{pp}^{h/ac,\mathrm{CFD}}$ is computed using either the hydrodynamic pressure p_h provided by LES or the acoustic pressure p_a computed with the acoustic analogy. Once again the acoustic contribution clearly dominates and the overall energy is respected between predicted and measured vibrations using the acoustic loads alone. Note that calculations were performed using a frequency step $\Delta f = 20$ Hz corresponding to about 0.3 s of CFD simulated physical time.

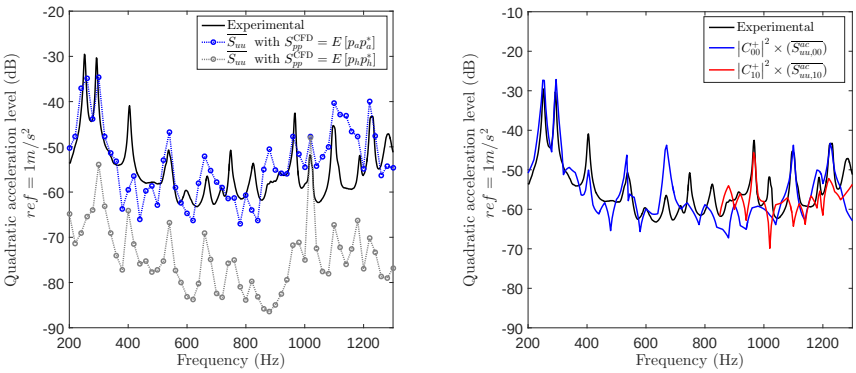

Fig. 10. Quadratic acceleration using (a) the direct approach and (b) the modal approach.

5.2.2 Modal approach Since the acoustic part is dominant, it is fair to assume that only acoustic modes propagating downstream are considered as the primary source of excitation. In this case, we have simply

$$I_{mn}(\omega) = \left|C_{pq}^{+}\right|_{\mathrm{CFD}}^{2} j_{mnpq}^{2\pm}(\omega) \tag{21}$$

where $j_{mnpq}^{2\pm}(\omega)$ is the joint acceptance function describing the coupling between a structural mode (m,n) and a duct acoustic mode (p,q). Note that it is computed analytically. The modal approach permits to save computation time as

the storage of the CSD matrix requires high memory capacity. Fig. 10(b) shows the quadratic acceleration due to each contribution and good agreements can be observed. Here, a linear interpolation (in frequency) is applied to $\left|C_{00}^{+}\right|_{\mathrm{CFD}}^{2}$ and $\left|C_{10}^{+}\right|_{\mathrm{CFD}}^{2}$ coefficients. This allows to refine the frequency analysis so as peaks at the resonance frequencies of the structure are better predicted.

6 Conclusion

The vibrational response of a rectangular duct of finite length excited by an internal turbulent flow was investigated both numerically and experimentally. The pressure loading on the structure expressed in terms of CSD accounts for both hydrodynamic and acoustic contributions. A CFD analysis coupled with an acoustic analogy is used to compute these two contributions and assess their relative influence on the vibrational response. Amplitudes of acoustic waves are measured using either a cross-spectra based method or the $2N$-port method. The vibrational levels have been investigated for two scenarios (i) a straight duct with no obstacle and (ii) with a flow constriction (i.e. a diaphragm) inserted upstream. In both cases, the acoustic pressure field has been shown to have a great impact on the vibrational response. Measured vibrational levels are found to be in good agreement with our numerical simulations.

References

[1] Durant C, Robert G, Filippi P, Mattei PO (2000) Vibroacoustic response of a thin cylindrical shell excited by a turbulent internal flow: comparison between numerical prediction and experimentation. J Sound Vib 229(5):1115–1155

[2] Corcos GM (1963) Resolution of Pressure in Turbulence. J Acoust Soc Am 35(2):192

[3] Hwang S, Moon Y (2017) On the computation of low-subsonic turbulent pipe flow noise with a hybrid LES/LPCE method. Int J Aeronaut Sp Sci 18(1)

[4] Nelson P, Morfey C (1981) Aerodynamic sound production in low speed flow ducts. J Sound Vib 79(2):263–289

[5] Norton MP, Karczub DG (2003) Fundamentals of Noise and Vibration Analysis for Engineers. Cambridge University Press

[6] David A, Hugues F, Dauchez N, Perrey-Debain E (2017) Vibrational response of a rectangular duct of finite length excited by a turbulent internal flow. J Sound Vib (in Press)

[7] Hwang YF, Bonness WK, Hambric SA (2003) On modeling structural excitations by low speed turbulent boundary layer flows. Tech. rep., ARL/Penn State Technical Report 03-008

[8] Caiazzo A, DAmico R, Desmet W (2016) A Generalized Corcos model for modelling turbulent boundary layer wall pressure fluctuations. J Sound Vib 372:192–210

[9] Hambric SA, Hwang YF, Bonness WK (2004) Vibrations of plates with clamped and free edges excited by low-speed turbulent boundary layer flow. J Fluids Struct 19(1):93–110

[10] Norton MP (1979) The effects of internal flow disturbances on the vibration response of and the acoustic radiation from pipes. PhD thesis, University of Adelaide

[11] Lavrentjev J, Åbom M, Bodén H (1995) A measurement method for determining the source data of acoustic two-port sources. J Sound Vib 183(3):517–531

[12] Bennouna S, Naji S, Cheriaux O, Moreau S, Ouedraogo B, Ville JM (2015) Aeroacoustic Prediction Methods of Automotive HVAC Noise. In: SAE Tech. Pap., SAE International

[13] Papaxanthos N, Perrey-Debain E, Bennouna S, Ouedraogo B, Moreau S, Ville JM (2017) Pressure-based integral formulations of LighthillCurle's analogy for internal aeroacoustics at low Mach numbers. J Sound Vib 393:176–186

[14] Hambric S, Hwang YF, States U, America O (2000) Vibrations of Flat Plates Excited By Low Mach Number Turbulent Boundary Layers. In: 29th Int. Congr. Exhib. Noise Control Eng. 27-30 August 2000, Nice, Fr., August, pp 1–6

Additional results

In this section complementary information to the published work presented in this chapter are shown. The computed sound power level L_w and acoustic duct modes amplitudes $\left|C^+_{pq}(\omega)\right|^2$ using the Kårekull model (presented in Chapter 2 and 4) are compared to the published results of the Flinovia paper.

Fig. 5.1(a) shows the computed and measured sound power level L_w due to a diaphragm inserted in the duct at 6.5 m/s. It is reminded that two regimes are dissociated in the Kårekull model: one corresponds to a plane wave propagation until the first duct frequency cut on (continuous line) and the other is associated to high order acoustic modes propagating in the duct (dashed line). The global level is respected between the measurement and the computed power level using (i) CFD and aeroacoustic analogy and (ii) the Kårekull model. Some discrepancies are observed near the duct frequency cut on. This can be reduced using a longer CFD calculation time to achieve a converged spectrum. Note that the computed power obtained from CFD is taken from only the outlet surface of the duct. It is reminded that additional information about the CFD procedure and the adopted aeroacoustic analogy can be found in [166]. Fig. 5.1(b) shows the corresponding acoustic duct modes amplitudes for the plane wave and the first transverse mode. The amplitudes are obtained using Eq.(4.13) of Chapter 4. Good agreements between computed and measured data are observed.

Fig. 5.2 shows additional measured quadratic acceleration levels at different flow speeds. The measured mass flow rate is 565, 648, and 734 kg/h which corresponds to an average velocity over the duct section of 6.5, 7.5 and 8.5 m/s respectively. Two cases are distinguished: Fig. 5.2(a) shows the quadratic acceleration level of the vibrating structure situated at $L = 10$ cm and (b) at $L = 40$ cm downstream from the diaphragm. For the case $L = 40$ cm, the global measured quadratic acceleration level is around 3 dB higher than the case $L = 10$ cm. Some shifts can be observed regarding the damped resonant frequencies. It is likely due to disassembling and reassembling the test section between measurement periods which introduced slight structural differences. However, the effect of the flow can be observed between 400 and 950 Hz regarding the peak amplitudes and the associated damping.

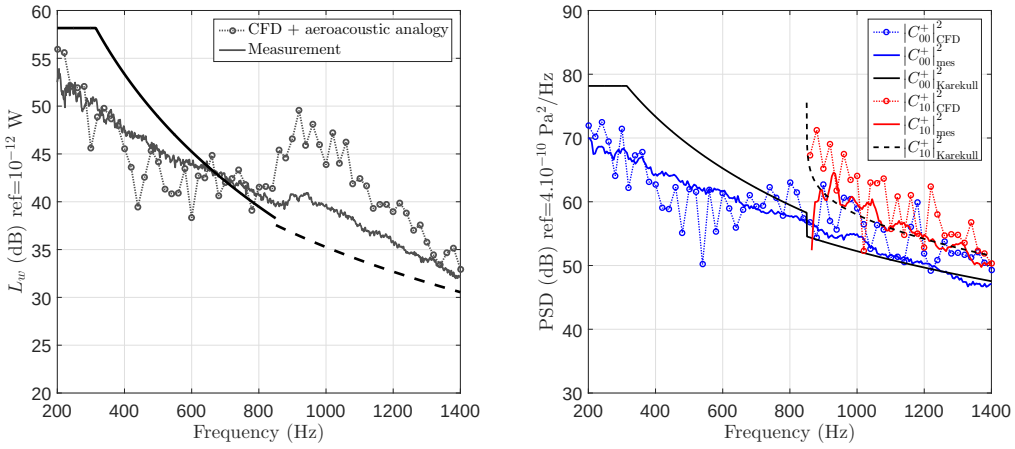

(a) (b)

Figure 5.1: Comparison of the Kårekull model to the published results of the Flinovia paper. (a) Kårekull sound power prediction for the plane wave (—) and multimodal propagation (---). (b) Measured acoustic duct mode amplitudes compared to predictions.

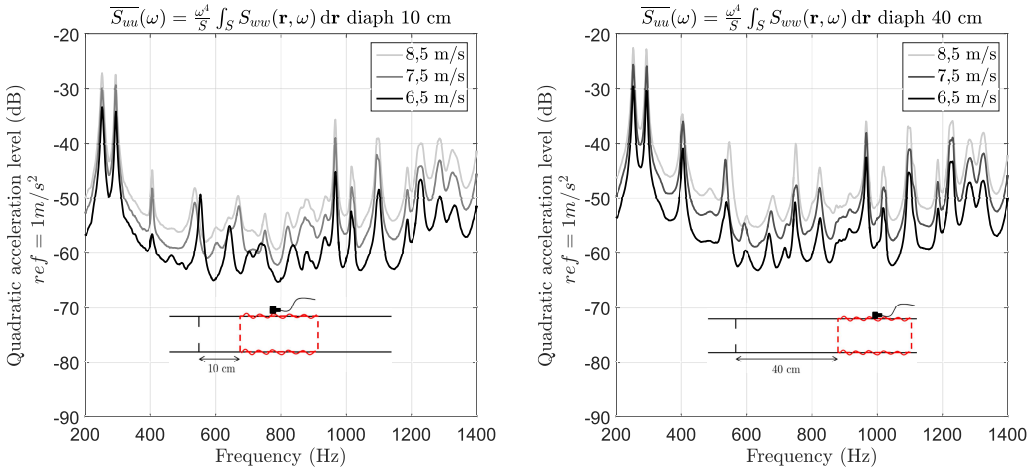

(a) (b)

Figure 5.2: Additional measured quadratic accelerations of the vibrating structure situated at: (a) $L = 10$ cm (b) $L = 40$ cm.

Conclusion and perspectives

As stated in the introduction, the purpose of this research is to develop a framework for studying and modelling pipe flow noise and vibration which links CFD, analytical and empirical models to efficient random analysis techniques. The pipe rig at the Roberval research laboratory was used to perform aero-acoustic test campaign through 2 scenarios: (i) a straight duct with no singularity and (ii) a straight duct with a diaphragm inserted upstream generating a localized acoustic source. The relative contributions of turbulent and acoustic wall pressure fluctuations has been investigated through cross-spectra based measurement methods. The collected data was used as a basis for discussing and suggesting improvements to existing CPSD empirical models in a context of internal flow with or not disturbances. Analytical models of simply supported ducts with circular and rectangular cross-sections have been developed to analyze the coupling between the duct section and the excitation. Finally, full and hybrid numerical analysis have been performed and confronted with measurements for the two scenarios.

Summary of results

The measurement campaign has allowed to estimate the acoustic and turbulent energy for the two scenarios at low Mach number flows. Although the pipe rig was originally design for acoustic measurements, attempts were made to characterize the wall pressure fluctuations beneath a turbulent boundary layer. The obtained overall dimensionless point spectrum is satisfactory in terms of shape and level, but the adopted TBL parameters are less convincing. Particular attention has to be taken on the entrance region effect and the position of the vibrating surface under study. In our case, the ratio x/D_h is too small due to facility integration issue. In addition, uncertainties remain on the nature of a TBL in 'complex' ducts here of rectangular cross-section. It is understood to a much lesser extent compared to canonical flows in plane channels and circular pipes, particularly with respect to turbulence modeling

close to the wall and corner regions. It is also difficult to create a piping system with perfectly flush joints with an interior surface uniformly smooth. These effects may alter the TBL wall pressure spectrum. Despite these difficulties, the acoustic contribution has been well extracted from the turbulent flow for the case with a singularity and compared successfully to a universal spectrum obtained from the Nelson & Morfey scaling law. Multi-modal decomposition has been performed to measure duct acoustic mode amplitudes. It has been confronted successfully to CFD predictions using aeroacoustic analogies. For the case without obstacle, the measured acoustic amplitudes was used to predict the vibrational level of a rectangular duct. Good agreement has been found suggesting that the acoustic contribution was responsible of the duct vibration. This key result has raised our interest to complete the study for cylindrical cross section since previous works has shown different conclusions, suggesting that the TBL alone was responsible of the duct response.

Appropriate duct structural models have been proposed to compute the duct vibration. Due to the high number of discretization points required to solve both flexural and turbulent wavelengths, analytical modal FRFs for simply supported geometry have been chosen to obtain reasonable computation time. Experimental modal analysis of a finite rectangular duct was confronted to an analytical model of a rectangular duct. The analytical mode shapes have shown good correlations suggesting that simple analytical modal FRFs for simply supported geometry can be used as a guide to tackle more complex geometry with complex BCs since it follows similar trends in terms of modal pattern and energy. The main sources of uncertainties in modal parameters is likely due to disassembling and reassembling the test apparatus between measurement periods which introduced slight structural differences rather than the effect of the flow. The effects of the boundary conditions and acoustic radiation have been studied using either a commercial vibro-acoustic FEM solver or from measurements performed in a *vacuo* chamber. This investigation has ensured that the weak coupling assumption is reasonable for air fluid and that internal acoustic radiation could be neglected. Simple analytical modal FRFs for simply supported geometry have also been adopted in order to facilitate numerical treatments for the calculation of the coupling between the turbulent flow and the structure.

One of the originality of this PhD is to write the forcing function on the basis of a sum of an hydrodynamic contribution provided by the Corcos's model and an acoustic part given by the coherence function of high order modes in the spirit of Norton's work. For the case of flow constriction, few research was carried out for considering high order acoustic modes in the duct structural response along with the contribution

of the hydrodynamic contribution. In this PhD, a distinction is made between the 'near-field' and the 'far-field' of the studied obstacle. Despite some uncertainties about the relative level of the TBL point spectrum in the undisturbed mean flow zone, fully developed TBL point spectra are considered with Corcos type coherence functions. Numerical prediction of pipe flow noise and vibration was investigated for two cross-sections: rectangular and circular. The acoustic energy has been calculated according to scaling laws providing realistic acoustic duct modes amplitudes based on experimental results. The spatial coupling has been investigated between the section mode shapes and the excitation through the analysis in the wavenumber space. It has suggested the use of a modified version of the original Corcos model since the latter overestimates the levels in the subconvective domain which is the zone where the duct mostly accepts the flow energy for our frequency range of interest and flow speeds. An innovative approach to represent the duct response for each contribution has been proposed. In particular, a multi modal representation have shown the importance of considering high order acoustic modes in the prediction of duct vibration. A parametric study has allowed to answer the question why TBL is often considered alone for circular pipe flow with no discontinuities.

Finally in chapter 5, in the vicinity of an obstacle placed in the duct, the 'near-field' is associated with strongly turbulent flow. Therefore, the flow forcing function was calculated using CFD and aeroacoustic analogies to tackle complex and no homogeneous flow in the vicinity of a diaphragm. An existing procedure based on Lighthill's aeroacoustic analogy has been used. The simulation method is a two-step approach assuming the decoupling of noise generation and propagation. The commercial software Star-CCM+ was used to calculate the hydrodynamic pressure associated to the incompressible flow. Results have been post-processed in Matlab to compute the acoustic pressure accounting for compressible effects. The CSD matrix associated to CFD data has been mapped on a regular grid discretized with triangular cells and assuming a constant variation on an elementary surface. Due to the difference in size of acoustic and turbulent wavelengths, precautions had to be taken in terms of grid resolution. It corresponds to the grid used for the aeroacoustic analogy computation. It has been shown that the only mere of the acoustic contribution was sufficient to compute the duct vibration in the vicinity of a diaphragm.

Key conclusions

The specific goal of this thesis was to address the relative contributions of turbulent and acoustic wall pressure fluctuations on the vibrational response of a finite duct at low Mach number. Several key conclusions were made about the prediction of pipe flow noise and vibration, and are summarized as follows:

1. The energy ratio between the acoustic and hydrodynamic parts decreases with frequency from approximately 10 %(-10 dB) to 0.1 %(-30 dB) for the case without obstacle (Chapter 2).

2. In a context of internal flow for rectangular cross-section, the wall pressure fluctuation TBL levels are uncertain due to the lack of reliable model in the subconvective region. But in any case, it was found to be negligible (Chapter 2).

3. The Lysak fit of the Chase-Howe model provides a satisfactory point spectrum in term of shape and spectral levels. The downstream distance, *ie*, the distance from the pipe entrance region to the fully developed region or the hydraulic diameter can be used as characteristic lengths for the Reynold number definition leading to uncertainties for the prediction of TBL parameters (Chapter 2 and 4).

4. It is difficult to determine the origin of the acoustic excitation for the case without singularity. Due to the non local behavior of the acoustic source, it can not be concluded that the acoustic energy is only produced by the TBL, but its contribution can not be neglected in any case for the prediction of rectangular duct vibration (Chapter 2 and 5).

5. The circular duct does not respond as strongly as for the rectangular case to acoustic excitations. Multi modal acoustic propagation must be taken into account in the flow forcing function above the first duct frequency cut on (Chapter 4).

6. Analytical modal FRFs for simply supported geometry facilitate numerical treatments for the calculation of the coupling between the turbulent flow and the structure. The effects of BCs and acoustic radiation do not alter the vibration level and the weak coupling assumption is reasonable for air fluid (Chapter 3).

Recommendations for future work

Future experiments may be implemented to quantify the TBL parameters of a rectangular duct along with the acoustic and turbulent energy by using non intrusive techniques such as Laser Doppler Velocimetry (LDV).

Additional work could be performed to develop scaling laws and scaled spectra data base for different internal flow obstacles in order to be used in a more qualitative manner to predict pipe vibration.

Furthermore, a non-modal approach such as a k-space method could be explored for computing the pipe vibration response. More advanced modeling techniques such as sub-structuring approaches which allow to couple semi-analytical models with finite element method (FEM) could also be used to include flanges or other expansion joints. This could be used as efficient tool to describe the dynamic behavior of waveguides whose cross-section can be multi-physics and may eliminate bias caused by the ideal simply-supported boundary conditions. For instance, the noise and vibration could be mitigated by optimizing the distance between flanges or by including non-periodic part with the aim of testing anti-vibration solutions.

Alternatively, a new analytical model of duct structure could be developed including in-plane longitudinal and in-plane shear waves induced at corner junctions. In the same way, the analytical shell model could be extended to higher order shear deformation theories including multilayer skins to control the vibration using smart materials. These considerations would lead to more advanced structural models which could serve to indirectly measure the internal wall pressure fluctuations features in a context of inverse problem.

Research could also be performed to evaluate the 2D wavenumber spectrum of pressure fluctuations obtained from unsteady aeroacoustic computations. 2D spatial Fourier Transform could be performed to obtain more accurate TBL features in the transition zone which overlaps the pipe entrance region to the fully developed region.

Bibliography

[1] Antoine David. *Vibration study of gas transport ductwork in the aluminium industry.* PhD thesis, Université de Technologie de Compiègne, 2016. *3 quotations pages 1, 2, et 30*

[2] Saad Bennouna. *Aeroacoustics characterization of elements and associations of automobile air ventilation systems.* PhD thesis, Université de Technologie de Compiègne, 2016. *2 quotations pages 1 et 28*

[3] Nicolas Papaxanthos. *Integral methods for the caculation of the air flow noise in ducts in the presence of fixed obstacles.* PhD thesis, Université de Technologie de Compiègne, 2016. *quoted page 1*

[4] A. David, F. Hugues, N. Dauchez, and E. Perrey-Debain. Vibrational response of a rectangular duct of finite length excited by a turbulent internal flow. *J. Sound Vib.*, 422:146–160, 2018. *2 quotations pages 2 et 108*

[5] F. Hugues, N. Dauchez, E. Perrey-Debain, and N. Papaxanthos. Determination of the Acoustic and Hydrodynamic Contributions to the Vibrational Response of an Air-Conveying Rectangular Duct. In *Flinovia—Flow Induc. Noise Vib. Issues Asp.*, pages 217–231. Springer International Publishing, 2019. *3 quotations pages 2, 31, et 109*

[6] William K. Blake. *Mechanics of flow-induced sound and vibration. volume 1, General concepts and elementary sources.* *quoted page 4*

[7] William K. Blake. *Mechanics of flow-induced sound and vibration. Volume 2, Complex flow-structure interactions.* *3 quotations pages 4, 42, et 124*

[8] M P Norton and D G Karczub. *Fundamentals of Noise and Vibration Analysis for Engineers.* Cambridge University Press, 2003. *3 quotations pages 4, 23, et 108*

[9] Stephen A. Hambric, Yun Fan Hwang, and Thomas S. Chyczewski. Noise Sources and Transmission in Piping Systems. In *Noise Control Acoust.*, volume 2002, pages 79–90. ASME, jan 2002. *quoted page 4*

[10] Stephen A. Hambric, L. Joel Peltier, John B. Fahnline, David A. Boger, and John E. Poremba. Structural and Acoustic Noise Sources Due to Turbulent Flow Through an Elbow: Formulation of Analysis Methods. In *Noise Control Acoust.*, volume 2003, pages 69–80. ASME, jan 2003. *quoted page 4*

[11] C. Durant. *Etude expérimentale de l'excitation et de la réponse vibroacoustique d'une conduite sollicitée par un écoulement interne [Experimental study of the vibroacoustic response of a thin cylindrical shell excited by a turbulent internal flow].* PhD thesis, Ecole Centrale de Lyon, 1999. *4 quotations pages 4, 7, 45, et 48*

[12] C. Durant, G. Robert, P.J.T. Filippi, and P.-O. Mattei. Vibroacoustic response of a thin cylindrical shell excited by a turbulent internal flow: comparison between numerical prediction and experimentation. *J. Sound Vib.*, 229(5):1115–1155, feb 2000. *8 quotations pages 4, 7, 15, 47, 48, 108, 113, et 133*

[13] William K Bonness. *Low wavenumber turbulent boundary layer wall pressure and shear stress measurements from vibration data on a cylinder in pipe flow.* PhD thesis, Pennsylvania State University, 2009. *quoted page 4*

[14] William K Bonness, Dean E Capone, and Stephen A Hambric. Low-wavenumber turbulent boundary layer wall-pressure measurements from vibration data on a cylinder in pipe flow. *J. Sound Vib.*, 329:4166–4180, 2010. *6 quotations pages 4, 12, 47, 108, 111, et 113*

[15] Stéphane Caro, Vincent Cotoni, Phil Shorter, and Fred Mendonça. Turbulent Surface Pressure Field in Low Speed Flow. In *Flinovia - Flow Induc. Noise Vib. Issues Asp.*, pages 91–100. Springer International Publishing, 2015. *quoted page 5*

[16] M. J. Lighthill. On sound generated aerodynamically I. General theory. *Proc. R. Soc. London. Ser. A. Math. Phys. Sci.*, 211(1107):564 LP – 587, mar 1952. *quoted page 6*

[17] M. J. Lighthill. On sound generated aerodynamically II. Turbulence as a source of sound. *Proc. R. Soc. London A Math. Phys. Eng. Sci.*, 222(1148):1–32, 1954. *pas de citations*

[18] J. E. Ffowcs-Williams and D. L. Hawkings. Sound generation by turbulence and surfaces in arbitrary motion. *Philos. Trans. R. Soc. London. Ser. A, Math. Phys. Sci.*, 264(1151):321 LP – 342, may 1969. *quoted page 6*

[19] Xavier Gloerfelt. Noise from automotive components. In *Aerodyn. noise from wall-bounded flows*, pages 9–13. jan 2009. *quoted page 6*

[20] D. G. Crighton, A. P. Dowling, J. E. Ffowcs Williams, M. Heckl, and F. G. Leppington. *Modern Methods in Analytical Acoustics*. Springer London, London, 1992. *2 quotations pages 6 et 25*

[21] Robert H Kraichnan. Diffusion by a Random Velocity Field. *Phys. Fluids*, 13(1):22–31, 1970. *quoted page 7*

[22] C Bailly, W Bechara, P Lafon, and S Candel. Jet noise predictions using a k-epsilon turbulence model. In *15th Aeroacoustics Conf.*, Aeroacoustics Conferences. American Institute of Aeronautics and Astronautics, oct 1993. *quoted page 7*

[23] Walid Bechara, Christophe Bailly, Philippe Lafon, and Sebastien M Candel. Stochastic approach to noise modeling for free turbulent flows. *AIAA J.*, 32(3):455–463, mar 1994. *quoted page 7*

[24] C Bailly, P Lafon, and S Candel. Computation of noise generation and propagation for free and confined turbulent flows. In *Aeroacoustics Conf.*, Aeroacoustics Conferences. American Institute of Aeronautics and Astronautics, may 1996. *pas de citations*

[25] Christophe Bailly and Daniel Juve. A stochastic approach to compute subsonic noise using linearized Euler's equations. In *5th AIAA/CEAS Aeroacoustics Conf. Exhib.*, Aeroacoustics Conferences. American Institute of Aeronautics and Astronautics, may 1999. *quoted page 7*

[26] Magdi Omais, Bastien Caruelle, Stephane Redonnet, Eric Manoha, and Pierre Saguat. Jet Noise Prediction Using RANS CFD Input. In *14th AIAA/CEAS Aeroacoustics Conf. (29th AIAA Aeroacoustics Conf.*, Aeroacoustics Conferences. American Institute of Aeronautics and Astronautics, may 2008. *quoted page 7*

[27] Thomas Le Garrec, Eric Manoha, and Stéphane Redonnet. Flow Noise Predictions Using RANS/CAA Computations. In *16th AIAA/CEAS Aeroacoustics*

Conf., Aeroacoustics Conferences. American Institute of Aeronautics and Astronautics, jun 2010. *pas de citations*

[28] Anthony Lafitte, Thomas Le Garrec, Christophe Bailly, and Estelle Laurendeau. Turbulence Generation from a Sweeping-Based Stochastic Model. *AIAA J.*, 52(2):281–292, jan 2014. *quoted page 7*

[29] Christopher K W. Tam and Laurent Auriault. Jet Mixing Noise from Fine-Scale Turbulence. *AIAA J.*, 37(2):145–153, feb 1999. *quoted page 7*

[30] Nan Hu, Nils Reiche, and Roland Ewert. Simulation of turbulent boundary layer wall pressure fluctuations via Poisson equation and synthetic turbulence. *J. Fluid Mech.*, 826:421–454, 2017. *quoted page 7*

[31] Roland Ewert. Broadband slat noise prediction based on CAA and stochastic sound sources from a fast random particle-mesh (RPM) method. *Comput. Fluids*, 37(4):369–387, may 2008. *quoted page 7*

[32] R. Ewert, J. Dierke, J. Siebert, A. Neifeld, C. Appel, M. Siefert, and O. Kornow. CAA broadband noise prediction for aeroacoustic design. *J. Sound Vib.*, 330(17):4139–4160, aug 2011. *quoted page 7*

[33] L.J. Peltier and S.A. Hambric. Estimating turbulent-boundary-layer wall-pressure spectra from CFD RANS solutions. *J. Fluids Struct.*, 23(6):920–937, aug 2007. *quoted page 7*

[34] Y F Hwang, W K Bonness, and S A Hambric. On modeling structural excitations by low speed turbulent boundary layer flows. Technical report, ARL/Penn State Technical Report 03-008, 2003. *3 quotations pages 7, 11, et 110*

[35] M.K. Bull. Wall-Pressure Fluctuations Beneath Turbulent Boundary Layers: Some Reflections on Forty Years of Research. *J. Sound Vib.*, 190(3):299–315, 1996. *2 quotations pages 7 et 9*

[36] Theodore M Farabee and Mario J Casarella. Spectral features of wall pressure fluctuations beneath turbulent boundary layers. *Phys. Fluids A Fluid Dyn.*, 3(10):2410–2420, oct 1991. *quoted page 7*

[37] William K Blake. Chapter 2 - Essentials of Turbulent Wall Pressure Fluctuations. In William K Blake, editor, *Mech. Flow-Induced Sound Vib. Vol. 2 (Second Ed.*, pages 81–177. Academic Press, 2017. *3 quotations pages 7, 12, et 25*

[38] W. W. Willmarth and C. E. Wooldridge. Measurements of the fluctuating pressure at the wall beneath a thick turbulent boundary layer. *J. Fluid Mech.*, 14(02):187, oct 1962. *quoted page 7*

[39] M K Bull. Wall-pressure fluctuations associated with subsonic turbulent boundary layer flow. *J. Fluid Mech.*, 28(4):719–754, 1967. *2 quotations pages 7 et 52*

[40] G. M. Corcos. Resolution of Pressure in Turbulence. *J. Acoust. Soc. Am.*, 35(2):192, 1963. *2 quotations pages 7 et 45*

[41] Francois Vanherpe, Diego Baresh, Philippe Lafon, and Mehdi Bordji. Wavenumber-Frequency Analysis of the Wall Pressure Fluctuations in the Wake of a Car Side Mirror. In *17th AIAA/CEAS Aeroacoustics Conf. (32nd AIAA Aeroacoustics Conf.*, Aeroacoustics Conferences. American Institute of Aeronautics and Astronautics, jun 2011. *quoted page 8*

[42] J A B Wills. Measurements of the wave-number/phase velocity spectrum of wall pressure beneath a turbulent boundary layer. *J. Fluid Mech.*, 45(1):65–90, 1971. *quoted page 9*

[43] William K Blake and David M Chase. Wavenumber-Frequency Spectra of Turbulent-Boundary-Layer Pressure Measured by Microphone Arrays. *J. Acoust. Soc. Am.*, 49(3B):862–877, mar 1971. *quoted page 9*

[44] B M Abraham and W L Keith. Direct Measurements of Turbulent Boundary Layer Wall Pressure Wavenumber-Frequency Spectra. *J. Fluids Eng.*, 120(1):29–39, mar 1998. *quoted page 9*

[45] Klaus Ehrenfried and Lars Koop. Pressure Fluctuations Beneath a Compressible Turbulent Boundary Layer. In *14th AIAA/CEAS Aeroacoustics Conf. (29th AIAA Aeroacoustics Conf.*, Aeroacoustics Conferences. American Institute of Aeronautics and Astronautics, may 2008. *quoted page 9*

[46] Blandine Arguillat, Denis Ricot, Gilles Robert, and Christophe Bailly. Measurements of the wavenumber-frequency spectrum of wall pressure fluctuations under turbulent flows. In *11th AIAA/CEAS Aeroacoustics Conf.*, Aeroacoustics Conferences. American Institute of Aeronautics and Astronautics, may 2005. *quoted page 9*

[47] Olivier Robin, Stephane Moreau, Thomas Padois, and Alain Berry. Measurement of the wavenumber-frequency spectrum of wall pressure fluctuations:

spiral-shaped rotative arrays with pinhole-mounted quarter inch microphones. In *19th AIAA/CEAS Aeroacoustics Conf.*, Aeroacoustics Conferences. American Institute of Aeronautics and Astronautics, may 2013. *quoted page 9*

[48] Robert H Kraichnan. Pressure Fluctuations in Turbulent Flow over a Flat Plate. *J. Acoust. Soc. Am.*, 28(3):378–390, may 1956. *quoted page 9*

[49] O. M. Phillips. On the aerodynamic surface sound from a plane turbulent boundary layer. *Proc. R. Soc. London A Math. Phys. Eng. Sci.*, 234(1198):327–335, 1956. *quoted page 9*

[50] P Leehey. Structural Excitation by a Turbulent Boundary Layer: An Overview. *J. Vib. Acoust. Stress. Reliab. Des.*, 110(2):220–225, apr 1988. *quoted page 9*

[51] D.M. Chase. Modeling the wavevector-frequency spectrum of turbulent boundary layer wall pressure. *J. Sound Vib.*, 70(1):29–67, may 1980. *quoted page 11*

[52] D.M. Chase. The character of the turbulent wall pressure spectrum at subconvective wavenumbers and a suggested comprehensive model. *J. Sound Vib.*, 112(1):125–147, jan 1987. *pas de citations*

[53] D M Chase. Fluctuations in wall-shear stress and pressure at low streamwise wavenumbers in turbulent boundary-layer flow. *J. Fluid Mech.*, 225:545–555, 1991. *pas de citations*

[54] D.M. Chase. A Semi-empirical Model for the Wavevector-Frequency Spectrum of Turbulent Wall-Shear Stress. *J. Fluids Struct.*, 7(6):639–659, aug 1993. *quoted page 11*

[55] B Efimtsov. Characteristics of the Field of Turbulent Wall Pressure Fluctuations at Large Reynolds Numbers. *Sov. Phys. Acoust.*, 28(4):289–292, 1982. *quoted page 11*

[56] J E Ffowcs Williams. Boundary-layer pressures and the Corcos model: a development to incorporate low-wavenumber constraints. *J. Fluid Mech.*, 125:9–25, 1982. *quoted page 11*

[57] James M. Witting. A Spectral Model of Pressure Fluctuations at a Rigid Wall Bounding an Incompressible Fluid, Based on Turbulent Structures in the Boundary Layer. *Noise Control Eng. J.*, 26(1):28, 1986. *quoted page 11*

[58] A V Smol'Yakov, V M Tkachenko, and J S Wood. Model of a field of pseudosonic turbulent wall pressures and experimental data. *Sov. physics. Acoust.*, 37(6):627–631, 1991. *quoted page 11*

[59] Sung H. Ko. Analytical evaluation of a flush-mounted hydrophone array response to a modified Corcos turbulent wall pressure spectrum. Technical report, Naval Underwater Systems Center Tech. Rep. 8943, 1991. *quoted page 11*

[60] W L Keith, D A Hurdis, and B M Abraham. A Comparison of Turbulent Boundary Layer Wall-Pressure Spectra. *J. Fluids Eng.*, 114(3):338–347, sep 1992. *quoted page 11*

[61] Y. F. Hwang, William K. Bonness, and Stephen A. Hambric. Comparison of semi-empirical models for turbulent boundary layer wall pressure spectra. *J. Sound Vib.*, 319(1-2):199–217, 2009. *2 quotations pages 12 et 13*

[62] Teresa S Miller, Judith M Gallman, and Mark J Moeller. Review of Turbulent Boundary Layer Models for Acoustic Analysis. *J. Aircr.*, 49(6):1739–1754, nov 2012. *quoted page 11*

[63] A V Smol'yakov. Calculation of the spectra of pseudosound wall-pressure fluctuations in turbulent boundary layers. *Acoust. Phys.*, 46(3):342–347, 2000. *quoted page 12*

[64] Michael Goody. Empirical Spectral Model of Surface Pressure Fluctuations. *AIAA J.*, 42(9):1788–1794, sep 2004. *4 quotations pages 12, 45, 48, et 111*

[65] Howard H Schloemer. Effects of Pressure Gradients on Turbulent-Boundary-Layer Wall-Pressure Fluctuations. *J. Acoust. Soc. Am.*, 42(1):93–113, 1967. *quoted page 12*

[66] Yannick Rozenberg, Gilles Robert, and Stéphane Moreau. Wall-Pressure Spectral Model Including the Adverse Pressure Gradient Effects. *AIAA J.*, 50(10):2168–2179, oct 2012. *quoted page 12*

[67] Thomas L. Paez. The history of random vibrations through 1958. *Mech. Syst. Signal Process.*, 20(8):1783–1818, nov 2006. *quoted page 13*

[68] S Crandall. Random Vibration. New York, 1958. Technology Press of MIT and Wiley. *quoted page 13*

[69] Julius S Bendat and Allan G Piersol. *Random Data: Analysis and Measurement Procedures*. Wiley Series in Probability and Statistics. John Wiley & Sons, Inc., Hoboken, NJ, USA, 2010. *2 quotations pages 13 et 45*

[70] David Edward Newland. *An introduction to random vibrations, spectral & wavelet analysis*. Courier Corporation, 2012. *quoted page 13*

[71] Isaac Elishakoff. *Probabilistic Methods in the Theory of Structures: Strength of Materials, Random Vibrations, and Random Buckling*. World Scientific, 2017. *quoted page 13*

[72] F. Fahy and P. Gardonio. *Sound and Structural Vibration : Radiation, Transmission and Response*. Elsevier/Academic, 2007. *4 quotations pages 14, 19, 81, et 125*

[73] Laurent Maxit and Jean-Marc Ginoux. Prediction of the vibro-acoustic behavior of a submerged shell non periodically stiffened by internal frames. *J. Acoust. Soc. Am.*, 128(1):137–151, jul 2010. *2 quotations pages 14 et 124*

[74] M L Gobert and J M Mencik. A wave finite element-based approach for the prediction of the vibroacoustic behavior of fluid-filled pipes of arbitrary-shaped cross-sections. In *Int. Conf. Noise Vib. Eng. (ISMA 2016), Leuven, Belgium*, 2016. *quoted page 14*

[75] T. Gras, M.-A. Hamdi, M. Ben Tahar, O. Tanneau, and L. Beaubatie. On a coupling between the Finite Element (FE) and the Wave Finite Element (WFE) method to study the effect of a local heterogeneity within a railway track. *J. Sound Vib.*, 429:45–62, sep 2018. *quoted page 15*

[76] D.G. Crighton. The 1988 Rayleigh medal lecture: Fluid loading—The interaction between sound and vibration. *J. Sound Vib.*, 133(1):1–27, aug 1989. *quoted page 15*

[77] P.J.T. Filippi, P.-O. Mattei, C. Maury, A.H.P. Van Der Burgh, and C.J.M. De Jong. Sound transmission through a thin baffled plate: validation of a light fluid approximation with numerical and experimental results. *J. Sound Vib.*, 229(5):1157–1169, feb 2000. *quoted page 15*

[78] Colin Hansen. *Foundations of Vibroacoustics*. CRC Press, 2018. *3 quotations pages 15, 76, et 78*

[79] Roger Ohayon and Christian Soize. *Structural Acoustics and Vibration*. Academic Press, 1998. *quoted page 16*

[80] Miguel C. Junger and David. Feit. *Sound, structures, and Their Interaction*. MIT Press, 1986. *2 quotations pages 17 et 19*

[81] E A Skelton and J H James. *Theoretical Acoustics of Underwater Structures*. Imperial College Press, 1997. *2 quotations pages 17 et 19*

[82] J.L. Guyader and B. Laulagnet. Structural acoustic radiation prediction: Expanding the vibratory response on a functional basis. *Appl. Acoust.*, 43(3):247–269, jan 1994. *quoted page 17*

[83] B. Laulagnet and J.L. Guyader. Modal analysis of a shell's acoustic radiation in light and heavy fluids. *J. Sound Vib.*, 131(3):397–415, jun 1989. *quoted page 18*

[84] Noureddine Atalla and Franck Sgard. *Finite element and boundary methods in structural acoustics and vibration*. CRC Press, 2015. *2 quotations pages 18 et 85*

[85] Stephen A Hambric, Shung H Sung, and Donald J Nefske. *Engineering Vibroacoustic Analysis: Methods and Applications*. John Wiley & Sons, 2016. *quoted page 18*

[86] Alan Powell. On the Fatigue Failure of Structures due to Vibrations Excited by Random Pressure Fields. *J. Acoust. Soc. Am.*, 30(12):1130–1135, dec 1958. *quoted page 19*

[87] John F Wilby. The response of simple panels to turbulent boundary layer excitation. Technical report, AFFDL-TR-67-70, 1967. *quoted page 19*

[88] Ira Dyer. Response of Plates to a Decaying and Convecting Random Pressure Field. *J. Acoust. Soc. Am.*, 31(7):922–928, 1959. *quoted page 19*

[89] Gideon Maidanik. Response of Ribbed Panels to Reverberant Acoustic Fields. *J. Acoust. Soc. Am.*, 34(6):809–826, jun 1962. *quoted page 19*

[90] H S Ribner. Response of a Flexible Panel to Turbulent Flow: Running-Wave versus Modal-Density Analysis. *J. Acoust. Soc. Am.*, 40(3):721–726, sep 1966. *quoted page 19*

[91] Lucio Maestrello. Measurement and analysis of the response field of turbulent boundary layer excited panels. *J. Sound Vib.*, 2(3):270–292, jul 1965. *quoted page 19*

[92] L. Maestrello. Use of turbulent model to calculate the vibration and radiation responses of a panel, with practical suggestions for reducing sound level. *J. Sound Vib.*, 5(3):407–448, may 1967. *quoted page 19*

[93] Pritchard H White. Transduction of Boundary-Layer Noise by a Rectangular Panel. *J. Acoust. Soc. Am.*, 40(6):1354–1362, dec 1966. *quoted page 19*

[94] Huw G Davies. Sound from Turbulent-Boundary-Layer-Excited Panels. *J. Acoust. Soc. Am.*, 49(3B):878–889, mar 1971. *quoted page 19*

[95] Wayne A Strawderman. Turbulence-Induced Plate Vibrations: an Evaluation of Finite- and Infinite-Plate Models. *J. Acoust. Soc. Am.*, 46(5B):1294–1307, nov 1969. *quoted page 19*

[96] Earl G Williams. *Fourier Acoustics: Sound Radiation and Nearfield Acoustical Holography*. Elsevier, 1999. *quoted page 19*

[97] Micah R. Shepherd and Stephen A. Hambric. Comment on plate modal wavenumber transforms in Sound and Structural Vibration [Academic Press (1987, 2007)] (L). *J. Acoust. Soc. Am.*, 132(4):2155–2157, oct 2012. *2 quotations pages 20 et 125*

[98] Olivier Robin, Alain Berry, Noureddine Atalla, Stephen A Hambric, and Micah R Shepherd. Experimental evidence of modal wavenumber relation to zeros in the wavenumber spectrum of a simply supported plate. *J. Acoust. Soc. Am.*, 137(5):2978–2981, may 2015. *quoted page 20*

[99] William K Blake. Chapter 3 - Response of Arrays and Structures to Turbulent Wall Flow and Random Sound. In William K Blake, editor, *Mech. Flow-Induced Sound Vib. Vol. 2 (Second Ed.*, pages 179–296. Academic Press, second edi edition, 2017. *2 quotations pages 20 et 125*

[100] W.R. Graham. Boundary layer induced noise in aircraft, part I: the flat plate model. *J. Sound Vib.*, 192(1):101–120, apr 1996. *quoted page 20*

[101] W.R. Graham. Boundary layer induced noise in aircraft, part II: the trimmed flate plate model. *J. Sound Vib.*, 192(1):121–138, apr 1996. *pas de citations*

[102] W.R. Graham. A comparison of models for the wavenumber-frequency spectrum of turbulent boundary layer pressures. *J. Sound Vib.*, 206(4):541–565, oct 1997. *quoted page 20*

[103] C. Maury, P. Gardonio, and S.J. Elliott. A wavenumber approach to modelling the response of a randomly excited panel, Part I: general theory. *J. Sound Vib.*, 252(1):83–113, 2002. *quoted page 20*

[104] C. Maury, P. Gardonio, and S.J. Elliott. A wavenumber approach to modelling the response of a randomly excited panel, Part II: application to aircraft panels excited by a turbulent boundary layer. *J. Sound Vib.*, 252(1):115–139, 2002. *quoted page 20*

[105] Y.F. Hwang and G. Maidanik. A wavenumber analysis of the coupling of a structural mode and flow turbulence. *J. Sound Vib.*, 142(1):135–152, oct 1990. *quoted page 20*

[106] S. A. Hambric, Y. F. Hwang, and W. K. Bonness. Vibrations of plates with clamped and free edges excited by low-speed turbulent boundary layer flow. *J. Fluids Struct.*, 19(1):93–110, 2004. *quoted page 20*

[107] Paul Bremner and John Wilby. Aero-Vibro-Acoustics: Problem Statement and Methods for Simulation-based Design Solution. In *8th AIAA/CEAS Aeroacoustics Conf. Exhib.*, Aeroacoustics Conferences. American Institute of Aeronautics and Astronautics, jun 2002. *quoted page 22*

[108] Charles Pezerat, Océane Grosset, Justine Carpentier, Jean-Hugh Thomas, and Frédéric Ablitzer. Wall Pressure Identification by Using the Force Analysis Technique in Automotive, Naval and Aeronautic Applications BT - Flinovia—Flow Induced Noise and Vibration Issues and Aspects-II. pages 39–57, Cham, 2019. Springer International Publishing. *quoted page 21*

[109] D. Lecoq, C. Pézerat, J. H. Thomas, and W. P. Bi. Extraction of the acoustic component of a turbulent flow exciting a plate by inverting the vibration problem. *J. Sound Vib.*, 333(12):2505–2519, 2014. *5 quotations pages 21, 25, 108, 111, et 130*

[110] M.K. Bull and M.P. Norton. The proximity of coincidence and acoustic cut-off frequencies in relation to acoustic radiation from pipes with disturbed internal turbulent flow. *J. Sound Vib.*, 69(1):1–11, 1980. *quoted page 23*

[111] Manfred Heckl. Vibrations of Point-Driven Cylindrical Shells. *J. Acoust. Soc. Am.*, 34(10):1553–1557, oct 1962. *2 quotations pages 24 et 81*

[112] Benjamin F Cron and Charles H Sherman. Spatial-Correlation Functions for Various Noise Models. *J. Acoust. Soc. Am.*, 34(11):1732–1736, 1962. *quoted page 25*

[113] W.K. Blake and R.V. Waterhouse. The use of cross-spectral density measurements in partially reverberant sound fields. *J. Sound Vib.*, 54(4):589–599, oct 1977. *pas de citations*

[114] H Nélisse and J Nicolas. Characterization of a diffuse field in a reverberant room. *J. Acoust. Soc. Am.*, 101(6):3517–3524, jun 1997. *pas de citations*

[115] Boaz Rafaely. Spatial-temporal correlation of a diffuse sound field. *J. Acoust. Soc. Am.*, 107(6):3254–3258, may 2000. *2 quotations pages 25 et 111*

[116] Blandine Arguillat, Denis Ricot, Christophe Bailly, and Gilles Robert. Measured wavenumber: Frequency spectrum associated with acoustic and aerodynamic wall pressure fluctuations. *J. Acoust. Soc. Am.*, 128(4):1647–1655, 2010. *4 quotations pages 25, 26, 108, et 111*

[117] Abbas Hekmati, Denis Ricot, and Philippe Druault. Numerical synthesis of aeroacoustic wall pressure fields over a flat plate: Generation, transmission and radiationanalyses. *J. Sound Vib.*, 332(13):3163–3176, jun 2013. *3 quotations pages 25, 108, et 111*

[118] M P Norton. *The effects of internal flow disturbances on the vibration response of and the acoustic radiation from pipes.* PhD thesis, University of Adelaide, 1979. *2 quotations pages 27 et 112*

[119] David Charles Rennison. *The vibrational response of and the acoustic radiation from thin-walled pipes, excited by random fluctuating pressure fields / by D.C. Rennison.* PhD thesis, University of Adelaide, 1976. *quoted page 27*

[120] Hassen Trabelsi, Nicolas Zerbib, Jean-Michel Ville, and Félix Foucart. Passive and active acoustic properties of a diaphragm at low Mach number. Experimental procedure and numerical simulation. *Rev. Eur. mécanique numérique*, 20(1-4):49–71, may 2011. *2 quotations pages 28 et 60*

[121] Saad Bennouna, Said Naji, Olivier Cheriaux, Solene Moreau, Boureima Ouedraogo, and Jean Michel Ville. Aeroacoustic Prediction Methods of Automotive HVAC Noise. In *SAE Tech. Pap.* SAE International, jun 2015. *2 quotations pages 28 et 117*

[122] M Amielh, F Anselmet, Y Jiang, U Kristiansen, P.-O. Mattei, D Mazzoni, and C Pinhède. Aeroacoustic source analysis in a corrugated flow pipe using low-frequency mitigation. *J. Turbul.*, 15(10):650–676, oct 2014. *quoted page 28*

[123] Gaëtan Galeron, Daniel Mazzoni, Muriel Amielh, Pierre Olivier Mattei, and Fabien Anselmet. Experimental and Numerical Investigations of the Aeroacoustics in a Corrugated Pipe Flow BT - Turbulence and Interactions. pages 149–156, Cham, 2018. Springer International Publishing. *quoted page 28*

[124] J. Lavrentjev, M. Åbom, and H. Bodén. A measurement method for determining the source data of acoustic two-port sources. *J. Sound Vib.*, 183(3):517–531, jun 1995. *quoted page 28*

[125] J. Lavrentjev and M. Åbom. Characterization of fluid machines as acoustic multi-port sources. *J. Sound Vib.*, 197(1):1–16, oct 1996. *2 quotations pages 28 et 60*

[126] Hermann Schlichting and Klaus Gersten. *Boundary-Layer Theory*. Springer Berlin Heidelberg, Berlin, Heidelberg, 2017. *quoted page 37*

[127] N S Dickey, A Selamet, and M S Ciray. An experimental study of the impedance of perforated plates with grazing flow. *J. Acoust. Soc. Am.*, 110(5):2360–2370, oct 2001. *2 quotations pages 38 et 114*

[128] William K. Blake and Jason M. Anderson. The Acoustics of Flow over Rough Elastic Surfaces. In *Flinovia - Flow Induc. Noise Vib. Issues Asp.*, pages 1–23. Springer International Publishing, 2015. *quoted page 42*

[129] Paul R. Donavan and Wlliam K. Blake. Measurement, Prediction, and Reduction of High-Frequency Aerodynamic Noise Generated and Radiated from Surfaces of Various Textures. In *Flinovia—Flow Induc. Noise Vib. Issues Asp.*, pages 147–154. Springer International Publishing, 2019. *quoted page 42*

[130] Yunus-A Cengel and John-M Cimbala. *Fluid Mechanics - Fundamentals and Applications*. 3rd editio edition, 2013. *2 quotations pages 42 et 114*

[131] Peter D Lysak. Modeling the Wall Pressure Spectrum in Turbulent Pipe Flows. *J. Fluids Eng.*, 128(2):216–222, aug 2005. *quoted page 48*

[132] Micah R Shepherd. Structural-acoustic optimization of structures excited by turbulent boundary layer flow. 2014. *quoted page 48*

[133] Micah R Shepherd and Stephen A Hambric. Minimizing the acoustic power radiated by a fluid-loaded curved panel excited by turbulent boundary layer flow. *J. Acoust. Soc. Am.*, 136(5):2575–2585, nov 2014. *quoted page 48*

[134] Zhipeng Duan, M M Yovanovich, and Y S Muzychka. Pressure Drop for Fully Developed Turbulent Flow in Circular and Noncircular Ducts. *J. Fluids Eng.*, 134(6):61201–61210, jun 2012. *quoted page 49*

[135] Sergio Pirozzoli. On turbulent friction in straight ducts with complex cross-section: the wall law and the hydraulic diameter. *J. Fluid Mech.*, 846:R1, 2018. *quoted page 49*

[136] B GALLETTI and A BOTTARO. Large-scale secondary structures in duct flow. *J. Fluid Mech.*, 512:85–94, 2004. *quoted page 49*

[137] Branislav Stankovic, Srdjan Belosevic, Nenad Crnomarkovic, Andrijana Stojanovic, Ivan Tomanovic, and Aleksandar Milicevic. Specific aspects of turbulent flow in rectangular ducts. *Therm. Sci.*, 21(suppl. 3):663–678, 2017. *quoted page 49*

[138] Kamal Selvam, Emir Öngüner, Jorge Peixinho, El-Sayed Zanoun, and Christoph Egbers. Wall Pressure in Developing Turbulent Pipe Flows. *J. Fluids Eng.*, 140(8):81203–81207, mar 2018. *quoted page 49*

[139] Sung H Ko. Performance of various shapes of hydrophones in the reduction of turbulent flow noise. *J. Acoust. Soc. Am.*, 93(3):1293–1299, mar 1993. *quoted page 52*

[140] P.A. Nelson and C.L. Morfey. Aerodynamic sound production in low speed flow ducts. *J. Sound Vib.*, 79(2):263–289, 1981. *5 quotations pages 63, 68, 108, 114, et 116*

[141] Mats Abom, Sabry Allam, and Susann Boij. Aero-Acoustics of Flow Duct Singularities at Low Mach Numbers. In *12th AIAA/CEAS Aeroacoustics Conf. (27th AIAA Aeroacoustics Conf.*, Aeroacoustics Conferences. American Institute of Aeronautics and Astronautics, may 2006. *3 quotations pages 63, 108, et 114*

[142] Oscar Kårekull, Gunilla Efraimsson, and Mats Åbom. Prediction model of flow duct constriction noise. *Appl. Acoust.*, 82:45–52, aug 2014. *9 quotations pages 63, 66, 67, 68, 69, 108, 114, 115, et 116*

[143] Oscar Kårekull, Gunilla Efraimsson, and Mats Åbom. Revisiting the Nelson–Morfey scaling law for flow noise from duct constrictions. *J. Sound Vib.*, 357:233–244, nov 2015. *5 quotations pages 66, 67, 69, 108, et 116*

[144] P Durrieu, G Hofmans, G Ajello, R Boot, Y Aurégan, A Hirschberg, and M C A M Peters. Quasisteady aero-acoustic response of orifices. *J. Acoust. Soc. Am.*, 110(4):1859–1872, oct 2001. *2 quotations pages 67 et 116*

[145] H G Davies and J E Ffowcs Williams. Aerodynamic sound generation in a pipe. *J. Fluid Mech.*, 32(4):765–778, 1968. *quoted page 68*

[146] F. VAN HERPE and D. G. CRIGHTON. Noise generation by turbulent flow in ducts. *J. Phys. IV Fr.*, 04:C5–947–C5–950, 1994. *quoted page 68*

[147] Arthur W Leissa. *Vibration of Shells*. Scientific and Technical Information Office, National Aeronautics and Space Administration Washington, 1993. *3 quotations pages 74, 82, et 122*

[148] K. Daneshjou, M.M. Shokrieh, M. Ghorbani Moghaddam, and R. Talebitooti. Analytical model of sound transmission through relatively thick FGM cylindrical shells considering third order shear deformation theory. *Compos. Struct.*, 93(1):67–78, dec 2010. *quoted page 74*

[149] Werner Soedel and Mohamad S. Qatu. *Vibrations of Shells and Plates, Third Edition*, volume 117. 2005. *2 quotations pages 80 et 121*

[150] Stephen A Hambric. Structural acoustics tutorial-Part 1: vibrations in structures. *Acoust. Today*, 2(4):21–33, 2006. *quoted page 80*

[151] L. Cremer, M. Heckl, and B.A.T. Petersson. *Structure-Borne Sound*. Springer Berlin Heidelberg, Berlin, Heidelberg, 2005. *quoted page 81*

[152] Yeongbin Ko, Phill-Seung Lee, and Klaus-Jürgen Bathe. The MITC4+ shell element and its performance. *Comput. Struct.*, 169:57–68, jun 2016. *quoted page 83*

[153] M D McCollum and J M Cuschieri. Bending and in-plane wave transmission in thick connected plates using statistical energy analysis. *J. Acoust. Soc. Am.*, 88(3):1480–1485, sep 1990. *quoted page 88*

[154] A.N. Bercin and R.S. Langley. Application of the dynamic stiffness technique to the in-plane vibrations of plate structures. *Comput. Struct.*, 59(5):869–875, jun 1996. *pas de citations*

[155] Nicole J Kessissoglou. Power transmission in L-shaped plates including flexural and in-plane vibration. *J. Acoust. Soc. Am.*, 115(3):1157–1169, feb 2004. *2 quotations pages 88 et 121*

[156] G Robert. *Modélisation et simulation du champ excitateur induit sur une structure par une couche limite turbulence [Modeling and simulation of the excitation field induced on a structure by a boundary layer turbulence]*. PhD thesis, Ecole Centrale de Lyon, 1984. *quoted page 111*

[157] Bilong Liu, Leping Feng, Anders Nilsson, and Marco Aversano. Predicted and measured plate velocities induced by turbulent boundary layers. *J. Sound Vib.*, 331(24):5309–5325, 2012. *2 quotations pages 111 et 129*

[158] Nicolas Papaxanthos, Emmanuel Perrey-Debain, Boureima Ouedraogo, Solène Moreau, Jean-Michel Ville, Felix Foucart, and Saâd Bennouna. Prediction of air flow noise in ducts due to the presence of fixed obstacles. In *Proc. Euronoise 2015*, Maastricht, 2015. *quoted page 117*

[159] Laurent Maxit, Marion Berton, Christian Audoly, and Daniel Juvé. Discussion About Different Methods for Introducing the Turbulent Boundary Layer Excitation in Vibroacoustic Models. In *Flinovia - Flow Induc. Noise Vib. Issues Asp.*, pages 249–278. Springer International Publishing, 2015. *quoted page 119*

[160] S. De Rosa and F. Franco. Exact and numerical responses of a plate under a turbulent boundary layer excitation. *J. Fluids Struct.*, 24(2):212–230, feb 2008. *quoted page 119*

[161] William K Bonness, John B Fahnline, Peter D Lysak, and Micah R Shepherd. Modal forcing functions for structural vibration from turbulent boundary layer flow. 2017. *quoted page 119*

[162] Alexander Peiffer, Stephan Bruhl, and Daniel Redmann. Hybrid modelling of random excitation of shell structures. In *INTER-NOISE Congr. Conf. Proc.*, volume 2009, pages 701–710. Institute of Noise Control Engineering, 2009. *quoted page 124*

[163] Anders Nilsson and Bilong Liu. *Vibro-Acoustics, Volume 2*. Springer Berlin Heidelberg, Berlin, Heidelberg, 2016. *quoted page 129*

[164] Stephen J. Elliott, Cédric Maury, and Paolo Gardonio. The synthesis of spatially correlated random pressure fields. *J. Acoust. Soc. Am.*, 117(3):1186–1201, mar 2005. *quoted page 129*

[165] F. Franco, S. De Rosa, and E. Ciappi. Numerical approximations on the predictive responses of plates under stochastic and convective loads. *J. Fluids Struct.*, 42:296–312, oct 2013. *quoted page 129*

[166] N. Papaxanthos, E. Perrey-Debain, Saad Bennouna, Boureima Ouedraogo, Solene Moreau, and Jean-Michel Ville. Pressure-based integral formulations of Lighthill–Curle's analogy for internal aeroacoustics at low Mach numbers. *J. Sound Vib.*, 393:176–186, apr 2017. *quoted page 153*

[167] Mats Åbom and Hans Bodén. Error analysis of two-microphone measurements in ducts with flow. *J. Acoust. Soc. Am.*, 83(6):2429–2438, jun 1988. *quoted page 183*

[168] Seung-Ho Jang and Jeong-Guon Ih. On the multiple microphone method for measuring in-duct acoustic properties in the presence of mean flow. *J. Acoust. Soc. Am.*, 103(3):1520–1526, mar 1998. *quoted page 184*

Appendix A

Spectral analysis

The Fourier Transform (FT) of a random signal $p(\mathbf{s}, t)$ at a given sensor position $\mathbf{s}$ is defined as

$$p(\mathbf{s}, f) = \int_{-\infty}^{+\infty} p(\mathbf{s}, t) \mathrm{e}^{-\mathrm{i}\omega t} \mathrm{d}t, \tag{A.1}$$

and

$$p(\mathbf{s}, \omega) = \frac{1}{2\pi} p(\mathbf{s}, f). \tag{A.2}$$

The inverse Fourier Transform is defined as

$$p(\mathbf{s}, t) = \int_{-\infty}^{+\infty} p(\mathbf{s}, \omega) \mathrm{e}^{\mathrm{i}\omega t} \mathrm{d}t = \int_{-\infty}^{+\infty} p(\mathbf{s}, f) \mathrm{e}^{\mathrm{i}2\pi f t} \mathrm{d}t. \tag{A.3}$$

For finite random signals, the Fourier Transform writes

$$p(\mathbf{s}, f, T) = \int_{0}^{T} p(\mathbf{s}, t) \mathrm{e}^{-\mathrm{i}\omega t} \mathrm{d}t. \tag{A.4}$$

The Fourier Transform used in spectrum analysis instrumentation is referred to as the discrete Fourier transform (DFT), for which the functions $p(\mathbf{s}, f)$ and $p(\mathbf{s}, t)$ are sampled in both the time and frequency domains. Thus:

$$p(\mathbf{s}, t_k) = \sum_{n=0}^{N-1} p(\mathbf{s}, f_n) \mathrm{e}^{\mathrm{i}2\pi nk/N} \quad k = 0, 1, ..., (N-1), \tag{A.5}$$

$$p(\mathbf{s}, f_n) = \frac{1}{N} \sum_{k=0}^{N-1} p(\mathbf{s}, t_k) \mathrm{e}^{-\mathrm{i}2\pi nk/N} \quad n = 0, 1, ..., (N-1), \tag{A.6}$$

where k and n represent discrete sample numbers in the time and frequency domain respectively. The spacing between frequency components, in Hz, is dependent on the time, T, to acquire the N samples of data in the time domain and is equal to f_s/N

where f_s is the sampling frequency.

The signal energy associated to a random signal can be estimated by the two-sided power spectral density (PSD) defined as:

$$S_{pp}(\mathbf{s}, f) = \lim_{T\to\infty} \frac{1}{T}\mathbb{E}\left[p(\mathbf{s}, f, T)p^*(\mathbf{s}, f, T)\right] = \lim_{T\to\infty} \frac{1}{T}\mathbb{E}\left[|p(\mathbf{s}, f, T)|^2\right] \tag{A.7}$$

or

$$S_{pp}(\mathbf{s}, \omega) = \lim_{T\to\infty} \frac{(2\pi)^2}{T}\mathbb{E}\left[p(\mathbf{s}, \omega, T)p^*(\mathbf{s}, \omega, T)\right] = \lim_{T\to\infty} \frac{(2\pi)^2}{T}\mathbb{E}\left[|p(\mathbf{s}, \omega, T)|^2\right], \tag{A.8}$$

where 'two-sided' indicates that the spectrum extends to negative as well as positive frequencies. In practice, the single-sided power spectrum, $G_{pp}(\mathbf{s}, f)$ (positive frequencies only), is the one of interest and this is expressed in terms of the two-sided power spectrum density $S_{pp}(\mathbf{s}, f)$ as:

$$G_{pp}(\mathbf{s}, f) = 2S_{pp}(\mathbf{s}, f) \quad f > 0, \tag{A.9}$$

$$G_{pp}(\mathbf{s}, f) = S_{pp}(\mathbf{s}, 0) \quad f = 0. \tag{A.10}$$

In the same manner, the cross power spectral density (CPSD) between two sensors located in $\mathbf{s}_1$ and $\mathbf{s}_2$ writes

$$S_{pp}(\mathbf{s}_1, \mathbf{s}_2, \omega) = \lim_{T\to\infty} \frac{(2\pi)^2}{T}\mathbb{E}\left[p(\mathbf{s}_1, \omega, T)p^*(\mathbf{s}_2, \omega, T)\right]. \tag{A.11}$$

For stationary random process and ergodic signals, the (cross) power spectral density can be obtained by the Fourier Transform of the cross/auto correlation function via the Wiener-Khinchin theorem and writes

$$S_{pp}(\mathbf{s}_1, \mathbf{s}_2, \omega) = \int_{-\infty}^{+\infty} R_{pp}(\mathbf{s}_1, \mathbf{s}_2, \tau)\mathrm{e}^{-\mathrm{i}\omega\tau}\mathrm{d}\tau. \tag{A.12}$$

Thus, the cross correlation function between two signals $p(\mathbf{s}_1, t)$ and $p(\mathbf{s}_2, t)$ writes

$$R_{pp}(\mathbf{s}_1, \mathbf{s}_2, \tau, t) = \mathbb{E}\left[p(\mathbf{s}_1, t)p^*(\mathbf{s}_2, t+\tau)\right] = \lim_{T\to\infty} \frac{1}{T}\int_0^T p(\mathbf{s}_1, t)p^*(\mathbf{s}_2, t+\tau)\mathrm{d}t. \tag{A.13}$$

Assuming 'ergodicity', the cross correlation function is no longer time dependent and writes

$$R_{pp}(\mathbf{s}_1, \mathbf{s}_2, \tau, t) = R_{pp}(\mathbf{s}_1, \mathbf{s}_2, \tau). \tag{A.14}$$

The spatial cross correlation function is defined by:

$$R_{pp}(\mathbf{s}_1, \mathbf{s}_2, \xi, t) = \mathbb{E}\left[p(\mathbf{s}_1, t)p^*(\mathbf{s}_2 + \xi, t)\right] = \lim_{D\to\infty} \frac{1}{D} \int_D p(\mathbf{s}_1, t)p^*(\mathbf{s}_2 + \xi, t)\mathrm{d}t, \quad \text{(A.15)}$$

with D the spatial domain. For spatially homogeneous fields, the spatial cross correlation function is only function of the separation vector $\xi = \mathbf{s}_1 - \mathbf{s}_2$ such as $R_{pp}(\mathbf{s}_1, \mathbf{s}_2, \xi, t) = R_{pp}(\xi, t)$. The root mean square (RMS) value of signal $p(\mathbf{s}, t)$ is given by

$$p_{\mathrm{RMS}} = \sqrt{R_{pp}(\mathbf{s}, \tau = 0)} = \sqrt{\mathbb{E}\left[p(\mathbf{s}, t)p^*(\mathbf{s}, t)\right]} = \sqrt{\lim_{T\to\infty} \frac{1}{T} \int_0^T |p(\mathbf{s}, t)|^2 \,\mathrm{d}t}. \quad \text{(A.16)}$$

The mean square value of p can be given by the following relation

$$p^2_{\mathrm{RMS}}(\mathbf{s}) = \int_{-\infty}^{+\infty} S_{pp}(\mathbf{s}, f)\mathrm{d}f = \int_0^{+\infty} G_{pp}(\mathbf{s}, f)\mathrm{d}f. \quad \text{(A.17)}$$

In practice, acquisition systems estimate the single-sided auto power spectrum $G_{pp}(\mathbf{s}, f)$ by averaging a large number of squared spectrum, $p(\mathbf{s}, f_n)$. It is divided by 2 or not to account for conversion from an amplitude squared spectrum to an RMS squared spectrum and an additional scaling S_A to account for the application of a windowing function to the sampled data. Thus, an estimator for the single-sided autopower spectrum, using M averages writes

$$G_{pp}(f_n) = \frac{S_A}{M} \sum_{i=1}^{M} p_i(\mathbf{s}, f_n)p_i^*(\mathbf{s}, f_n) = \frac{S_A}{M} \sum_{i=1}^{M} |p_i(\mathbf{s}, f_n)|^2 \qquad n = 0, 1, ..., (N-1), \quad \text{(A.18)}$$

where i is the windowed Direct Fourier Transform of a block i, according to Eq.(A.6), with a certain segmentation with or without overlap processing. The larger the value of M, the more closely will the estimate of $G_{pp}(\mathbf{s}, f)$ approach its true value. This estimator has square units, that is, if voltage is measured, the units of the autopower spectrum becomes [V^2]. The power spectral density can be obtained from the auto power spectrum by dividing the amplitudes of each frequency component by the frequency spacing Δf and units becomes [V^2/Hz]. The Welch's method represents the most commonly used method of spectral analysis in instrumentation and computer software, such as MATLAB's ® **pwelch** function.

Appendix B

$2N$ port method

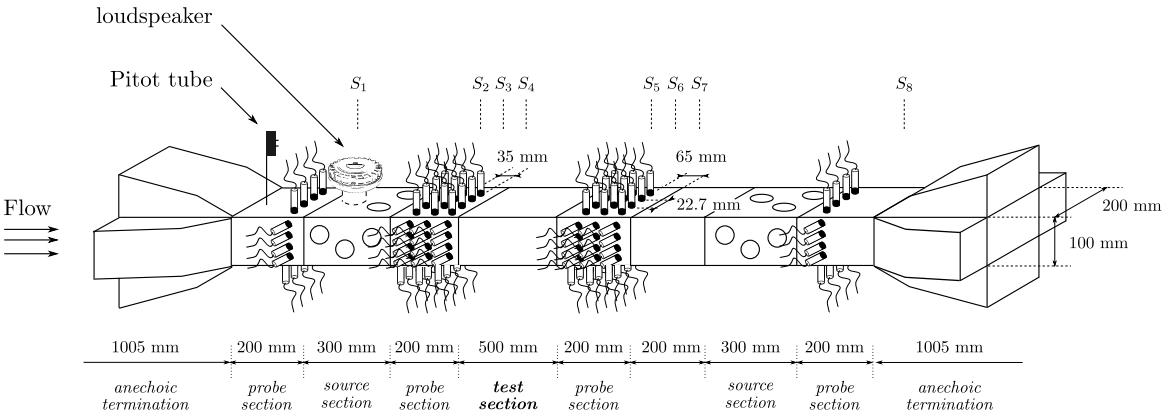

Figure B.1: Sketch of the pipe rig.

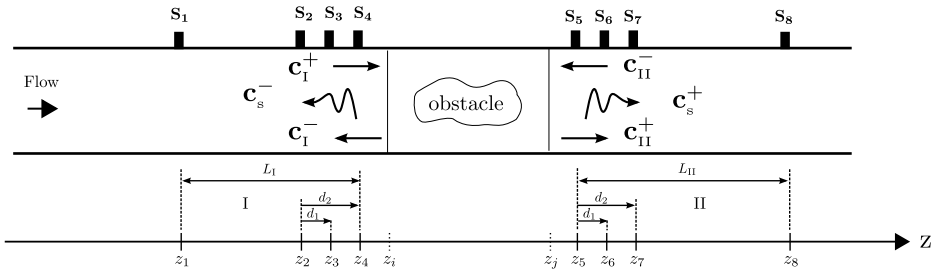

Figure B.2: An illustration of the acoustic multi-port. The indices I and II denote the upstream and downstream side of the multi-port.

The multiport formulation in a duct, as in Fig. B.2, can be written in a compact form

$$\mathbf{a}^{\text{out}}(\omega) = \mathbf{S}(\omega)\mathbf{a}^{\text{in}}(\omega) + \mathbf{a}^{s}(\omega), \tag{B.1}$$

with

$$\mathbf{a}^{\text{out}} = \begin{bmatrix} \mathbf{c}_{\text{I}}^{-} \\ \mathbf{c}_{\text{II}}^{+} \end{bmatrix}, \quad \mathbf{a}^{\text{in}} = \begin{bmatrix} \mathbf{c}_{\text{I}}^{+} \\ \mathbf{c}_{\text{II}}^{-} \end{bmatrix} \text{ and } \mathbf{a}^{\text{s}} = \begin{bmatrix} \mathbf{c}_{s}^{+} \\ \mathbf{c}_{s}^{-} \end{bmatrix}. \tag{B.2}$$

The scattering matrix $\mathbf{S} \in \mathbb{C}^{[2N\times 2N]}$ contains the transmission and reflection of all N modes at the inlet and the outlet. The complex vectors $\mathbf{a}^{\text{in,out}} \in \mathbb{C}^{[2N\times 1]}$ are respectively the incident and outgoing modal pressure amplitudes. The source vector $\mathbf{a}^{s} \in \mathbb{C}^{[2N\times 1]}$ contains the sound waves which are generated by the element itself under reflection-free conditions.

The pressure field in the duct satisfies the convected Helmholtz equation and is written as a sum of propagating modes, for instance at point $\mathbf{s}_1 = (s_1, z_1) = (x_1, y_1, z_1)$

$$p_{ac}(\mathbf{s}_1, \omega) = \sum_{pq} C_{pq}^{+}\psi_{pq}(s_1)e^{\mathrm{i}k_{pq}^{+}z_1} + \sum_{pq} C_{pq}^{-}\psi_{pq}(s_1)e^{\mathrm{i}k_{pq}^{-}z_1}, \tag{B.3}$$

where the normalized duct modes ψ_{pq} writes

$$\psi_{pq}(x, y) = \frac{\cos(\frac{p\pi x}{L_x})\cos(\frac{q\pi y}{L_y})}{\sqrt{N_{pq}}}, \tag{B.4}$$

where

$$N_{pq} = L_x L_y \Lambda_p \Lambda_q \quad \text{with} \quad \begin{cases} \Lambda_p = 1 & p = 0, \\ \Lambda_q = 1 & q = 0, \\ \Lambda_p = 1/2 & p > 0, \\ \Lambda_q = 1/2 & q > 0. \end{cases} \tag{B.5}$$

and $C_{pq}^{\pm}$ stands for amplitude of the downstream (+) and upstream (-) propagating mode. The flow is assumed uniform and thermo-viscous attenuation is neglected so that the axial wavenumbers $k_{pq}^{\pm}$ writes

$$k_{pq}^{\pm} = \frac{kM \pm \sqrt{k^2 - (1 - M^2)\, k_{\perp}^2}}{1 - M^2}, \tag{B.6}$$

where M is the Mach number and $k_{\perp}$ is the transverse wavenumber. For a rectangular

section, it writes

$$k_{\perp}^2 = \left(\frac{p\pi x}{L_x}\right)^2 + \left(\frac{q\pi y}{L_y}\right)^2. \tag{B.7}$$

Considering $l = 12$ sensor points in a section, we can rewrite Eq.(B.3) in matrix notation

$$\mathbf{p}^z(\omega) = \mathbf{M}\mathbf{a}_{\alpha}^{\pm,z}(\omega), \tag{B.8}$$

with

$$\mathbf{a}_{\alpha}^{\pm,z}(\omega) = \mathbf{c}_{\alpha}^{+,z} + \mathbf{c}_{\alpha}^{-,z} = \begin{pmatrix} C_0^+(\omega)\mathrm{e}^{\mathrm{i}k_r^+ z} \\ \vdots \\ C_r^+(\omega)\mathrm{e}^{\mathrm{i}k_r^+ z} \\ \vdots \\ C_N^+(\omega)\mathrm{e}^{\mathrm{i}k_N^+ z} \end{pmatrix} + \begin{pmatrix} C_0^-(\omega)\mathrm{e}^{\mathrm{i}k_r^- z} \\ \vdots \\ C_r^-(\omega)\mathrm{e}^{\mathrm{i}k_r^- z} \\ \vdots \\ C_N^-(\omega)\mathrm{e}^{\mathrm{i}k_N^- z} \end{pmatrix}, \quad \text{and } \alpha = \mathrm{I}, \mathrm{II}. \tag{B.9}$$

Note that the index $r = (p, q)$ and modes are sorted by ascending cut-on frequencies. $\mathbf{p}^z(\omega) \in \mathbb{C}^{[l\times 1]}$ is the vector of sampled pressures at the section position z, $\mathbf{a}_{\alpha}^{\pm,z}(\omega) \in \mathbb{C}^{[N\times 1]}$ is the vector of modal pressure amplitudes in both directions and $\mathbf{M} \in \mathbb{C}^{[l\times N]}$ is the modal matrix containing the N duct modes as following

$$\mathbf{M} = \begin{bmatrix} |\psi_1| & \dots & |\psi_N \end{bmatrix}. \tag{B.10}$$

A transfer function method is implemented so that the measured pressure signals at $l = 12$ sensor points in a section contained in $\mathbf{p}^z(\omega)$ are expressed formally by:

$$p(s_l, z, \omega) = H_{\mathrm{e}/l}^z(\omega)e(\omega), \tag{B.11}$$

where e is the electrical signal (set to 1V) driving the external loudspeaker and $H_{\mathrm{e}/l}^z$ the transfer function between the lth microphone at section located in z and the electrical signal.

The transfer function between the reference electrical signal and the lth microphone is measured according to the H_1 estimator:

$$H_{\mathrm{e}/l} = G_{\mathrm{e},l}/G_{\mathrm{e,e}} \quad \text{in V/V}, \tag{B.12}$$

where $G_{\mathrm{e,e}}$ is the autospectrum of the electrical signal and $G_{\mathrm{e},i}$ the cross-spectrum between electrical signal and the lth microphone. This transfer function is corrected with the transfer function obtained from the calibration procedure $H_{\mathrm{ref}/i}$ defined in

Eq.(2.3) so that

$$p(s_l, z, \omega) = \frac{H^z_{\mathrm{e}/l}(\omega)}{H_{\mathrm{ref}/l}} e(\omega) \tag{B.13}$$

is expressed in Pa/V with the electrical signal set to 1V.

The modal decomposition technique is performed by solving the over-determined system Eq.(B.8), in our case, for 2×10 different load cases according to the 10 loudspeaker positions upstream and the 10 others downstream designed for the pipe rig as shown Fig. B.1. Another aspect is the separation of propagating waves in the downstream and upstream directions. The well-known two microphone decomposition method fails when the intermediate distance between the microphones equals half an acoustical wavelength [167]. A multiple microphones enables an extension of the two microphone method into an over-determined system of equations written as

$$\mathbf{a}^{\pm}_{\alpha}(\omega) = \mathbf{E}(\omega)\mathbf{c}^{\pm}_{\alpha}(\omega), \tag{B.14}$$

with $\mathbf{a}^{\pm}_{\alpha}(\omega) \in \mathbb{C}^{[3N\times 1]}$, $\mathbf{c}^{\pm}_{\alpha}(\omega) \in \mathbb{C}^{[2N\times 1]}$ defined as

$$\mathbf{a}^{\pm}_{\alpha}(\omega) = \begin{bmatrix} \mathbf{a}^{\pm,z_2}_{\alpha}(\omega) \\ \mathbf{a}^{\pm,z_3}_{\alpha}(\omega) \\ \mathbf{a}^{\pm,z_4}_{\alpha}(\omega) \end{bmatrix}, \quad \mathbf{c}^{\pm}_{\alpha}(\omega) = \begin{bmatrix} \mathbf{c}^{+,z_2}_{\alpha} \\ \mathbf{c}^{-,z_2}_{\alpha} \end{bmatrix}, \tag{B.15}$$

and $\mathbf{E}(\omega) \in \mathbb{C}^{[3N\times 2N]}$ defined as

$$\mathbf{E}(\omega) = \begin{bmatrix} \mathbf{I}_N & \mathbf{I}_N \\ \begin{bmatrix} \ddots & \\ & \mathrm{e}^{\mathrm{i}k_r^+ d_1} \end{bmatrix}_{N\times N} & \begin{bmatrix} \ddots & \\ & \mathrm{e}^{\mathrm{i}k_r^- d_1} \end{bmatrix}_{N\times N} \\ \begin{bmatrix} \ddots & \\ & \mathrm{e}^{\mathrm{i}k_r^+ d_2} \end{bmatrix}_{N\times N} & \begin{bmatrix} \ddots & \\ & \mathrm{e}^{\mathrm{i}k_r^- d_2} \end{bmatrix}_{N\times N} \end{bmatrix}, \tag{B.16}$$

where distances $d_1 = z_3 - z_2$ and $d_2 = z_4 - z_2$ correspond to the separation between respectively sections $[S_2, S_3]$ and $[S_3, S_4]$. Note that modal pressure amplitudes are obtained here in z_2 (case $\alpha = \mathrm{I}$) and can be transported to z_i multiplying by a transfer vector $\gamma^{\pm,z_i}_{\alpha} \in \mathbb{C}^{[2N\times 1]}$ defined as

$$\gamma^{\pm,z_i}_{\alpha} = \begin{bmatrix} \mathrm{e}^{\mathrm{i}k_r^+(z_i - z_2)} \\ \mathrm{e}^{\mathrm{i}k_r^-(z_i - z_2)} \end{bmatrix}. \tag{B.17}$$

It would be the same thing for the case $\alpha = \text{II}$, replacing respectively (z_2,z_3,z_4,z_i) by (z_5,z_6,z_7,z_j). Once a again, the over-determined system Eq.(B.14) induced singular solution following the relative positions of measurement sensors. Jang [168] found that the equidistant positioning of sensors yields to the most accurate solution.

Finally, the modal pressure amplitudes $\mathbf{a}^{\text{in}}$ and $\mathbf{a}^{\text{out}}$ are obtained by solving both Eq.(B.8) and Eq.(B.14) for the 2×10 load cases using transfer functions measured according to Eq.(B.13) as input data. The scattering matrix can be extracted solving Eq.(B.1) such as

$$\mathbf{S} = \mathbf{a}^{\text{out}}(\omega) \left(\mathbf{a}^{\text{in}}(\omega)\right)^{-1}, \tag{B.18}$$

where $(\cdots)^{-1}$ denotes the pseudo-inverse, matrix $\mathbf{a}^{\text{in}}$ and $\mathbf{a}^{\text{out}}$ contain the decomposed acoustic fields for each test case $1, 2, ..., 2N$ (denoted by the superscript), as columns and writes

$$\mathbf{a}^{\text{in}} = \begin{bmatrix} \begin{bmatrix} \mathbf{c}_{\text{I}}^{+} \\ \mathbf{c}_{\text{II}}^{-} \end{bmatrix}_1 & \begin{bmatrix} \mathbf{c}_{\text{I}}^{+} \\ \mathbf{c}_{\text{II}}^{-} \end{bmatrix}_2 & \cdots & \begin{bmatrix} \mathbf{c}_{\text{I}}^{+} \\ \mathbf{c}_{\text{II}}^{-} \end{bmatrix}_{2N} \end{bmatrix} \tag{B.19}$$

and

$$\mathbf{a}^{\text{out}} = \begin{bmatrix} \begin{bmatrix} \mathbf{c}_{\text{I}}^{-} \\ \mathbf{c}_{\text{II}}^{+} \end{bmatrix}_1 & \begin{bmatrix} \mathbf{c}_{\text{I}}^{-} \\ \mathbf{c}_{\text{II}}^{+} \end{bmatrix}_2 & \cdots & \begin{bmatrix} \mathbf{c}_{\text{I}}^{-} \\ \mathbf{c}_{\text{II}}^{+} \end{bmatrix}_{2N} \end{bmatrix}. \tag{B.20}$$

In a second step, the source vector is solved using cross-spectrum densities between the four different sections S_1, S_4, S_7, S_8. The matrix of the test rig terminations is introduced as follows

$$\mathbf{R} = \mathbf{a}^{\text{in}} \left(\mathbf{a}^{\text{out}}\right)^{-1} = \begin{bmatrix} \mathbf{R}_{z_i} & 0 \\ 0 & \mathbf{R}_{z_j} \end{bmatrix}, \tag{B.21}$$

and calculated using the same data to solve the scattering problem Eq.(B.18). The excitations at the downstream side is used to determine the reflection of the termination at the upstream side and vice versa. The matrix of the test rig termination couples the incident and the outgoing modal pressure so that Eq.(B.1) can be rearranged to solve for the modal source vector as following

$$\mathbf{a}^{s} = [\mathbf{I}_{2N} - \mathbf{SR}]\, \mathbf{a}^{\text{out}}. \tag{B.22}$$

The source vector expressed in z_i and z_j writes

$$\mathbf{a}^s = [\mathbf{I}_{2N} - \mathbf{SR}]\,\widetilde{\mathbf{M}}\mathbf{p}_{z_j}^{z_i} = \mathbf{C}_1\mathbf{p}_{z_j}^{z_i}, \tag{B.23}$$

where $\widetilde{\mathbf{M}} \in \mathbb{C}^{[2N\times 2l]}$ decomposes the sound fields at both sides of the multi-port as following

$$\widetilde{\mathbf{M}} = \begin{bmatrix} \mathbf{M}\left[\mathbf{R}_{z_i} + \mathbf{I}_N\right] & 0 \\ 0 & \mathbf{M}\left[\mathbf{R}_{z_j} + \mathbf{I}_N\right] \end{bmatrix}^{-1}, \tag{B.24}$$

$(\cdots)^{-1}$ denotes the pseudo-inverse and $\mathbf{p}_{z_j}^{z_i} \in \mathbb{C}^{[2l\times 1]}$ is the vector which contains the pressure field at section z_i and z_j.

The algorithm is built to post-process cross-spectra between section S_1, S_4, S_7, S_8. Hence, sections S_4 and S_7 are defined as inlet and outlet so that in all previous equations, $z_i = z_4$ and $z_j = z_7$. In addition, Eq.(B.23) can be transported to the furthest upstream and downstream sections S_1 and S_8 so that

$$\mathbf{a}^s = \mathbf{C}_2\mathbf{p}_{z_8}^{z_1}, \tag{B.25}$$

where $\mathbf{C}_2$ contains transport matrices. It writes

$$\mathbf{C}_2 = \mathbf{\Gamma}_{\text{out}}^{-1}\left[\mathbf{I}_{2N} - \mathbf{S}'\mathbf{R}'\right]\widetilde{\mathbf{M}}'. \tag{B.26}$$

where $'$ denotes the transformations for the $\mathbf{S}$, $\mathbf{R}$ and $\widetilde{\mathbf{M}}$ matrices from z_4, z_1 to z_1, z_8 using diagonal transfer matrices $\mathbf{\Gamma}_{\text{in}} \in \mathbb{C}^{[2N\times 2N]}$ and $\mathbf{\Gamma}_{\text{out}} \in \mathbb{C}^{[2N\times 2N]}$ obtained from

$$\mathbf{\Gamma}_{\pm}(L_\alpha) = \begin{bmatrix} \ddots & & \\ & \mathrm{e}^{\mathrm{i}k_r^{\pm}L_\alpha} & \\ & & \ddots \end{bmatrix}_{N\times N}, \tag{B.27}$$

such as

$$\mathbf{\Gamma}_{\text{out}} = \left[\begin{array}{c|c} \mathbf{\Gamma}_-^{-1}(L_{\text{I}}) & 0 \\ \hline 0 & \mathbf{\Gamma}_+(L_{\text{II}}) \end{array}\right], \quad \mathbf{\Gamma}_{\text{in}} = \left[\begin{array}{c|c} \mathbf{\Gamma}_+^{-1}(L_{\text{I}}) & 0 \\ \hline 0 & \mathbf{\Gamma}_-(L_{\text{II}}) \end{array}\right], \tag{B.28}$$

and L_{I} and L_{II} ar the distances from the reference cross-sections z_4, z_1 to the new cross-sections z_1, z_8 as shown Fig. B.2. The translation of matrices along the duct are finally given by

$$\mathbf{S}' = \mathbf{\Gamma}_{\text{out}}\mathbf{S}\mathbf{\Gamma}_{\text{in}}^{-1}, \tag{B.29}$$

$$\mathbf{R}' = \mathbf{\Gamma}_{\text{in}}\mathbf{R}\mathbf{\Gamma}_{\text{out}}^{-1} = \begin{bmatrix} \mathbf{R}_{z_1} & 0 \\ 0 & \mathbf{R}_{z_8} \end{bmatrix}, \tag{B.30}$$

$$\widetilde{\mathbf{M}'} = \begin{bmatrix} \mathbf{M}\left[\mathbf{R}_{z_1} + \mathbf{I}_N\right] & 0 \\ 0 & \mathbf{M}\left[\mathbf{R}_{z_8} + \mathbf{I}_N\right]. \end{bmatrix}^{-1}. \tag{B.31}$$

The source vector $\mathbf{a}^s$ at sections S_4 and S_7 is expressed in term of a source cross-spectrum matrix $\mathbf{G}^s \in \mathbb{C}^{[2N\times 2N]}$ to get a formulation valid for random signals. One finally get

$$\mathbf{G}^s = \mathbb{E}\left[\mathbf{a}^s\left(\mathbf{a}^s\right)^c\right], \tag{B.32}$$

where the superscript c denotes transpose and complex conjugate. The diagonal terms represent the modal auto-spectra respectively at the section S_4 and S_7:

$$\mathbf{G}^s = \left[\begin{array}{ccc|ccc} \ddots & & \mathbb{E}\left[C_{pq}^-(\omega)C_{rs}^-(\omega)^*\right] & & \text{Modal cross terms: } \mathbb{E}\left[\mathbf{c}_s^{-,z_4}(\mathbf{c}_s^{+,z_7})^*\right] & \\ & \mathbb{E}\left[\left|C_{pq}^-(\omega)\right|^2\right] & & & & \\ & & \ddots & & & \\ \hline & \text{Modal cross terms: } \mathbb{E}\left[\mathbf{c}_s^{+,z_7}(\mathbf{c}_s^{-,z_4})^*\right] & & \ddots & & \mathbb{E}\left[C_{pq}^+(\omega)C_{rs}^+(\omega)^*\right] \\ & & & & \mathbb{E}\left[\left|C_{pq}^+(\omega)\right|^2\right] & \\ & & & & & \ddots \end{array}\right].$$

One can rewrite Eq.(B.32) in terms of measurable quantities using equations Eq.(B.23) and Eq.(B.25) such as

$$\mathbf{G}^s = \mathbb{E}\left[\left(\mathbf{C}_1\mathbf{p}_{z_7}^{z_4}\right)\left(\mathbf{C}_2\mathbf{p}_{z_8}^{z_1}\right)^c\right] = \mathbf{C}_1\mathbb{E}\left[\mathbf{p}_{z_7}^{z_4}(\mathbf{p}_{z_8}^{z_1})^c\right]\mathbf{C}_2^c = \mathbf{C}_1\left[\begin{array}{c|c} \mathbf{S}_{pp}^{L_1} & \mathbf{S}_{pp}^{L_2} \\ \hline \mathbf{S}_{pp}^{L_3} & \mathbf{S}_{pp}^{L_4} \end{array}\right]\mathbf{C}_2^c, \tag{B.33}$$

with $\mathbf{S}_{pp}^{L_k} \in \mathbb{C}^{[l\times l]}$ the CSD matrix associated to the kth cross spectrum. Note that if the test rig terminations are supposed perfect ($\mathbf{R}$ is set to 0) then $\mathbf{C}_1 = \mathbf{C}_2 = \widehat{\mathbf{M}}$ with

$$\widehat{\mathbf{M}} = \left[\begin{array}{c|c} \mathbf{M} & 0 \\ \hline 0 & \mathbf{M} \end{array}\right]^{-1} \tag{B.34}$$

and $(\cdots)^{-1}$ denotes the pseudo-inverse. Then, the source cross-spectrum matrix writes

$$\mathbf{G}^s = \mathbb{E}\left[\left(\widehat{\mathbf{M}}\mathbf{p}_{z_7}^{z_4}\right)\left(\widehat{\mathbf{M}}\mathbf{p}_{z_8}^{z_1}\right)^c\right]. \tag{B.35}$$

Appendix C

Simply supported solution for different shell theories

This Appendix recalls the coefficients k_{ij} of the eigenproblem Eq.(3.27) for the Donnell–Mushtari, Goldenveizer–Novozhilov, Reissner-Naghdi-Berry and Flügge shell theories. They writes

$$k_{11} = K\left[\left(\frac{m\pi}{L_z}\right)^2 + \frac{1-\nu}{2}\left(\frac{n}{R}\right)^2\right] + \underbrace{\frac{D}{R^2}\frac{1-\nu}{2}\left(\frac{n}{R}\right)^2}_{\text{Flügge}}, \tag{C.1}$$

$$k_{12} = K\frac{1+\nu}{2}\frac{m\pi}{L_z}\frac{n}{R}, \tag{C.2}$$

$$k_{13} = \frac{\nu K}{R}\frac{m\pi}{L} + \underbrace{\frac{D}{R}\left[\left(\frac{m\pi}{L_z}\right)^3 - \frac{(1-\nu)}{2}\frac{m\pi}{L_z}\left(\frac{n}{R}\right)^2\right]}_{\text{Flügge}}, \tag{C.3}$$

$$k_{21} = k_{12}, \tag{C.4}$$

$$k_{22} = K\left[\frac{1-\nu}{2}\left(\frac{m\pi}{L_z}\right)^2 + \left(\frac{n}{R}\right)^2\right] + \underbrace{\frac{D}{R^2}\frac{3\,(1-\nu)}{2}\left(\frac{m\pi}{L_z}\right)^2}_{\text{Flügge}}, \tag{C.5}$$

$$k_{23} = -K\frac{n}{R^2} - \underbrace{D\frac{n}{R^2}\frac{(3-\nu)}{2}\left(\frac{m\pi}{L_z}\right)^2}_{\text{Flügge}}, \tag{C.6}$$

$$k_{31} = \frac{\nu K}{R}\frac{m\pi}{L_z} - \underbrace{\frac{D}{R}\left[\left(\frac{m\pi}{L_z}\right)^3 - \frac{(1-\nu)}{2}\frac{m\pi}{L_z}\left(\frac{n}{R^2}\right)\right]}_{\text{Flügge}}, \tag{C.7}$$

$$k_{32} = -K\frac{n}{R^2} - \underbrace{D\frac{n}{R^2}\frac{(3-\nu)}{2}\left(\frac{m\pi}{L_z}\right)^2}_{\text{Flügge}}, \tag{C.8}$$

$$k_{33} = \frac{K}{R^2} + D\left[\left(\frac{m\pi}{L_z}\right)^2 + \left(\frac{n}{R}\right)^2\right]^2 + \underbrace{\frac{D}{R^4}\left(1-2n^2\right)}_{\text{Flügge}}. \tag{C.9}$$

For the Goldenveizer–Novozhilov shell operator, coefficients yield:

$$k_{22} = K\left[\frac{1-\nu}{2}\left(\frac{m\pi}{L_z}\right)^2 + \left(\frac{n}{R}\right)^2\right] + \underbrace{\frac{D}{R^2}\left[2(1-\nu)\left(\frac{m\pi}{L_z}\right)^2 + \left(\frac{n}{R}\right)^2\right]}_{\text{Goldenveizer}} \tag{C.10}$$

and

$$k_{23} = -K\frac{n}{R^2} - \underbrace{D\frac{n}{R^2}\left[(2-\nu)\left(\frac{m\pi}{L_z}\right)^2 + \left(\frac{n}{R^2}\right)^2\right]}_{\text{Goldenveizer}}. \tag{C.11}$$

For Reissner-Naghdi-Berry shell operator:

$$k_{22} = K\left[\frac{1-\nu}{2}\left(\frac{m\pi}{L_z}\right)^2 + \left(\frac{n}{R}\right)^2\right] + \underbrace{\frac{D}{R^2}\left[\frac{1-\nu}{2}\left(\frac{m\pi}{L_z}\right)^2 + \left(\frac{n}{R}\right)^2\right]}_{\text{Reissner}} \tag{C.12}$$

and

$$k_{23} = -K\frac{n}{R^2} - \underbrace{D\frac{n}{R^2}\left[\left(\frac{m\pi}{L_z}\right)^2 + \left(\frac{n}{R^2}\right)^2\right]}_{\text{Reissner}}. \tag{C.13}$$

The coefficients D and K write respectively:

$$D = \frac{Eh^3}{12(1-\nu^2)} \quad \text{and} \quad K = \frac{Eh}{1-\nu^2}. \tag{C.14}$$

The coeficients a_1, a_1 and a_1 from Eq.(3.25) writes

$$a_1 = -\frac{1}{\rho h}\left[k_{11} + k_{22} + k_{33}\right], \tag{C.15}$$

$$a_2 = \frac{1}{(\rho h)^2}\left[k_{11}k_{22} + k_{11}k_{33} + k_{22}k_{33} - k_{12}k_{21} - k_{13}k_{31} - k_{23}k_{32}\right], \tag{C.16}$$

$$a_3 = \frac{1}{(\rho h)^3}\left[k_{11}k_{23}k_{32} + k_{12}k_{21}k_{33} + k_{12}k_{23}k_{31} + k_{13}k_{21}k_{32} + k_{13}k_{22}k_{31} - k_{11}k_{22}k_{33}\right]. \tag{C.17}$$

The solutions of the bi-cubic equation are

$$\omega_{1mn}^2 = -\frac{2}{3}\sqrt{a_1^2 - 3a_2}\cos\frac{\alpha}{3} - \frac{a_1}{3}, \tag{C.18}$$

$$\omega_{2mn}^2 = -\frac{2}{3}\sqrt{a_1^2 - 3a_2}\cos\frac{\alpha + 2\pi}{3} - \frac{a_1}{3}, \tag{C.19}$$

$$\omega_{3mn}^2 = -\frac{2}{3}\sqrt{a_1^2 - 3a_2}\cos\frac{\alpha + 4\pi}{3} - \frac{a_1}{3}, \tag{C.20}$$

where

$$\alpha = \cos^{-1}\frac{27a_3 + 2a_1^3 - 9a_1a_2}{2\sqrt{\left(a_1^2 - 3a_2\right)^3}}. \tag{C.21}$$

The eigenvector components are given by

$$\frac{A_i}{C_i} = -\frac{k_{13}\left(\rho h\omega_{imn}^2 - k_{22}\right) - k_{12}k_{23}}{\left(\rho h\omega_{imn}^2 - k_{11}\right)\left(\rho h\omega_{imn}^2 - k_{22}\right) - k_{12}^2}, \tag{C.22}$$

$$\frac{B_i}{C_i} = -\frac{k_{23}\left(\rho h\omega_{imn}^2 - k_{11}\right) - k_{21}k_{13}}{\left(\rho h\omega_{imn}^2 - k_{11}\right)\left(\rho h\omega_{imn}^2 - k_{22}\right) - k_{12}^2}. \tag{C.23}$$

The normalization factor $N_{mn} = \int\limits_S ||\mathbf{q}||^2 \mathrm{d}\mathbf{s}$ becomes for $n \neq 0$ and $m \neq 0$,

$$N_{mni} = \left[\left(\frac{A_{mni}}{B_{mni}}\right)^2 + \left(\frac{B_{mni}}{C_{mni}}\right)^2 + 1\right]\frac{L_z R\pi}{2} \tag{C.24}$$

and for $n = 0$, $m \neq 0$,

$$N_{mni} = \left[\left(\frac{A_{mni}}{B_{mni}}\right)^2 + 1\right] L_z R\pi. \tag{C.25}$$